MICROMECHANICS BASED CONSTITUTIVE MODEL FOR GRANULAR SOLIDS AND ITS IMPLEMENTATION INTO MESHFREE NUMERICAL METHOD

By

Miriam Beatriz Lusk

Submitted to the graduate degree program in the Department of Civil, Environmental, and Architectural Engineering and the Graduate Faculty of the University of Kansas in partial fulfillment of the requirements for the degree of Doctor of Philosophy in Civil Engineering.

_____

Chairperson: Dr. Anil Misra

_____

Dr. Jie Han

_____

Dr. Stanley Rolfe

_____

Dr. Adolfo Matamoros

_____

Dr. Judy Wu

_____

Dr. Christine Sundstrom

Date Defended: September 2nd, 2011.

The Dissertation Committee for Miriam Beatriz Lusk

certifies that this is the approved version of the following dissertation:

MICROMECHANICS BASED CONSTITUTIVE MODEL FOR GRANULAR SOLIDS AND ITS IMPLEMENTATION INTO MESHFREE NUMERICAL METHOD

_____

Chairperson: Dr. Anil Misra

Date approved: September 2nd, 2011.

Abstract

To capture the fracture process and non-linear behavior at the element and structural level of granular materials, concrete, under the presence of pre-existing imperfections, a constitutive model and a mesh free method is derived in this study. For the constitutive model, a micromechanical approach with 2^{nd} gradient theory is used to derive the stress-strain and double stress – strain gradient response of the material. For the mesh-free method, an element-free-Galerkin formulation is used. Results of the simulations show that the model qualitatively describes the failure mechanism and processes at the element and structural level. At the element level, the model describes the failure mechanisms, evolution, and behavior of concrete for different loading conditions (uniaxial, bi-axial, tri-axial, and shear). In addition, the model parameters are related to the material's mechanical properties and geometry, and therefore they have physical meaning. This model can be used to study the material's properties that need to be enhanced and/or modified for a particular interest. At the structural level, the mesh-free method captures the fracture process and evolution of a 2D concrete plate under the presence of two types of inclusions subjected to tensile and compressive loading. Moreover, simulation results show that the proposed element-free-Galerkin mesh-free method overcomes the mesh-subjectivity and does not need adaptive analysis as it is observed in finite element methods.

Keywords: Micromechanics, multi-scale modeling, granular materials, strain-softening, element-free-Galerkin, gradient theory.

Acknowledgement

I will always be grateful to the University of Kansas in the Civil, Environmental, and Architectural Engineering (CEAE) Department, the School of Engineering, and Research & Graduate Studies for the institutional and financial support; and also to the National Science Foundation for its valuable support through the grant NSF-1068528.

My gratitude to the professors of the Civil Engineering Department for all their invaluable teachings, kind advice and the support received from them; many thanks to the committee professors for kindly accepting to be part of my PhD defense committee, and my special thanks to my advisor Prof. Dr. Anil Misra for his dedication, teachings, patience and sound professional advice to do this work.

Also thanks to the staff of the CEAE Department and to Bioengineering Research Center – BERC for their assistance and support; to my fellow students and KU Geotechnical Society - KUGS for their fellowship.

My profound gratitude to my parents, my brothers, and my husband for always being there for me. And, overall my special and deepest gratitude to God for having His strength always at my side.

Table of Contents

Table of Figures

CHAPTER 1. Introduction.

1.1. Introduction.

Concrete is a cohesive and brittle material widely used in the construction industry and its failure behavior is one of the main subjects of study in the civil engineering profession. Numerical models that can accurately describe mechanical properties and the complexity of concrete's non-linear strain-softening behavior are very important in engineering analysis, especially in the presence of imperfections in which increases the strain-softening damage effect on concrete. Moreover, models that can predict concrete's failure response are crucial for designing structures under extreme loading conditions (i.e. earthquake, impact, blast). Most of the current approaches lead to: mathematical models with unstable solutions, mesh-subjectivity and sensitivity that generate unrealistic results, or solutions that have a very high degree of complexity. These deficiencies can be addressed by developing accurate, realistic, and relatively simple models that can be applied in the engineering practice.

1.2. Background.

Strain-softening is a serious phenomenon that triggers catastrophic failure of the material and potentially in the structure. This phenomenon initiates when the material and/or the structure reaches its maximum load-carrying capacity leading to a progressive loss of its carrying capacity and increases in localized deformations. The presence of pre-existing localized deformations will

accelerate this failure process; therefore, we need to understand its fracture behavior to effectively derive a model that captures the failure process. Models based on the traditional continuum mechanics cannot capture this phenomenon because of the continuous-field assumption. Once localized damage exists the material can no longer be treated as a continuous medium. The macro-behavior exhibited under strain-softening can be explained by understanding the underlying mechanism at the micro-level. Thus, the use of micromechanics-based models is appropriate for describing the strain-softening and fracture behavior of the material at the macro-level.

Micromechanics approach offers the advantage that the model parameters are related to the material's structure and properties, and therefore they have physical meaning. Moreover, with the understanding of the model parameters' role on the material response, the model can be used to identify the properties of the material that need to be improved/modify for a specific application. Within micromechanical models the material's structure is visualized as a set of grains/particles in which the particle-to-particle interaction laws determine the constitutive strain-stress relationships which consider the displacement with/without rotational effects. Misra and Yang (2010) derived a micromechanical model to simulate the concrete response under different loading conditions (Figures 1.1-1.3); simulation results show that the model correlates well with experimental data (Figure 1.1). In their model, the particle-to-particle force-displacement interaction is determined by potential functions which are governed by the model parameters.

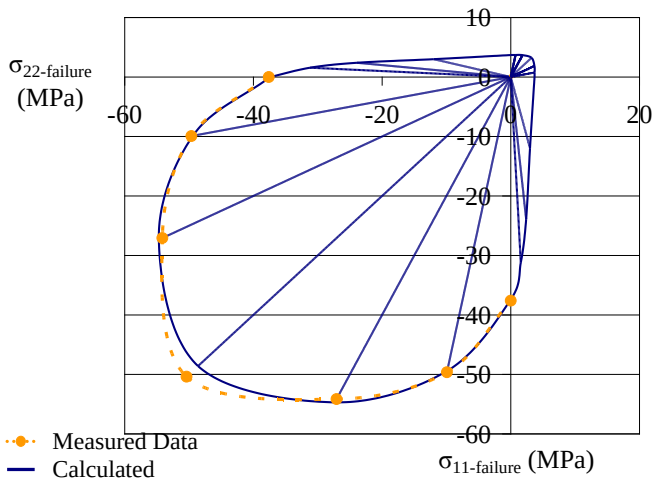

Figure 1.1 Calculated failure envelope under biaxial loading for $\sigma_{33}=0$ showing comparison with measured data (Yin et al. 1989). (Misra and Yang, 2010)

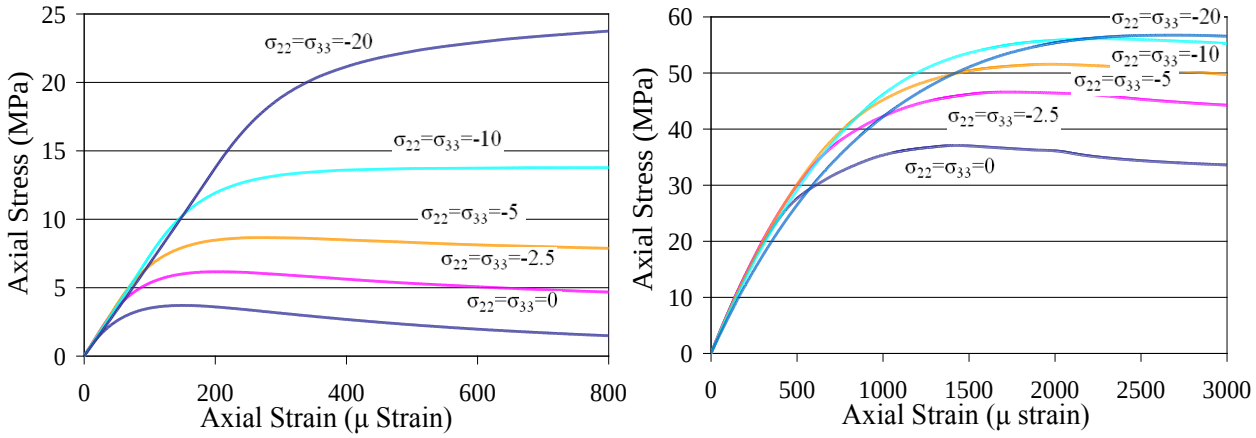

(a) (b)

Figure 1.2 Axisymmetric triaxial stress-strain relationship for (a) tension and (b) compression. (Misra and Yang, 2010)

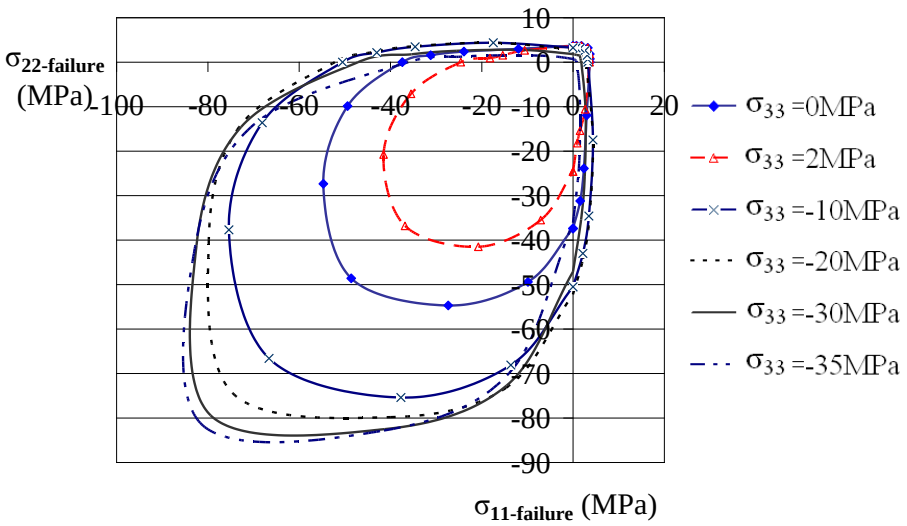

Figure 1.3 Predicted failure envelopes under true triaxial loading calculated for varying σ_{33}. (Misra and Yang, 2010)

Previous studies have shown that the challenge to model the concrete failure behavior using the classical elasticity or elasto-plasticity theory with finite element methods lays in solving for the tangent moduli upon strain-softening of the concrete. Strain-softening changes the sign of the tangent moduli slope to a negative value; this problem causes numerical instabilities and mesh-sensitivity, in which the solutions may lack physical meaning. Mesh-sensitivity problems have been solved in the past using mesh-free formulations such as the element-free-Galerkin (EFG) formulation, which compared to the finite element formulation, is superior in solving solid mechanics strain-softening problems with accuracy (Liu and Gu, 2005).

Proposed solutions to the numerical instabilities by the specialized literature use four different approaches within continuum mechanics. These approaches use four theories: the micropolar, the viscous effects regularization, the non-local, and the gradient theory. The first theory considers an additional rotational degree of freedom which is independent from the displacement field (Mindlin (1969); Chang et al. (2002)). The second considers viscous effects to

derive the constitutive models (Nemes and Speciel (1996); Sandler (1984); de Borst et al. (1993); Needleman (1988)). The third is the non-local theory, in which stresses and strains around a point are derived using a convolution type of integral that evaluates the history of displacements in a finite neighborhood area with respect to the point of interest (Bazant, Belytschko and Chang (1984)). Incorporation of these theories requires the model to consider an additional degree of freedom, time dependence, and define the influence functions for the convolution integral. The fourth theory provides a simpler and more attractive way and considers two approaches: one that takes into account higher order strain gradients and the other that does higher order strains and stress gradients.

The first approach allows localized deformation at finite strain areas in the constitutive models; however, it still presents numerical difficulties when solving the strain-softening phenomena (i.e. the tangent moduli does not retain positive definiteness throughout the strain-softening phenomena). Conversely, the second approach not only provides unconditionally stable numerical solutions but also a realistic description of the strain-softening phenomenon (Chang, Askes and Sluys, 2002). However, this approach presents a very high degree of numerical complexity by requiring additional boundary conditions to solve the partial differential equations (Peerlings, de Borst, Brekelmans, and de Vree (1996); de Borst, Pamin, Peerling and Sluys (1995)).

From these studies, we can conclude that we need a realistic and relative simpler approach that describes the strain-softening behavior of concrete in the presence of imperfections and also overcomes the mesh-subjectivity of the finite element formulation.

1.3. Problem statement, objective and approach.

Mechanical models of the strain-softening phenomena indicate a need for a realistic and relatively simple approach, in which the constitutive models can describe the strain-softening behavior in the presence of imperfections. Furthermore, the discretization of the model governing equations can eliminate the mesh-subjectivity. In this study, we model the strain-softening of concrete, in the presence of localized pre-existing deformations (imperfections), by using 2^{nd} gradient theory to derive the constitutive model. The derived constitutive model includes rotational effects in addition to displacement effects; the latter ones are considered in the evaluation of the model's performance at the element level and structural level. At the structural level, a mesh-free program is developed by implementing the 2^{nd} gradient theory model in a mesh-free (EFG) formulation.

The gradient constitutive laws are based on the micromechanics approach that is based on a pseudo-granular structure to model the macroscopic behavior of the material. The micromechanics approach realistically describes the concrete strain behavior under different loading conditions (uniaxial, biaxial, and triaxial) (Misra and Yang, 2010). Also, the gradient theory implemented into element-free-Galerkin (EFG) method successfully describes the load-deformation behavior of a plate in the presence of a pre-existing imperfection (Yang and Misra, 2010). To simplify our model, an isotropic granular packing structure is used and the 2^{nd} gradient constitutive equations including non-linear strain-softening are derived. Based on an energy approach, the equilibrium equations of the systems are derived and by using the penalty method the enforcement of the boundary conditions is performed. Discretization of the system governing equations is performed using the EFG formulation. Then, the model applicability and ability to

compute and describe the fracture behavior is demonstrated by performing a numerical analysis at the element and structural level. At the element level, the model's performance to qualitatively simulate the behavior of concrete under different loading conditions and the effect of particle size is evaluated. At the structural level, we evaluate the behavior of a 2D plate with two types of inclusions (band and square) subjected to tensile and compressive displacements.

1.4. Overview of next chapters.

Chapter 1 presents an introduction to the study, current status of concrete strain-softening modeling and its deficiencies, the objectives of the study, and the approach used to derive a realistic and relative simpler model that describes the concrete strain-softening phenomenon in the presence of imperfections. Chapter 2 reviews relevant studies on mathematical models applied to describe the strain-softening behavior of concrete. Chapter 3 provides the physical idealization of the concrete and the derivation of the constitutive stress-strain relationships using gradient theory and a micromechanics approach based on a pseudo-granular structure. Chapter 4 describes the discretization of the system governing equations using the EFG formulation and mesh-free method for the numerical implementation and development of a mesh-free program. Chapter 5 provides a qualitative evaluation of the model's performance in the simulation of the fracture process. For the evaluation, we use a 2D concrete plate with two types of inclusions under applied tensile and compressive displacements and different constrained conditions. Finally, chapter 6 presents a summary and conclusions of this study.

CHAPTER 2. Literature Review.

2.1. Introduction.

Strain-softening phenomenon in granular materials (i.e. concrete, ceramics, rocks) can generate substantial damage and cause structural failure. Once the material reaches its maximum load-carrying capacity, we observe a reduction in its structural capability with increasing localized-deformations. The presence of pre-existing imperfections aggravates this phenomenon. Thus we need to understand the material fracture behavior to effectively derive a model that captures the failure process. Traditional continuum mechanics models are based on Hooke's law and assume a continuous material field in the modeling of the material behavior; thus, this approach is not useful when modeling strain-softening and localized deformation effects. On the other hand, the macro failure behavior of the material can be explained by the underlying mechanisms occurring at the microstructural level. In view of this, a micromechanical model offers a promising method for understanding and describing the strain-softening and fracture behavior in the material.

Micro-granular models idealize the material as a network of particles in which modeling of the inter-particle interaction laws is very important. Some researchers have considered displacement effects and others have included rotational effects within the inter-particle relationships. A very good model correlation with experimental data is observed in Misra and Yang's (2010) model. In their model, the particle interactions occur through pseudo-bonds and

are derived using a force-displacement relationship, which is formulated in terms of a potential function that incorporates damage effects and does not need to incorporate a separate damage law (Misra et al. 2003). This approach is inspired by the atomic approach, is also suggested by van Mier (2007). However, this model does not include the rotational effect between particles, which would provide a better representation of the actual loading-restraining conditions.

The scope of this review is to evaluate micromechanics based models that describe the strain-softening and fracture behavior of granular materials and strain-softening modeling approaches. Within the models, we evaluate the inter-particle interaction laws, the model's complexity, and its implementation into numerical methods. In this chapter we first evaluate micromechanics-based granular models used to describe the strain-softening and fracture behavior of granular materials. In this section, the focus is on the idealization of the material structure and the inter-particle interaction relationships to derive the constitutive stress-strain relationships. In the next section, we evaluate the approaches/theories used to model strain-softening, the model's performance when implemented into numerical methods, and the benefits/drawbacks of finite-element and mesh-free numerical methods. Finally, we discuss the best approaches and models and propose a guideline for an accurate, realistic, and relatively simple model.

2.2. Microstructural models.

Granular materials such as concrete, soils, ceramics, and brittle materials can be visualized as a random or regular network/lattice of particles in which the macro-mechanical properties strongly depend on the granular configuration and particle-to-particle contact stiffness at the micro-level. To describe the mechanical failure and fracture behavior of granular materials

(i.e. strain-softening, crack-growth), the traditional continuum mechanics cannot be used since these conditions violate the continuous-field assumption once failure initiates. Therefore, a micromechanics-based approach is needed to derive the macroscopic behavior and the constitutive relationships of the system. Alternative constitutive models of granular materials visualize the material as a set of particles in which virtual internal bonds (VIB), stiffeners, or contact forces act between two-interconnecting particles. Other models simulate the failure and fracture behavior by incorporating higher-order gradients in their constitutive model. These constitutive models are described in this section.

Gao and Klein (1998) propose a VIB model that integrates the atomistic and cohesive surface models. The model simulates the strain-softening and crack-growth phenomena without the need of a pre-defined fracture criterion. In this model, the atoms are viewed as randomly distributed particles connected by cohesive bonds as a substitute for atom potentials. Also, the model incorporates a cohesive law into a random network of cohesive bonds instead of an imposed set of discrete surfaces that is used in surface models. Through the Cauchy-Born rule of crystal elasticity, a cohesive law is directly implemented into the constitutive material's law to derive the constitutive relationships that describes the stress-strain relationships within the material. In the VIB model, radial displacement between two connected particles is restricted by the internal bond. The constitutive relationships between the micro-discrete and macro-continuum level are derived by applying energy principles and the Cauchy-Born rule. The material macro properties, Young's modulus and Poisson's ratio, are related to the bond stiffness property at the micro-discrete level. The use of this model is limited to isotropic materials with a fixed Poisson's ratio. Thiagarajan and Misra (2004) overcome this limitation by modifying and

improving the model. They propose a VIB model that addresses anisotropic materials with a broader range of Poisson's ratios. In their model, anisotropy is incorporated using a density bond function with spherical harmonic expansions to describe the bond orientation concentration. With these modifications, the applicability of the VIB models is extended to a broader range of materials, thus the model provides a more realistic approach (i.e. modeling of anisotropic materials).

A modified version of the VIB model is later introduced by Zhang and Ge (2005), Zhang, Ge, and Li (2006) and Zhang and Ge (2006), who propose a model with virtual multi-dimensional internal bonds (VMIB). The model incorporates an R-bond (shear-bond) in addition to the traditional L-bond (normal bond). The former restricts the relative rotation freedom, while the latter restricts the radial displacement in a two-interconnected particle idealized system. In this model, local deformations and softening of the material are described in a bond-density reduction, which allows researchers to evaluate the underlying failure phenomena at the micro-level by averaging the properties at this level. The bond-density is later integrated over the volume of the material to determine the average stresses and strains. In addition, the model overcomes the Poisson's ratio limitation and thus broader range of ratios can be evaluated.

Taking an alternative granular mechanics approach, Chang and Gao (1996) derive a microstructural model for granular materials. The mechanical properties of the material are dependent on the properties at the micro-level, geometric configuration and contact stiffness between interacting particles. Researchers have proposed to derive the stress-strain relationships that can describe the failure behavior of the material based on interaction of particles. In granular

materials, particle-interaction can also include the rotational effects in addition to the particle displacement upon an applied load or deformation.

As mentioned previously, particle interactions within the granular structure can be visualized as a model equivalent to the lattice network of beam model developed by van Mier (1997) to model fracture behavior of concrete. Chang, Wang, Sluys, and van Mier (2002) propose a model based on the Cosserat theory in which the material is visualized as a lattice network of randomly distributed particles. Within the network, the particles are interconnected by two types of springs: a displacement spring that considers normal and shear stiffnesses, and a rotational spring that considers twisting and rolling stiffnesses.

Movement of a particle is represented by the translation and rotation of the particle; the relative displacements and rotations are obtained from the motion of two-connected-particles. The force-displacement relationships in the model are derived by describing the kinematics of the interacting particles; the relative displacement and rotation are related to the contact force and moment of the inner particle contact. For the derivation of the strain-stress relationships, the lattice network is treated as an equivalent continuum as a replacement of the discrete system. A linear displacement and rotational field are constructed assuming a triangle cell that consists of three particles connected by springs. The Cauchy and couple stresses are obtained by applying the energy balance principle and deriving the strain-stress relationship.

In this model, the material properties (shear modulus, Poisson's ratio, spin modulus and bending modulus) are related to the stiffness constants at the micro-structure level of the lattice spring system. In addition, the damage evolution in the material is dictated by the fracture of the lattice structure with the incorporation of a damage scalar in their formulations. Chang, Wang,

Sluys and van Mier (2002) perform numerical simulations on double edge-notched specimens under uniaxial loading, on double edge-notched specimens under biaxial loading, and on shear-box specimens; results show that this model can describe the concrete's failure and fracture behavior.

In the same line of theory, Misra and Yang (2010) propose a micromechanical model to derive the stress-strain, fracture, and failure behavior of cohesive materials. In this model, the granular material is visualized as a set of grains whose centroids are represented as nodes and the interaction between grains is represented by cohesive-bonds (pseudo-bonds). The behavior of the pseudo-bonds between particles is based on force-laws derived by Misra et al. (2003), which describes the force-displacement relationships that were inspired by the atomic-scale interactions. This approach is recommended by Van Mier (2007), which concludes that the force-displacement approach captures the underlying strain-softening mechanism at the micro-level from which the mechanical behavior at the macro-level can be better described. The model uses a displacement deformation approach that considers the normal and tangential inter-granular behavior; rotational effects are not considered in the derivation of the model. The model successfully correlates to experimental concrete data on uniaxial, biaxial, and triaxial loading tests.

As previously mentioned, discrete models at the micro-structure level have the advantage of accounting for all the microscopic effects; yet in large specimens, the large number of required equations means their use is limited. To address this drawback, researchers who solve this deficiency through continuous models consider the microscopic phenomena by using an average of the microscopic material properties in the model. Traditional continuum models relate

stresses to strains by Hooke's law. This approach does not consider higher-order terms, and is limited to elastic behavior, thus the strain-softening and fracture behavior phenomenon cannot be modeled. Chang, Askes, and Sluys (2002) enhance classical continuous models with higher-order terms of the state variables, which can be either higher-order spatial terms or higher-order temporal (viscous effects). The higher-order spatial terms are divided into gradient models and integral models. The latter models are difficult to implement in finite element analysis because of the difficulty they present in incorporating consistent tangent stiffness matrices and mesh-adaptivity (Pijaudier-Cabot and Huerta, 1991; de Vree et al. 1995).

To evaluate continuum enhanced models using gradient theory, Chang et al. (2002) use two classes of stress: i) standard stresses related to strains and higher-order derivatives of strain, and ii) standard stresses related to strains and higher-order stresses related to the higher-order derivatives of strain. The models also incorporate a linear softening-damage evolution-law into the constitutive equations to describe the strain-softening phenomenon. Evaluation of the models show that the absence of the higher-order stresses lead to instabilities, while the incorporation of higher-order stresses and their conjugate higher-order strains resulted in unconditionally stable solutions that can realistically describe the strain-softening phenomena.

These studies show that the strain-softening phenomenon and fracture behavior at the macro-level are captured by modeling the underlying mechanism at the micro-level. Thus, a micromechanics approach is necessary to establish the constitutive properties at this level to predict the material's behavior at the macro-level. Under this approach, micromechanics based models idealize the material as a network of grains in which the particle-to-particle interaction relationships determine the constitutive laws within the material. The findings suggest that

strain-softening phenomenon and fracture behavior of granular materials, such as concrete, can be successfully modeled with a micro-granular approach that combines gradient theory with force-displacement inter-particle relationships. Also, some studies consider rotational effects within the particle-interactions; therefore, for a more realistic model particle rotation is included in our constitutive model.

2.3. Strain-softening modeling approaches and implementation into numerical simulations.

Modeling of strain-softening phenomenon with the standard continuum theories such as classical elasticity or elastoplasticity can lead to ill-posed problems, invalidation of the uniqueness theorem, and numerical simulations with extreme mesh-sensitivity (i.e. sensitive widths and orientation of localized band deformations). Once the material's tangent-moduli becomes negative, the governing equations become hyperbolic and the loss of ellipticity affects the propagation of the failure zone along the mesh lines. Moreover, solutions that suggest increasing the mesh refinement for convergence yield zero dissipation of energy during failure, which is physically unrealistic (Bazant, Belytschko, and Chang (1984); de Borst el al. (1993); Pietruszczak and Mroz (1981); Sandler (1984); Frantziskonis and Desai (1986); Bazant (1976)). To remedy the numerical deficiencies in the classical theories and to enhance the strain-softening model, four approaches have been proposed: micropolar theory, incorporation of rate-dependence theory or viscous effects, non-local theory, and gradient theory.

Known as the Cosserat theory, micropolar theory considers a rotational field in addition to a displacement field with the corresponding couple and force stresses. This approach describes the damage at the macro-level by evaluating the behavior at the micro-level in which the

commencement of cracks and their propagation throughout the softening period starts. Once damage takes place within in the material, the material becomes anisotropic and its axis rotates which is reflected in the stiffness matrix; this conduct is described by the model but cannot be captured under traditional continuum theories (Mindlin (1969); Chang et al. (2002)).

The rate-dependent theory introduces viscous effects within the constitutive models, as a regularization technique, and leads to well-posed dynamic behavior governing equations that overcome the mesh-size effects. For static behaviors, an equivalent quasi-static loading condition with a long-time limit of dynamic behavior subjected to slow-loading can be used (Nemes and Speciel (1996); Sandler (1984); de Borst et al. (1993), Needleman (1988)). This results in well-posed equations, but the integration of the differential equations under a constant rate has a rate effect on the stress-strain curve; at higher rates, the stress-strain curve vales are magnified (Bazant, Belytscho, and Chang (1984)).

Non-local theory is initially proposed by Kroner (1967) and further implemented on strain-softening models by Bazant, Belytschko and Chang (1984). In this theory, stresses at a point are related to displacements and the displacement history, within a finite volume, located in an area proximate to the point; the history of displacement is accounted for with a convolution type of integral. The theory may also consider the strains and strain gradients history to determine strains and stresses at the point of interest. This approach prevents damage-localization on a zero measure, decreases the progressive deformation, and restricts the localization to a domain with a definite size; ensuring energy dissipation during strain-softening. On the other hand, this approach is sensitive to strain gradients and requires double averaging (strains and stresses) to obtain symmetry in the stiffness matrix. Furthermore, the constitutive

equations need to be divided into two laws: local and nonlocal. The latter one is used on strain-softening only. This is to ensure stable numerical solutions (Belytschko, Bazant, Hyun, and Chang (1986); de Vree, Brekelmans, and van Gils (1995); Murakami, Kendall, and Valanis (1992)).

Gradient theories have been proposed that incorporate higher-order deformation gradients into the constitutive law. These approaches not only solve the ellipticity problem, but also provide a simpler method. Also, the gradient approach has no rate effects and no dependence on "weak zones" in the solid. Moreover, it does not require determining influence functions for the convolution integrals used in the classical non-local models (Triantafyllidis and Bardenhagen (1993)). Gradient theory grants locality, in a mathematical sense, and can be successfully incorporated into damage models to simulate the localization phenomenon; a length scale factor is introduced that determines the size of the localization zone. Localization of deformation is observed when failure in small zones occurs within the material. High strain levels develop rapidly in the failure zone while very small strains are observed in the rest of the material. Along with these localizations, a decrease in the load-carrying capacity within the material is observed, which is known as strain-softening. However, incorporation of these strain gradients creates a difficulty, in that additional boundary conditions are needed to solve the partial differential equation and the equilibrium equations (Peerlings, de Borst, Brekelmans, and de Vree (1996); de Borst, Pamin, Peerlings and Sluys (1995)). Gradient theory can be divided into two classes: higher-order strain gradient theory and higher-order strains and stress gradient theory, the latter is more rigorous.

Models with higher-order strain theory model the localized-deformation phenomenon at finite strains, yet the tangent moduli does not retain positive definiteness throughout the strain-softening phenomenon. This leads to mathematical difficulties when modeling strain-softening. Conversely, higher-order gradient theory, which considers strains and their conjugate stresses, provides a more complex but robust approach that leads to unconditional stable solutions (Chang, Askes and Sluys, 2002). Chang and his coworkers evaluate the higher-order gradient models in which the Cauchy stresses and higher-order stresses are expressed in terms of the strains and higher-order strain. They also include a length scale parameter in the model through the homogenization process of the discrete particle model. Two analyses are performed. In the first analysis the stresses are related to the strains and higher-order strains; higher order stresses are not considered in this analysis but are included in the second analysis. The results show that the second approach leads to stable and realistic solution, while the first lacks stability.

Evidently higher order gradient theory, strains and their conjugate stresses, lead to unconditionally stable mathematical models that can best describe the strain-softening phenomenon. On the other hand, to obtain an accurate and realistic simulation, mesh-sensitivity needs to be addressed in the numerical implementation of these mathematical models.

Mesh-sensitive problems in numerical simulations have also been addressed and successfully solved by using mesh-free methods such as the element-free-Galerkin method (EFGM). Mesh-free formulations have overcome the drawbacks of the traditional finite element approach which is widely used in solving engineering problems. The finite element approach divides the geometry of a continuum into finite elements that are connected by nodes in a properly defined manner, while the mesh-free formulation only requires a set of nodes with no

interconnectivity information or need for meshing. FEM has limitations including: i) High cost in creating a mesh and dependence in the quality of the mesh creation for adequate modeling, ii) Low accuracy of stresses, in general the stresses at the interfaces are discontinuous and a post-processing stage is needed for accurate stresses, iii) Difficulty in adaptive analysis to ensure the desired accuracy, which requires re-meshing to ensure proper connectivity, and iv) Limitation in the analysis of problems under large deformations (loss of accuracy), problems to simulate crack-growth and breakage of material (Liu and Gu, 2005). We can avoid dealing with elements or meshing in the formulation phase and overcome the FEM deficiencies by using mesh-free methods. These methods use a set of nodes distributed within the domain and its boundary to represent the problem's domain and boundaries. This suppresses the need for a mesh and a pre-defined node-relationship to derive the approximate field functions (Liu and Gu, 2005). In addition, the use of mesh-free methods (EFGM) with gradient-enhanced continuum theories has shown to incorporate the higher-order gradients without increasing the size problem (Askes, Pamin, and de Borst (2000); Pamin, Askes and de Borst (2003)).

Belytschiko, Lu and Gu (1994) evaluate the behavior of a cantilever beam with a parabolic-shear end load, a square plate with a circular hole subjected to unidirectional tensile stresses, and a plate with an edge crack under uniaxial tensile stress using the element-free-Galerkin method. In the model, the moving-least-square approximation method is used to derive the approximation/interpolation function. The dependent variable and its gradient are continuous within the entire domain. Results show that EFGM is very effective and accurate. The model can adequately simulate crack problems and capture the crack-growth process. In addition, advantages over finite element are observed. The performance of the model is not affected by the

nodal arrangement and no post-processing is needed since the output of strains, stresses, and field variables are the actual values. Yang and Misra (2010) propose a constitutive model that incorporates 2^{nd} gradient theory into a mesh-free element-free-Galerkin method using a micromechanics based approach with a granular structure. Evaluation of the model on the strain-softening behavior in 2D plates, with pre-existing imperfections, shows that the model provides a stable and simpler approach to model localized deformations.

The EFGM approach, to enhanced continuous models with gradient theory, has a promising future in developing mathematical models that can be implemented into numerical simulations of granular materials failure and fracture behavior (i.e. strain-softening, crack growth). The gradient theory, with higher-order strain and stress gradients, is unconditionally stable and generates realistic solutions that do not have time dependence, do not require and additional degree of freedom, and do not need to determine influence functions for the convolution integral. Furthermore, the EFGM provides accuracy, efficiency, and mesh-independency to the model. Therefore, the strain-softening phenomenon and fracture behavior on granular materials can be derived in an accurate, realistic, efficient, and relatively simple model.

2.4. Conclusions.

Strain-softening and fracture behavior of granular materials cannot be modeled under the traditional continuum. The underlying failure mechanism relies on the micro-structure and thus micromechanics based approaches provide a solution to this problem. Another challenge is the numerical simulation of this phenomena, traditional finite element presents its drawbacks that can be solved by the use of mesh-free formulations such as the element-free Galerkin method.

Based on the findings of afore-mentioned research, we can draw the following conclusions: First, constitutive models based on force-displacement inter-particle relationships can successfully represent the strain-softening behavior under different load conditions, although the rotational effects are not considered and need to be incorporated. Second, gradient theory provides stable and realistic solutions in strain-softening and fracture behavior. Third, mesh-free formulations such as element-free Galerkin method provide accuracy and mesh-independency in the model which is desirable as no adaptive analysis and mesh are needed. Also, when EFGM is combined with the higher-order gradient theory, localized deformations can be successfully modeled.

Combining these observations and accounting for rotational effects, a micromechanics based constitutive model for granular solids and their implementation into mesh-free numerical methods can be derived. This model will result in a realistic, accurate, and relatively simpler approach to model failure behavior of granular materials in the presence of pre-existing irregularities.

CHAPTER 3. Description of the Granular System and Derivation of the Constitutive Model with Gradient Theory.

This chapter is composed of nine sections. The first section describes the idealization of the material in our model and the kinematics of the granular system. The second section focuses on the local inter-particle constitutive relationships (strain-stress and rotation-moment). The third section presents the derivation of the force-displacement and moment-rotation potential relationships used in our model that include damage effects. In the fourth section, the system with 1st gradient constitutive equations and relationships are derived. The performance of the model under different loading conditions is evaluated in the fifth section at the element and contact levels. In the sixth section, a 2nd gradient constitutive model that considers strain gradients and double stresses is derived. The effect of strain gradients on the Cauchy stresses at the element level is evaluated in section seven. Evaluation of the 2nd gradient constitutive model on qualitatively capturing the effect of particle size on concrete and consolidated nano-iron is performed in section eight. The effect of aggregate gradation on concrete behavior is described in the last section.

3.1. Idealization and kinematics of the granular system.

The material is idealized as a lattice of spherical grains connected by pseudo-bonds. The centroids of the grains are represented as points in Figure 3.1 in which each grain has six degrees of freedom: three displacements and three rotational degrees of freedom (Misra et al. 2003).

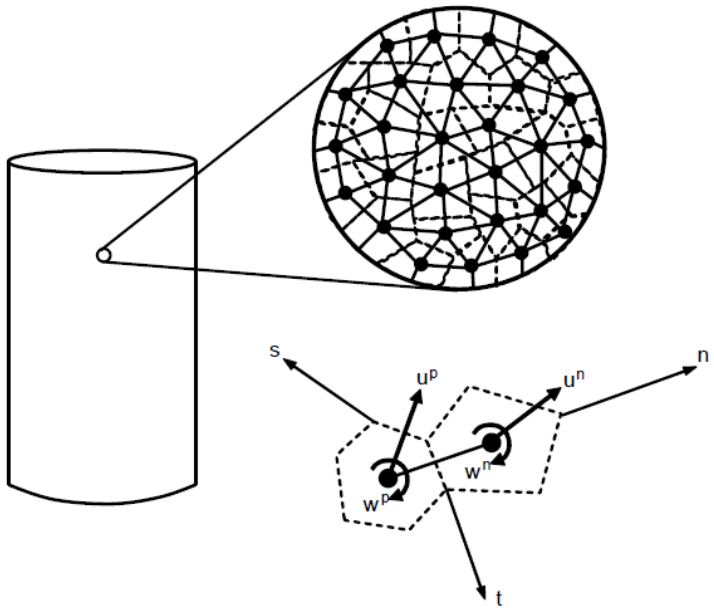

Figure 3.1: Schematic of granular model of a continuum (Misra et al. 2003).

At the contact surface, three unit vectors (*n*, *s*, *t*) are considered to form a Cartesian coordinate system, where *n* is normal to the contact surface and the other two orthogonal vectors, *s*, *t* are on the contact surface (Figure 3.2). These vectors are defined in a spherical coordinate system as follows:

$$n = \cos\theta\, e_1 + \sin\theta\cos\phi\, e_2 + \sin\theta\sin\phi\, e_3$$

$$s = \frac{\partial n}{\partial \theta} = -\sin\theta\, e_1 + \cos\theta\cos\phi\, e_2 + \cos\theta\sin\phi\, e_3 \tag{3.1}$$

$$t = n \times s = -\sin\phi\, e_2 + \cos\phi\, e_3$$

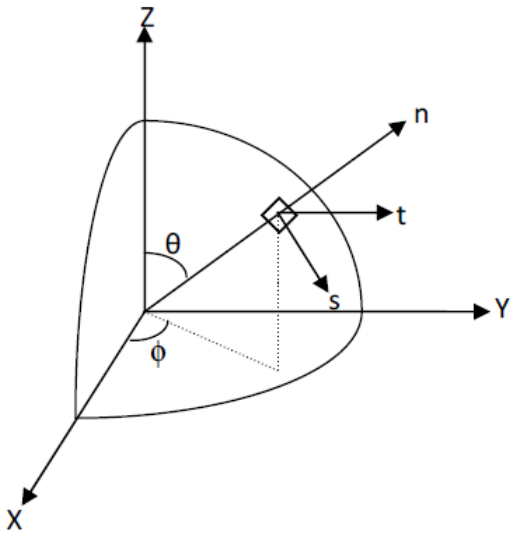

Figure 3.2: Local coordinate system at the particle-to-particle contact surface (Yang and Misra, 2010).

Under an applied load, these grains may undergo displacements and/or rotations, where the relative displacement δ_i^{pn} and rotation θ_i^{pn} between two particles is described by the following motion equations:

$$\delta_i = u_i^n - u_i^p + e_{ijk}\left(\omega_j^n r_k^n - \omega_j^p r_k^p\right) \tag{3.2}$$

$$\theta_i = \omega_i^n - \omega_i^p \tag{3.3}$$

Where u_i = particle displacement; ω_j = particle rotation; r_k = particle centroid-contact vector; e_{ijk} = permutation symbol.

The relative displacement and rotation between two particles can be decomposed into four components: two displacements and two rotations which are described in equations 3.4-3.7. From the two displacement components, δ_n is the normal component acting along the pseudo-

bond that connects two particles and the other component is tangential to the pseudo-bond and is denoted by δ_w. From the two rotation components, θ_n is the normal component along the pseudo-bond and θ_s is component along the tangential direction.

$$\delta_n = \delta_i n_i \tag{3.4}$$

$$\delta_w = \sqrt{(\delta_i s_i)^2 + (\delta_i t_i)^2} \tag{3.5}$$

$$\theta_n = \theta_i n_i \tag{3.6}$$

$$\theta_s = \sqrt{(\theta_i s_i)^2 + (\theta_i t_i)^2} \tag{3.7}$$

Following an increment of deformation, the distance between two particles, L_0, becomes $L_o+\delta_n$, where L_0 is the initial center-to-center distance between two particles and the tangential distortion between two particles, w, becomes δ_w. Similarly, the rotation between two particles, θ_0, becomes $\theta_0+\delta\theta_0$, where θ_0 is the initial inter-particle rotation and the tangential rotation, θ_s, becomes $\delta_{\theta s}$.

3.2. Inter-particle local constitutive relationships.

Interactions between two neighboring particles: incremental contact force and moment, Δf_i^c and Δm_i^c, can be related to relative incremental displacement and rotation, $\Delta\delta_i$ and $\Delta\theta_i$, through the contact displacement stiffness K_{ij}^c and the contact rotational stiffness G_{ij}^c. This relationship is explained as:

$$\Delta f_i^c = K_{ij}^c \Delta \delta_j^c \tag{3.8}$$

$$\Delta m_i^c = G_{ij}^c \Delta \theta_i^c \tag{3.9}$$

Where K_{ij}^c and G_{ij}^c are written in terms of the stiffness components in the normal direction K_n, G_n, and tangential direction K_w, G_s as:

$$K_{ij}^c = K_n^c n_i n_j + K_w^c \left(s_i s_j + t_i t_j \right) \tag{3.10}$$

$$G_{ij}^c = G_n^c n_i n_j + G_s^c \left(s_i s_j + t_i t_j \right) \tag{3.11}$$

As mentioned previously, n, s, and t are the unit vectors of the local coordinate system at each contact surface (Figure 3.2).

3.3. Contact force-displacement and moment-rotation relationship.

Inspired in the atomic-interaction potentials and using an energy approach, the particle-to-particle interaction through the pseudo-bond is formulated in terms of potential functions, $\Phi(L, w)$, by considering the center-to-center distance, *L*, and the tangential distortion, *w*, between two inter-connected particles from the initial equilibrium position (Misra et al. 2003). Similarly, rotational effects can be incorporated in terms of potential functions, $\Phi(\theta_n, \theta_s)$, by considering the relative rotation in the normal and tangential direction (θ_n, θ_s). These potentials are calculated by the addition of a central potential and a non-central potential, $\phi(L) + \varphi(w)$ and $\phi(\theta_n) + \varphi(\theta_s)$, respectively.

$$\Phi(L, w) = \phi(L) + \varphi(w) \tag{3.12a}$$

$$\Phi(\theta_n, \theta_s) = \phi(\theta_n) + \varphi(\theta_s) \tag{3.12b}$$

These potential functions represent the behavior of the pseudo-bonds between two inter-connected particles (stretching, sliding, twisting, and rolling). The pseudo-bond is expected to account for the sub-granular scale mechanisms, scale yielding, and damage within the material when subjected to different loading conditions. For example, under compression in contrast to tension, greater energy is needed to initiate damage resulting in a deeper potential, with a well shape, for the non-central potential $\phi(w)$. Figure 3.3 shows schematic shapes for the potential functions, from which the point of lowest potential corresponds to the point of equilibrium. At this point, $L = L_o$ and $w = 0$.

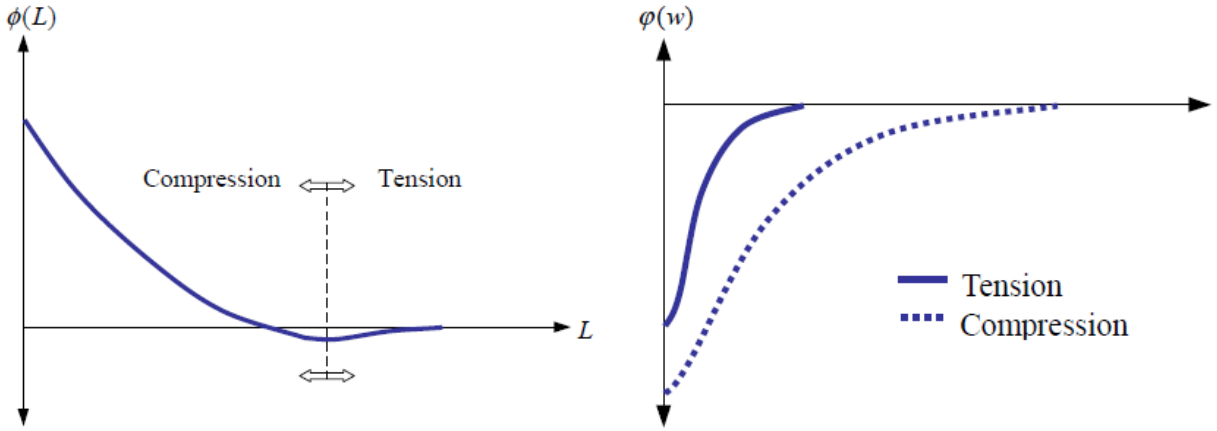

Figure 3.3: Schematic pseudo-potential functions in normal and tangential direction (Misra et al. 2003)

When considering the rotational effects, twisting and rolling, the lowest potential corresponds to the equilibrium position when θ_n and θ_s are zero. Figure 3.4 shows the schematic for rotational potential functions.

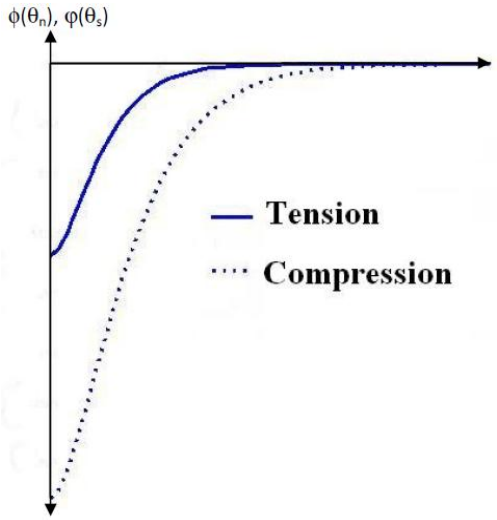

Figure 3.4: Schematic pseudo-potential rotational functions in normal and tangential direction.

The pseudo-potential functions that govern the normal and tangential functions were derived by Misra et al (2003), from which the normal and tangential contact-force functions are obtained by differentiating the potential functions.

$$f_n = \frac{\partial \Phi}{\partial L} = A\delta_n e^{-\left(\frac{\delta_n}{B}\right)} \qquad \text{for tension} \qquad (3.13)$$

$$f_n = \frac{\partial \Phi}{\partial L} = A\delta_n - \frac{A}{2\alpha_1}\left[\ln\left(1-\tanh\alpha_1\delta_n\right) - \ln\left(1+\tanh\alpha_1\delta_n\right)\right] \qquad \text{for compression} \qquad (3.14)$$

$$f_w = \frac{\partial \Phi}{\partial w} = C\delta_w e^{-\left(\frac{\delta_w}{D}\right)} \qquad \text{for tension} \qquad (3.15)$$

$$f_w = \frac{\partial \Phi}{\partial w} = C\delta_w e^{-\left(\frac{\delta_w}{\alpha_2 D}\right)} \qquad \text{for compression} \qquad (3.16)$$

Similarly, the contact-moment functions are derived as follows:

$$m_n = \frac{\partial \Phi}{\partial \theta_n} = g_n \delta_{\theta n} e^{-\left(\frac{\delta_{\theta n}}{Mn}\right)} \qquad \text{for tension} \qquad (3.17)$$

$$m_n = \frac{\partial \Phi}{\partial \theta_n} = g_n \delta_{\theta n} e^{-\left(\frac{\delta_{\theta n}}{\alpha_3 Mn}\right)} \qquad \text{for compression} \qquad (3.18)$$

$$m_s = \frac{\partial \Phi}{\partial \theta_s} = g_s \delta_{\theta s} e^{-\left(\frac{\delta_{\theta s}}{Ms}\right)} \qquad \text{for tension} \qquad (3.19)$$

$$m_s = \frac{\partial \Phi}{\partial \theta_s} = g_s \delta_{\theta s} e^{-\left(\frac{\delta_{\theta s}}{\alpha_4 Ms}\right)} \qquad \text{for compression} \qquad (3.20)$$

Figure 3.5 and 3.6 plot the force and moment functions with respect to the normal and tangential deformation of the pseudo-bonds. From figure 3.5, we can observe that under compression the gradual damage, or scale yielding, in the material is reflected by the flattening of the central-force and by the softening-like behavior in the tangential force.

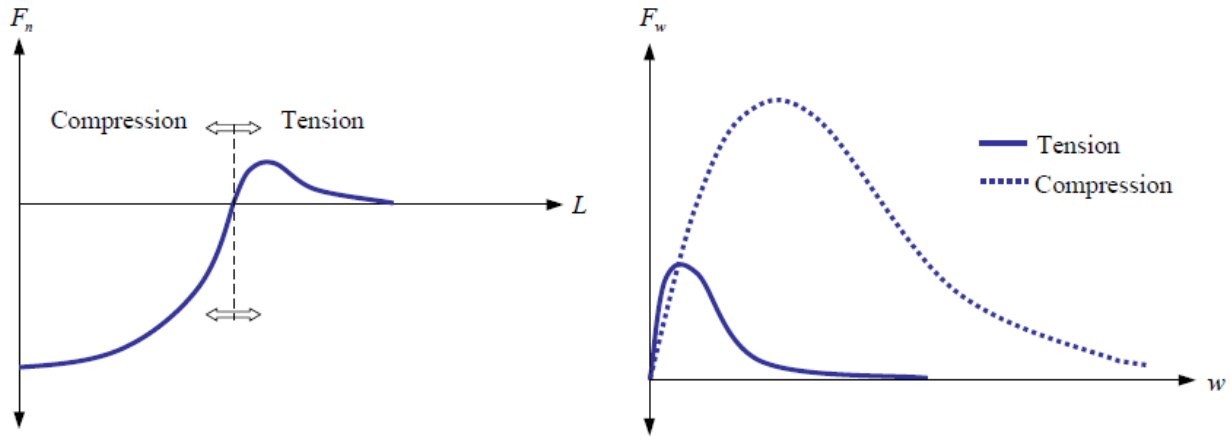

Figure 3.5: Force functions in the normal and tangential directions (Misra et al. 2003).

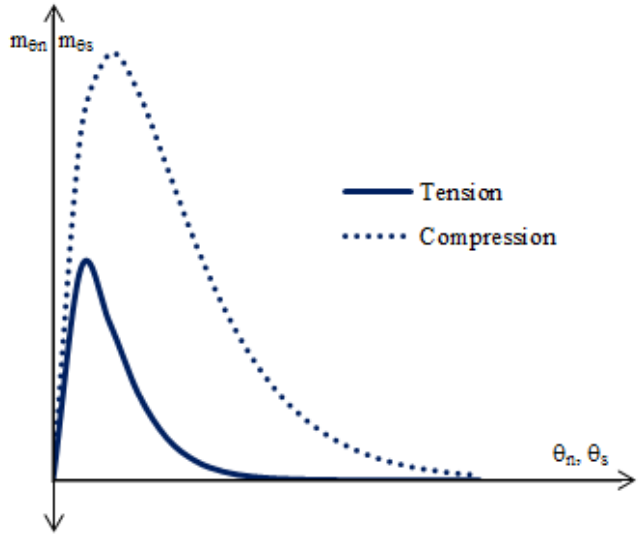

Figure 3.6: Moment functions in the normal and tangential directions.

In Figure 3.6, the rotational effects will either have a twisting or rolling effect among the particles. Under twisting, similar to shear, a softening of the material following the peak moment is expected. Similarly, under rolling effects, we can assume that debonding among particles is initiated and softening of the material is expected to happen. In addition, we consider that there is coupling between stretching stresses and rotational stresses, and thus the material is expected to be stronger in compression than in tension.

Based on these force and moment functions, the particle-to-particle increment in force and moment, Δf_i and Δm_i, can be related to the increment of the relative displacement $\Delta\delta_i$ and relative rotation $\Delta\theta_i$, through the displacement stiffness K_{ij} and rotational stiffness G_{ij}, respectively.

$$\Delta f_i = K_{ij}\Delta\delta_j \tag{3.21}$$

$$\Delta m_i = G_{ij}\Delta\theta_j \tag{3.22}$$

Where the displacement stiffness, K_{ij}, and the rotational stiffness, G_{ij}, are written in terms of the normal and tangential direction as shown in equations (3.10-3.11). The displacement and rotational stiffnesses in the normal direction, K_n and G_n, and in the tangential direction, K_w and G_s, are obtained by differentiation of the force functions as follows:

$$K_n = \frac{\partial f_n}{\partial L} = -\frac{A\, e^{-\left(\frac{\delta_n}{B}\right)}\left(-B+\delta_n\right)}{B} \qquad \text{for tension} \tag{3.23}$$

$$K_n = \frac{\partial f_n}{\partial L} = A\left[1+\tanh\left(\alpha_1\delta_n\right)\right] \qquad \text{for compression} \tag{3.24}$$

$$K_w = \frac{\partial f_w}{\partial w} = \frac{C\, e^{-\left(\frac{\delta_w}{D}\right)}\left(D-\delta_w\right)}{D} \qquad \text{for tension} \tag{3.25}$$

$$K_w = \frac{\partial f_w}{\partial w} = \frac{C\, e^{-\left(\frac{\delta_w}{\alpha_2 D}\right)}\left(\alpha_2 D-\delta_w\right)}{\alpha_2 D} \qquad \text{for compression} \tag{3.26}$$

$$G_n = \frac{\partial m_n}{\partial \theta_n} = g_n e^{-\left(\frac{\delta_{\theta n}}{Mn}\right)} \frac{\left(M_n - \delta_{\theta n}\right)}{M_n} \quad \text{for tension} \qquad (3.27)$$

$$G_n = \frac{\partial m_n}{\partial \theta_n} = g_n e^{-\left(\frac{\delta_{\theta n}}{\alpha_3 Mn}\right)} \frac{\left(\alpha_3 M_n - \delta_{\theta n}\right)}{\alpha_3 M_n} \quad \text{for compression} \qquad (3.28)$$

$$G_s = \frac{\partial m_s}{\partial \theta_s} = g_s e^{-\left(\frac{\delta_{\theta s}}{Ms}\right)} \frac{\left(M_s - \delta_{\theta s}\right)}{M_s} \quad \text{for tension} \qquad (3.29)$$

$$G_s = \frac{\partial m_s}{\partial \theta_s} = g_s e^{-\left(\frac{\delta_{\theta s}}{\alpha_4 Ms}\right)} \frac{\left(\alpha_4 M_s - \delta_{\theta s}\right)}{\alpha_4 M_s} \quad \text{for compression} \qquad (3.30)$$

Figures 3.7 and 3.8 show stiffness relationships with respect to the normal, tangential, and rotational deformation of the pseudo-bonds.

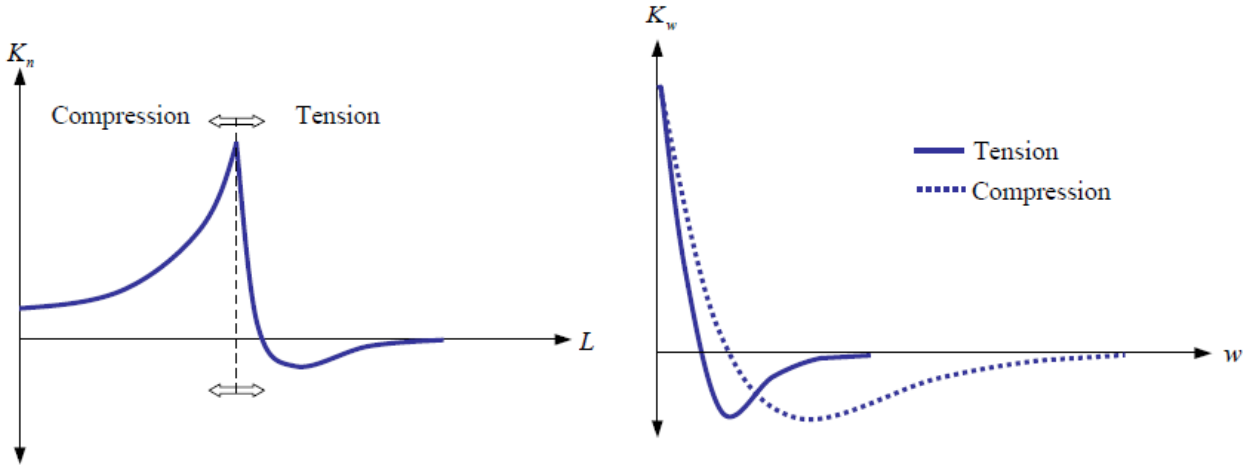

Figure 3.7: Displacement stiffness functions in the normal and tangential directions. (Misra et al. 2003)

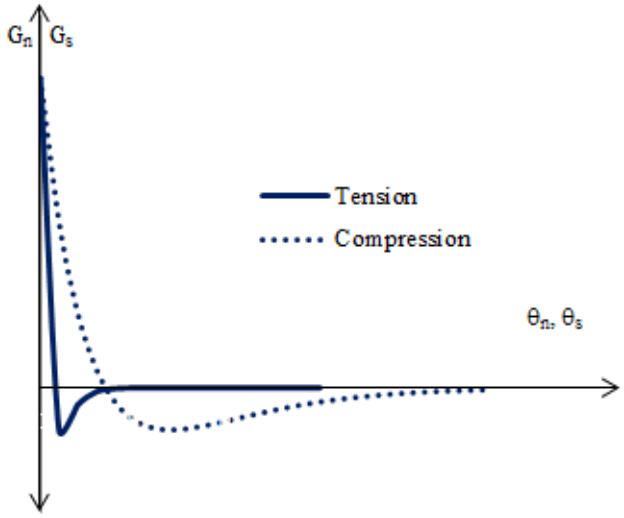

Figure 3.8: Rotational stiffness functions in the normal and tangential directions.

3.4. Constitutive relationship for the idealized system using the 1st gradient theory.

Following Chang and Ma (1991) and Chang et al. (2002) approaches, a displacement and rotational field are determined using a Taylor series expansion, upon which the displacement and rotation at the particle *n* can be determined by using the gradients at the reference point, x^0. This point is defined as the center of the representative volume as follows:

$$u_i\left(x^n\right)=u_i\left(x^0\right)+u_{i,j}\left(x^0\right)x_j \tag{3.31}$$

$$\omega_i\left(x^n\right)=\omega_i\left(x^0\right)+\omega_{i,j}\left(x^0\right)x_j \tag{3.32}$$

Where x_i^n is the coordinate of the particle *n* centroid. $u_{i,j}$, and $\omega_{i,j}$ are the gradients of displacement and rotation, respectively.

Assuming a uniform particle radius *r* and that the origin of the local coordinates is at the pth particle, and by substituting equations (3.31) and (3.32) into equations (3.2) and (3.3), the relative displacement and rotation at the contact surface becomes:

$$\delta_i^c = \left(u_{i,k} - e_{ijk}\omega_j\right)l_k^c - e_{ijk}\omega_{j,l}J_{kl}^c \tag{3.33}$$

$$\theta_i^c = \omega_{i,j}l_j^c \tag{3.34}$$

Where the geometric quantities:

$$\begin{aligned} l_j^c &= x_j^n - x_j^p \\ l_j^c r_k^c &= x_j^n r_k^n - x_j^p r_k^p \\ J_{jk}^c &= \frac{1}{2}l_j^c l_k^c = l_j^c r_k^c \end{aligned} \tag{3.33.a}$$

And:

$$\begin{aligned} l_j^c &= 2rn_j^c \\ l_j^c r_k^c &= 2r^2 n_j^c \end{aligned} \tag{3.33.b}$$

From equations (3.33) and (3.34), we determine the polar strain γ_{jl}^0 and the deformation strain tensors ε_{ik}^0 as:

$$\gamma_{jl}^0 = \omega_{j,l} \tag{3.35}$$

$$\varepsilon_{ik}^0 = u_{i,k} - e_{ijk}\omega_j \tag{3.36}$$

In addition, the following substitutions are performed:

$$\gamma_{jl}^{0} = \frac{\partial \omega_j}{\partial x_l} \tag{3.35a}$$

$$\phi_i = u_i - e_{ijk}\omega_j x_k \tag{3.36a}$$

$$\varepsilon_{ik}^{0} = \phi_{ik} = u_{i,k} - e_{ijk}\omega_j = \frac{\partial \phi_i}{\partial x_k} \tag{3.36b}$$

Where the symmetric part of ϕ_{ik}, in equation (3.36b), corresponds to the symmetrical part of the displacement gradient and represents the stretch strain (Chang and Ma, 1991).

$$\phi_{(ik)} = u_{(i,k)} = \frac{1}{2}\left(u_{i,k} + u_{k,i}\right) \tag{3.37}$$

The non-symmetric part of ϕ_{ik} is given by the difference between the rigid body rotation and angular rotation as follows:

$$\phi_{[ik]} = u_{[ik]} - e_{ijk}\omega_j = \frac{1}{2}\left(u_{i,k} - u_{k,i}\right) - e_{ijk}\omega_j \tag{3.38}$$

Where the angular rotation ψ, corresponding to the rigid body rotation, becomes:

$$e_{ijk}\psi_j = u_{[ik]} \tag{3.39}$$

And equation (3.38) represents the rotational difference between particle and rigid body rotation, which is known as the *net particle spin* (Chang and Ma, 1991), and it is rewritten as:

$$\phi_{[ik]} = e_{ijk}\left(\psi_j - \omega_j\right) = e_{ijk}\left(u_{[ik]} - \omega_j\right) \tag{3.40}$$

From an energy approach, the counter part of the polar strain and the deformation strain tensors, described in equations (3.35) and (3.36), are the couple and Cauchy stresses. The constitutive relationships can be derived by considering a representative volume *V*, in which the strain energy can be written in terms of forces/moments and in term of stresses as described in equations (3.41) and (3.42):

$$W = \frac{1}{2V}\sum_{c=1}^{N} f_i^{\,c}\delta_i^{\,c} + m_i^{\,c}\theta_i^{\,c} \tag{3.41}$$

$$W = \frac{1}{2V}\sum_{c=1}^{N}\left(\sigma_{ik}^{\,0}\varepsilon_{ik}^{\,0} + M_{il}^{\,0}\gamma_{il}^{\,0}\right) \tag{3.42}$$

Where *N* refers to the total number of contacts within the representative volume V, and σ_{ij} and M_{ij} corresponds to the Cauchy and couple stresses, respectively.

By substituting equations (3.33-3.34) into (3.41-3.42), the stresses can be rewritten as:

$$\sigma_{ik}^{0} = \frac{1}{2V}\sum_{c=1}^{N} f_i l_k \tag{3.43}$$

$$M_{jl}^{0} = \frac{1}{2V}\sum_{c=1}^{N} \delta_{ij} m_i^c l_l - f_i^c e_{ijk} J_{kl} \tag{3.44}$$

By substituting equations (3.8-3.9) into incremental form of (3.43-3.44), the constitutive stress-strain relationships are determined and written as:

$$\Delta \sigma^{0}_{ik} = A_{ikql}\Delta \varepsilon^{0}_{ql} + B_{ikjm}\Delta \gamma^{0}_{jm}$$
$$\Delta M^{0}_{jl} = C_{jlmp}\Delta \varepsilon^{0}_{mp} + D_{jlqr}\Delta \gamma^{0}_{qr} \tag{3.45}$$

For further consideration, we know that B_{ikjm} and C_{jlmp} are zero; therefore, equation (3.45) becomes:

$$\Delta \sigma^{0}_{ik} = A_{ikql}\Delta \varepsilon^{0}_{ql}$$
$$\Delta M^{0}_{jl} = D_{jlqr}\Delta \gamma^{0}_{qr} \tag{3.46}$$

where:

$$A_{ikql} = K_{iq} l_l l_k$$
$$D_{jlqr} = \left(G_{iq} l_l \delta_{ij} l_r + e_{ijk} J^{c}_{kl} K_{im} e_{mqp} J^{c}_{pr}\right) \tag{3.47}$$

Which can also be written as:

$$A_{ikql} = \frac{4r^2}{2V}\sum_{c=1}^{N} K_{iq} n_l n_k$$
$$D_{jlqr} = \frac{4r^2}{2V}\sum_{c=1}^{N}\left(G_{iq} n_l \delta_{ij} n_r + r^2 e_{ijk} n_k n_l K_{im} e_{mqp} n_p n_r\right) \tag{3.48}$$

The summation of the inter-granular interactions over the entire representative volume can be expressed in an integral form by using a directional truncated density function in terms of spherical harmonic expansions (Yang and Misra, 2010) as follows:

$$\xi(\theta,\phi) = \frac{1}{4\pi}\left[1 + \frac{1}{4}a_{20}(3\cos 2\theta + 1) + 3\sin^2\theta\left(a_{22}\cos 2\phi + b_{22}\sin 2\phi\right)\right] \tag{3.49}$$

where: a_{20}, a_{22}, b_{22} are the fabric parameters that determine the anisotropy of the material. Then, equation (3.48) can be written into an integral form as:

$$A_{ikql} = \frac{4r^2 N}{2V} \int_{\Omega} K_{iq} n_k n_l \xi(\theta,\phi) d\Omega$$
$$D_{jlqr} = \frac{4r^2 N}{2V} \int_{\Omega} \left(G_{iq} n_l \delta_{ij} n_r + r^2 e_{ijk} n_k n_l K_{im} e_{mqp} n_p n_r \right) \xi(\theta,\phi) d\Omega \quad (3.50)$$

Where the integration $\int_{\Omega}(\ )d\Omega = \int_0^{2\pi}\int_0^{\pi}(\ )\sin\theta d\theta d\phi$; and $N\xi(\theta,\phi)$ is the number of contacts in the interval Ω to $\Omega + d\Omega$ multiplied by the directional bond density function.

Within this derived theory, we can identify two main factors that play an important role in the material's behavior: strain (ε_{ql}^0) and rotation gradient (γ_{qr}^0). To determine and fully understand the complex role of these two factors on the material's failure behavior, they need be studied separately. Therefore, in this study we pursue the study of the strain's role alone. Study of the strain effect on the 1st gradient theory constitutive model is described in section 3.5. Study of the rotational gradient effects along, and combined, with the strain effects using this model will be performed in a future work.

To study the coupling effect described in the constitutive equations, a higher order term is incorporated in the displacement field on section 3.6 and a new constitutive model is derived. This modification enhances the 1st gradient theory to a 2nd gradient theory model that incorporates strain gradients to the constitutive equations, which cannot be added with the traditional continuum mechanics approach.

For infinitesimally small strains, the stiffnesses K_n and K_w reduce to a constant value and the initial moduli A_{ikql} can be obtained from the closed form integration where:

$$\Delta\sigma_{ik} = A_{ikql}\Delta\varepsilon_{ql}$$

$$\begin{bmatrix}\Delta\sigma_{11}\\ \Delta\sigma_{22}\\ \Delta\sigma_{33}\\ \Delta\sigma_{12}\\ \Delta\sigma_{13}\\ \Delta\sigma_{23}\\ \Delta\sigma_{21}\\ \Delta\sigma_{31}\\ \Delta\sigma_{32}\end{bmatrix} = \begin{bmatrix} A_{1111} & A_{1122} & A_{1133} & 0 & 0 & A_{1123} & 0 & 0 & A_{1132}\\ & A_{2222} & A_{2233} & A_{2212} & 0 & A_{2223} & 0 & 0 & A_{2232}\\ & & A_{3333} & 0 & 0 & A_{3323} & A_{3332} & 0 & 0\\ & & & A_{1212} & A_{1213} & 0 & A_{1221} & A_{1231} & 0\\ & & & & A_{1313} & 0 & A_{1321} & A_{1331} & 0\\ & & \text{Symmetric} & & & A_{2323} & 0 & 0 & A_{2332}\\ & & & & & & A_{2121} & A_{2131} & 0\\ & & & & & & & A_{3131} & 0\\ & & & & & & & & A_{3232}\end{bmatrix}\begin{bmatrix}\Delta\varepsilon_{11}\\ \Delta\varepsilon_{22}\\ \Delta\varepsilon_{33}\\ \Delta\varepsilon_{12}\\ \Delta\varepsilon_{13}\\ \Delta\varepsilon_{23}\\ \Delta\varepsilon_{21}\\ \Delta\varepsilon_{31}\\ \Delta\varepsilon_{32}\end{bmatrix} \tag{3.51}$$

$$A_{1111} = L_0^2 N_p\left[\frac{1}{105}\left(14K_w + 12K_n a_{20} + 21K_n + 2K_w a_{20}\right)\right] \tag{3.52}$$

$$A_{1122} = L_0^2 N_p\left[-\frac{1}{105}\left(-6K_n a_{22} + 6K_w a_{22} - K_n a_{20} + K_w a_{20} - 7K_n + 7K_w\right)\right] \tag{3.53}$$

$$A_{1133} = L_0^2 N_p\left[\frac{1}{105}\left(-6K_n a_{22} + 6K_w a_{22} + K_n a_{20} - K_w a_{20} + 7K_n - 7K_w\right)\right] \tag{3.54}$$

$$A_{1123} = L_0^2 N_p\left[-\frac{2}{35}\left(b_{22}K_n + b_{22}K_w\right)\right] \tag{3.55}$$

$$A_{1132} = L_0^2 N_p\left[-\frac{2}{35}\left(-b_{22}K_n + b_{22}K_w\right)\right] \tag{3.56}$$

$$A_{2222} = L_0^2 N_p\left[\frac{1}{105}\left(-K_w a_{20} + 36K_n a_{22} + 21K_n - 6K_n a_{20} + 6K_w a_{22} + 14K_w\right)\right] \tag{3.57}$$

$$A_{2233} = L_0^2 N_p\left[\frac{1}{105}\left(7K_n - 7K_w - 2K_n a_{20} + 2K_w a_{20}\right)\right] \tag{3.58}$$

$$A_{2223} = L_0^2 N_p \left[-\frac{6}{35}\left(-b_{22}K_n + b_{22}K_w\right) \right] \tag{3.59}$$

$$A_{2232} = L_0^2 N_p \left[\frac{2}{35}\left(3b_{22}K_n + 4b_{22}K_w\right) \right] \tag{3.60}$$

$$A_{3333} = L_0^2 N_p \left[-\frac{1}{105}\left(K_w a_{20} + 36K_n a_{22} - 21K_n + 6K_n a_{20} + 6K_w a_{22} - 14K_w\right) \right] \tag{3.61}$$

$$A_{3323} = L_0^2 N_p \left[\frac{2}{35}\left(3b_{22}K_n + 4b_{22}K_w\right) \right] \tag{3.62}$$

$$A_{3332} = L_0^2 N_p \left[-\frac{6}{35}\left(-b_{22}K_n + b_{22}K_w\right) \right] \tag{3.63}$$

$$A_{1212} = L_0^2 N_p \left[-\frac{1}{105}\left(-13K_w a_{20} - 7K_n - K_n a_{20} + 6K_w a_{22} - 6K_n a_{22} - 28K_w\right) \right] \tag{3.64}$$

$$A_{1213} = L_0^2 N_p \left[-\frac{2}{35}\left(-b_{22}K_n + b_{22}K_w\right) \right] \tag{3.65}$$

$$A_{1221} = L_0^2 N_p \left[-\frac{1}{105}\left(-6K_n a_{22} + 6K_w a_{22} - K_n a_{20} + K_w a_{20} - 7K_n + 7K_w\right) \right] \tag{3.66}$$

$$A_{1231} = L_0^2 N_p \left[-\frac{2}{35}\left(-b_{22}K_n + b_{22}K_w\right) \right] \tag{3.67}$$

$$A_{1313} = L_0^2 N_p \left[\frac{12}{105}\left(13K_w a_{20} + 7K_n + K_n a_{20} + 6K_w a_{22} - 6K_n a_{22} + 28K_w\right) \right] \tag{3.68}$$

$$A_{1321} = L_0^2 N_p \left[-\frac{2}{35}\left(-b_{22}K_n + b_{22}K_w\right) \right] \tag{3.69}$$

$$A_{1331} = L_0^2 N_p \left[\frac{1}{105}\left(-6K_n a_{22} + 6K_w a_{22} + K_n a_{20} - K_w a_{20} + 7K_n - 7K_w\right) \right] \tag{3.70}$$

$$A_{2323} = L_0^2 N_p \left[\frac{1}{105} \left(42K_w a_{22} + 28K_w - 5K_w a_{20} + 7K_n - 2K_n a_{20} \right) \right] \tag{3.71}$$

$$A_{2332} = L_0^2 N_p \left[\frac{1}{105} \left(7K_n - 7K_w - 2K_n a_{20} + 2K_w a_{20} \right) \right] \tag{3.72}$$

$$A_{2121} = L_0^2 N_p \left[\frac{1}{105} \left(-8K_w a_{20} + 7K_n + K_n a_{20} + 36K_w a_{22} + 6K_n a_{22} + 28K_w \right) \right] \tag{3.73}$$

$$A_{2131} = L_0^2 N_p \left[\frac{2}{35} \left(b_{22} K_n + 6K_w \right) \right] \tag{3.74}$$

$$A_{3131} = L_0^2 N_p \left[-\frac{1}{105} \left(8K_w a_{20} - 7K_n - K_n a_{20} + 36K_w a_{22} + 6K_n a_{22} - 28K_w \right) \right] \tag{3.75}$$

$$A_{3232} = L_0^2 N_p \left[-\frac{1}{105} \left(42K_w a_{22} - 28K_w + 5K_w a_{20} - 7K_n + 2K_n a_{20} \right) \right] \tag{3.76}$$

To recover the traditional, or classical, continuum mechanics stresses, the symmetric and non-symmetric stress terms are defined as:

$$\tau = \frac{\sigma_{ij} + \sigma_{ji}}{2}$$
$$T = \frac{\sigma_{ij} - \sigma_{ji}}{2} \tag{3.77}$$

The symmetric and non-symmetric terms of strain are defined as:

$$\psi_{ij} = \varepsilon_{ij} + \varepsilon_{ji} = u_{j,i} + u_{i,j}$$

$$\Psi_{ij} = u_{i,j} - u_{j,i} + e_{jil} 2\omega_l \tag{3.78}$$

Where the following energy condition is satisfied:

$$\tau_{ij}\psi_{ij} + T_{ij}\Psi_{ij} = \sigma_{ij}\varepsilon_{ij} + \sigma_{ji}\varepsilon_{ji} \tag{3.79}$$

To satisfy this condition the A_{ikql} and D_{jlqr} need to be symmetrized. In this section, we will describe in detail the symmetrization of the A_{ikql} matrix; the other matrices are symmetrized in the same fashion.

First, we rearrange the columns:

For $q \neq l$ and $q < l$ (the symmetric part)

$$A_{ikql} = \left(\frac{A_{ikql} + A_{iklq}}{2} \right) \tag{3.80}$$

For $q \neq l$ and $q > l$ (the non-symmetric part)

$$A_{ikql} = \left(\frac{A_{ikql} - A_{iklq}}{2} \right) \tag{3.90}$$

Second, we rearrange the rows:

For $i \neq k$ and $i < k$ (the symmetric part)

$$A_{ikql} = \left(\frac{A_{ikql} + A_{kiql}}{2} \right) \tag{3.91}$$

For $i \neq k$ and $i > k$ (the non-symmetric part)

$$A_{ikql} = \left(\frac{A_{ikql} - A_{kiql}}{2} \right) \tag{3.92}$$

So, that:

$$\Delta\sigma_{ik} = A_{ikql}\Delta\varepsilon_{ql}$$

$$\begin{bmatrix} \Delta\sigma_{11} \\ \Delta\sigma_{22} \\ \Delta\sigma_{33} \\ \Delta\tau_{12} \\ \Delta\tau_{13} \\ \Delta\tau_{23} \\ \Delta T_{21} \\ \Delta T_{31} \\ \Delta T_{32} \end{bmatrix} = \begin{bmatrix} A_{1111} & A_{1122} & A_{1133} & 0 & 0 & A_{1123} & 0 & 0 & 0 \\ & A_{2222} & A_{2233} & 0 & 0 & A_{2223} & 0 & 0 & A_{2232} \\ & & A_{3333} & 0 & 0 & A_{3323} & 0 & 0 & A_{3332} \\ & & & A_{1212} & A_{1213} & 0 & A_{1221} & A_{1231} & 0 \\ & & & & A_{1313} & 0 & A_{1321} & A_{1331} & 0 \\ & & \text{Symmetric} & & & A_{2323} & 0 & 0 & A_{2332} \\ & & & & & & A_{2121} & A_{2131} & 0 \\ & & & & & & & A_{3131} & 0 \\ & & & & & & & & A_{3232} \end{bmatrix} \begin{bmatrix} \Delta\varepsilon_{11} \\ \Delta\varepsilon_{22} \\ \Delta\varepsilon_{33} \\ \Delta\varepsilon_{12} + \Delta\varepsilon_{21} \\ \Delta\varepsilon_{13} + \Delta\varepsilon_{31} \\ \Delta\varepsilon_{23} + \Delta\varepsilon_{32} \\ \Delta\varepsilon_{12} - \Delta\varepsilon_{21} \\ \Delta\varepsilon_{13} - \Delta\varepsilon_{31} \\ \Delta\varepsilon_{23} - \Delta\varepsilon_{32} \end{bmatrix} \tag{3.93}$$

$$A_{1111} = L_0^2 N_p \left[\frac{1}{105} \left(14K_w + 12K_n a_{20} + 21K_n + 2K_w a_{20} \right) \right] \tag{3.94}$$

$$A_{1122} = L_0^2 N_p \left[\frac{1}{105} \left(6K_n a_{22} - 6K_w a_{22} + K_n a_{20} - K_w a_{20} + 7K_n - 7K_w \right) \right] \tag{3.95}$$

$$A_{1133} = L_0^2 N_p \left[\frac{1}{105} \left(-6K_n a_{22} + 6K_w a_{22} + K_n a_{20} - K_w a_{20} + 7K_n - 7K_w \right) \right] \tag{3.96}$$

$$A_{1123} = L_0^2 N_p \left[\frac{2}{35} \left(b_{22} K_n + b_{22} K_w \right) \right] \tag{3.97}$$

$$A_{2222} = L_0^2 N_p \left[-\frac{1}{105} \left(+ K_w a_{20} - 36K_n a_{22} - 21K_n + 6K_n a_{20} - 6K_w a_{22} - 14K_w \right) \right] \tag{3.98}$$

$$A_{2233} = L_0^2 N_p \left[-\frac{1}{105} \left(-7K_n + 7K_w + 2K_n a_{20} - 2K_w a_{20} \right) \right] \tag{3.99}$$

$$A_{2232} = L_0^2 N_p \left[\frac{b_{22}}{35} \left(6K_n + K_w \right) \right] \tag{3.100}$$

$$A_{3333} = L_0^2 N_p \left[-\frac{1}{105} \left(K_w a_{20} + 36K_n a_{22} - 21K_n + 6K_n a_{20} + 6K_w a_{22} - 14K_w \right) \right] \tag{3.101}$$

$$A_{3323} = L_0^2 N_p \left[\frac{b_{22}}{35} \left(6K_n + K_w \right) \right] \tag{3.102}$$

$$A_{3332} = L_0^2 N_p \left[\frac{b_{22}}{5} \left(K_w \right) \right] \tag{3.103}$$

$$A_{1212} = L_0^2 N_p \left[\frac{1}{420} \left(24K_n a_{22} + 18K_w a_{22} + 3K_w a_{20} + 4K_n a_{20} + 42K_w + 28K_n \right) \right] \tag{3.104}$$

$$A_{1213} = L_0^2 N_p \left[\frac{b_{22}}{70} \left(4K_n + 3K_w \right) \right] \tag{3.105}$$

$$A_{1221} = L_0^2 N_p \left[\frac{K_w}{20} \left(-2a_{22} + a_{20} \right) \right] \tag{3.106}$$

$$A_{1231} = L_0^2 N_p \left[\frac{b_{22}}{10} \left(-K_w \right) \right] \tag{3.107}$$

$$A_{1313} = L_0^2 N_p \left[\frac{1}{420} \left(-24K_n a_{22} - 18K_w a_{22} + 3K_w a_{20} + 4K_n a_{20} + 42K_w + 28K_n \right) \right] \tag{3.108}$$

$$A_{1321} = L_0^2 N_p \left[\frac{b_{22}}{5} \left(-K_w \right) \right] \tag{3.109}$$

$$A_{1331} = L_0^2 N_p \left[\frac{K_w}{20} \left(2a_{22} + a_{20} \right) \right] \tag{3.110}$$

$$A_{2323} = L_0^2 N_p \left[-\frac{1}{210} \left(-21K_w + 3K_w a_{20} + 4K_n a_{20} - 14K_n \right) \right] \tag{3.111}$$

$$A_{2332} = L_0^2 N_p \left[\frac{1}{5} \left(K_w a_{22} \right) \right] \tag{3.112}$$

$$A_{2121} = L_0^2 N_p \left[\frac{K_w}{60} \left(6a_{22} + a_{20} + 10 \right) \right] \tag{3.113}$$

$$A_{2131} = L_0^2 N_p \left[\frac{b_{22}}{10} \left(K_w \right) \right] \tag{3.114}$$

$$A_{3131} = L_0^2 N_p \left[\frac{K_w}{105} \left(-6a_{22} + a_{20} + 10 \right) \right] \tag{3.115}$$

$$A_{3232} = L_0^2 N_p \left[-\frac{K_w}{30} \left(-5 + a_{20} \right) \right] \tag{3.116}$$

With these constitutive relations and adequate bond density parameters, a_{20}, a_{22}, and b_{22}, the type of material symmetry is incorporated in the model and so are the material' properties (i.e., Young's modulus, E, Poisson's ratio, ν, and shear modulus, G) for each bond direction. For an isotropic material (where $a_{20}=a_{22}=b_{22}=0$) under infinitesimal initial strain (normal, $\delta_n \to 0$, and tangential, $\delta_w \to 0$), K_n and K_w are reduced to A and C, respectively. Thus, the initial Young's modulus E and Poisson's ratio ν are given as:

$$E = L_0^2 N_p \frac{A\left(2A + 3C\right)}{3(4A + C)} \tag{3.117}$$

$$\upsilon = \frac{A - C}{4A + C} \tag{3.118}$$

For positive values of the parameters A and C equation 3.118 predicts a Poison's ratio in the range of -1 to 0.25. In the same way, material properties for transversely isotropic and

orthotropic materials can be expressed in terms of the tangential and normal force laws in addition to the density parameters.

By performing a parametric study for an isotropic material, the parameters *A* and *C* can be derived from experimental values of the Young's modulus and Poisson's ratio using the following equations:

$$A = \frac{3E}{(1-2\upsilon)L_0^2 N_p} \tag{3.119}$$

$$C = \frac{3E(4-4\upsilon)}{(1-2\upsilon)(\upsilon+1)L_0^2 N_p} \tag{3.120}$$

By factorizing the product $L_0^2 N_p$, the bond length (L_0) and the number of bonds per unit volume (bond density) (N_p), new parameters can be incorporated into the pseudo-bond model. With this approach, there is no need to know the numerical values of the bond length or bond density. These new parameters, A_1 and C_1, are derived as follows:

$$A_1 = AL_0^2 N_p \tag{3.121}$$

$$C_1 = CL_0^2 N_p \tag{3.122}$$

The rest of the parameters, *B*, *D*, α_1, and α_2 can be numerically obtained from the measured peak stress-strain curve values under uniaxial tensile and compressive loading. Of these, *B* and *D* are closely related to uniaxial tensile tests and α_1 and α_2 are related to uniaxial compressive tests

(Misra and Yang, 2010). Similar to *A* and *B*, these parameters are derived by performing a parametric study.

Following a parametric study, performed by Misra and Yang (2010) to model concrete behavior, the performance of the pseudo-model is analyzed in section 3.5 with A_1= 0.7 MPa, B= 3.4×10^{-7}, C_1=0.2 MPa , D=1.3×10^{-4} , α_1=2×10^{5} , and α_2=7 under the following loading conditions: Uniaxial tension, uniaxial compression, equi-biaxial compression 'CC', equi-biaxial tension 'TT', biaxial compression/tension 'CT', hydrostatic compression 'CCC', hydrostatic tension 'TTT', triaxial compression/compression/tension 'CCT', and shear. The tangential and normal forces at the contact level corresponding to each bond direction are plotted along with the force/displacements values for each material's plane. In addition, for each loading condition, a stress-strain curve is presented and evaluated.

In addition, derivation of the model parameters shows that the parameters are related to the material's mechanical properties and geometry, and have physical meaning. Therefore, this model can be used in the future works to analyze/study the role of the material properties in the material's response so they can be better understood, enhanced and/or modified.

3.5. Materials behavior under different loading conditions.

Material's behavior under uniaxial, biaxial, triaxial, and shear loading is simulated and evaluated in this section. A strain controlled simulation is used for uniaxial loading which considers tension and compression loading conditions. For the other loading cases, a stress controlled simulation is applied. For biaxial simulation, equi-biaxial compression 'CC', tension 'TT', and a combination of compression-tension 'CT' loadings are considered. Triaxial

simulation consists of hydrostatic compression ‘CCC’, tension ‘TTT’, and a combination of compression and tension ‘CCT’ loading conditions. Finally, for shear simulation, positive shear stresses are applied in the analysis.

For each loading case, the stress-strain curve at the element level is shown and the normalized normal and tangential force bond-distribution surface plots at the contact level with their corresponding normalized force-displacement curves at two loading stages are presented. Normalization of the forces and displacements is based on the material’s maximum tensile capacity ($P_{nt\ max}$, $\delta_{nt\ max}$, $P_{wt\ max}$, $\delta_{wt\ max}$). The first loading stage refers to the beginning of loading, while the second loading stage refers to the load prior to failure. In the case of the shear loading, the material exhibits strain-hardening behavior; therefore, an additional force bond-distribution plot is provided for this loading stage. The force bond-distribution plots illustrate the evolution of the load carrying capacity within the material at the contact level; each value represents the force behavior at a specific bond orientation plane, within the material. Each plane undergoes softening-evolution that is related to the overall stress-strain behavior. In general, two types of dominant behavior are observed within the material: compression and tension. The failure mechanism under these loading conditions is clearly described in these force bond-distribution function plots. Failure mechanism within the material under tension exhibits tensile softening in the normal direction, while under compression describes tangential softening. Both behaviors are recognized in the force bond-distribution plots presented in this section.

3.5.1. Uniaxial loading in tension.

A strain control simulation is performed under uniaxial tension to evaluate the failure mechanism and the softening evolution within the material. Figure 3.9 shows the stress-strain curve of the material at the element level. Evolution of the material's softening and failure at the contact level is evaluated and presented in Figures 3.10 and 3.11. This evaluation is performed by analyzing the normalized normal and tangential force bond-distribution surface plots and force-displacement curves. Normalization of the forces and displacements is based on the material's maximum tensile capacity ($P_{nt\ max}$, $\delta_{nt\ max}$, $P_{wt\ max}$, $\delta_{wt\ max}$). Results show that under tensile behavior, the dominant failure mechanism is tensile normal softening, which is observed in Figure 3.10.

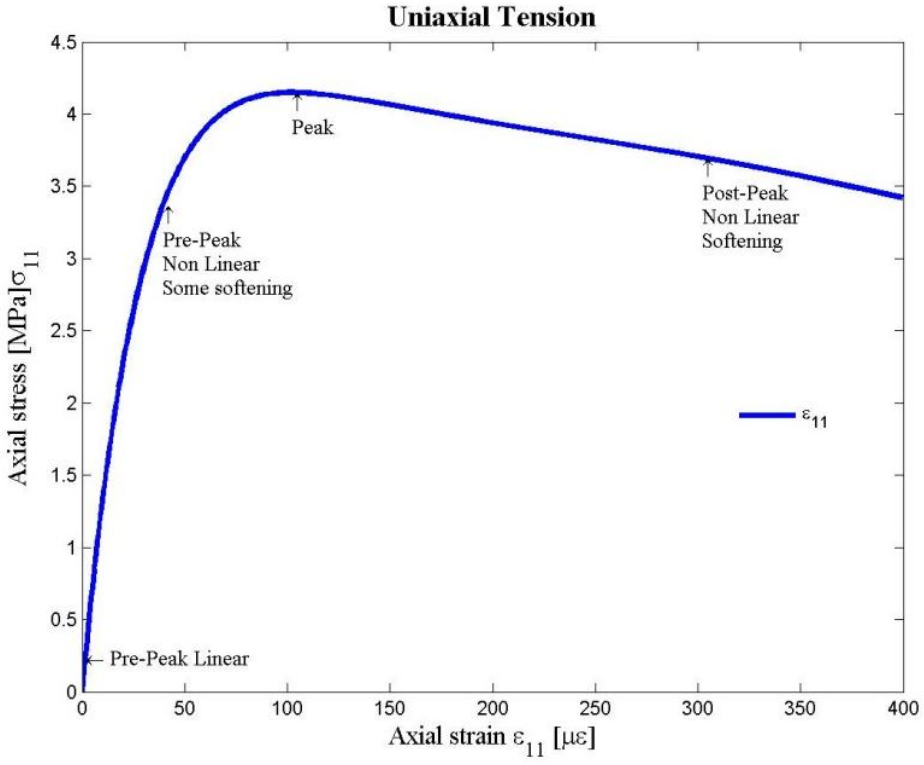

Figure 3.9: Uniaxial tension at the element level - Stress versus strain.

In Figure 3.9, stress versus strain relationship for uniaxial tensile loading at the element level is shown. The curve can be divided into two regimens, a pre-peak and a post-peak regimen. Within the pre-peak regimen, a linear followed by a non-linear behavior is observed. Also, this initial linearity in experimental measurements exhibits a slight curvature suggesting that microcracking within the material occurs from the beginning of loading, and thus, softening (van Mier, 1997). The evolution of this softening behavior is captured by our model and described in the material's bond behavior at the contact level shown in Figures 3.10 and 3.11.

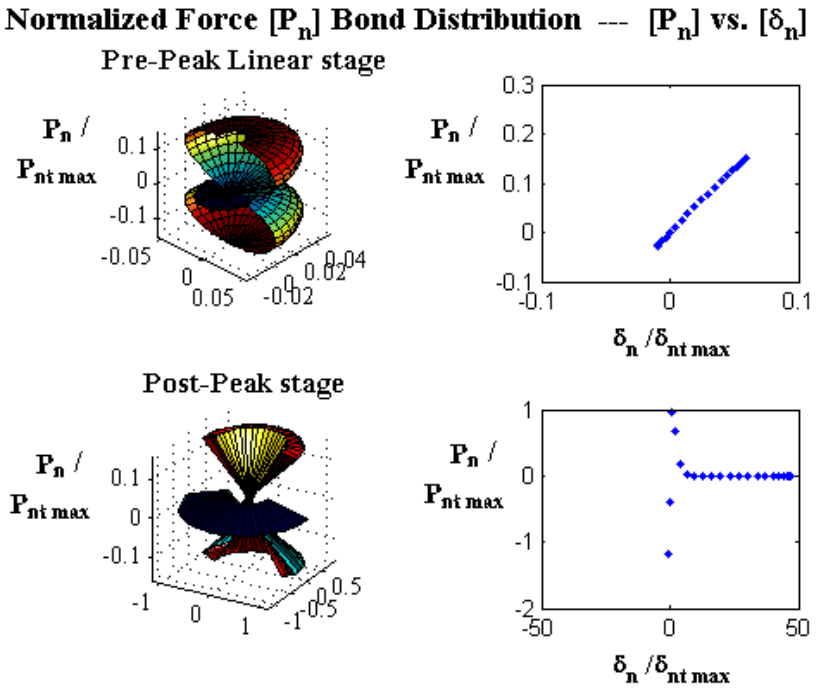

Figure 3.10: Uniaxial tension at the contact level – Normalized normal force bond-distribution.

Figure 3.10, describes the normalized normal force bond-orientation distribution at the contact level under uniaxial tension for two stages, an initial stage, 'pre-peak' stage, and a final stage prior failure ('post-peak' stage). At the initial stage, the normal distribution surface plot

describes a peanut shape surface with tension at the top and bottom surfaces (red color) and compression towards the center (blue color). The force-displacement curve describes a slightly non-linear curve in tension and linear in compression, suggesting that some tensile softening has been initiated. At the 'post-peak' stage, a significant tensile softening is observed in the force-displacement curve, where several bond orientations have reached failure. In addition, bond orientations under compression, within the curve, do not exhibit softening. This supports the afore-mentioned observation that under tension the controlling failure mechanism is tensile normal softening. Also, this tensile softening is described in the surface plot by exhibiting an increased flat blue surface and by the transformation of the peanut shape surface into a cone-like surface shape. The red color flat surface observed in the surface plot is also reflected in the force-displacement curve, which is represented by the maximum compressive force.

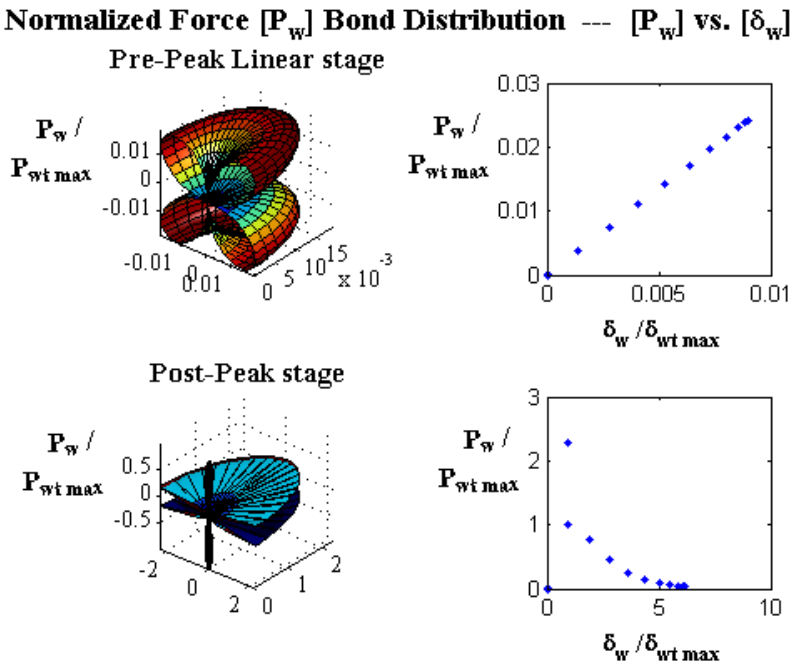

Figure 3.11: Uniaxial tension at the contact level –Normalized tangential force bond-distribution.

Figure 3.11 shows the normalized tangential force bond-orientation distribution at the contact level for two loading stages: pre-peak and post-peak. Within the surface plots, a maximum shear force (red color) is observed at the top and bottom surfaces of the pre-peak stage and a linear behavior is described in the force-displacement curve. Softening of bonds is observed at the post-peak stage in both; the force-displacement curve and surface plot. Failure within the bonds (zero force value) is observed only on few orientations. In addition, a change in the surface shape is observed, at this stage, that reflects the softening effects within the material.

3.5.2. Uniaxial loading in compression.

In this section, a strain control simulation is performed under uniaxial compression to evaluate the failure mechanism and the softening evolution within material. Figure 3.12 shows the stress-strain curve of the material at the element level. Evolution of the material softening and failure in the normal and tangential direction at the contact level is shown by the force bond-distribution surface plots and their force-displacement corresponding curves, which are normalized and shown in Figures 3.13 and 3.14. Normalization is performed with respect to the maximum tensile force and displacement values for the normal and tangential directions ($P_{nt\ max}$, $\delta_{nt\ max}$, $P_{wt\ max}$, $\delta_{wt\ max}$). Two loading stages are considered in these figures: an initial stage ('pre-peak') and a final stage prior to failure ('post-peak' stage). Under compression, the material's behavior describes tangential softening as the dominant failure mechanisms (Figure 3.14).

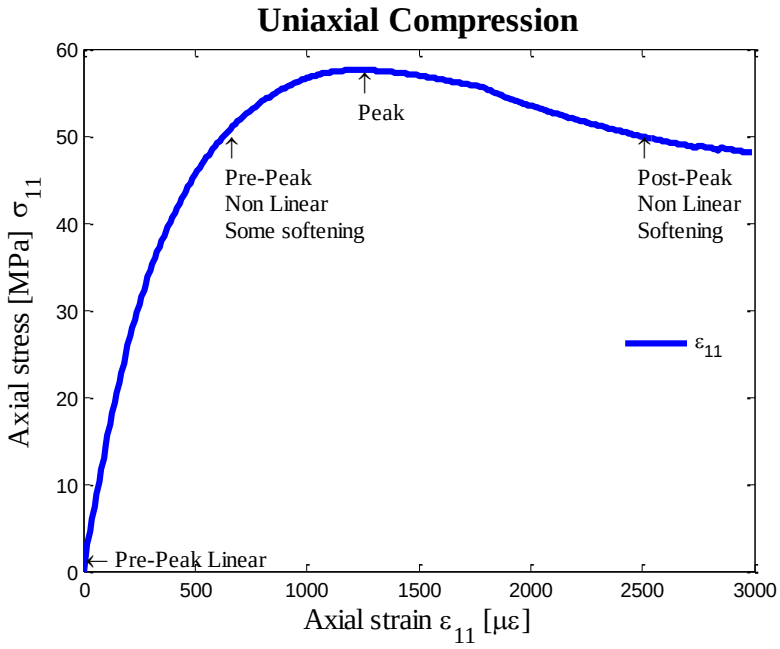

Figure 3.12: Uniaxial compression at the element level- Stress versus strain.

Figure 3.12 exhibits the material's stress strain behavior at the element level for uniaxial compression. Similarly to uniaxial tension the curve, a pre and post-peak regimen are identified in the curve. The pre-peak regimen describes an initial linear behavior followed by a nonlinear behavior; while the post-peak regime describes a nonlinear softening behavior. The non-linearity of the pre-peak stage suggests that microcracks within the material occur from beginning of the initial loading. This softening evolution is reflected in the force bond-orientation distribution surface plots at the contact level and their corresponding force-displacement curves.

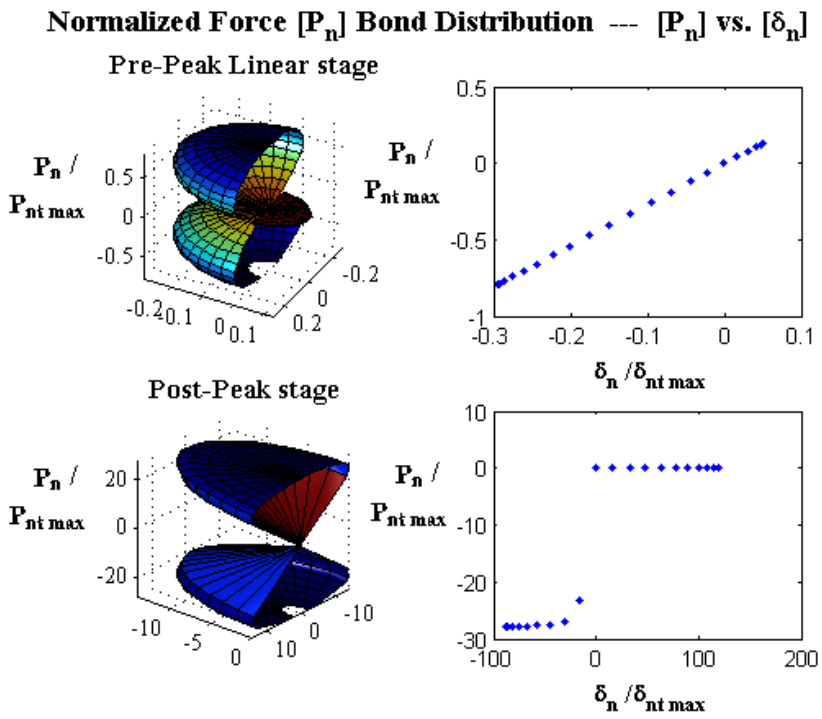

Figure 3.13: Uniaxial compression at the contact level- Normalized normal force bond-distribution.

Normalized normal force bond-distribution within the material at the contact level is shown in Figure 3.13. At the pre-peak loading stage, the normal force bond-distribution surface plot describes a peanut shape with maximum compressive stresses (blue color) at the top and bottom surfaces. Also, the force-displacement curve at this stage exhibits a linear relationship with no presence of softening. At the post-peak loading stage, the peanut shape force-distribution surface plot becomes a cone shape surface where softening of the bonds is observed at the center. At the center, tensile softening/failure is described with zero force values. Compression softening is described by the flat blue top and bottom surfaces. The normalized force displacement curve illustrates as well the failure and softening behaviors in the bonds. Softening of the bonds under compression is described by reaching the asymptotic force value, while failure of the bonds in tension is described by exhibiting zero force values. These behaviors provide a clear description

of the model's tension and compression potential force functions in the normal direction. Once softening occurs, the force function in tension starts decreasing until it fails reaching a zero value, while in compression it increases until it reaches an asymptotic compressive value.

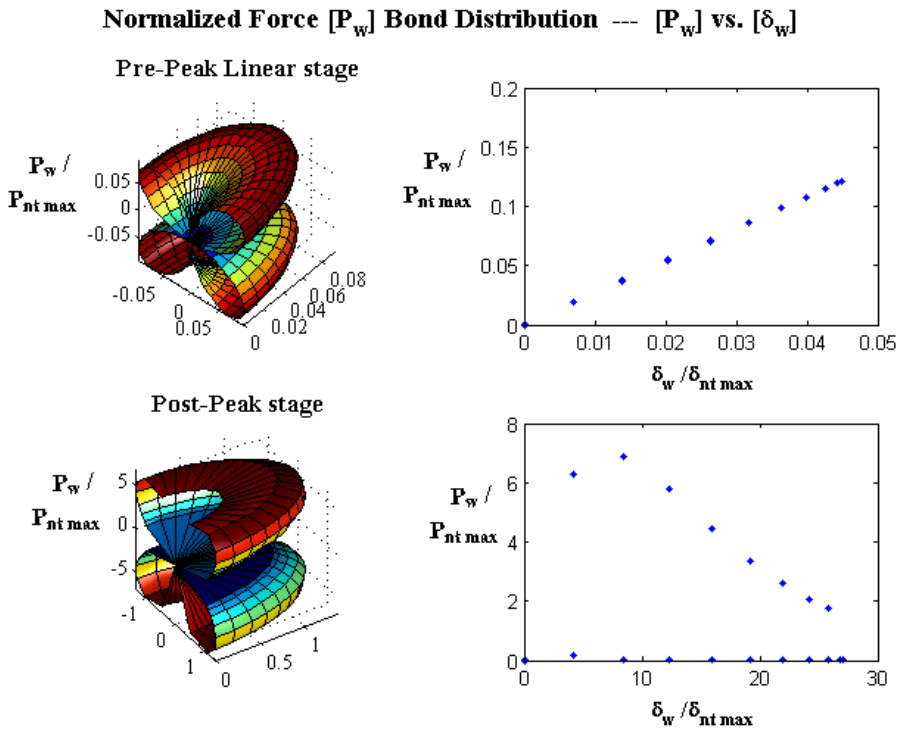

Figure 3.14: Uniaxial compression at the contact level - Normalized tangential force bond-distribution.

Figure 3.14 shows the normalized tangential force distribution at the contact level under compression loading at two loading stages, pre and post-peak stages. As mentioned before, under compression loading the material is expected to exhibit tangential softening as its dominant failure mechanism, which is shown in figure 3.14. At the initial phase (pre-peak stage), a general linear behavior in the force-displacement curve is observed. Then, at the final phase (post-peak stage), softening accompanied by failure behavior is observed in the force-displacement curve. This is also identified on the surface plot by the transformation of the surface into a cone-like

shape towards the center. Also, softening and failure at the post-peak stage is described within the surface plot by the increase of the blue color (minimum force values) and decrease of the red color (maximum force values).

3.5.3. Equi-biaxial compression loading – (CC).

In this section, equi-biaxial compression CC loading is simulated in the material by applying stresses in the 11 and 22 directions. Figure 3.15 presents the stress-strain curve of the material at the element level. Surface plots of the normalized normal and tangential force bond-distributions within the material at the contact level are shown with their corresponding force-displacement curves in Figures 3.16 and 3.17. Normalization of these plots is based on the maximum tensile values of the normal and tangential bond-force and displacement values ($P_{nt\ max}$, $\delta_{nt\ max}$,. $P_{wt\ max}$, $\delta_{wt\ max}$). Two loading stages are described in these figures, an initial stage ('pre-peak'), and a final stage close to failure of the material ('peak' state). Softening and failure evolution of the material under CC is well described in these plots. As expected tangential softening is the controlling failure mechanism under biaxial compression (Figure 3.17).

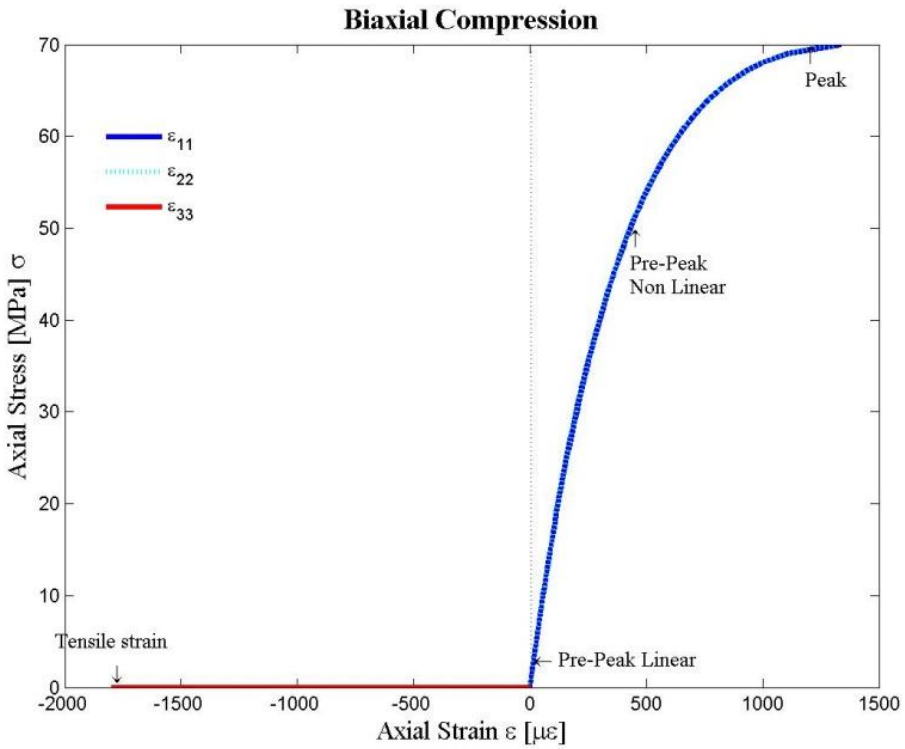

Figure 3.15: Equi-biaxial compression at the element level- Stress versus strain.

Figure 3.15 describes the stress-strain curve of the material at the element level under biaxial compression CC loading in the 11 and 22 directions. A linear followed by a non-linear behavior is observed within the curve prior to the peak stress. This suggests initiation of softening from the beginning of the loading, which is described in the subsequent force bond-distribution plots at the contact level. In addition, strain in the 33 direction (normal to the loading) is plotted and it shows dilatation of the material in that direction (tensile strains). Also, it was observed that the compressive strength of the material under CC loading is about 20 percent higher than the case of uniaxial compressive loading.

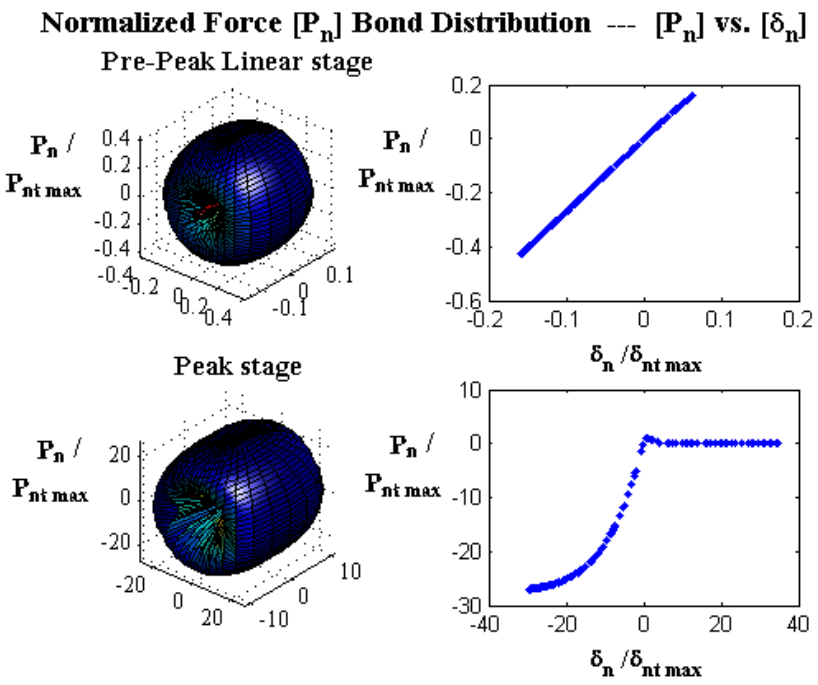

Figure 3.16: Equi-biaxial compression at the contact level – Normalized normal force bond-distribution for pre-peak and peak stages.

Figure 3.16 illustrates the normalized normal force bond-distribution of the material at the contact level under biaxial CC loading. Two loading stages are evaluated: an initial stage ('pre-peak') and a final stage preceding failure ('peak' stage). At the initial loading stage, the biaxial compression is shown by the blue color in the surface plot, and the red color represents tension of the bonds in the direction normal to the loading. This was described in the previous figure where the stress strain curve showed a tensile strain in the 33 direction. In the force-displacement figure for 'pre-peak' stage, the material describes a linear behavior in tension and compression. During the final stage, 'peak', softening of the material is observed in the surface plot and force-displacement curve. The surface plot exhibits an increase in the compressive force, blue color, and a softening/failure of the bonds under tension, red color. This is better described in the force-displacement curve where several bonds in tension have softened and failed (zero normal force)

and the bonds in compression describe a well-defined softening curve. Thus, a significant tangential softening is expected within the material.

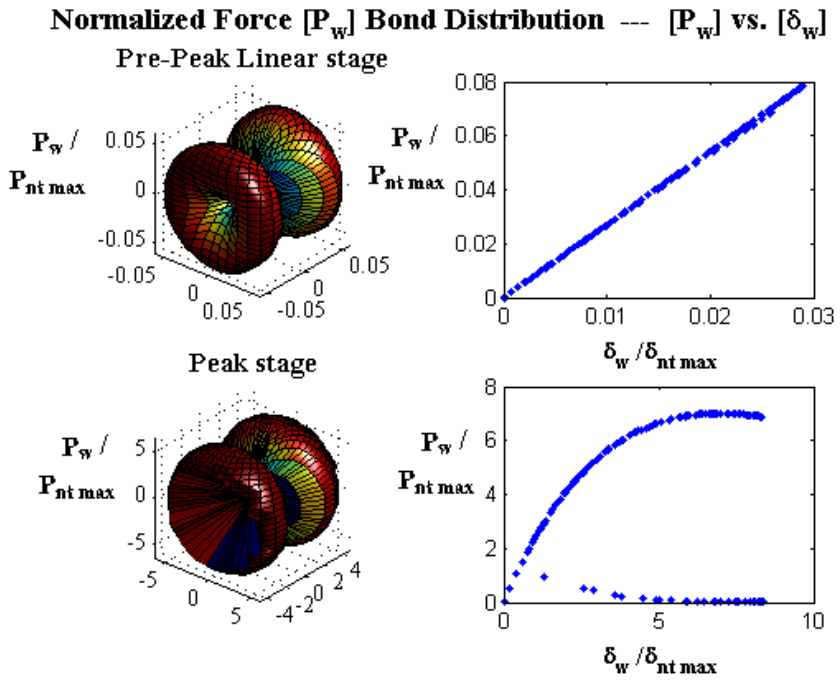

Figure 3.17: Equi-biaxial compression at the contact level - Normalized tangential force bond-distribution for pre-peak and peak stages.

Figure 3.17 exhibits the normalized tangential force bond-distribution behavior of the material at the contact level under CC loading at two stages, an initial stage (‘pre-peak’) and a final stage prior failure of the material (‘peak’ stage). As previously mentioned, under compression the failure controlling mechanism is tangential softening which is well described in figure 3.17. At the initial stage (‘pre-peak’), a linear force-displacement relationship is observed within the material with no softening-like behavior. In addition, the surface plot at this stage shows a well distributed tangential force within the material with maximum tangential forces at the contours (red color). At the final stage prior failure (‘peak’), a cone-like shape wants to form within the surface plot, and softening of the bonds is distinguished by the blue color. The force-

displacement curve is better at illustrating the softening and failure of the bonds within the material.

3.5.4. Equi-biaxial tension loading – (TT).

The equi-biaxial tension (TT) loading simulation is performed under a stress control fashion in this section. The results of the stress-strain curve at the element level are presented in Figure 3.18. Under tension the material failure mechanism is expected to be tensile softening in the normal direction, which is observed in the normalized normal force bond-distribution surface plots and force-displacement curves at the contact level presented in Figure 3.19. In addition, the normalized tangential force bond-distribution behavior of the material at the contact level is presented in Figure 3.20. Normalization of the normal and tangential force bond distribution is performed with respect to the maximum normal and tangential bond-force and displacement, respectively ($P_{nt\ max}$, $\delta_{nt\ max}$,. $P_{wt\ max}$, $\delta_{wt\ max}$). The last two figures illustrate the softening evolution within the material by presenting two loading stages: an initial one (‘pre-peak’ stage), and a final one prior to failure (‘post-peak’ stage).

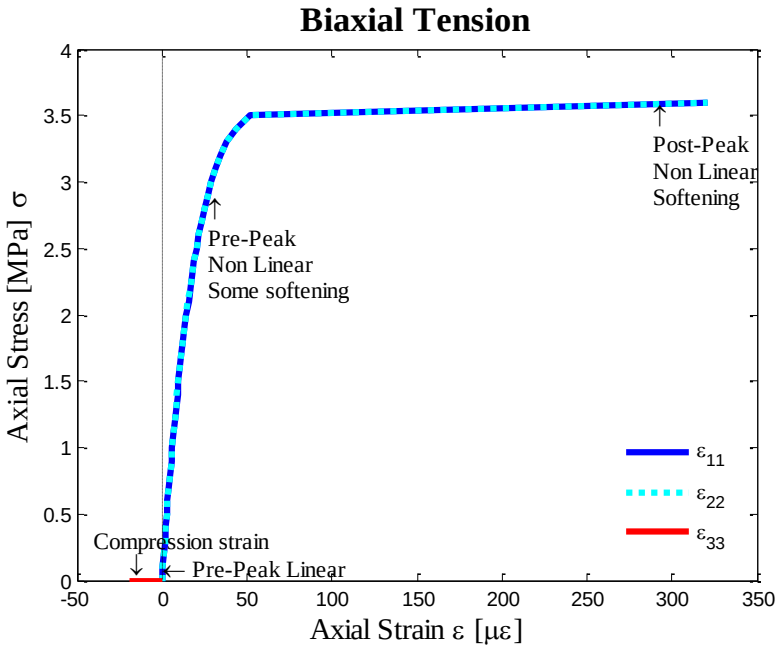

Figure 3.18: Equi-biaxial tension at the element level - Stress versus strain curve.

Figure 3.18 describes the stress-strain behavior of the material at the element level under equi-biaxial tension. Within the curve, a pre-peak linear and non-linear regimen is observed prior to the peak stress in the 11 and 22 directions, while the 33 direction shows some compressive strains (contractive behavior). This behavior is reflected at the contact level in Figure 3.19.

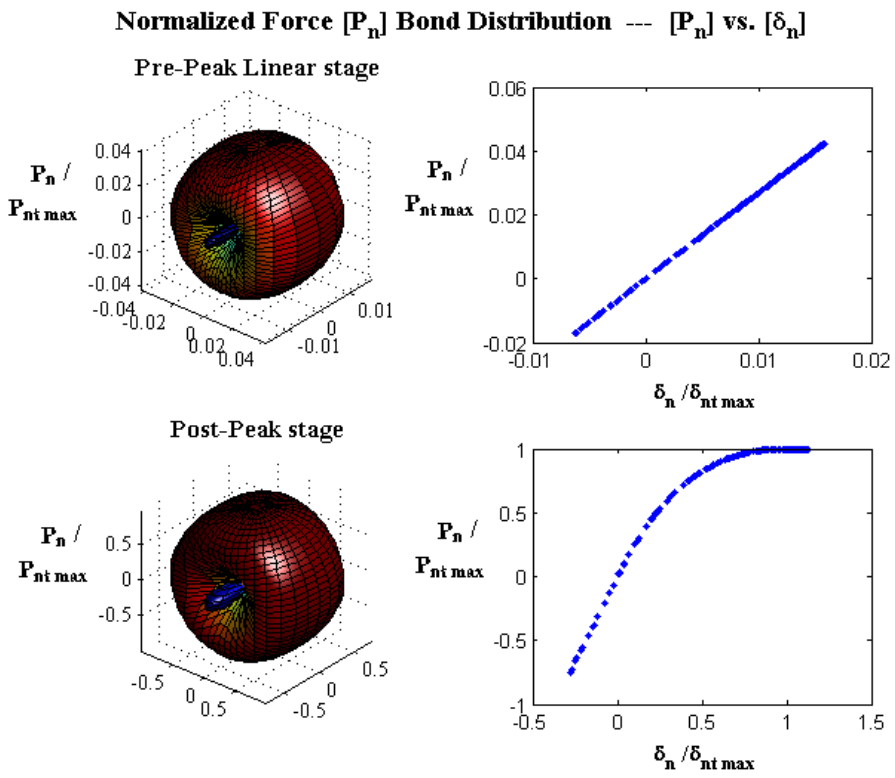

Figure 3.19: Equi-biaxial tension at the contact level – Normalized normal force bond-distribution for pre and post-peak stages.

Figure 3.19 describes the normalized normal force bond-distribution within the material at the contact level under equi-biaxial TT loading. At the initial loading stage (‘pre-peak’), tension in the 11 and 22 directions (red color) is observed. In addition, in the 33 direction, normal to loading, some compression (blue color) is described. The force-displacement figure at the ‘pre-peak’ stage describes a linear behavior. At the ‘post-peak’ stage (prior to failure), an increase in tension and compression is observed in the surface plot. In the force-displacement curve, softening of the bonds in tension and an increasing linear behavior in the bonds under compression are observed. As previously mentioned, the failure mechanism in the material is described by normal tensile softening.

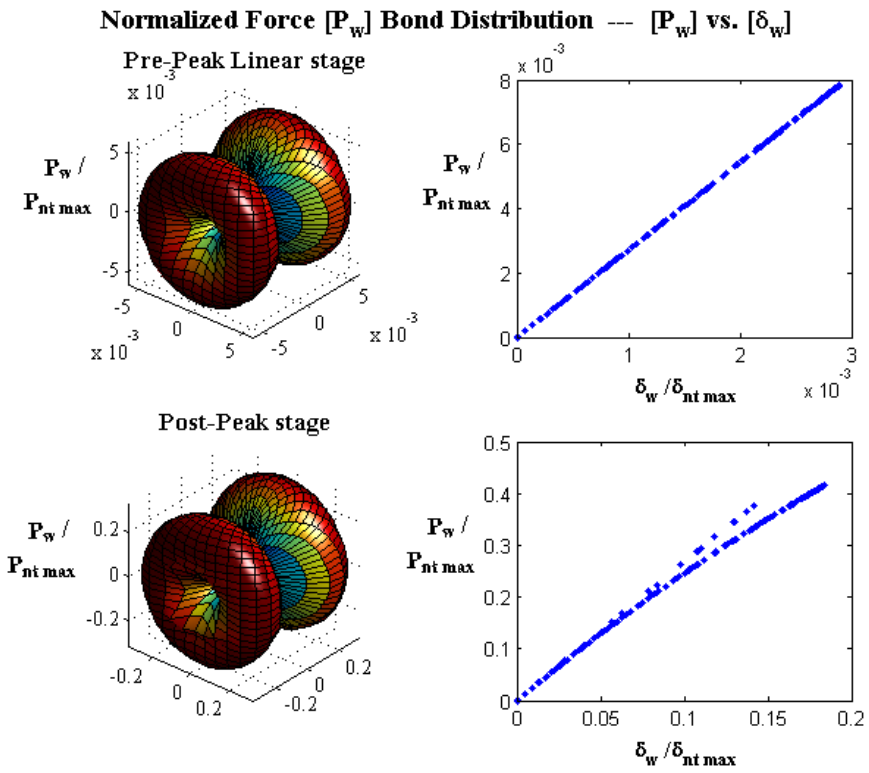

Figure 3.20: Equi-biaxial tension at the contact level - Normalized tangential force bond-distribution for pre and post-peak stages.

Figure 3.20 illustrates the normalized tangential force-bond distribution within the material at the contact level under equi-biaxial TT loading. As afore-mentioned tangential softening is not the controlling failure mechanisms, thus very little tangential softening between the 'pre-peak' and 'post-peak' stage prior to failure is observed in the surface and force-displacement plots.

3.5.5. Biaxial loading - Compression/tension (CT).

In this section, a biaxial compression/tension CT stress controlled simulation is performed in the material. The stress-strain curve at the element level is presented in Figure 3.21. The presence of tensile stresses reduces the compressive strength of the material and leads to a tensile normal softening failure mechanism. Figures 3.22 and 3.23 describe the softening evolution at

the contact level within the material at two stages: an initial ('pre-peak') stage and a final ('post-peak') stage prior to failure of the material. In these figures, the normalized normal and tangential force bond-distributions, with their corresponding force-displacement curves, are presented. Normalization is performed with respect to the maximum tensile values for normal and tangential bond-force and displacement ($P_{nt\ max}$, $\delta_{nt\ max}$,. $P_{wt\ max}$, $\delta_{wt\ max}$).

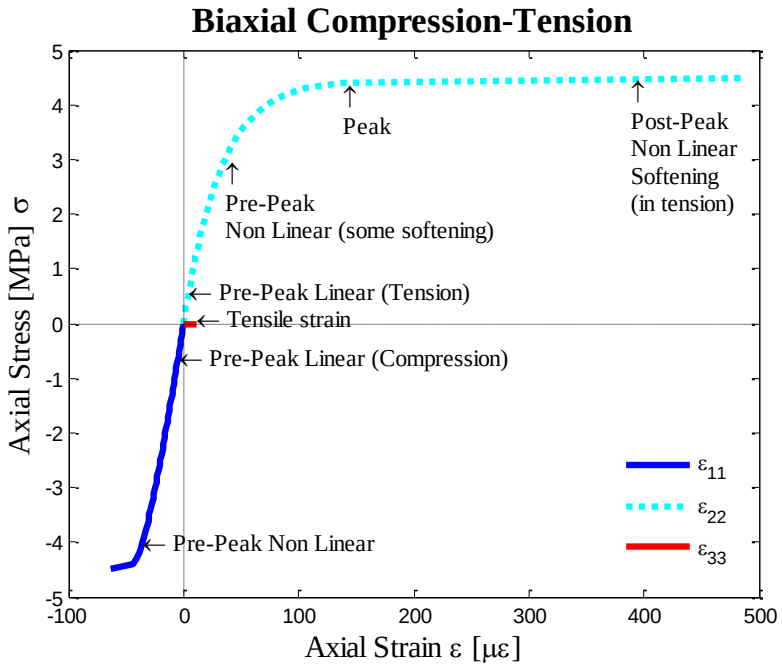

Figure 3.21: Equi-biaxial compression-tension at the element level - Stress versus strain curve.

Figure 3.21 presents the stress strain curve of the material at the element level under equi-biaxial CT loading. The presence of tensile stresses in this curve has shown to reduce the compressive strength. This is illustrated in Figure 3.21, where softening in the tension curve is well described compared to the compression curve. Within the curves, a linear and non-linear behavior is observed prior peak. This suggests that softening within the material initiates from the beginning of loading. Under this loading condition, the expected controlling failure

mechanism is tensile softening in the normal direction. This observation is described at the contact level in Figure 3.22.

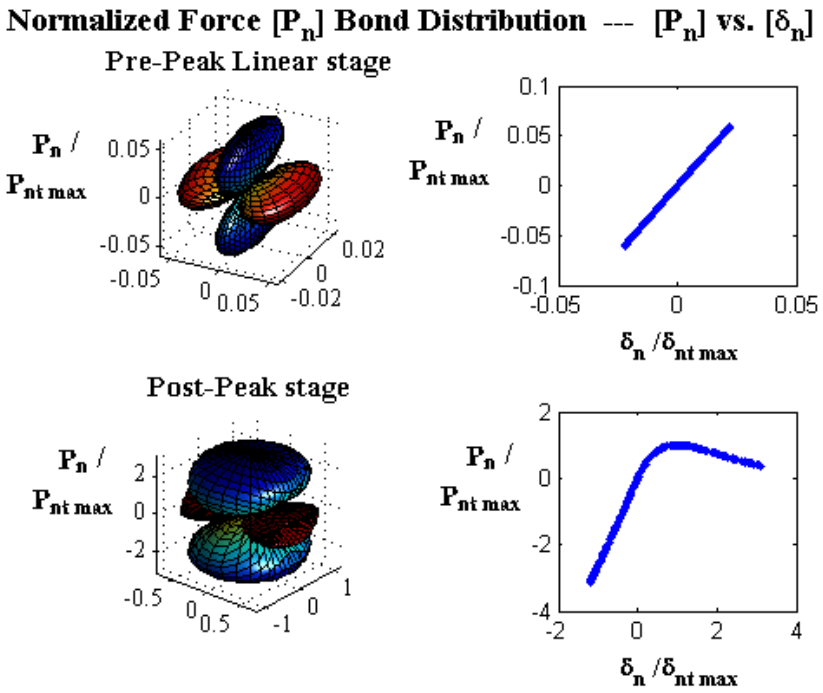

Figure 3.22: Equi-biaxial compression tension at the contact level - Normalized normal force bond-distribution for pre and post-peak stages.

Figure 3.22 exhibits the normalized normal force bond-distribution at the contact level under equi-biaxial CT loading. At the initial 'pre-peak' stage, a well-defined compression (blue color) and tension (red color) distribution is observed with a linear force-displacement relationship among the directions of the bonds. At the 'post-peak stage', softening of the bonds under tension and increase in compression forces are observed in the surface plot. The force-displacement curve, at the peak stage, exhibits a well-defined softening behavior of the bonds under tension, from which some of the bonds are close to failure (zero force value). On the other hand, the bonds under compression describe a linear force-displacement relationship where the softening

asymptotic value is not distinguished yet. From these plots, we can observe that the dominant failure mechanism for this loading condition is tensile softening in the normal direction.

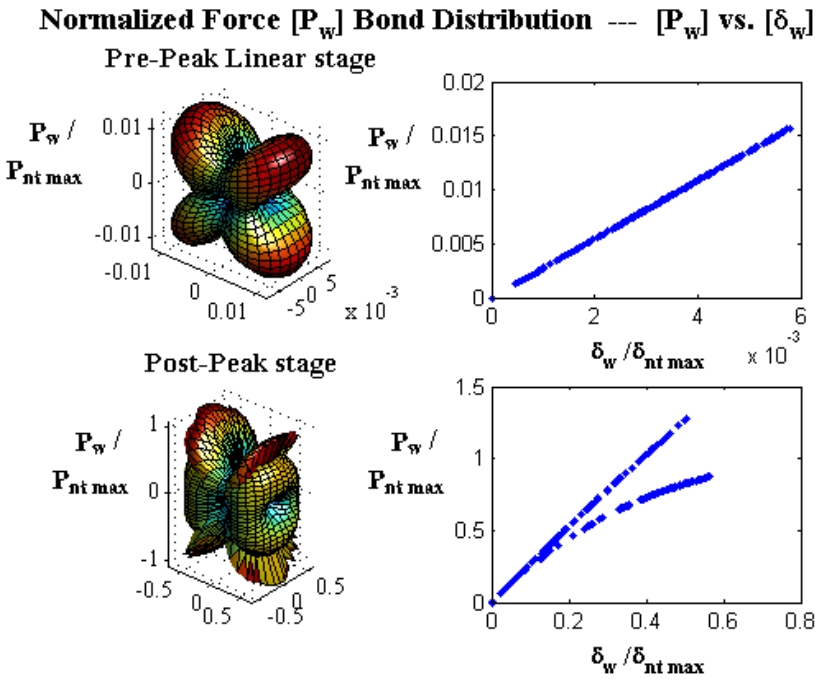

Figure 3.23: Equi-biaxial compression-tension at the contact level - Normalized tangential force bond-distribution for pre and post-peak stages.

Figure 3.23 shows the normalized tangential force bond-distribution at the contact level under CT loading. As previously mentioned, when tensile loading is applied, tangential softening is not significant and failure occurs due to softening in the normal direction due to tension. The figure describes the behavior of the material in the initial stage (‘pre-peak’), prior the peak stress, and prior to failure of the material (‘post-peak’). At the ‘pre-peak’ state, a linear force-displacement relationship is observed followed by some softening of the bonds shown in the ‘post-peak’ force-displacement figure. The softening-evolution of the bonds can be observed in the surface plot by changes in the shape (slimmer) and in the color; maximum and minimum force values are represented by red and blue color, respectively.

3.5.6. Hydrostatic compression (CCC).

In this section the material is subjected to a hydrostatic compression (CCC). The stress-strain curve at the element level is presented in Figure 3.24. In Figures 3.25 and 3.26, the normalized normal and tangential force bond-distribution behavior at the contact level with their corresponding force-displacement curves are shown. Normalization is based on the maximum tensile values of the normal and tangential force-bond and displacement ($P_{nt\ max}$, $\delta_{nt\ max}$,. $P_{wt\ max}$, $\delta_{wt\ max}$). Two loading stages are evaluated: an initial stage prior the peak stress ('pre-peak') and a second stage prior to failure of the material ('peak' stage). As expected, the material under this loading condition, in Figure 3.25, exhibits a point-like normal force bond-distribution behavior. In the tangential direction, the obtained results exhibited very small tangential forces which were not expected. This is attributed to the numerical approach used to evaluate the bond density function.

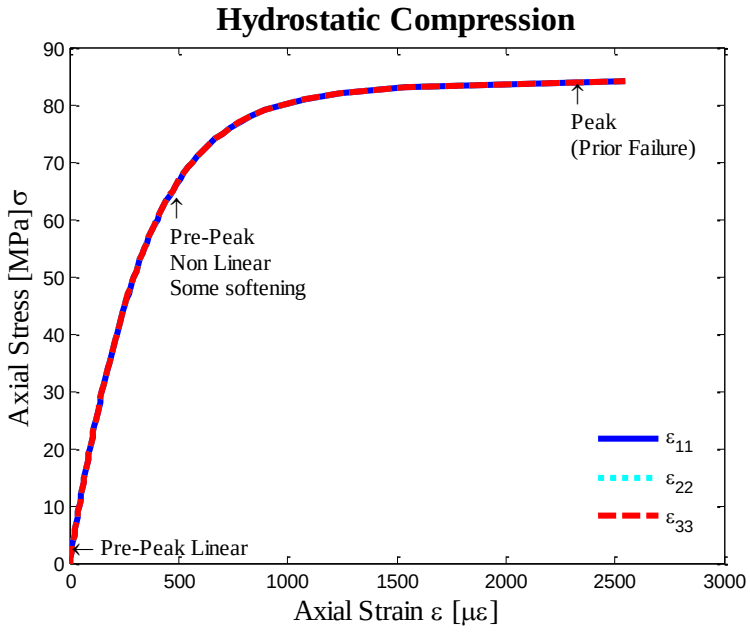

Figure 3.24: Hydrostatic compression at the element level - Stress versus strain curve.

Figure 3.24 describes the stress strain behavior of the material at the element level under hydrostatic compression. The curve presents a linear and non-linear behavior in the pre-peak regime followed by a softening branch preceding the peak load prior to failure.

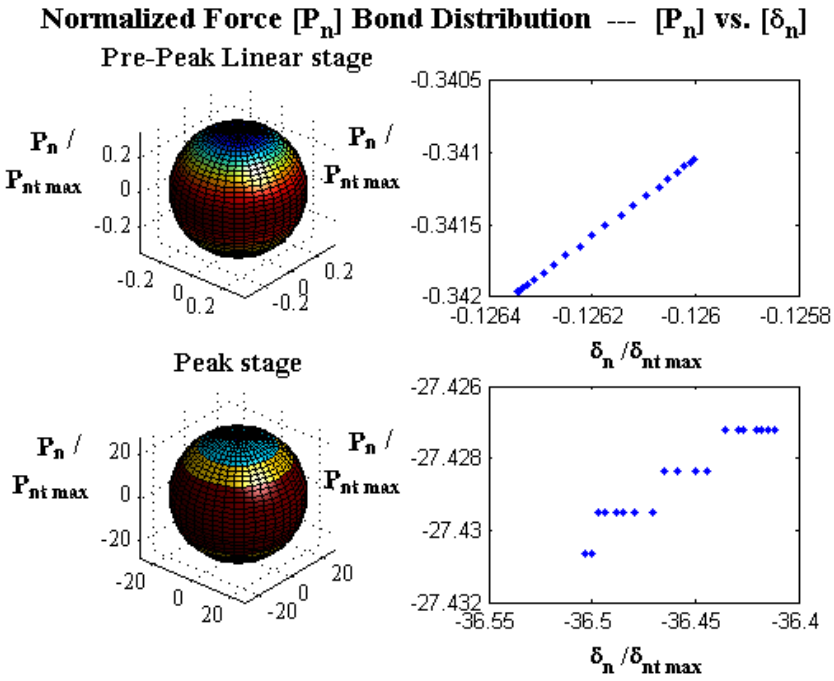

Figure 3.25: Hydrostatic compression at the contact level – Normalized normal force bond-distribution for pre-peak and peak prior failure stages.

Figure 3.25 shows the normalized normal force bond-distribution within the material at the contact level, which for 'pre-peak' and 'peak' stage prior to failure the force values are very close to each other and the displacements is approximately zero. As expected, when a material is subjected to a hydrostatic loading condition, a point stress distribution is expected which is described in these plots.

Figure 3.26 exhibits the normalized tangential force bond-distribution at the contact level under hydrostatic compression which is expected to be zero. Despite that values are close to each

other and close to zero, they are not zero as expected. This is attributed to the numerical approach used to calculate the bond density function.

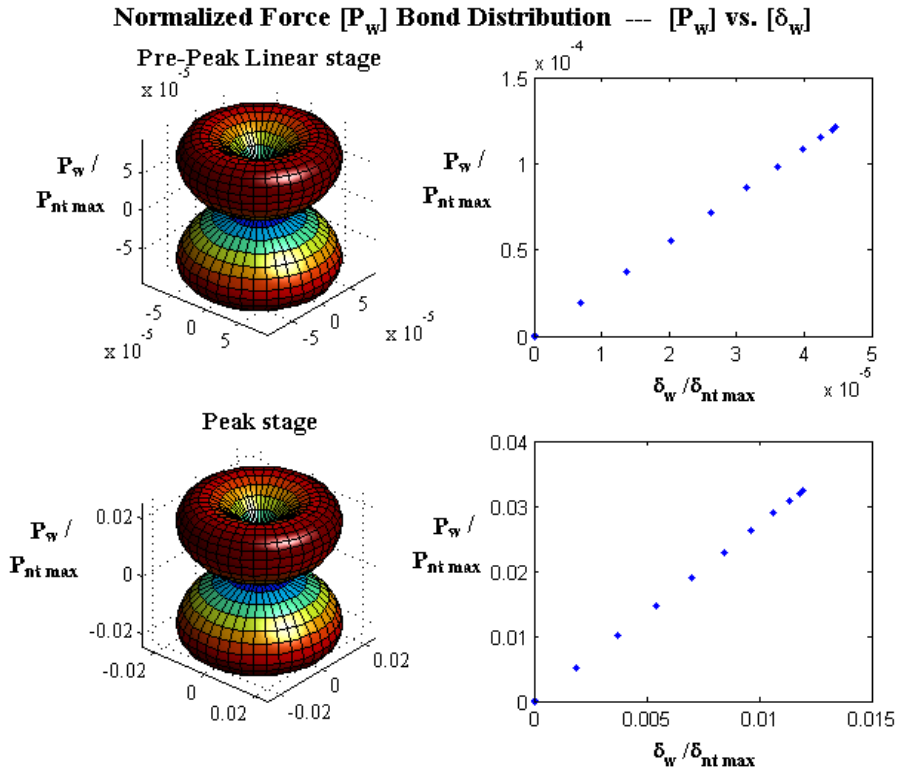

Figure 3.26: Hydrostatic compression at the contact level. Normalized tangential force bond-distribution for the pre-peak and peak prior failure stages.

3.5.7. Hydrostatic tension (TTT).

Hydrostatic tension (TTT) simulation of the material was performed in this section. The stress-strain curve at the element level is presented in Figure 3.27. The normalized normal and tangential force bond-distribution plots at the contact level with their corresponding force-displacement curves are shown in Figures 3.28 and 3.29, respectively. The normalization is based on the maximum tensile values of the normal and tangential force-bond and displacement ($P_{nt\,max}$, $\delta_{nt\,max}$,. $P_{wt\,max}$, $\delta_{wt\,max}$). Plots of the normalized normal force bond-distributions described

a point like force distribution, which is expected under this loading condition. On the other hand, very small stresses were obtained in the tangential direction, which were expected to be zero. These results are attributed to the numerical approximation approach used to integrate the bond density function.

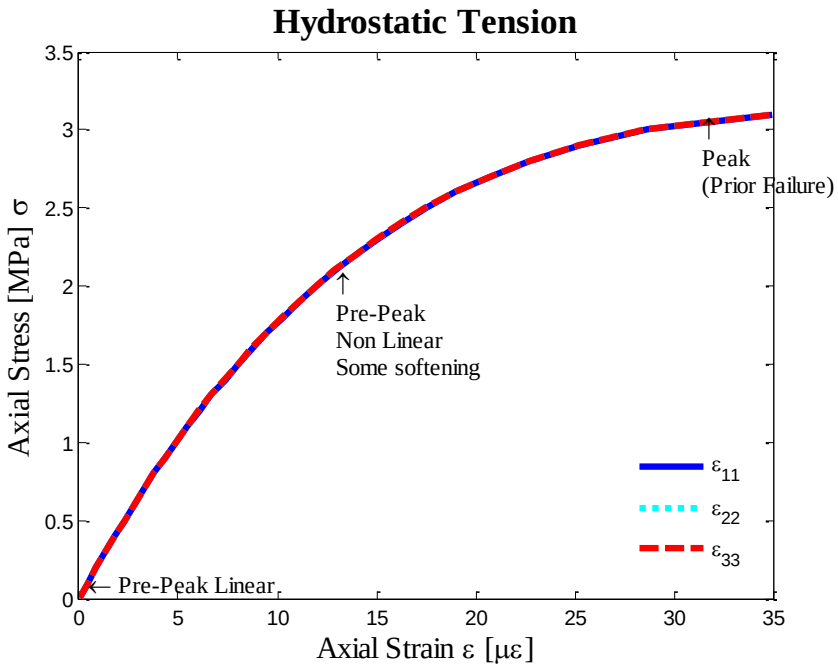

Figure 3.27: Hydrostatic tension at the element level – Stress versus strain curve.

Figure 3.27 describes the stress-strain behavior of the material at the element level under hydrostatic tension (TTT). Compared to the hydrostatic compression (CCC), the material is significantly weaker as expected. This is reflected in the stress-strain curve, where the strain deformation values prior to failure are *very small*. Yet, within this *very small* range, a linear and non-linear pre-peak stage and a peak stage prior to failure are observed.

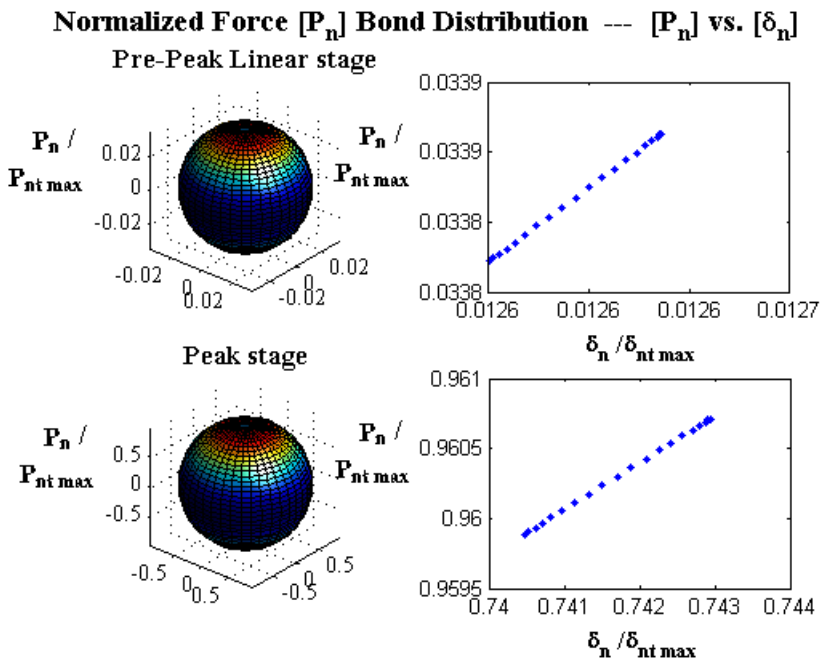

Figure 3.28: Hydrostatic tension at the contact level - Normalized normal force bond-distribution at the pre-peak and peak prior failure stages.

Figure 3.28 exhibits the normalized normal force bond-distribution at the contact level within the material in two stages: at the beginning of loading ('pre-peak') and at the end stage prior to failure of the material ('peak' stage). By observing the force distribution surface plots and the corresponding force-displacement curves, the material can be considered to describe a point-like behavior force distribution and force-displacement behavior.

Figure 3.29 shows the normalized tangential force bond-distribution at the contact level within the material. No tangential forces are expected to occur under this loading condition. However, the plots in this figure show very small non-zero values that are approximately zero. This outcome is attributed to the numerical approach used to calculate the bond density in the model.

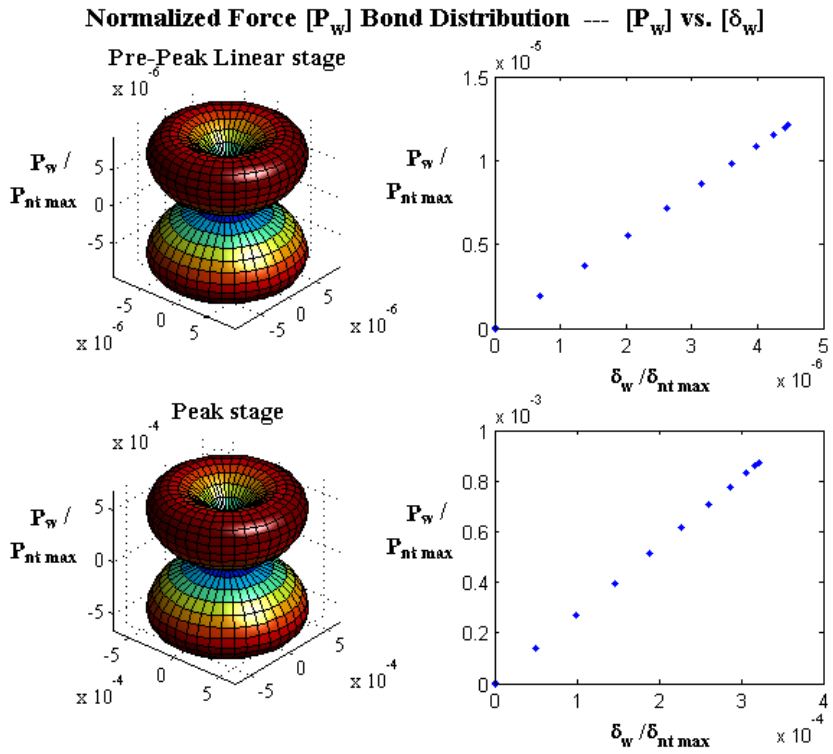

Figure 3.29: Hydrostatic tension at the contact level - Normalized tangential force bond-distribution in the pre-peak and peak prior failure stages.

3.5.8. Equi-triaxial loading compression/compression/tension (CCT).

An equi-triaxial loading simulation was performed by applying compressive stresses in the 11 and 22 directions and a tensile stress in the 33 direction. The stress-strain curve at the element level is shown in Figure 3.30, where the effect of applying tensile stress notoriously reduces the strength of the material in compression which avoids the evolution of compression-softening. This effect is translated into the material by having tensile normal softening as the main failure mechanism while tangential softening is shown to be developing. Figures 3.31 and 3.32 describe the normalized normal and tangential force bond-distribution plots at the contact level with their corresponding force-displacement curves at two loading stages. These stages describe the failure evolution within the material at an initial loading stage (‘pre-peak’) and prior to failure of the

material ('peak' stage). The normalization on Figures 3.31 and 3.32 are based on the maximum tensile values of the normal and tangential force-bond and displacement ($P_{nt\ max}$, $\delta_{nt\ max}$,. $P_{wt\ max}$, $\delta_{wt\ max}$).

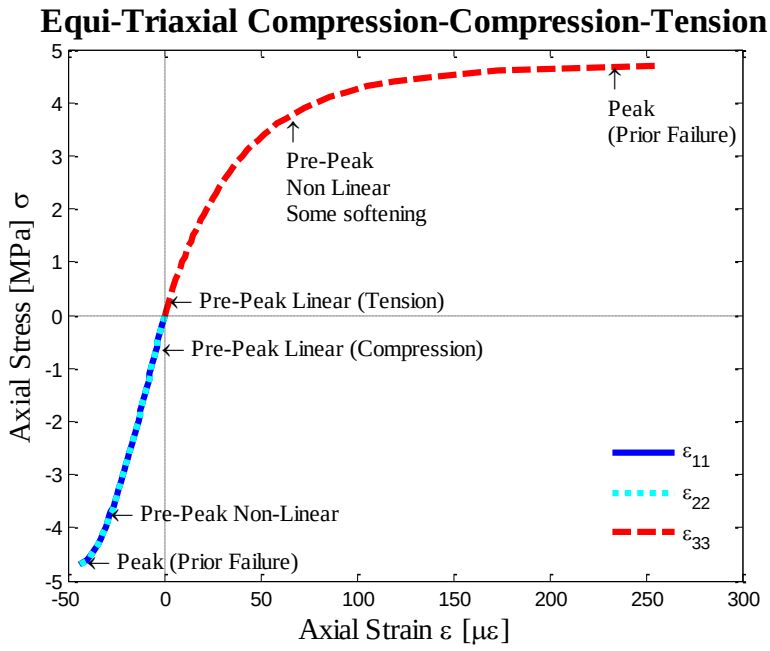

Figure 3.30: Equi-triaxial CCT at the element level - Stress versus strain curve.

Figure 3.30 shows the stress strain curve of the material at the element level under equi-triaxial CCT loading. The effect of the tensile loading in the materials behavior is similar as the one observed in the case of equi-biaxial CT loading, where the compressive strength is compromised and reduced by the presence of tensile stresses. In addition, within the curve a linear followed by a non-linear stress-strain relationship is observed in the stages prior to the peak loading and prior to failure of the material, suggesting that softening actually starts from the time of loading. Comparing the softening branch of the curve in tension with the one in compression, it is observed that tension dominates. This indicates that the dominating failure

mechanism is tensile normal softening of the bonds; some tangential softening will also develop. Figures 3.31 and 3.32 support this observation.

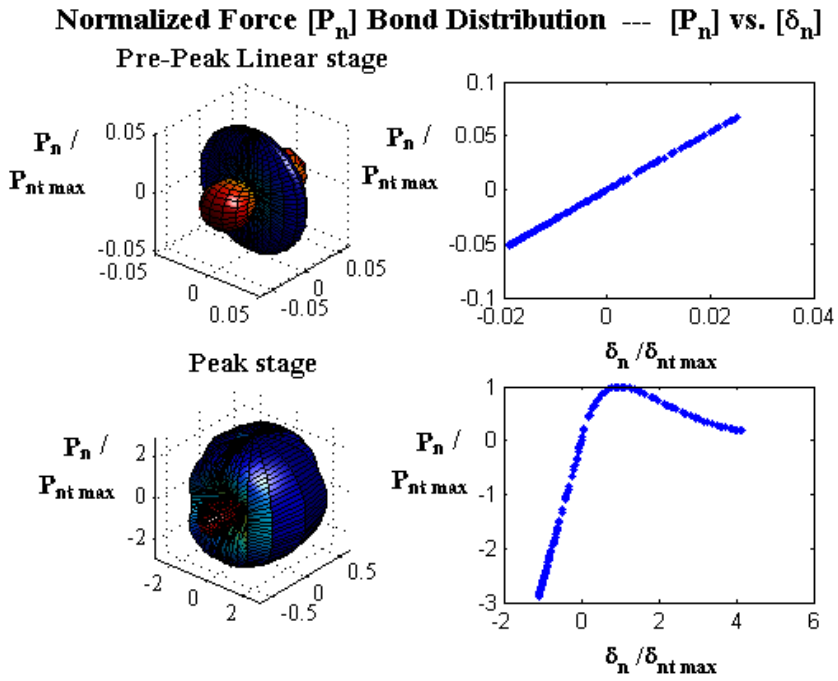

Figure 3.31: Equi-Triaxial CCT at the contact level - Normalized normal force bond-distribution in the pre-peak and peak prior failure stages.

Figure 3.31 shows the normalized normal force bond-distribution within the material at the contact level under CCT loading at two stages: initial and prior failure of the material. At the initial stage (‘pre-peak’), compressive forces (blue color) are observed in the 11 and 22 directions, while tensile forces are shown in the 33 direction (red color). At this stage, the force-displacement curve describes a linear behavior within the material for compression and tension. Then, prior to failure (‘peak’ stage) the surface plot is transformed, the tensile forces are reduced and the compressive forces increased. The physical meaning of this transformation is that the bonds under tension undergo softening and failure and the ones in compression are carrying more load. The force-displacement curve reveals softening of the bonds in tension, where some

are close to failure (zero force value), and an increasing linear behavior for the bonds under compression.

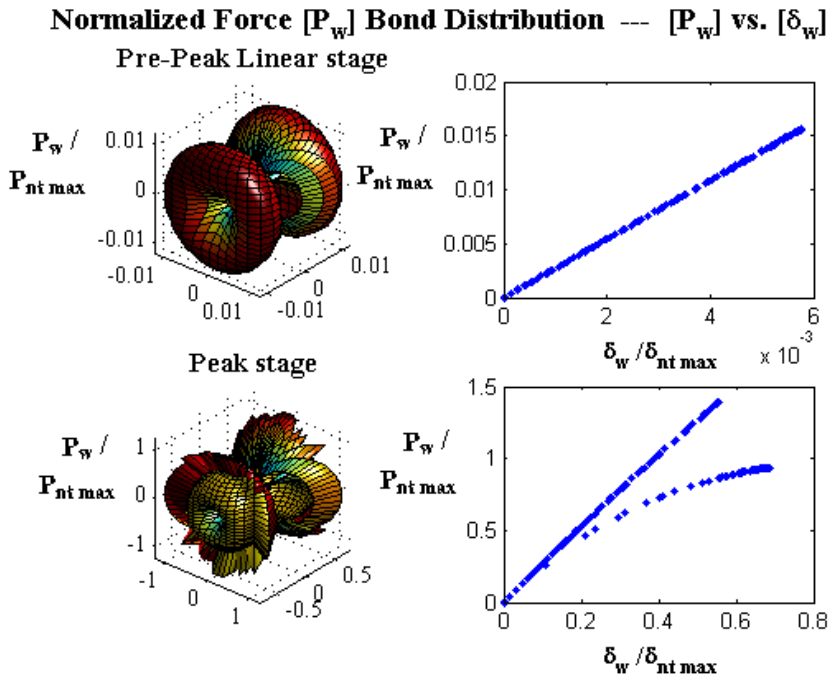

Figure 3.32: Equi-triaxial CCT at the contact level - Normalized tangential force bond-distribution at pre-peak and peak prior failure stages.

Figure 3.32 shows the normalized tangential force bond-distribution of the bonds at the contact level under equi-triaxial CCT loading. Two stages are presented in this figure: the 'pre-peak' stage, representing an initial loading stage, and the 'peak' stage representing a loading time prior failure. As mentioned before, under the presence of tensile stresses, tangential softening is not expected to be the dominating failure mechanism and thus no considerable development of softening is observed in these plots. The material described a linear force-displacement behavior at the initial stage ('pre-peak'), followed of some softening behavior with a non-linear force-displacement behavior prior to failure ('peak' stage).

3.5.9. Shear loading.

In this section, a shear simulation was performed by applying positive shear stresses to the material. The shear stress-strain curve at the element level is shown in Figure 3.33, where the strain values for the axial directions, 11, 22, and 33, and the shear direction (12) are plotted with respect to the shear stress. Strain-hardening is observed in the stress-strain curve in addition to softening behavior prior to failure. For a better understanding of the material's behavior and failure mechanism, the normalized normal and tangential force bond-distribution surface plots at the contact level along with their force-displacement curves are presented in this section. The normalization is based on the maximum tensile values of the normal and tangential force-bond and displacement ($P_{nt\ max}$, $\delta_{nt\ max}$,. $P_{wt\ max}$, $\delta_{wt\ max}$). The normalized material's behavior in the normal direction is presented in Figures 3.34 and 3.35, while the behavior in the tangential direction is shown in Figures 3.36 and 3.37. Three stages are evaluated in these figures: initial stage, 'pre-peak' (stage prior failure), final stage prior failure, 'peak', and an intermediate stage were strain-hardening is observed. In general, the figures show that under shear the material is subjected to compression and tension. The final failure mechanism is dictated by compression failure which is described by showing a significant tangential softening.

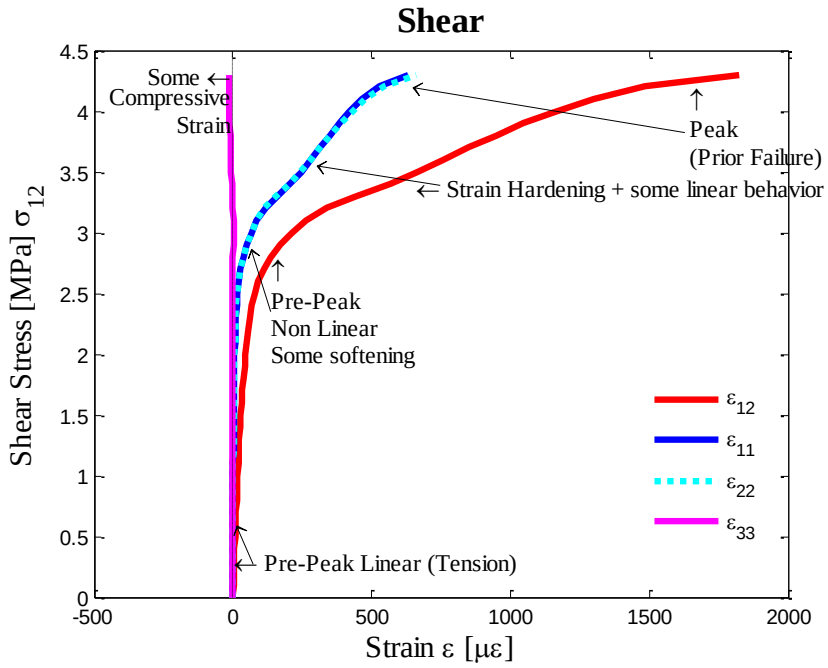

Figure 3.33: Shear at the element level – Stress versus strain curve.

Figure 3.33 describes the shear stress-strain curve of the material at the element level under shear loading. In this curve, a combination of softening with strain-hardening, prior to reaching failure, is observed in the 12, 11, and 33 directions; some contraction prior failure is observed in the 33 direction. Evaluation of the strain values in the 11, 22, and 12 directions, show a linear followed by a non-linear behavior prior to strain-hardening region and prior to failure of the material. The non-linear behavior at the initial stage suggests that softening within the material starts from the beginning of the loading. Then, the strain-hardening behavior suggests that the bonds under tension fail first and the bonds under compression take over the load offering resistance until they are softened. Therefore, normal softening and tangential softening is expected in the force bond-distribution plots at the contact level.

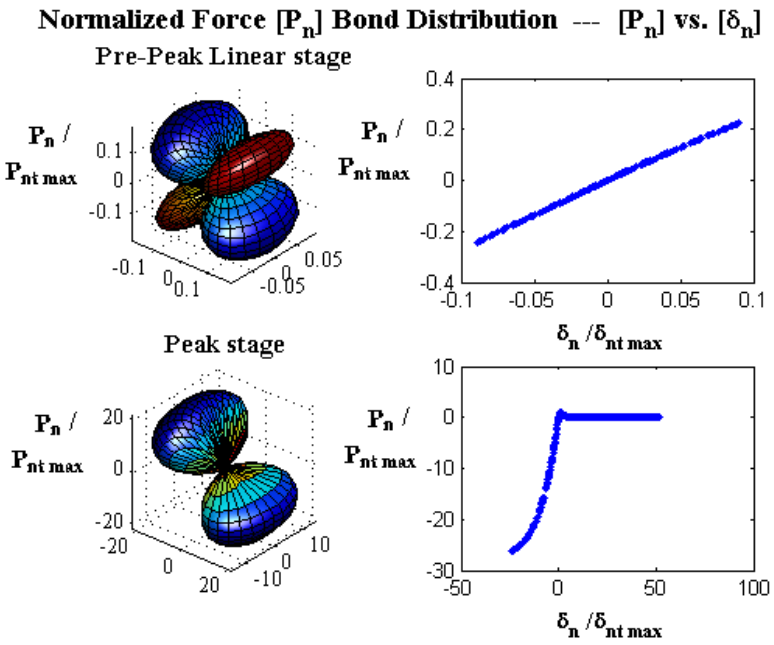

Figure 3.34: Shear at the contact level- Normalized normal force bond-distribution for the pre-peak and peak prior stages.

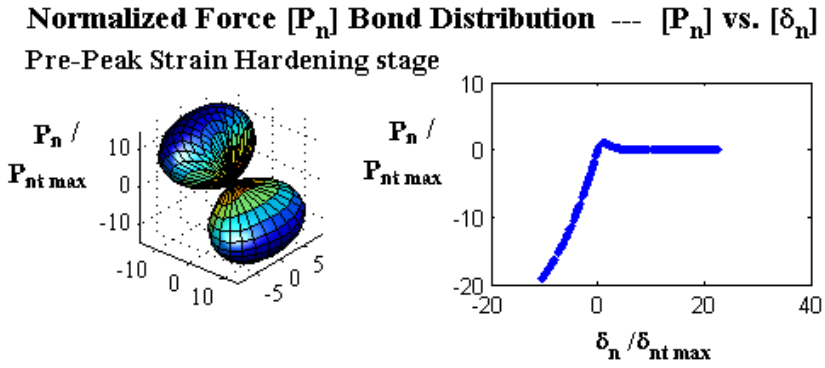

Figure 3.35: Shear at the contact level - Normalized normal force bond-distribution at the strain-hardening stage.

As mentioned in the previous paragraph, in Figure 3.34 the normalized normal force bond-distribution at the contact level at the initial stage ('pre-peak'), shows that the material is subjected to tension and compression and it also describes a linear behavior in the force-displacement curve. Then, the damage-evolution at the strain-hardening stage is illustrated in Figure 3.35. During this stage, the bonds under tension have softened or failed and the bonds in

compression have taken over the load by increasing their normal force values in the surface plot and force-displacement curve. This behavior is reflected in the normalized force-displacement curve where the softening and failure of the bonds (zero force value) in tension are observed and a linear behavior in compression is described. Finally, the behavior at the contact level prior to failure ('peak' stage) is described in Figure 3.34. In this stage, the failure of the tension bonds is more notorious as so it is the softening behavior of the bonds under compression where the asymptotic value can be distinguished.

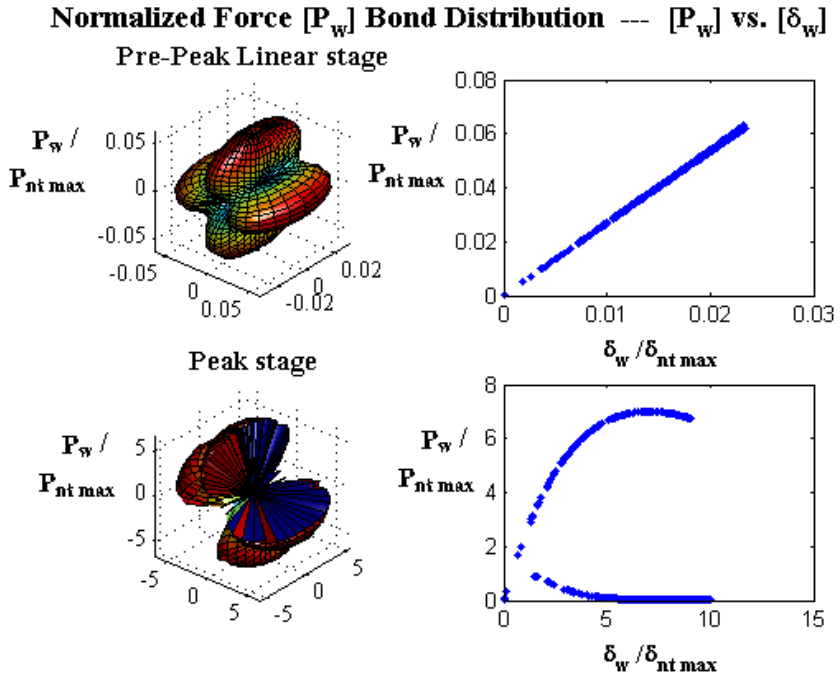

Figure 3.36: Shear at the contact level - Normalized tangential force bond-distribution for the pre-peak and peak prior failure stages.

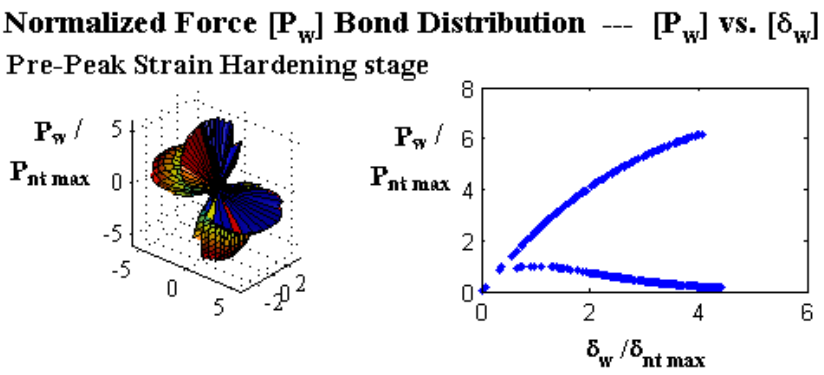

Figure 3.37: Shear at the contact level – Normalized tangential force bond-distribution at the strain-hardening stage.

The development of the softening and failure behavior in the material is also observed when analyzing the normalized tangential force bond-distribution within the material at the contact level in the three loading stages: initial ('pre-peak') stage, strain-hardening, and prior to failure ('peak') stage. Figure 3.36 shows the initial stage ('pre-peak') of the force bond-distribution, which is similar to the normal forces and it describes a linear behavior in the force-displacement curve. As we move towards a higher loading and reach the strain-hardening stage (Figure 3.37), tangential softening of the material is observed in the surface plot and it is better illustrated in the force-displacement curve. In this curve, some bonds describe softening behavior and others an increasing linear behavior. Then, figure 3.36 shows the 'peak' stage (prior to failure) of the force-bond distribution where the force-displacement curve illustrates two type of behavior among the bonds: an increasing non-linear and softening failure behavior. In which, the latter is illustrated by exhibiting zero tangential bond force.

3.6. Constitutive relationship for the idealized system using 2nd gradient theory.

Similar to section 3.4, by incorporating higher order terms up to the second order to the displacement field, we obtain:

$$u_i(x^n) = u_i(x^0) + u_{i,j}(x^0)x_j + \frac{1}{2}u_{i,jk}(x^0)x_j x_k$$
$$\omega_i(x^n) = \omega_i(x^0) + \omega_{i,j}(x^0)x_j \tag{3.123}$$

Where x_i^n is the coordinate of the centroid of the particle n. $u_{i,j}$, $u_{i,jk}$, and $\omega_{i,j}$ are the gradients of displacement and rotation, respectively.

Assuming a uniform particle radius r and that the origin of the local coordinates is at the p[th] particle, and by substituting equations (3.123) into equations (3.2) and (3.3), the relative displacement and rotation at the contact surface becomes:

$$\delta_i^c = (u_{i,k} - e_{ijk}\omega_j)l_k^c + (u_{i,kl} - e_{ijk}\omega_{j,l})J_{kl}^c \tag{3.124}$$

$$\theta_i^c = \omega_{i,j}l_j^c \tag{3.125}$$

Where the geometric quantities:

$$\begin{aligned} l_j^c &= x_j^n - x_j^p \\ l_j^c r_k^c &= x_j^n r_k^n - x_j^p r_k^p \\ l_j^c l_k^c &= x_j^n x_k^n - x_j^p x_k^p \\ J_{jk}^c &= \frac{1}{2}l_j^c l_k^c = l_j^c r_k^c \end{aligned} \tag{3.124a}$$

$$\begin{aligned} l_j^c &= 2rn_j^c \\ l_j^c r_k^c &= 2r^2 n_j^c \end{aligned} \tag{3.124b}$$

From equations (3.124) and (3.125) we determine the polar strain (γ_{jl}^{0}) and the deformation strain and strain gradient tensors ($\varepsilon_{ik}^{0}, \varepsilon_{ikl}^{I}$) as:

$$\gamma_{jl}^{0} = \omega_{j,l} \tag{3.126}$$

$$\begin{aligned} \varepsilon_{ik}^{0} &= u_{i,k} - e_{ijk}\omega_{j} \\ \varepsilon_{ikl}^{I} &= u_{i,kl} - e_{ijk}\omega_{j,l} \end{aligned} \tag{3.127}$$

In addition the following substitutions are performed:

$$\gamma_{jl}^{0} = \frac{\partial \omega_{j}}{\partial x_{l}} \tag{3.126a}$$

$$\phi_{i} = u_{i} - e_{ijk}\omega_{j}x_{k} \tag{3.127a}$$

$$\varepsilon_{ik}^{0} = \phi_{ik} = u_{i,k} - e_{ijk}\omega_{j} = \frac{\partial \phi_{i}}{\partial x_{k}} \tag{3.127b}$$

$$\varepsilon_{ikl}^{I} = \phi_{ikl} = u_{i,kl} - e_{ijk}\omega_{j,l} = \frac{\partial^{2} \phi_{i}}{\partial x_{l}\partial x_{k}} \tag{3.127c}$$

Where the symmetric part of ϕ_{ik}, in equation (3.127b), corresponds to the symmetrical part of the displacement gradient and represents the stretch strain (Chang and Ma, 1991).

$$\phi_{(ik)} = u_{(i,k)} = \frac{1}{2}\left(u_{i,k} + u_{k,i}\right) \tag{3.128}$$

The non-symmetric part of ϕ_{ik} is given by the difference between the rigid body rotation and angular rotation as follows:

$$\phi_{[ik]} = u_{[ik]} - e_{ijk}\omega_j = \frac{1}{2}\left(u_{i,k} - u_{k,i}\right) - e_{ijk}\omega_j \tag{3.129}$$

Where the angular rotation ψ corresponding to the rigid body rotation becomes:

$$e_{ijk}\psi_j = u_{[ik]} \tag{3.130}$$

Equation (3.129) represents the rotational difference between particle and rigid body rotation, which is known as the *net particle spin* (Chang and Ma, 1991), and it is rewritten as:

$$\phi_{[ik]} = e_{ijk}\left(\psi_j - \omega_j\right) = e_{ijk}\left(u_{[ik]} - \omega_j\right) \tag{3.131}$$

Similarly, the symmetric and non-symmetric part of the equation (3.127c) can be written as:

$$\begin{aligned} \phi_{(ik)l} &= u_{(i,k)l} = \frac{1}{2}\left(u_{i,kl} + u_{k,il}\right) \\ \phi_{[ik]l} &= u_{[ik]l} - e_{ijk}\omega_{j,l} = \frac{1}{2}\left(u_{i,kl} - u_{k,il}\right) - e_{ijk}\omega_{j,l} \end{aligned} \tag{3.132}$$

Where the symmetric part represents the gradient of the stretch strain and the angular rotation corresponding to the gradient of the rigid body rotation; this can be written as:

$$e_{ijk}\psi_{j,l} = u_{[ik]l} \tag{3.133}$$

where:

$$\phi_{[ik]l} = e_{ijk}\left(\psi_{j,l} - \omega_{j,l}\right) \tag{3.134}$$

And equation (3.134) represents the *gradient of the net particle spin*.

From an energy approach, the counter part of the polar strain, the deformation strain, and deformation gradient strain tensors described in equations (3.126) and (3.127) are the couple, Cauchy, and double stresses. The constitutive relationships can be derived by considering a representative volume *V*, in which the strain energy can be written in terms of forces/moments and stresses as described in equations (3.135) and (3.136):

$$W = \frac{1}{2V}\sum_{c=1}^{N} f_i^c \delta_i^c + m_i^c \theta_i^c \tag{3.135}$$

$$W = \frac{1}{2V}\sum_{c=1}^{N}\left(\sigma_{ik}^0 \varepsilon_{ik}^0 + \sigma_{ikl}^I \varepsilon_{ikl}^I + \mu_{il}^0 \gamma_{il}^0\right) \tag{3.136}$$

Where *N* refers to the total number of contacts within the representative volume *V* and σ_{ik}^0 , σ_{ikl}^I , and μ_{il}^0 corresponds to the Cauchy, double, and couple stresses, respectively.

By substituting equations (3.124-3.125) into (3.135), the stresses can be rewritten as:

$$\begin{aligned} \sigma_{ik}^0 &= \frac{1}{2V}\sum_{c=1}^{N} f_i l_k \\ \sigma_{ikl}^I &= \frac{1}{2V}\sum_{c=1}^{N} f_i^c J_{kl}^c \end{aligned} \tag{3.137}$$

$$\mu_{il}^{0} = \frac{1}{2V}\sum_{c=1}^{N} m_i^c l_l \tag{3.138}$$

By substituting equations (3.8-3.9) into incremental form of (3.137-3.138), the constitutive stress-strain relationships are determined and written as:

$$\begin{aligned}
\Delta\sigma_{ik}^{0} &= A_{ikql}\Delta\varepsilon_{ql}^{0} + B_{ikqlm}\Delta\varepsilon_{qlm}^{I} \\
\Delta\sigma_{ikl}^{I} &= D_{iklqr}\Delta\varepsilon_{qr}^{0} + E_{iklqrm}\Delta\varepsilon_{qrm}^{I} \\
\Delta\mu_{il}^{0} &= G_{ilqr}\Delta\gamma_{qr}^{0}
\end{aligned} \tag{3.139}$$

For further consideration, we know that B_{ikqlm} and D_{iklqr} are zero, therefore equation (3.139) becomes:

$$\begin{aligned}
\Delta\sigma_{ik}^{0} &= A_{ikql}\Delta\varepsilon_{ql}^{0} \\
\Delta\sigma_{ikl}^{I} &= E_{iklqrm}\Delta\varepsilon_{qrm}^{I} \\
\Delta\mu_{il}^{0} &= G_{ilqr}\Delta\gamma_{qr}^{0}
\end{aligned} \tag{3.140}$$

where:

$$\begin{aligned}
A_{ikql} &= \frac{1}{2V}\sum_{c=1}^{N} K_{iq} l_k l_l \\
E_{iklqrm} &= \frac{1}{2V}\sum_{c=1}^{N} K_{iq} J_{kl}^{c} J_{rm} \\
G_{ilqr} &= \frac{1}{2V}\sum_{c=1}^{N} G_{iq} l_l l_r
\end{aligned} \tag{3.141}$$

Which can also be written as:

$$\begin{aligned}
A_{ikql} &= \frac{4r^2}{2V}\sum_{c=1}^{N} K_{iq} n_k n_l \\
E_{iklqrm} &= \frac{4r^4}{2V}\sum_{c=1}^{N} K_{iq} n_k n_l n_r n_m \\
G_{ilqr} &= \frac{4r^2}{2V}\sum_{c=1}^{N} G_{iq} n_l n_r
\end{aligned} \tag{3.142}$$

The summation of the inter-granular interactions over the entire representative volume can be expressed in an integral form by using a directional truncated density function in terms of spherical harmonic expansions (Yang and Misra, 2010) as follows:

$$\xi(\theta,\phi)=\frac{1}{4\pi}\left[1+\frac{1}{4}a_{20}(3\cos 2\theta+1)+3\sin^2\theta(a_{22}\cos 2\phi+b_{22}\sin 2\phi)\right] \tag{3.143}$$

Where a_{20}, a_{22}, and b_{22} are the fabric parameters that determine the anisotropy of the material. Then, equations (3.142) can be written into an integral form as:

$$\begin{aligned} A_{ikql} &= \frac{4r^2N}{2V}\int_{\Omega} K_{iq}n_k n_l \xi(\theta,\phi)d\Omega \\ E_{iklqrm} &= \frac{4r^4N}{2V}\int_{\Omega} K_{iq}n_k n_l n_r n_m \xi(\theta,\phi)d\Omega \\ G_{ilqr} &= \frac{4r^2N}{2V}\int_{\Omega} G_{iq}n_l n_r \xi(\theta,\phi)d\Omega \end{aligned} \tag{3.144}$$

Where the integration $\int_{\Omega}(\ )d\Omega=\int_0^{2\pi}\int_0^{\pi}(\ )\sin\theta d\theta d\phi$ and $N\xi(\theta,\phi)$ is the number of contacts in the interval Ω to $\Omega+d\Omega$ multiplied by the directional bond density function.

Within this derived theory we can identify three main factors that play an important role in the material's behavior: strain (ε_{qr}^0), strain gradient (ε_{qrm}^I), and rotation gradient (γ_{qr}^0). To determine and fully understand the complex role of these three factors on the material's failure behavior, strain and strain gradients need to be studied separately from rotation gradients. Therefore, in this study we pursue the study of the strain and strain gradient's role alone. Study

of the rotational gradient effects alone and combined with the strain and strain gradient using this model will be performed in a future work.

Gradient theories incorporate the effects of strain gradient on the material's behavior and are becoming more popular to date; they provide a closer representation of the material's failure behavior. This is an advantage over the traditional continuum mechanics approach in which strain gradients are not considered. Evaluation of the strain and strain gradient using our 2nd gradient theory model is performed in section 3.7 using the same model parameters from section 3.5 where: A_1= 0.7 MPa, B= 3.4×10^{-7}, C_1=0.2 MPa , D=1.3×10^{-4} , α_1=2×10^{5} , and α_2=7.

Evaluation of the 2nd gradient theory constitutive model is presented in the following two sections. Section 3.7 describes the effect of the double stresses and section 3.8 qualitatively simulates the effect of particle size on the behavior of concrete and consolidated nano-iron. The first evaluation reveals that double stresses at the element level do not have a significant effect on the Cauchy stresses, yet become very valuable when simulating fracture process at the structural level (Chapter 5). Evaluations in section 3.8 reveal how our model is able to capture the mechanisms of material behavior at the element level. For the cases of the concrete under tension and consolidated nano-iron in compression, an increase in failure stresses and strains is described by the model when using smaller particle sizes.

3.7. Material's behavior under the presence of double stresses.

Using the same parameters as section 3.5, the material's behavior under the presence of strain and strain gradient is studied in this section. Three loading cases are considered: loading in the 11, 12, and 21 directions accompanied with their respective strain gradients 111, 121, and 211.

Figures 3.38 –3.40 show the stress strain behavior of the material with and without the inclusion of strain gradients. From these figures, it can be concluded that at the element level strain gradients have no significant effect on the stress strain behavior within the material. Yet, their contribution becomes very valuable when modeling structures, solving boundary value problems, and simulating the post failure behavior and fracture process within the structure as it is described in Chapter 5.

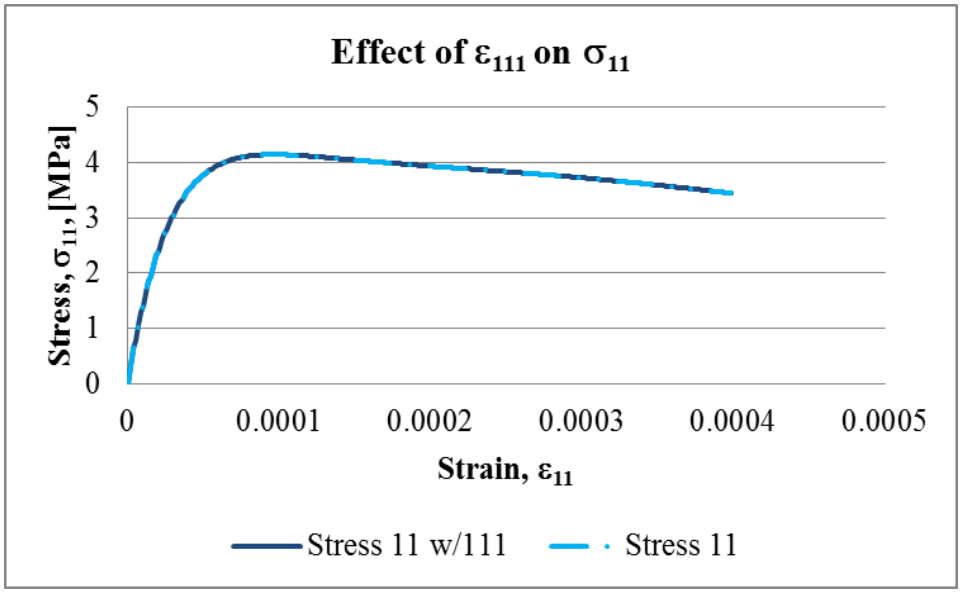

Figure 3.38: Cauchy stresses (σ_{11}) with and without the effects of strain gradient (ε_{111}).

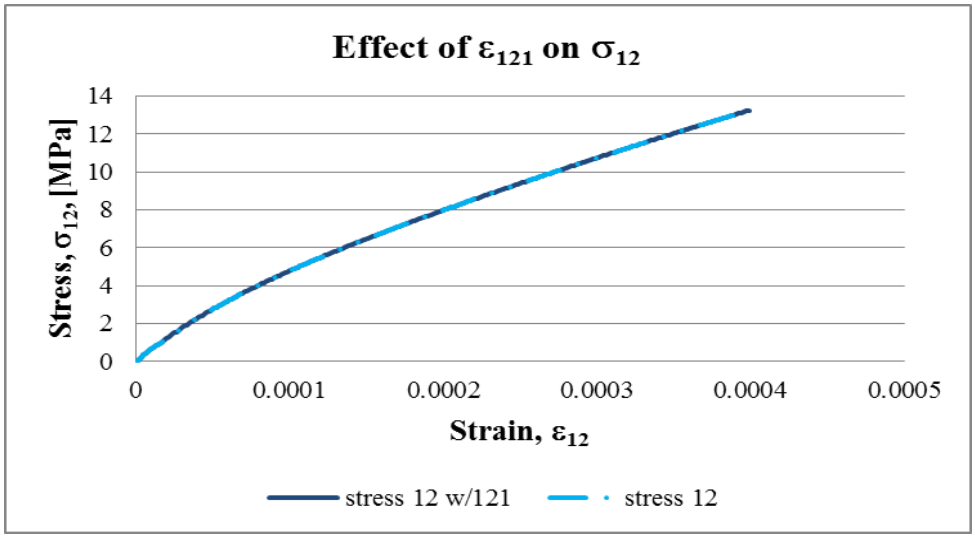

Figure 3.39: Cauchy stresses (σ_{12}) with and without the effects of strain gradient (ε_{121}).

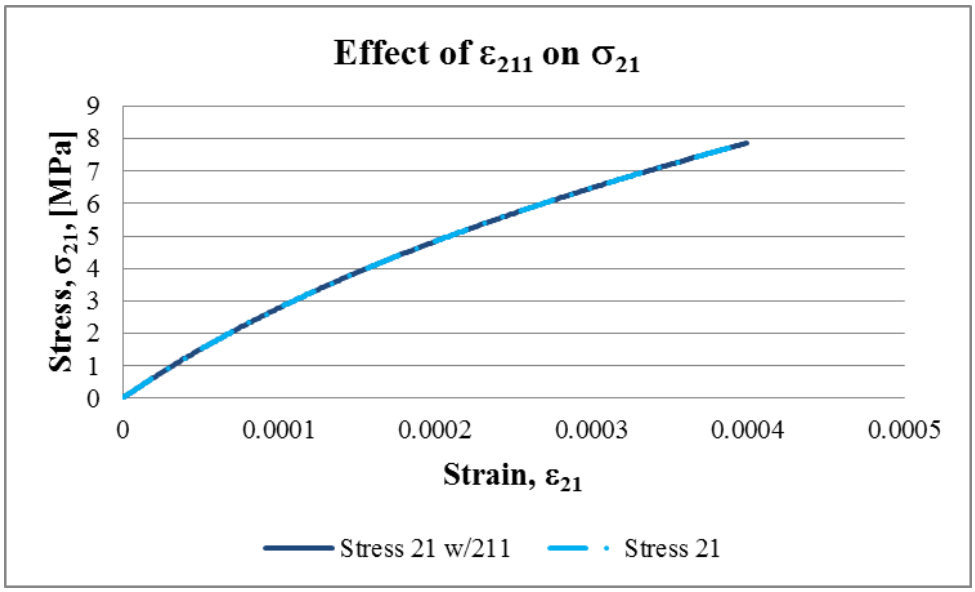

Figure 3.40: Cauchy stresses (σ_{21}) with and without the effects of strain gradient (ε_{211}).

3.8. Material's behavior under different particle size.

In this section, using the derived 2nd gradient constitutive model, the model is adapted to qualitatively simulate the effect of particle size on the stress-strain behavior. The model stiffness parameters were modified to account for the geometrical changes due to particle size. In our

model the particles are idealized as spherical particles and the stiffness parameters A_1, B, C_1, and D, are calculated based on the values used on the reference model. The stiffnesses parameters (A_1^{new} and C_1^{new}) are determined by considering the change in particle bond-length (L_0), and change in number of contacts within particles (N_p). And, the parameters related to the peak stress and corresponding strain measured under uniaxial tension (B^{new} and D^{new}) are determined based on the particle diameter ratio between the new particle size and the reference particle size. The new parameters are obtained as follows:

$$
\begin{aligned}
A_1^{new} &= A_1^{reference} f_{Lo}^{stiffness} f_{Np} \\
C_1^{new} &= C_1^{reference} f_{Lo}^{stiffness} f_{Np} \\
f_{Lo} &= \left(\frac{L_0^{new}}{L_0^{reference}} \right)^2 \\
f_{Np} &= \left(\frac{V_{sphere}^{reference}}{V_{sphere}^{new}} \right) = \left(\frac{D^{reference}}{D^{new}} \right)^3 = \left(\frac{L_0^{reference}}{L_0^{new}} \right)^3
\end{aligned}
\tag{3.145}
$$

where L_0=Particle size diameter (bond-length). And:

$$
\begin{aligned}
B^{new} &= B^{reference} \; f_{Lo}^{stress\text{-}strain} \\
D^{new} &= D^{reference} \; f_{Lo}^{stress\text{-}strain} \\
f_{Lo}^{stress\text{-}strain} &= \left(\frac{L_0^{reference}}{L_0^{new}} \right)
\end{aligned}
\tag{3.146}
$$

For the analyses, the following three particle sizes are considered for concrete: 6 mm, 8 mm, and 10 mm (Hughes and Chapman 1966, Mindess et al. 2003) with the reference particle size of 10mm. In addition, we simulate the behavior of consolidated nano-iron with the following

particle sizes 80 nm, 138 nm, and 268 nm (Jia et al. 2003), with the reference particle size of 100 nm. Table 3.1 gives the reference parameters for the concrete and consolidated nano-iron simulations.

Table 3-1 . Reference parameters for concrete and nano-iron

	$A_1^{reference}$	$C_1^{reference}$	$B^{reference}$	$D^{reference}$	$L_0^{reference}$
Concrete	0.7 MPa	0.2 MPa	3.4×10^{-4}	1.3×10^{-4}	10 mm
Nano-iron	14 GPa	4 GPa	3.4×10^{-4}	1.3×10^{-4}	100 nm

3.8.1. Particle size effect on concrete.

The tensile simulation results show that the model captures the typical effect of particle size within concrete, where smaller particle sizes lead to larger peak stresses and failure strains. Similar trends are described by Hughes and Chapman (1966) study, on river gravel, and by Mindess et al. (2003) in the typical stress-strain behavior of concrete, mortar, and cement paste. In addition, double stress-strain gradient behavior at failure show that smaller particle sizes lead higher peak double stresses and failure gradient strains. Figure 3.41 shows the stress-strain and double stress-strain gradient behavior for different particle sizes.

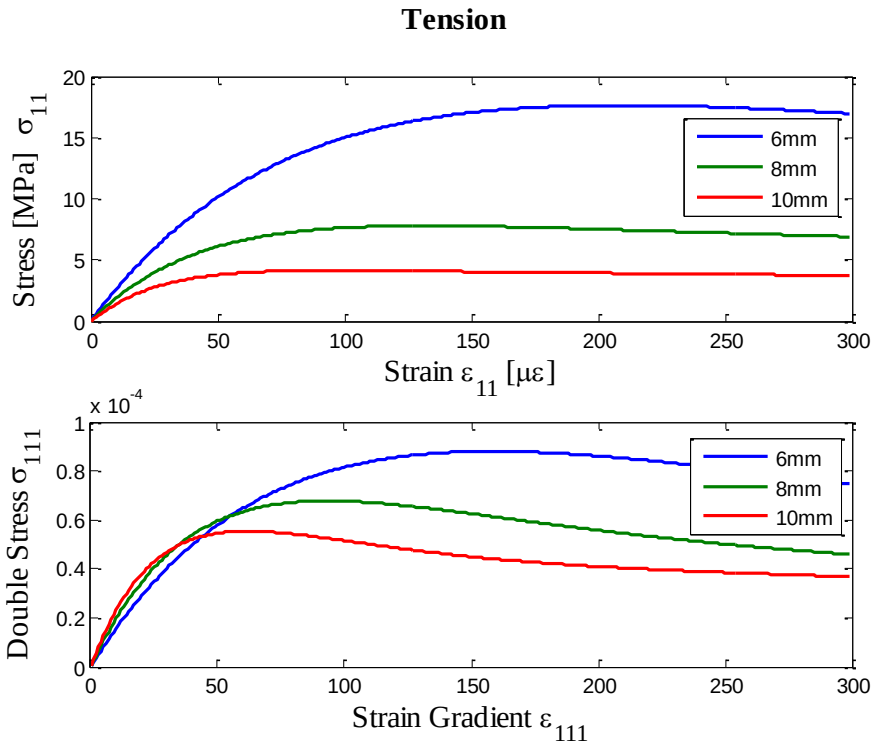

Figure 3.41: Stress versus strain and double stress versus strain gradient for different particle sizes of concrete.

3.8.2. Particle size effect for consolidated nano-iron.

Results of the compressive simulation for consolidated nano-iron show that particle size has an effect on the stress-strain response of the material where smaller particle sizes lead to larger failure strains and larger peak stresses. Strain gradient results corresponding to the peak double stresses show larger values and smaller failure strain gradients for larger particle sizes (Figure 3.42). Similar behavior is described by a typical stress-strain curve of consolidated nano-iron under quasistatic uniaxial compression (Jie et al., 2003).

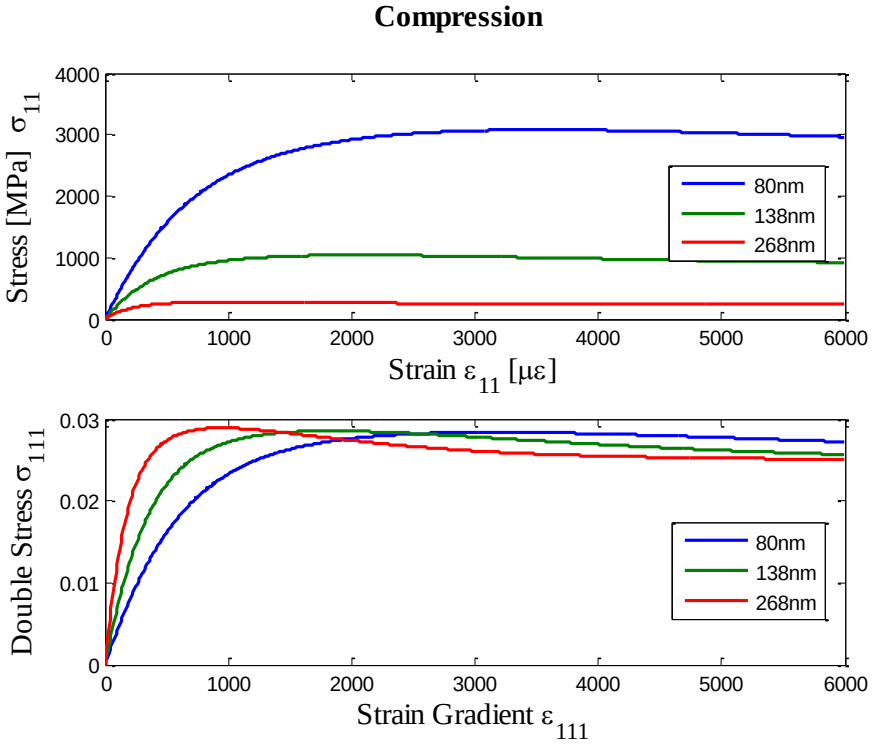

Figure 3.42: Stress versus strain and double stress versus strain gradient for different particle sizes of consolidated nano-iron.

3.9. Aggregate gradation and its effect on material's behavior.

Literature suggests aggregate gradation has no significant effect on the behavior of concrete. According to Komlos' study (1969), the effect of aggregate gradation on the materials stress strain behavior under tension is not significant if the maximum size aggregate remains the same. Then, gradation effects on concrete compressive strength were addressed in a combined study by Karthik et al. (2008) and the National Ready Mixed Concrete Association (2007), where it was concluded that gradation does not have a significant effect on strength results. There is some controversy found on Warda and Munaz study (2011), which suggests that aggregate gradation effects on compressive strength can be associated with their workability and coarseness factors.

Although the study recommends further testing to increase the pool of data points prior defining their effect on concrete's behavior.

Our model is based on micromechanics theory and idealizes the material as a set of spherical particles of the same size with pseudo-bonds, which would represent the cement paste and aggregate within concrete. At a deeper level one could look into the interaction between particles and cement paste to simulate the role of the workability and coarseness factor within the material; a factor to account for this could be also determined. Based on the literature findings, we believe that this would not lead to a significant change in the material's behavior. Therefore, we do not pursue the modeling and study of the aggregate gradation's effect on concrete.

CHAPTER 4. Numerical Implementation of the Model.

This chapter describes in four sections the procedures used to perform the numerical implementation of our model. The first section describes the derivation of the energy functional and weak-form of the constitutive model with the 1st and 2nd gradient theory. The second section provides an overview of the mesh-free method. The third and fourth sections describe the moving least square (MLS) method and element-free-Galerkin (EFG) formulation used to perform the numerical implementation and development of the mesh-free program. The numerical implementation of the model is performed based on the 2nd gradient theory assuming a plane strain condition and considering displacement effects only; rotational parameters will be included and studied separately in future work to understand, in depth, their role on the material's behavior.

4.1. Derivation of the energy functional and weak-form.

Following Yang and Misra (2010) approach and the strain-gradient theory proposed by (Fleck and Hutchinson, 1997), the strain potential energy for the 1st and 2nd gradient constitutive models is determined in the following two sections.

4.1.1. Energy functional.

a) 1st gradient theory

First, the strain potential energy is expressed as:

$$\Delta W = \int_{\varepsilon^0} \Delta \sigma^0_{iq} d\varepsilon_{iq} + \int_{\gamma^0} \Delta M^0_{iq} d\gamma^0_{iq}$$
$$\Delta W = \int_{\varepsilon^0} A_{iqkl} \Delta \varepsilon^0_{kl} d\varepsilon^0_{iq} + \int_{\gamma^0} D_{iqjl} \Delta \gamma^0_{jl} d\gamma^0_{iq} \tag{4.1}$$

Then, the stationarity of the potential is evaluated by satisfying the following equations:

$$\frac{\partial \Delta W}{\partial \varepsilon^0_{iq}} = 0 \tag{4.2a}$$

$$\frac{\partial \Delta W}{\partial \gamma^0_{iq}} = 0 \tag{4.2b}$$

By applying the following substitution:

$$\phi_i = \Delta u_i - e_{ijk} \Delta \omega_j x_k; \qquad \Delta \varepsilon^0_{ik} = \Delta u_{i,k} - e_{ijk} \Delta \omega_j = \frac{\partial \phi_i}{\partial x_k};$$
$$\Delta \varepsilon^I_{ikl} = \Delta u_{i,kl} - e_{ijk} \Delta \omega_{j,l} = \frac{\partial^2 \phi_i}{\partial x_l \partial x_k}; \quad \Delta \gamma^0_{jl} = \frac{\partial \Delta \omega_j}{\partial x_l} \tag{4.3}$$

The equilibrium equation is determined and equations (4.2a-4.2b) become:

$$\frac{\partial \Delta W}{\partial \varepsilon^0_{iq}} = 0 = -\left(\frac{\partial A_{iqkl}}{\partial \varepsilon^0_{st}} \frac{\partial^2 \varphi_s}{\partial x_t \partial x_q} \frac{\partial \varphi_k}{\partial x_l} + A_{iqkl} \frac{\partial^2 \varphi_k}{\partial x_l \partial x_q} \right) \tag{4.4a}$$

$$\frac{\partial \Delta W}{\partial \gamma^0_{iq}} = 0 = -D_{iqjl} \frac{\partial^2 \Delta \omega_j}{\partial x_l \partial x_q} - \frac{\partial D_{iqjl}}{\partial \gamma^0_{st}} \frac{\partial \gamma^0_{st}}{\partial x_q} \frac{\partial \Delta \omega_j}{\partial x_l} = -D_{iqjl} \frac{\partial^2 \Delta \omega_j}{\partial x_l \partial x_q} - \frac{\partial D_{iqjl}}{\partial \gamma^0_{st}} \frac{\partial^2 \Delta \omega_s}{\partial x_t \partial x_q} \frac{\partial \Delta \omega_j}{\partial x_l} \tag{4.4b}$$

b) 2nd gradient theory

First, the strain potential energy is derived as follows:

$$\Delta W = \int_{\varepsilon^0} \Delta \sigma^0_{iq} d\varepsilon_{iq} + \int_{\varepsilon^I} \Delta \sigma^I_{ipq} d\varepsilon^I_{ipq} + \int_{\gamma^0} \Delta \mu^0_{iq} d\gamma^0_{iq}$$

$$\Delta W = \int_{\varepsilon^0} A_{iqkl} \Delta \varepsilon^0_{kl} d\varepsilon^0_{iq} + \int_{\varepsilon^I} E_{ipqklm} \Delta \varepsilon^I_{klm} d\varepsilon^I_{ipq} + \int_{\gamma^0} G_{iqjl} \Delta \gamma^0_{jl} d\gamma^0_{iq} \tag{4.5}$$

Then, we continue the derivation by using integration by parts and by neglecting the boundary terms, such that the energy functional can be rewritten as:

$$\Delta W = \int_{\varepsilon^0} A_{iqkl} \Delta \varepsilon^0_{kl} d\varepsilon^0_{iq} - \int_{\varepsilon^0} \left(E_{ipqklm} \frac{\partial^2 \Delta \varepsilon^0_{km}}{\partial x_l \partial x_p} + \frac{\partial E_{ipqklm}}{\partial x_p} \frac{\partial \Delta \varepsilon^0_{km}}{\partial x_l} \right) d\varepsilon^0_{iq} + \int_{\gamma^0} G_{iqjl} \Delta \gamma^0_{jl} d\gamma^0_{iq}$$

(4.5a)

Where the following substitution is used:

$$\Delta \varepsilon^I_{ipq} = \frac{\partial \Delta \varepsilon^0_{iq}}{\partial x_p} = d\varepsilon^0_{iq} \tag{4.6}$$

Then, the stationarity of the potential is evaluated by satisfying the following equations:

$$\frac{\partial \Delta W}{\partial \varepsilon^0_{iq}} = 0 \tag{4.7a}$$

$$\frac{\partial \Delta W}{\partial \gamma^0_{iq}} = 0 \tag{4.7b}$$

And, by applying the following substitution:

$$\phi_i = \Delta u_i - e_{ijk} \Delta \omega_j x_k; \qquad \Delta \varepsilon^0_{ik} = \Delta u_{i,k} - e_{ijk} \Delta \omega_j = \frac{\partial \phi_i}{\partial x_k};$$

$$\Delta \varepsilon^I_{ikl} = \Delta u_{i,kl} - e_{ijk} \Delta \omega_{j,l} = \frac{\partial^2 \phi_i}{\partial x_l \partial x_k}; \quad \gamma^0_{jl} = \frac{\partial \Delta \omega_j}{\partial x_l} \tag{4.8}$$

The equilibrium equations (4.7a-4.7b) become:

$$\frac{\partial \Delta W}{\partial \varepsilon_{iq}^{0}} = 0 = -\left(\frac{\partial A_{iqkl}}{\partial \varepsilon_{st}^{0}} \frac{\partial^2 \varphi_s}{\partial x_t \partial x_q} \frac{\partial \varphi_k}{\partial x_l} + A_{iqkl} \frac{\partial^2 \varphi_k}{\partial x_l \partial x_q} \right)$$
$$+\left(\frac{\partial E_{ipqklm}}{\partial \varepsilon_{st}^{0}} \frac{\partial^2 \varphi_s}{\partial x_t \partial x_q} \frac{\partial^3 \varphi_k}{\partial x_m \partial x_l \partial x_p} + E_{ipqklm} \frac{\partial^4 \varphi_k}{\partial x_m \partial x_l \partial x_p \partial x_q} \right)$$
$$+\left(\frac{\partial E_{ipqklm}}{\partial \varepsilon_{st}^{0}} \frac{\partial^3 \varphi_s}{\partial x_t \partial x_p \partial x_q} \frac{\partial^2 \varphi_k}{\partial x_m \partial x_l} + \frac{\partial E_{ipqklm}}{\partial \varepsilon_{st}^{0}} \frac{\partial^2 \varphi_s}{\partial x_t \partial x_p} \frac{\partial^3 \varphi_k}{\partial x_m \partial x_l \partial x_q} \right) \tag{4.9a}$$

$$\frac{\partial \Delta W}{\partial \gamma_{iq}^{0}} = 0 = -G_{iqjl} \frac{\partial^2 \Delta \omega_j}{\partial x_l \partial x_q} - \frac{\partial G_{iqjl}}{\partial \gamma_{st}^{0}} \frac{\partial \gamma_{st}^{0}}{\partial x_q} \frac{\partial \Delta \omega_j}{\partial x_l} = -G_{iqjl} \frac{\partial^2 \Delta \omega_j}{\partial x_l \partial x_q} - \frac{\partial G_{iqjl}}{\partial \gamma_{st}^{0}} \frac{\partial^2 \Delta \omega_s}{\partial x_t \partial x_q} \frac{\partial \Delta \omega_j}{\partial x_l} \tag{4.9b}$$

4.1.2. Weak-form derivation.

a) 1st gradient theory

The weak-form equation is derived using the Galerkin method in which equations (4.4a-4.4b) are pre-multiplied by δϕ and δω, respectively, and integrated over a 2D domain, Ω. Thus, the weak-form of these equations is written as:

$$\int_{\Omega} \frac{\partial \delta \phi_i}{\partial x_q} A_{iqkl} \frac{\partial \phi_k}{\partial x_l} d\Omega = \int_{\Gamma} \left[\delta \phi_i n_q \Delta \sigma_{iq}^{0}. \right] d\Gamma \tag{4.10a}$$

$$\int_{\Omega} \frac{\partial \delta \omega_i}{\partial x_q} \left[D_{iqjl} \frac{\partial \Delta \omega_j}{\partial x_l} \right] d\Omega = \int_{\Gamma} \delta \omega_i n_q \Delta M_{iq}^{0} d\Gamma \tag{4.10b}$$

Following Yang and Misra (2010)'s approach, the essential and natural boundary conditions are stated in the boundary integral terms, where the terms corresponding to the testing functions correspond to the essential boundary conditions and the coefficients related to the natural boundary conditions. Then, the essential and boundary conditions are stated as follows:

- **Essential boundary conditions:**

$$\phi_i \text{ and } \omega_i \tag{4.11a}$$

- **Natural Boundary conditions:**

$$\Delta\sigma_{iq}^{0} \text{ and } \Delta M_{iq}^{0} \tag{4.11b}$$

A detailed derivation of the equilibrium and weak-form equation is provided in Appendix (B.1).

Strain values and particle rotation are interrelated parameters where ϕ values depend on the particle rotation ω. By considering the symmetric and non-symmetric part of the Cauchy and couple stresses, equation (4.11b), the independent particle displacement and particle spin parameters are determined, which is advantageous since there is no need to decompose the strain parameters as it is proposed by Suiker, de Borst and Chang (2001)'s approach.

$$\begin{aligned} \Delta\sigma_{iq}^{0} &= 0 \\ \Delta M_{iq}^{0} &= 0 \end{aligned} \tag{4.12a}$$

$$\begin{aligned} &\Delta\sigma_{(iq)}^{0} = 0 \rightarrow \phi_{(iq)} \rightarrow \text{Independent particle displacement} \\ &\Delta\sigma_{[iq]}^{0} = 0 \rightarrow \phi_{[iq]} \rightarrow \text{Net particle spin} \\ &\Delta M_{\text{iq}}^{0} = 0 \rightarrow \omega \rightarrow \text{Particle rotation} \end{aligned} \tag{4.12b}$$

b) 2nd gradient theory

The weak-form equation is derived using the Galerkin method in which equation (4.9a-4.9b) are pre-multiplied by $\delta\phi$ and $\delta\omega$, respectively, and integrated over a 2D domain, Ω. Thus, the weak-form of these equations is written as:

$$\int_{\Omega} \frac{\partial \delta\phi_i}{\partial x_q} A_{iqkl} \frac{\partial \phi_k}{\partial x_l} d\Omega + \int_{\Omega} \frac{\partial^2 \delta\phi_i}{\partial x_q \partial x_p} \left[E_{ipqklm} \frac{\partial^2 \phi_k}{\partial x_m \partial x_l} \right] d\Omega = \int_{\Gamma} \left[\delta\phi_i n_q \left(\Delta\sigma_{iq}^0 - \frac{\partial \Delta\sigma_{ipq}^I}{\partial x_p} \right) . + n_p \frac{\partial \delta\phi_i}{\partial x_q} \Delta\sigma_{ipq}^I \right] d\Gamma \tag{4.13a}$$

$$\int_{\Omega} \frac{\partial \delta\omega_i}{\partial x_q} \left[G_{iqjl} \frac{\partial \Delta\omega_j}{\partial x_l} \right] d\Omega = \int_{\Gamma} \delta\omega_i n_q \Delta\mu_{iq}^0 d\Gamma \tag{4.13b}$$

Using the same approach as the 1st gradient theory, the essential and natural boundary conditions are stated as follows:

- **Essential boundary conditions:**

$$\phi_i, \phi_{i,q} \text{ and } \omega_i \tag{4.14a}$$

- **Natural Boundary conditions:**

$$\Delta\sigma_{iq}^0 - \frac{\partial \Delta\sigma_{iqp}^I}{\partial x_p}, \Delta\sigma_{iqp}^I \text{ and } \Delta\mu_{iq}^0 \tag{4.14b}$$

A detailed derivation of the equilibrium and weak-form equation is provided in Appendix (B.2).

Strain values and particle rotation are interrelated parameters where ϕ values depend on the particle rotation ω. The implementation of higher order stresses allows us to solve for these parameters without having to undergo decomposition of the parameters into independent particle displacements and particle spin terms as it is proposed by Suiker, de Borst and Chang (2001).

With higher order stresses, the following equilibrium equations need to be satisfied:

$$\begin{aligned} \Delta\sigma_{iq}^0 + \Delta\sigma_{iqp}^I &= 0 \\ \Delta\mu_{iq}^0 &= 0 \end{aligned} \tag{4.15a}$$

By considering the symmetric and non-symmetric terms, equation (4.14b) can be rewritten and the independent particle displacement, net particle spin, and particle rotation are determined.

$$\begin{aligned}
&\Delta\sigma^{0}_{(iq)} + \Delta\sigma^{I}_{(iq)p} = 0 \rightarrow \phi_{(iq)} \rightarrow \text{Independent particle displacement} \\
&\Delta\sigma^{0}_{[iq]} + \Delta\sigma^{I}_{[iq]p} = 0 \rightarrow \phi_{[iq]} \rightarrow \text{Net particle spin} \\
&\Delta\mu^{0}_{\text{iq}} = 0 \rightarrow \omega \rightarrow \text{Particle rotation}
\end{aligned} \tag{4.15b}$$

4.2. Mesh-free method overview.

According to Liu and Gu (2005), mesh-free methods use a set of nodes, *field nodes*, to represent the problem domain and its boundaries. Determination of the value of the field variables, at a specific sampling node, does not require nodal-connectivity information; these values are approximated by using shape functions based on a set of nodes within the local domain of the sampling node.

In general, for the global domain of the problem, a weak-form equation based on the Galerkin method is used with MLS approximation shape functions at the local domain to compute the value of a field variable at a specific node. In addition, a set of background cells are defined in the problem to evaluate the Galerkin weak-form integrals (Figure 4.1).

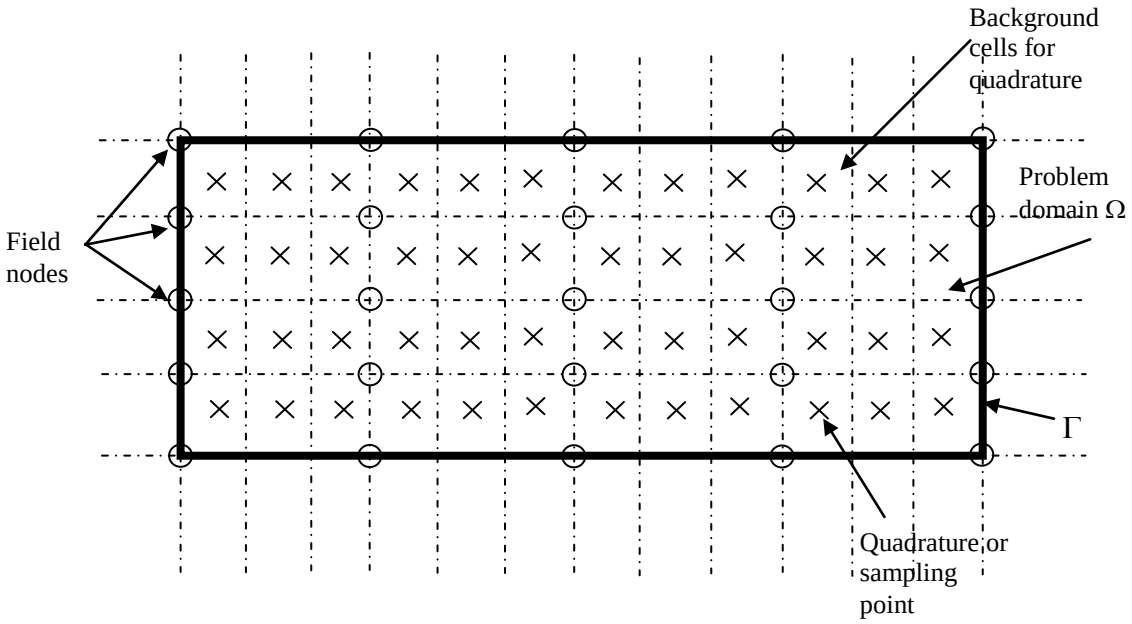

Figure 4.1: Schematic representation of the mesh-free method.

From sections 4.1.1 and 4.1.2 we obtain the Galerkin weak-form global equations of the problem and the natural and essential boundary conditions, from which the latter needs to be treated and enforced separately to proceed with the numerical implementation of the model. The next two sections describe the procedures used to develop the mesh-free program, which are based on Liu and Gu (2005) and Yang and Misra (2010).

4.3. Moving least square (MLS) approximation shape functions.

This method is widely used to compute mesh-free shape functions and uses a varitional principle to best approximate the unknown field function $\Delta u_{(x)}$ at any point of interest. MLS approximation is based on a *'local'* support domain, in which the nodes within this domain are used to perform the approximation of the unknown function at this point; nodal-connectivity is ruled by weight functions.

For a 2D problem, the weight function is the product of the weight functions in the *x* and *y* directions.

$$W_{i(x,y)} = W_{ix(x)} \cdot W_{iy(y)} \tag{4.16}$$

The weight functions are derived by using a cubic spline function and are expressed as:

$$W_{ix(x)} = \begin{Bmatrix} 2/3 - 4\bar{r}_{ix}^2 + 4\bar{r}_{ix}^3 \\ 4/3 - 4\bar{r}_{ix} - 4\bar{r}_{ix}^2 + 4/3\bar{r}_{ix}^3 \\ 0 \end{Bmatrix} \begin{matrix} \bar{r}_{ix} \le 0.5 \\ \text{for} \quad 0.5 < \bar{r}_{ix} \le 1 \\ \bar{r}_{ix} > 1 \end{matrix} \tag{4.17a}$$

$$W_{iy(y)} = \begin{Bmatrix} 2/3 - 4\bar{r}_{iy}^2 + 4\bar{r}_{iy}^3 \\ 4/3 - 4\bar{r}_{iy} - 4\bar{r}_{iy}^2 + 4/3\bar{r}_{iy}^3 \\ 0 \end{Bmatrix} \begin{matrix} \bar{r}_{iy} \le 0.5 \\ \text{for} \quad 0.5 < \bar{r}_{iy} \le 1 \\ \bar{r}_{iy} > 1 \end{matrix} \tag{4.17b}$$

where:

$$\bar{r}_{ix} = \frac{|x - x_i|}{d_{sx}}, \quad \bar{r}_{iy} = \frac{|y - y_i|}{d_{sy}}$$
$$d_{sx} = \beta \cdot d_{cx}, \quad d_{sy} = \beta \cdot d_{cy} \tag{4.18}$$

$|x - x_i|$: Distance from node x_i to the sampling node x.

$|y - y_i|$: Distance from node y_i to the sampling node y.

d_{cx}, d_{cy}: Nodal displacement in the *x* and *y* direction.

β: Dimensionless parameter with a value of 3.1.

d_{sx}, d_{sy}: domain of influence dimensions in the x and y direction.

For our study, a rectangular shape domain of influence is defined to determine the MLS approximation function. This function is defined as:

$$\Phi_{(x,y)} = \begin{Bmatrix} \phi_1 \\ \vdots \\ \phi_n \end{Bmatrix}_{(n \times 1)} \tag{4.19}$$

$$\Phi^T = \gamma^T_{(x,y)} B_{(x,y)} = p^T_{(x,y)} A^{-1}_{(x,y)} B_{(x,y)} \tag{4.20}$$

$$p^T_{(x,y)} = \begin{bmatrix} 1 & x & y & x^2 & xy & y^2 \end{bmatrix} \tag{4.21}$$

$$p_{(x,y)} = A_{(x,y)} \gamma_{(x,y)} \tag{4.22}$$

where:

n: number of nodes in the influence domain of the sampling point (x, y).

p: the polynomial based vector with a number of basic functions $m = 6$.

And the matrix A and the vector B are expressed as:

$$\begin{aligned} A_{(x)} &= \sum_{i=1}^{n} W_{i(x,y)} p_{i(x,y)} p^T_{i(x,y)} \\ B_{(x)} &= \begin{bmatrix} W_{1(x,y)} p_{1(x,y)} \cdots W_{n(x,y)} p_{n(x,y)} \end{bmatrix} \end{aligned} \tag{4.23}$$

In addition, the partial derivatives of the shape functions, Φ are expressed as:

$$\begin{aligned} \Phi^T_{,x} &= \gamma^T_{,x} B + \gamma^T B_{,x} \\ \Phi^T_{,y} &= \gamma^T_{,y} B + \gamma^T B_{,y} \\ \Phi^T_{,xy} &= \gamma^T_{,xy} B + \gamma^T_{,x} B_{,y} + \gamma^T_{,y} B_{,x} + \gamma^T B_{,xy} \\ \Phi^T_{,xx} &= \gamma^T_{,xx} B + \gamma^T_{,x} B_{,x} + \gamma^T_{,x} B_{,x} + \gamma^T B_{,xx} \\ \Phi^T_{,yy} &= \gamma^T_{,yy} B + \gamma^T_{,y} B_{,y} + \gamma^T_{,y} B_{,y} + \gamma^T B_{,yy} \end{aligned} \tag{4.24a}$$

where:

$$\begin{aligned} A\gamma_{,x} &= p_{,x} - A_{,x}\gamma \\ A\gamma_{,y} &= p_{,y} - A_{,y}\gamma \\ A\gamma_{,xy} &= p_{,xy} - \left(A_{,x}\gamma_{,y} + A_{,y}\gamma_{,x} + A_{,xy}\gamma\right) \\ A\gamma_{,xx} &= p_{,xx} - \left(A_{,x}\gamma_{,x} + A_{,x}\gamma_{,x} + A_{,xx}\gamma\right) \\ A\gamma_{,yy} &= p_{,yy} - \left(A_{,y}\gamma_{,y} + A_{,y}\gamma_{,y} + A_{,yy}\gamma\right) \end{aligned} \tag{4.24b}$$

Finally, the approximated MLS function for the sampling point (x, y) is expressed as:

$$\Delta u^{h}_{(x,y)} = \sum_{i}^{n} \phi_{i(x,y)} \Delta u_i = \Phi^T \Delta U \tag{4.25}$$

where:

ΔU : Displacement vector in the incremental form that collects the nodal parameters of the unknown field within the influence domain.

Φ : Vector of MLS shape functions corresponding to the *n* nodes within the influence domain of the sampling point (x, y).

4.4. Element-free-Galerkin method – EFG formulation.

Following the approaches by Liu and Gu (2005) and Yang and Misra (2010) on applying the element Galerkin method to derive the weak-form, the global equation for the problem domain is defined as:

- Galerkin constrained weak-form – 1st gradient theory

$$\begin{aligned}
&\int_{\Omega} \frac{\partial \delta\phi_i}{\partial x_q} A_{iqkl} \frac{\partial \phi_k}{\partial x_l} d\Omega + \int_{\Omega} \frac{\partial \delta\omega_i}{\partial x_q} \left[D_{iqjl} \frac{\partial \Delta\omega_j}{\partial x_l} \right] d\Omega - \int_{\Gamma} \left[\delta\phi_i n_q \Delta\sigma^0_{iq}. \right] d\Gamma - \int_{\Gamma} \delta\omega_i n_q \Delta M^0_{iq} d\Gamma \\
&- \frac{1}{2} \int_{\Gamma_u} \delta \left[(\Delta u_i - \Delta\bar{u}_i)^T \alpha (\Delta u_i - \Delta\bar{u}_i) \right] d\Gamma - \frac{1}{2} \int_{\Gamma_w} \delta \left[(\Delta w_i - \Delta\bar{w}_i)^T \alpha_w (\Delta w_i - \Delta\bar{w}_i) \right] d\Gamma = 0
\end{aligned} \tag{4.26}$$

For simplicity, the higher-order essential boundary conditions are ignored and the equation (4.26) becomes:

$$\begin{aligned}
&\int_{\Omega} \frac{\partial \delta\phi_i}{\partial x_q} A_{iqkl} \frac{\partial \phi_k}{\partial x_l} d\Omega + \int_{\Omega} \frac{\partial \delta\omega_i}{\partial x_q} \left[D_{iqjl} \frac{\partial \Delta\omega_j}{\partial x_l} \right] d\Omega \\
&- \int_{\Gamma} \left[\delta\phi_i n_q \Delta\sigma^0_{iq}. \right] d\Gamma - \int_{\Gamma} \delta\omega_i n_q \Delta M^0_{iq} d\Gamma - \int_{\Gamma_u} \delta \left(\Delta u_i{}^T \alpha \Delta\bar{u}_i \right) d\Gamma - \int_{\Gamma_u} \delta \left(\Delta\bar{u}_i{}^T \alpha \Delta u_i \right) d\Gamma \\
&- \int_{\Gamma_w} \delta \left(\Delta w_i{}^T \alpha_w \Delta\bar{w}_i \right) d\Gamma - \int_{\Gamma_w} \delta \left(\Delta\bar{w}_i{}^T \alpha_w \Delta w_i \right) d\Gamma = 0
\end{aligned} \tag{4.27}$$

- Galerkin constrained weak-form – 2nd gradient theory

$$\int_{\Omega}\frac{\partial\delta\phi_i}{\partial x_q}A_{iqkl}\frac{\partial\phi_k}{\partial x_l}d\Omega+\int_{\Omega}\frac{\partial^2\delta\phi_i}{\partial x_q\partial x_p}\left[E_{ipqklm}\frac{\partial^2\phi_k}{\partial x_m\partial x_l}\right]d\Omega+\int_{\Omega}\frac{\partial\delta\omega_i}{\partial x_q}\left[G_{iqjl}\frac{\partial\omega_j}{\partial x_l}\right]d\Omega$$
$$-\int_{\Gamma}\left[\delta\phi_i n_q\left(\Delta\sigma^0_{iq}-\frac{\partial\Delta\sigma^I_{ipq}}{\partial x_p}\right).+n_p\frac{\partial\delta\phi_i}{\partial x_q}\Delta\sigma^I_{ipq}\right]d\Gamma-\int_{\Gamma}\delta\omega_i n_q\Delta\mu^0_{iq}d\Gamma$$
$$-\frac{1}{2}\int_{\Gamma_u}\delta\left[\left(\Delta u_i-\Delta\bar{u}_i\right)^T\alpha\left(\Delta u_i-\Delta\bar{u}_i\right)\right]d\Gamma-\frac{1}{2}\int_{\Gamma_w}\delta\left[\left(\Delta w_i-\Delta\bar{w}_i\right)^T\alpha_w\left(\Delta w_i-\Delta\bar{w}_i\right)\right]d\Gamma=0 \tag{4.28}$$

For simplicity, the higher-order essential boundary conditions are ignored and equation (4.28) becomes:

$$\int_{\Omega}\frac{\partial\delta\phi_i}{\partial x_q}A_{iqkl}\frac{\partial\phi_k}{\partial x_l}d\Omega+\int_{\Omega}\frac{\partial^2\delta\phi_i}{\partial x_q\partial x_p}\left[E_{ipqklm}\frac{\partial^2\phi_k}{\partial x_m\partial x_l}\right]d\Omega+\int_{\Omega}\frac{\partial\delta\omega_i}{\partial x_q}\left[G_{iqjl}\frac{\partial\Delta\omega_j}{\partial x_l}\right]d\Omega$$
$$-\int_{\Gamma}\left[\delta\phi_i n_q\left(\Delta\sigma^0_{iq}-\frac{\partial\Delta\sigma^I_{ipq}}{\partial x_p}\right).+n_p\frac{\partial\delta\phi_i}{\partial x_q}\Delta\sigma^I_{ipq}\right]d\Gamma$$
$$-\int_{\Gamma}\delta\omega_i n_q\Delta\mu^0_{iq}d\Gamma-\int_{\Gamma_u}\delta\left(\Delta u_i{}^T\alpha\Delta\bar{u}_i\right)d\Gamma-\int_{\Gamma_u}\delta\left(\Delta\bar{u}_i{}^T\alpha\Delta u_i\right)d\Gamma$$
$$-\int_{\Gamma_w}\delta\left(\Delta w_i{}^T\alpha_w\Delta\bar{w}_i\right)d\Gamma-\int_{\Gamma_w}\delta\left(\Delta\bar{w}_i{}^T\alpha_w\Delta w_i\right)d\Gamma=0 \tag{4.29}$$

where:

$\Delta\bar{u}_i$: the prescribed displacement vector in incremental form.

$\Delta\bar{w}_i$: the prescribed rotational vector in incremental form.

α and α_w : the diagonal matrices of penalty '*k*' factors, where k=2 for 2D and k=3 for 3D. In general, these '*k*' factors are large positive constants. In our study we applied a penalty factor that is 10^6 times the maximum value of the stiffness matrix.

Since rotational effects are not considered in this simulation and it is performed based on the 2nd gradient theory, equation (4.29) can be rewritten as:

$$\int_{\Omega} \frac{\partial \delta\phi_i}{\partial x_q} A_{iqkl} \frac{\partial \phi_k}{\partial x_l} d\Omega + \int_{\Omega} \frac{\partial^2 \delta\phi_i}{\partial x_q \partial x_p} \left[E_{ipqklm} \frac{\partial^2 \phi_k}{\partial x_m \partial x_l} \right] d\Omega$$
$$- \int_{\Gamma} \left[\delta\phi_i n_q \left(\Delta\sigma^0_{iq} - \frac{\partial \Delta\sigma^I_{ipq}}{\partial x_p} \right). + n_p \frac{\partial \delta\phi_i}{\partial x_q} \Delta\sigma^I_{ipq} \right] d\Gamma - \int_{\Gamma_u} \delta\left(\Delta u_i{}^T \alpha \Delta \bar{u}_i \right) d\Gamma - \int_{\Gamma_u} \delta\left(\Delta \bar{u}_i{}^T \alpha \Delta u_i \right) d\Gamma = 0 \quad (4.30)$$

4.4.1. Formulation.

The weak-form equilibrium global equation over the problem domain is defined by a domain Ω and a boundary Γ; from which two boundaries conditions are defined: natural and essential boundary conditions. The former boundary conditions are treated in the formulation of the weak-form while the latter boundary conditions need to be treated and enforced separately. The weak-form equilibrium equation and the boundary conditions for our problem are presented below:

Weak-form of equilibrium equation:

$$\int_{\Omega} \frac{\partial \delta\phi_i}{\partial x_q} A_{iqkl} \frac{\partial \phi_k}{\partial x_l} d\Omega + \int_{\Omega} \frac{\partial^2 \delta\phi_i}{\partial x_q \partial x_p} \left[E_{ipqklm} \frac{\partial^2 \phi_k}{\partial x_m \partial x_l} \right] d\Omega = \int_{\Gamma} \left[\delta\phi_i n_q \left(\Delta\sigma^0_{iq} - \frac{\partial \Delta\sigma^I_{ipq}}{\partial x_p} \right). + n_p \frac{\partial \delta\phi_i}{\partial x_q} \Delta\sigma^I_{ipq} \right] d\Gamma \quad (4.13a)$$

Essential boundary conditions:

ϕ_i and $\phi_{i,q}$ (4.31a)

Natural boundary conditions are within the traction boundaries Γ:

$\Delta\sigma^0_{iq} - \frac{\partial \Delta\sigma^I_{iqp}}{\partial x_p}$ and $\Delta\sigma^I_{ipq}$ (4.31b)

Computation of the integrals requires a set of background cells, which are used to discretize the problem. The problem domain is represented by a set of field nodes, *N*, used to

compute the field displacement approximation function, Δu^h. This function is computed for each sampling node using MLS shape functions that are based on a separate set of nodes, *n*, within the '*local*' influence domain of each sampling node.

The approximated displacement field function is defined as:

$$\Delta u^h_{2x1} = \begin{Bmatrix} \Delta u \\ \Delta v \end{Bmatrix} = \begin{bmatrix} \phi_1 & 0 & \dots & \phi_n & 0 \\ 0 & \phi_1 & \dots & 0 & \phi_n \end{bmatrix} \begin{Bmatrix} \Delta u_1 \\ \Delta v_1 \\ \vdots \\ \Delta u_n \\ \Delta v_n \end{Bmatrix} = \Phi_{(2\times 2n)} \Delta u_{(2n\times 1)} \tag{4.32}$$

where:

Φ : matrix of shape functions.

n : number of nodes in the local support domain.

Δu : vector in the incremental form with the parameters of displacements for the *n* field nodes in the support domain.

Δu^h : approximated displacement vector in the incremental form at a point of interest.

This equation (4.32) is used to approximate displacements of a sampling point or a quadrature point.

In the same manner, $\delta\Delta u^h$ is computed as:

$$\delta\Delta u^h_{(2\times 1)} = \Phi_{(2\times 2n)} \delta\Delta u_{(2n\times 1)} \tag{4.33}$$

With the approximated displacement field function, strains and gradient of strains are defined as:

$$\Delta\varepsilon^0_{(3\times1)} = L^0\Delta u^h = L^0_{(3\times2)}\Phi_{(2\times2n)}\Delta u_{(2n\times1)} = B^0_{(3\times2n)}\Delta u_{(2n\times1)}$$

$$L^0 = \begin{bmatrix} \dfrac{\partial}{\partial x} & 0 \\ 0 & \dfrac{\partial}{\partial y} \\ \dfrac{\partial}{\partial y} & \dfrac{\partial}{\partial x} \end{bmatrix} \tag{4.34}$$

$$\Delta\varepsilon^1_{(8\times1)} = L^1\Delta u^h = L^1_{(8\times2)}\Phi_{(2\times2n)}\Delta u_{(2n\times1)} = B^1_{(8\times2n)}\Delta u_{(2n\times1)}$$

$$L^1 = \begin{bmatrix} \dfrac{\partial^2}{\partial x\partial x} & 0 \\ \dfrac{\partial^2}{\partial x\partial y} & 0 \\ \dfrac{\partial^2}{\partial x\partial y} & 0 \\ \dfrac{\partial^2}{\partial y\partial y} & 0 \\ 0 & \dfrac{\partial^2}{\partial x\partial x} \\ 0 & \dfrac{\partial^2}{\partial x\partial y} \\ 0 & \dfrac{\partial^2}{\partial x\partial y} \\ 0 & \dfrac{\partial^2}{\partial y\partial y} \end{bmatrix} \tag{4.35}$$

Similarly, $\delta\Delta\varepsilon^0$ and $\delta\Delta\varepsilon^1$ are defined as:

$$\delta\Delta\varepsilon^0_{(3\times1)} = L^0\Delta u^h = L^0_{(3\times2)}\Phi_{(2\times2n)}\delta\Delta u_{(2n\times1)} = B^0_{(3\times2n)}\delta\Delta u_{(2n\times1)} \tag{4.36}$$

$$\delta\Delta\varepsilon^1_{(8\times1)} = L^1\Delta u^h = L^1_{(8\times2)}\Phi_{(2\times2n)}\delta\Delta u_{(2n\times1)} = B^1_{(8\times2n)}\delta\Delta u_{(2n\times1)} \tag{4.37}$$

Equations (4.32-4.37) can be also written as a form of nodal summation within the local support domain as follows:

$$\Delta u^{h}_{(2\times1)} = \sum_{I}^{n} \begin{bmatrix} \phi_I & 0 \\ 0 & \phi_I \end{bmatrix} \begin{Bmatrix} \Delta u_I \\ \Delta v_I \end{Bmatrix} = \sum_{I}^{n} \Phi_I \Delta u_I \tag{4.38}$$

$$\delta\Delta u^{h}_{(2\times1)} = \sum_{I}^{n} \Phi_I \delta\Delta u_I \tag{4.39}$$

$$\Delta\varepsilon^{0}_{(3\times1)} = \sum_{I}^{n} B^{0}_{I} \Delta u_I \tag{4.40}$$

$$\Delta\varepsilon^{1}_{(8\times1)} = \sum_{I}^{n} B^{1}_{I} \Delta u_I \tag{4.41}$$

$$\delta\Delta\varepsilon^{0}_{(3\times1)} = \sum_{I}^{n} B^{0}_{I} \delta\Delta u_I \tag{4.42}$$

$$\delta\Delta\varepsilon^{1}_{(8\times1)} = \sum_{I}^{n} B^{1}_{I} \delta\Delta u_I \tag{4.43}$$

The stresses and double stresses in the incremental form can be obtained using the constitutive equations for the material at the point of the problem domain:

$$\begin{aligned} \Delta\sigma^{0}_{iq} &= A_{iqkl}\Delta\varepsilon^{0}_{kl} = \sum_{I}^{n} A_{iqkl} B^{0}_{I} \Delta u_I \\ \Delta\sigma^{I}_{ijq} &= E_{ijqklm}\Delta\varepsilon^{I}_{klm} = \sum_{I}^{n} E_{ijqklm} B^{1}_{I} \Delta u_I \end{aligned} \tag{4.44}$$

And the left side of equation (4.13a) is written as:

$$\begin{aligned} &\int_{\Omega} \left(L^{0}\delta\Delta u\right)^{T} \left(A_{iqkl} L^{0}\Delta u\right) d\Omega + \int_{\Omega} \left(L^{1}\delta\Delta u\right)^{T} \left(E_{ijqklm} L^{1}\Delta u\right) d\Omega = \\ &\int_{\Omega} \sum_{I}^{n}\sum_{J}^{n} \delta\Delta u_I^{T} \left[B_I^{0\,T} A_{iqkl} B_J^{0}\right] \Delta u_J \, d\Omega + \int_{\Omega} \sum_{I}^{n}\sum_{J}^{n} \delta\Delta u_I^{T} \left[B_I^{1\,T} E_{ijqklm} B_J^{1}\right] \Delta u_J \, d\Omega \end{aligned} \tag{4.45}$$

So far, the equations expressed in this section are based on the local influence domain, which consists of *n* nodes; where the subscripts *I* and *J* are based on the influence domain and

need to be converted to the global domain where *N* nodes are considered. This transformation is expressed in equation (4.46), which vanishes for the case when *I* and *J* are not in the same influence domain of the same quadrature point of integration. Equation (4.45) is written as:

$$\int_{\Omega}\left(L^0\delta\Delta u\right)^T\left(A_{iqkl}L^0\Delta u\right)d\Omega+\int_{\Omega}\left(L^1\delta\Delta u\right)^T\left(E_{ijqklm}L^1\Delta u\right)d\Omega=$$
$$\int_{\Omega}\sum_{I}^{N}\sum_{J}^{N}\delta\Delta u_I^T\left[B_I^{0T}A_{iqkl}B_J^0\right]\Delta u_J d\Omega+\int_{\Omega}\sum_{I}^{N}\sum_{J}^{N}\delta\Delta u_I^T\left[B_I^{1T}E_{ijqklm}B_J^1\right]\Delta u_J d\Omega=$$
$$\sum_{I}^{N}\sum_{J}^{N}\delta\Delta u_I^T\int_{\Omega}\left[B_I^{0T}A_{iqkl}B_J^0\right]\Delta u_J d\Omega+\sum_{I}^{N}\sum_{J}^{N}\delta\Delta u_I^T\int_{\Omega}\left[B_I^{1T}E_{ijqklm}B_J^1\right]\Delta u_J d\Omega \tag{4.46}$$

where:

$$K^0_{IJ(2N\times 2N)}=\int_{\Omega}B_I^{0T}A_{iqkl}B_J^0 d\Omega$$
$$K^1_{IJ(2N\times 2N)}=\int_{\Omega}B_I^{1T}E_{ijqklm}B_J^1 d\Omega$$
$$K_{IJ(2N\times 2N)}=K^0_{IJ(2N\times 2N)}+K^1_{IJ(2N\times 2N)} \tag{4.47}$$

And equation (4.46) is rewritten as:

$$\int_{\Omega}\left(L^0\delta\Delta u\right)^T\left(A_{iqkl}L^0\Delta u\right)d\Omega+\int_{\Omega}\left(L^1\delta\Delta u\right)^T\left(E_{ijqklm}L^1\Delta u\right)d\Omega=$$
$$\sum_{I}^{N}\sum_{J}^{N}\delta\Delta u_I^T\int_{\Omega}\left[K_{IJ}^0\right]\Delta u_J d\Omega+\sum_{I}^{N}\sum_{J}^{N}\delta\Delta u_I^T\int_{\Omega}\left[K_{IJ}^1\right]\Delta u_J d\Omega=$$
$$\sum_{I}^{N}\sum_{J}^{N}\delta\Delta u_I^T\int_{\Omega}\left[K_{IJ}^0+K_{IJ}^1\right]\Delta u_J d\Omega=\sum_{I}^{N}\sum_{J}^{N}\delta\Delta u_I^T\int_{\Omega}\left[K_{IJ}\right]\Delta u_J d\Omega \tag{4.48}$$

where:

K_{IJ} , is the global nodal stiffness matrix.

Then equation 4.46 becomes:

$$\sum_{I}^{N}\sum_{J}^{N}\delta\Delta u_I^T\int_{\Omega}\left[K_{IJ}\right]\Delta u_J d\Omega=\delta\Delta U^T K\cdot\Delta U \tag{4.49}$$

ΔU : *Global* displacement vector in the incremental form that collects all the nodal incremental displacement parameters within the entire problem domain, where:

$$\Delta U_{(2N\times 1)} = \begin{Bmatrix} \Delta u_1 \\ \Delta u_2 \\ \vdots \\ \Delta u_N \end{Bmatrix} = \begin{Bmatrix} \Delta u_1 \\ \Delta v_1 \\ \vdots \\ \Delta u_N \\ \Delta v_N \end{Bmatrix} \tag{4.50}$$

Then, neglecting body forces, the force vector in the incremental form is defined by:

$$\int_{\Gamma}\left[\delta\phi_i n_q\left(\Delta\sigma_{iq}^{0} - \frac{\partial\Delta\sigma_{ipq}^{I}}{\partial x_p}\right). + n_p\frac{\partial\delta\phi_i}{\partial x_q}\Delta\sigma_{ipq}^{I}\right]d\Gamma = \delta\Delta U^T\sum_{I}^{N}\Delta F_I = \delta\Delta U^T\Delta F \tag{4.51}$$

By replacing equations (4.49) and (4.51) into (4.13a), we obtain:

$$\delta\Delta U^T\left[K\cdot\Delta U - \Delta F\right] = 0 \tag{4.52}$$

Which is satisfied only if:

$$K\cdot\Delta U = \Delta F \tag{4.53}$$

Following this formulation, prior the numerical implementation procedure, the essential boundary conditions are treated and enforced.

4.4.2. Enforcement of essential boundary conditions (EBC).

The natural boundary conditions are treated in the formulation of the global weak-form, yet the essential boundary conditions need to be treated and enforced separately. Enforcement of the essential boundary conditions can be performed prior or after satisfying the global $K\cdot\Delta U = \Delta F$ equation (4.53).

Enforcement of the EBC can be done with the Lagrange multiplier method or the penalty method. The former method increases the number of field variables and the dimension of the system stiffness matrix, and thus offers a more complex and expensive solution. Furthermore, it leads to an un-banded and non-positive definite system stiffness matrix. Conversely, the penalty method does not increase the number of variables and it provides a banded, symmetric, and a positive definite system stiffness matrix when positive penalty factors are chosen (Liu and Gu, 2005). This method uses a simple algorithm that requires two changes in the matrices to determine the displacements. The first change affects the diagonal elements of the global stiffness matrix which are pre-multiplied by a 'penalty coefficient',α, that is larger than the stiffness matrix's elements. Then, the second change affects the elements of the global force vector. Applying these changes we obtain a modified global stiffness matrix and force vector as follows:

$$K_{ii} \to \alpha \cdot K_{ii} \tag{4.54}$$

$$\Delta F_j = \begin{cases} \Delta F_j - \alpha \cdot K_{ii} \cdot \overline{\Delta u_i} & i = j \\ \Delta F_j & i \neq j \end{cases} \tag{4.55}$$

The EBC are determined by solving the displacement components of the following equation:

$$K \cdot \Delta U = \Delta F \tag{4.53}$$

For accuracy in the results, proper selection of the penalty coefficient is important. Based on practice in FEM, a penalty coefficient $10^{4\sim}10^{8}$ times larger than the maximum value of the global stiffness matrix is recommended (Liu and Gu, 2005). The penalty factor used in this study is 10^{6} times the maximum diagonal element of the global stiffness matrix.

As afore-mentioned, rotational effects are not included in the numerical simulation of this study and will be performed in a future work. For that case, the following steps should be performed to enforce the essential boundary conditions using the penalty method.

The EBC's need to satisfy the following additional global condition:

$$G \cdot \Delta W = \Delta M \tag{4.56}$$

where:

G : Matrix with the global rotational stiffness.

ΔW : Vector in incremental form with the global rotation field parameters.

ΔM : Vector in incremental form with the global moments.

The modified rotational global stiffness matrix and moment vector defined as follows:

$$G_{ii} \rightarrow \alpha_w \cdot G_{ii} \tag{4.57}$$

$$\Delta M_j = \begin{cases} \Delta M_j - \alpha_w \cdot G_{ii} \cdot \Delta \overline{w_i} & i = j \\ \Delta M_j & i \neq j \end{cases} \tag{4.58}$$

And, the EBC's are determined by solving the rotational components of the following equation:

$$G \cdot \Delta W = \Delta M \tag{4.59}$$

4.4.3. Numerical implementation.

The integrals of the global weak-form equation over the global domain Ω and boundary Γ have been defined in the formulation section 4.4.1. For the integration of these integrals, the problem is discretized and a set of background cells, n^c, is defined. Then, integration is computed

as a summation of integrals over these background cells using Gauss quadrature scheme. The global integration for the problem and boundary domains (Ω,Γ) is described below:

$$\int_{\Omega} G d\Omega = \sum_{k}^{n_c} \int_{\Omega_k} G d\Omega$$

$$\int_{\Omega} G d\Omega = \sum_{k}^{n_c} \sum_{i=1}^{n_g} \widehat{w}_i G\left(x_{Qi}, y_{Qi}\right) \left| J_{ik}^{D} \right|$$

$$\int_{\Gamma} G d\Gamma = \sum_{l}^{n_{ct}} \sum_{i=1}^{n_{gt}} \widehat{w}_i G\left(x_{Qi}, y_{Qi}\right) \left| J_{il}^{B} \right| \tag{4.60}$$

where:

G : The integrant of the global domain, Ω_k,of to the k_{th} background cell.

$\widehat{w}_i$: the Gauss weighting factor for the i_{th} Gauss point at $\left(x_{Qi}, y_{Qi}\right)$

J_{ik}^{D}: the Jacobian matrix for the k_{th} curve integration of the sub-boundary at which the Gauss point is located.

J_{il}^{B}: the Jacobian matrix for the l_{th} background cell corresponding to the boundary.

n^c, n^g: number of background cells and Gauss points in the background cell.

n^{ct}, n^{gt}: number of curve cells in the boundary and Gauss points in the curve cell.

In the same manner, the nodal stiffness matrix K_{IJ} is obtained by the summation of the contribution from all the quadrature points, K_{IJ}^{ik}. Where the local support domain includes both the *Ith* and the *Jth* nodes, $K_{IJ}^{ik} \neq 0$, for other cases $K_{IJ}^{ik} = 0$.Therefore:

$$K_{IJ} = \sum_{k}^{n_c} \sum_{i=1}^{n_g} K_{IJ}^{ik} \tag{4.61}$$

By considering the quadrature and equation 4.47, K_{IJ}^{ik} is defined as:

$$K_{IJ}^{ik} = K_{IJ}^{0} + K_{IJ}^{1} = \widehat{w}_i B_I^{0T}\left(x_{Qi}, y_{Qi}\right) A_{iqkl} B_J^{0}\left(x_{Qi}, y_{Qi}\right)\left|J_{ik}^{D}\right| + \widehat{w}_i B_I^{1T}\left(x_{Qi}, y_{Qi}\right) E_{ijqklm} B_J^{1}\left(x_{Qi}, y_{Qi}\right)\left|J_{ik}^{D}\right| \tag{4.62}$$

where:

B^0 and B^1 are the strain and gradient strain matrices for the quadrature point $\left(x_{Qi}, y_{Qi}\right)$.

A_{iqkl} and E_{ijqklm} are the stiffness and gradient of stiffness matrices for the quadrature point $\left(x_{Qi}, y_{Qi}\right)$.

Similarly, the nodal force vector in the incremental form, ΔF_I, is defined as:

$$\Delta F_I = \sum_{k}^{n_{ct}} \sum_{i=1}^{n_{gt}} \widehat{w}_i \Delta F \left|J_{ik}^{B}\right| \tag{4.63}$$

4.4.4. Discretization and linearization.

By following all the procedures described in section 4.4, the following global discretized system equation is obtained with the EFG method:

$$\left[K_{IJ} + K_{IJ}^{\alpha}\right]\Delta U = \Delta F_I + \Delta F_I^{\alpha} \tag{4.64}$$

where:

$$K_{IJ}^{\alpha} = -\int_{\Gamma_u} \Phi_I^T \alpha \Phi_J \, d\Gamma$$

$$\Delta F_I^{\alpha} = -\int_{\Gamma_u} \Phi_I^T \alpha \Delta \bar{u} \, d\Gamma \tag{4.65}$$

$$\Delta U = \left[K_{IJ} + K_{IJ}^{\alpha}\right]^{-1}\left[\Delta F_I + \Delta F_I^{\alpha}\right] \tag{4.66}$$

K_{IJ} Global stiffness matrix described in equation (4.62).

K_{IJ}^{α}: Global penalty stiffness matrix (4.65).

ΔF_I : Global force vector described in equation (4.63).

ΔF_I^{α} : Global penalty force vector (4.65).

ΔU : Global nodal displacement parameters in incremental form (4.66).

$\Delta \bar{u}$: Prescribed displacement in the incremental form.

Φ : MLS shape functions (4.19).

α: Penalty coefficient of 10^6.

CHAPTER 5. Qualitative Evaluation of the Model's Numerical Simulation based on the 2nd Gradient Theory.

This chapter evaluates the performance of the 2nd gradient theory model on capturing and simulating the fracture process and failure behavior at the structural level in four sections. For this, a 2D-plate structure with a pre-existing imperfection is evaluated under four loading conditions. The model parameters and geometry of the structure are described in the first section, while the loading conditions are addressed in the second. The basis for the evaluation is presented in the third section. And the last section describes and evaluates the results of the numerical simulations.

5.1. Model parameters and geometry.

For the numerical simulations, a 2D plate, 45 cm long and 14 cm wide, is used with a softer inclusion located at the center of the plate. The inclusion's stiffness is sixty percent the stiffness of the plate. Model parameters used for the simulations are based on the values used in Chapter 3 where: A_1=0.7 MPa, B=3.4 10^{-7} , C_1=0.2 MPa, D=1.3 10^{-4} , α_1=2 10^5 , α_2=7, L_0=10 and 1 mm. The stiffness parameters for the inclusion are A_1=0.7×0.60 MPa and C_1=0.2×0.60 MPa.

The parameters used to perform the numerical simulation are categorized into four groups: shape functions, meshing, gauss-points computation, and penalty method. Shape functions are

computed based on a polynomial function, *p(x,y)*, with six monomials and a dimensionless factor of 3.1 used to compute the support domain.

$$p^{T}_{(x,y)} = \begin{bmatrix} 1 & x & y & x^2 & xy & y^2 \end{bmatrix} \tag{5.1}$$

Meshing of the 2D plate structure is performed by dividing the plate into 45x14 cells, and having nodal points at each intersection. This cell division configuration is based on the analysis of three configurations, 45x14, 36x12, and 27x10. For the analysis, the 2D plate with a band inclusion in the center, under tensile loading, and with transverse constraints is used (see Figure 5.5). Results show that up to the peak-load (failure) and small deformations beyond this load, all the configurations show similar behavior. For deformations that are far beyond the peak-load, the first configuration 45x14 show to converge. See Figure 5.1.

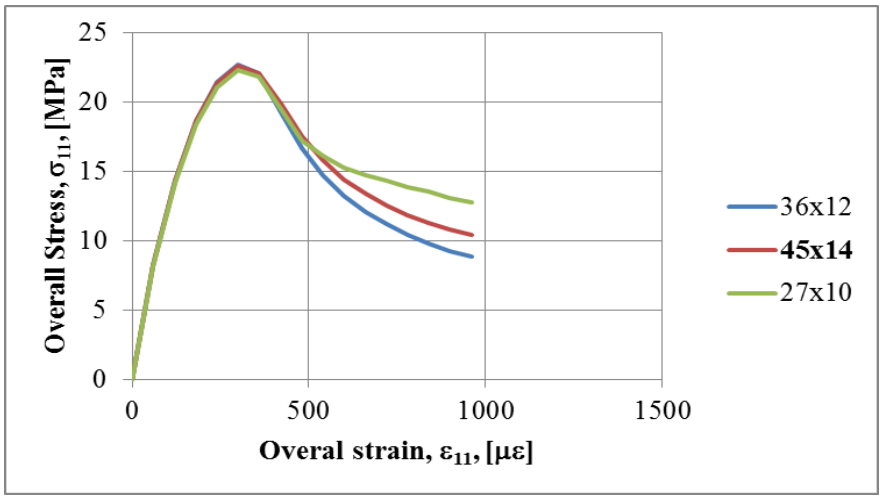

Figure 5.1: Overall stress-strain for different mesh-configurations (divisions).

Gauss-point computation is done by using four gauss points, and dividing the plate into 40x12 cells. Finally, enforcement of the essential boundary conditions is computed using the penalty method with a penalty factor of 10^6 times the maximum value of the stiffness matrix.

Geometry of the plate with two types of inclusions is defined in the following schematic figures 5.2 and 5.3.

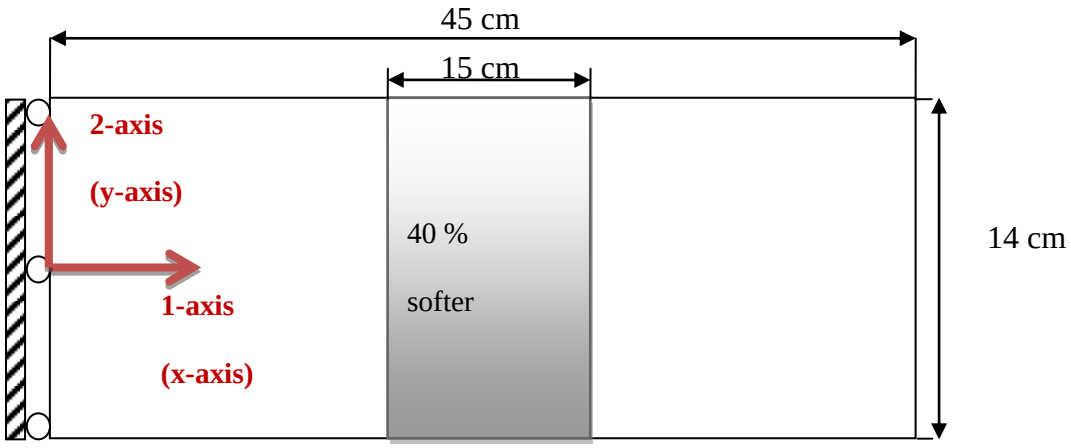

Figure 5.2: Geometry of 2D Plate with a band inclusion at the center.

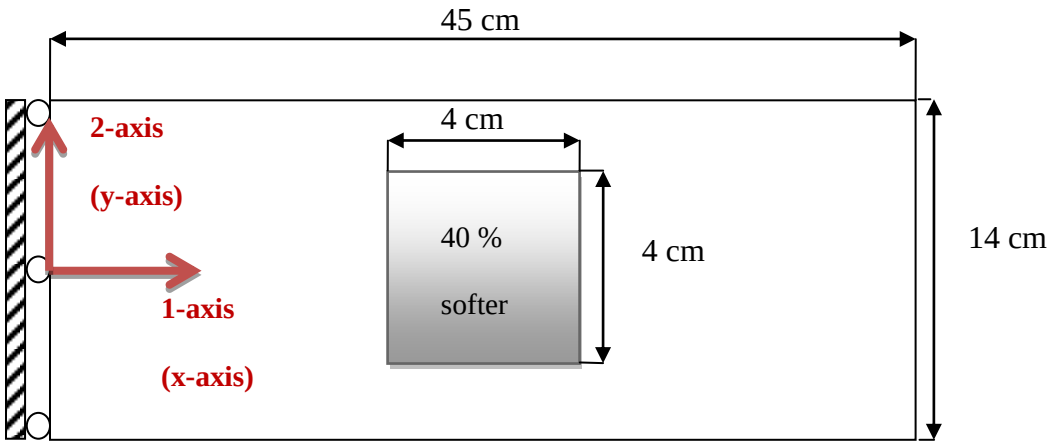

Figure 5.3: Geometry of 2D Plate with a square inclusion at the center.

5.2. Simulations and loading conditions.

To evaluate the capability of our second gradient theory model on capturing the fracture process, ten simulations are performed. For the loading conditions, two types of loadings and two types of constraints are used for each plate described in Figures 5.2-5.3. A tensile or compressive uniform loading is applied along the right border of the plate by subjecting the plate

to stretching or shrinking incremental displacements, respectively. The plate is constrained on the longitudinal 1-direction at the left border, while top and bottom sides are either constrained in the vertical 2-direction or have no constraints. Figures 5.4-5.5 describe the loading and constraint conditions for the plate with the band inclusion at the center. The conditions for the plate with the square inclusion at the center are described in Figures 5.6-5.7.

A total of ten simulations are performed: six under tensile loading and four under compressive loading. Table 5.1 provides a summary of the simulations with their loading and constraint conditions. The six tensile simulations are computed using a particle size of L_0=1 mm and 10 mm. Figures 5.4-5.7 describe the four loading conditions using L_0=1 mm. Figures 5.6-5.7 describe the two simulations with L_0=10 mm. Then, the four compressive simulations are performed using a particle size of L_0=10 mm and are described in Figures 5.4-5.7.

Table 5-1: Loading cases

Case	**Loading**	**Constraint for top and bottom**	**Inclusión**	**L_0 [mm]**
1	Tension	None	Band	1
2	Tension	y-axis	Band	1
3	Tension	None	Square	1
4	Tension	y-axis	Square	1
5	Tension	None	Square	10
6	Tension	y-axis	Square	10
7	Compression	None	Band	10
8	Compression	y-axis	Band	10
9	Compression	None	Square	10
10	Compression	y-axis	Square	10

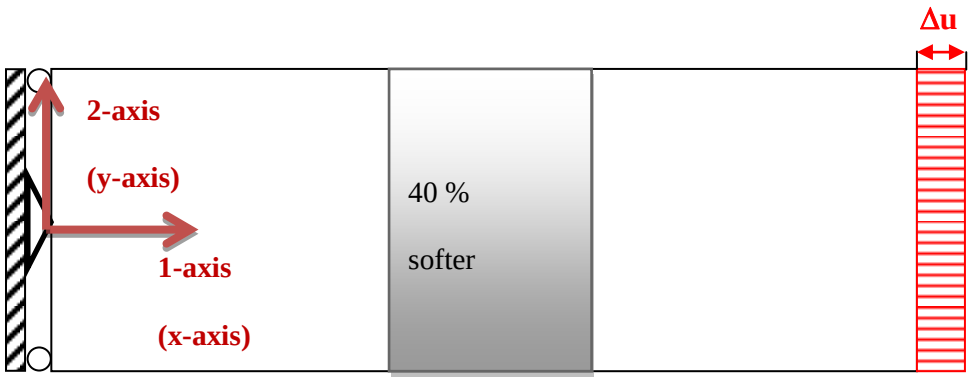

Figure 5.4: 2d Plate (45 cm by 14 cm) with a band inclusion and top and bottom with no constraint.

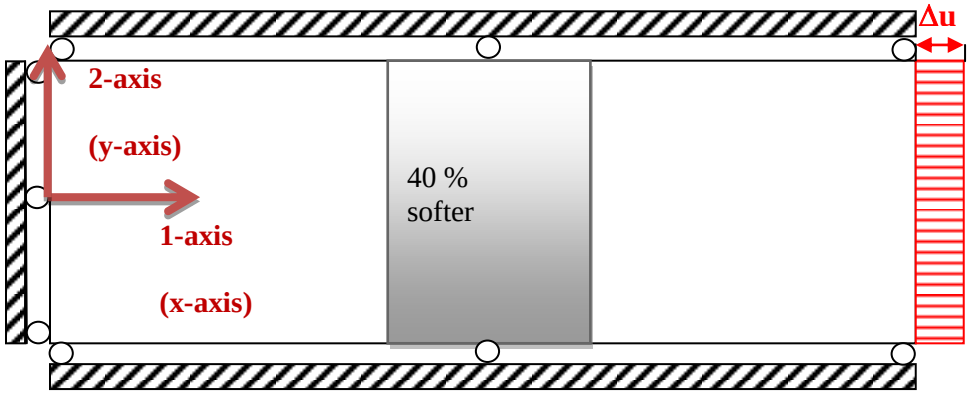

Figure 5.5: 2d Plate (45 cm by 14 cm) with a band inclusion and top and bottom constrained in the y-axis.

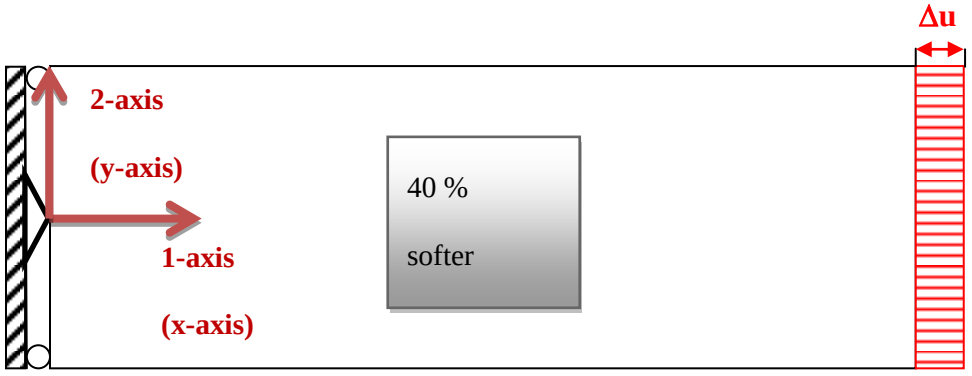

Figure 5.6: 2d Plate (45 cm by 14 cm) with a square inclusion and top and bottom with no constraint.

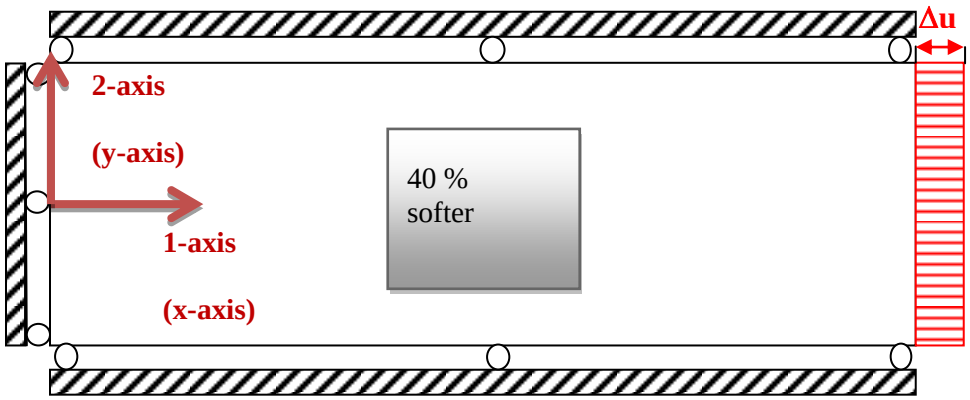

Figure 5.7: 2d Plate (45 cm by 14 cm) with a square inclusion and top and bottom constrained in the y-axis.

5.3. Basis for the evaluation – '*expected behavior*'.

Evaluation of the simulations is based on the model's capability on describing and computing the structure's behavior and fracture process. Stresses along the plate with the band inclusion are expected to be uniform. Stresses within the plate with the square inclusion are expected to describe stress concentrations around the top and bottom of the inclusion, and have lower stresses within the inclusion. Then, strain values are expected be higher within the inclusions. On the fracture process, when there is no vertical constraints for the tensile loading condition with the band inclusion, failure is expected to occur within the band and exhibit fractures normal to the load. For the case with the square inclusion, the fracture zone is expected to be initiated from the top and bottom faces of the inclusion and propagate mainly vertically exhibiting a fracture zone normal to the load. Then, for the band-inclusion case with vertical constraints, a biaxial state is generated, and vertical fractures with some inclination are expected within the band. For the square-inclusion, due to the biaxial-tensile condition, vertical fractures with some inclination are expected to form along the sides of the inclusion.

For the compressive loading condition, where there are no vertical constraints, fracture failure is expected to be well-defined within the inclusion exhibiting 'X' like shear fracture. Similar shear behavior is expected to be present within the square inclusion and propagating from it. On the other hand, for the constrained case with the band inclusion, failure is expected to occur within the band exhibiting fractures that are mainly vertical and perpendicular to the load. Similarly, vertical fractures perpendicular to the load with some inclination are expected for the plate with the square inclusion.

It is also expected that the model will capture the loading induced heterogeneity and the granular nature of the material by exhibiting tensile and compressive bands along the plate and by exhibiting a fracture zone.

5.4. Results and evaluation.

In this section, the ten simulations described in Table 5.1 are evaluated based on the 'expected behavior' described in section 5.3, and the suitability and applicability of our model on 1) successfully computing and 2) qualitatively describing the fracture process within the structure (2D plate) under the presence of a pre-existing imperfection (inclusion). For each simulation, nine figures of the structure's responses at different loading stages are shown: 1) overall stress-strain, 2) stress-strain in the 11-direction, 3) stress-strain in the 22-direction, 4) stress-strain in the 12-direction, 5) effective stress-strain, 6) double stress-strain gradient in the 111-direction, 7) double stress-strain gradient in the 222-direction, 8) effective double stress-strain gradient in the 1-direction, and 9) effective double stress-strain gradient in the 2-direction. For the tensile simulations, four loading stages are considered and shown in the figures: initial,

pre-peak, peak, and post-peak. On the other hand, for the compressive simulations, our model's compressive law describes failure in the stress-strain response by flattening the strain-stress curve without exhibiting a decrease in the stress response. Therefore, for the compressive simulations, the loading stages are shown in each figure: initial, pre-peak, and peak stage.

Computation of the effective strain, $\bar{\varepsilon}$, is computed by resultant of the summation of the principal strain components of the strain matrix and described by equation 5.1.

$$\bar{\varepsilon} = \sqrt{\varepsilon_1^2 + \varepsilon_2^2} \tag{5.1}$$

Similarly, the effective stresses are computed with the principal stresses as described by equation 5.2.

$$\bar{\sigma} = \sqrt{\sigma_1^2 + \sigma_2^2} \tag{5.2}$$

Computation of the effective gradient strain and double stress is described by equations 5.3 through 5.6:

$$\partial\varepsilon_x^I = \frac{\varepsilon_{11}}{\bar{\varepsilon}}\varepsilon_{111} + \frac{\varepsilon_{22}}{\bar{\varepsilon}}\varepsilon_{221} + \frac{1}{2}\cdot\frac{\varepsilon_{12}}{\bar{\varepsilon}}\left(\varepsilon_{121} + \varepsilon_{211}\right) \tag{5.3}$$

$$\partial\varepsilon_y^I = \frac{\varepsilon_{11}}{\bar{\varepsilon}}\varepsilon_{112} + \frac{\varepsilon_{22}}{\bar{\varepsilon}}\varepsilon_{222} + \frac{1}{2}\cdot\frac{\varepsilon_{12}}{\bar{\varepsilon}}\left(\varepsilon_{122} + \varepsilon_{212}\right) \tag{5.4}$$

$$\partial\sigma_x^I = \frac{\sigma_{11}}{\bar{\sigma}}\sigma_{111} + \frac{\sigma_{22}}{\bar{\sigma}}\sigma_{221} + \frac{1}{2}\cdot\frac{\sigma_{12}}{\bar{\sigma}}\left(\sigma_{121} + \sigma_{211}\right) \tag{5.5}$$

$$\partial\sigma_y^I = \frac{\sigma_{11}}{\bar{\sigma}}\sigma_{112} + \frac{\sigma_{22}}{\bar{\sigma}}\sigma_{222} + \frac{1}{2}\cdot\frac{\sigma_{12}}{\bar{\sigma}}\left(\sigma_{122} + \sigma_{212}\right) \tag{5.6}$$

Simulation results described in sections 5.4.1-5.4.12 demonstrate that our 2nd gradient constitutive model provides 'the necessary mathematical continuity' to compute and capture non-linear fracture behavior of the material at the structural level with the presence of a pre-existing imperfection.

5.4.1. Case One: Tensile loading with band inclusion and no constraints (L_0=1 mm).

In this simulation, the 2D plate is subjected to tension by applying stretch displacements along its right side. In addition, the plate has a centered band inclusion that is forty percent softer than the plate material and is modeled with a particle size of L_0=1 mm. The length and height of the plate and the inclusion are 45 cm×14 cm and 15cm×14 cm, respectively. The plate is constrained in the 1-direction along its left border while the top and bottom have no constraints (See Figure 5.4).

The response of the structure is shown in Figures 5.8-5.24 at four loading stages: initial, pre-peak, peak, and post-peak stage. Figure 5.8 shows the overall stress-strain response in the '11' and '22' directions. Figures 5.9-5.14 show the strain and stress responses in the '11', '22', and '12' directions, and their effective magnitudes are shown in Figures 5.15-5.16. Strain gradient and double stress responses are shown in Figures 5.17-5.20, and their corresponding effective magnitudes are described in Figures 5.21-5.24.

The overall stress-strain response of the plate in the '11' and '22' directions is described in Figure 5.8 and shows a uniaxial stress state with non-linear softening behavior. Past the peak-load, the failure of the structure is described by a deep drop on the stress response.

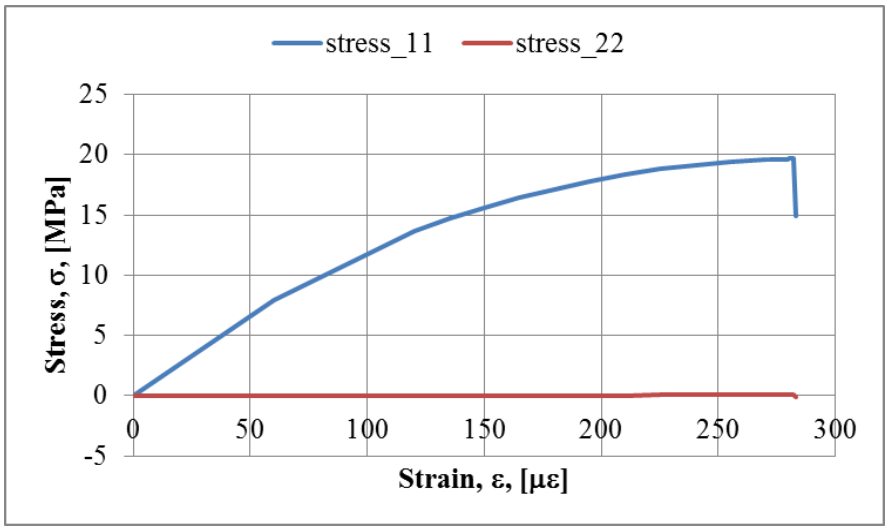

Figure 5.8: Case One: Overall stress strain behavior of the plate.

Figures 5.9 and 5.10 describe the strain and stress response of the structure in the 11-direction at the four loading stages afore mentioned. Stress response shows overall uniform stress distribution along the structure. Reduction in stress magnitudes is observed after the peak-load is reached indicating failure of the structure. Strain response show higher strains within the inclusion and strain concentrations at the peak and post-peak stage. At the latter stage, these concentrations become more severe suggesting the presence of fractures within the inclusion normal to the load.

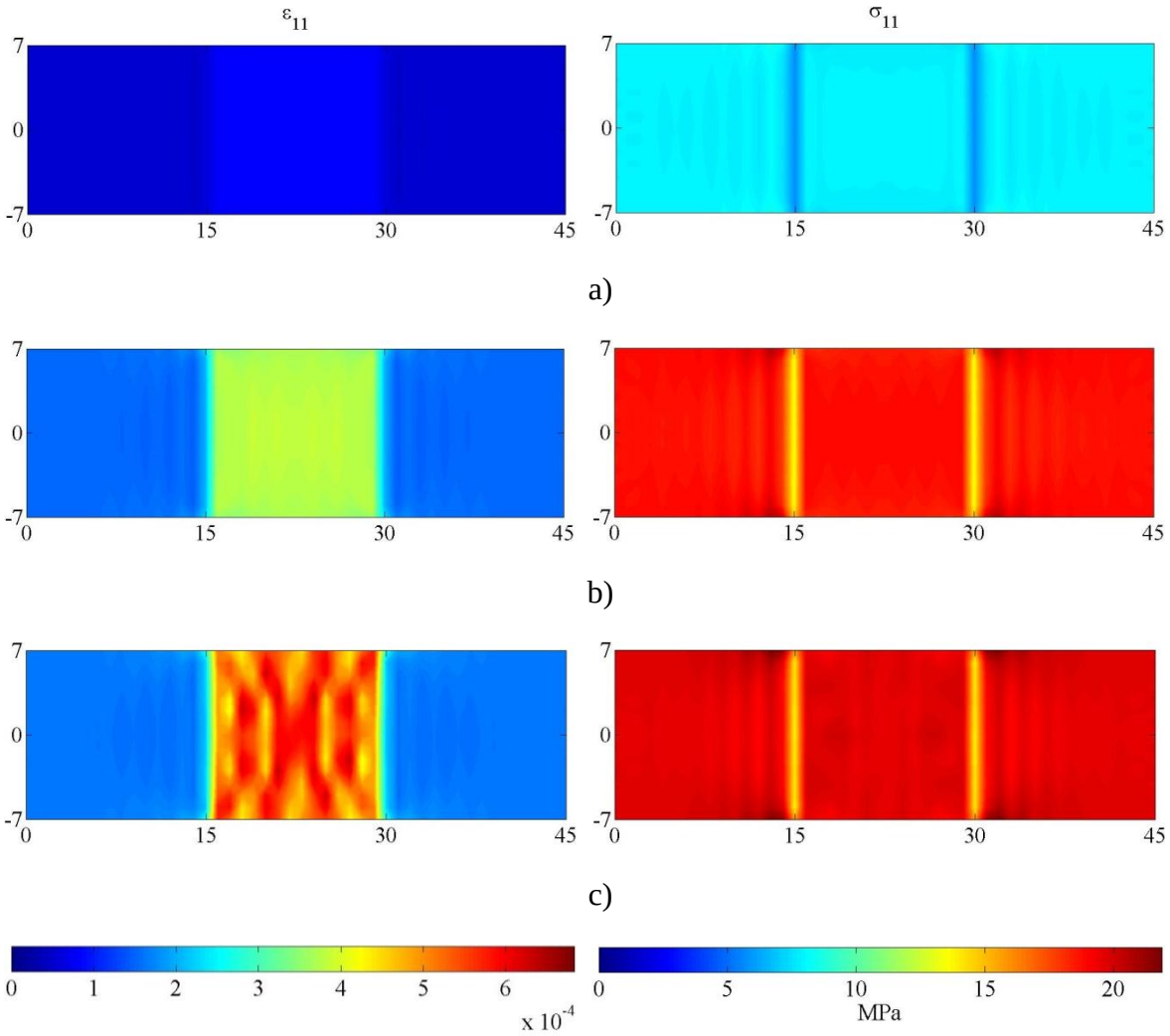

Figure 5.9: Case One – ε_{11} and σ_{11} for Δu= a) 0.0027cm, b) 0.0101 cm, and c) 0.0127 cm.

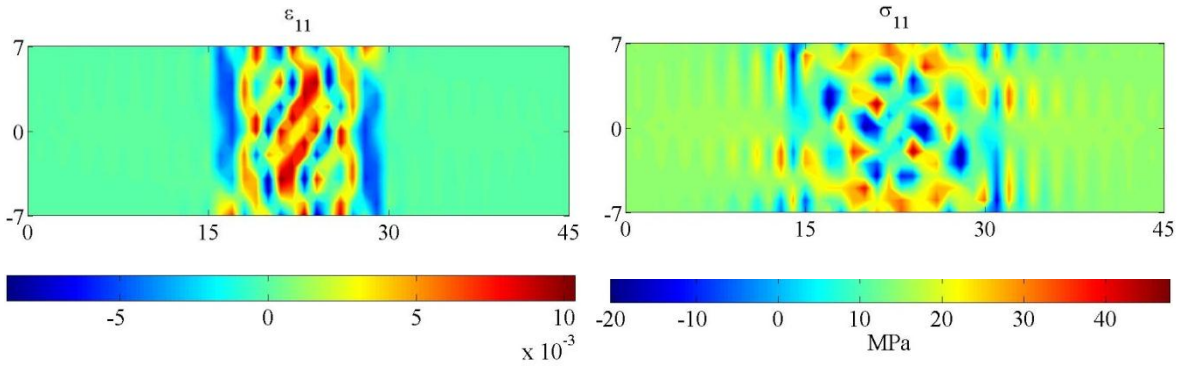

Figure 5.10: Case One – ε_{11} and σ_{11} for Δu= 0.01274 cm.

Figures 5.11 and 5.12 describe the strain and stress response of the structure in the 22-direction at the four loading stages afore mentioned. Stress response shows uniform zero stress distribution with stress concentrations at the inclusion-plate interface and within the inclusion at the peak and post-peak stages. Strain response shows higher strains within the inclusion and strain concentrations at the peak and post-peak stages.

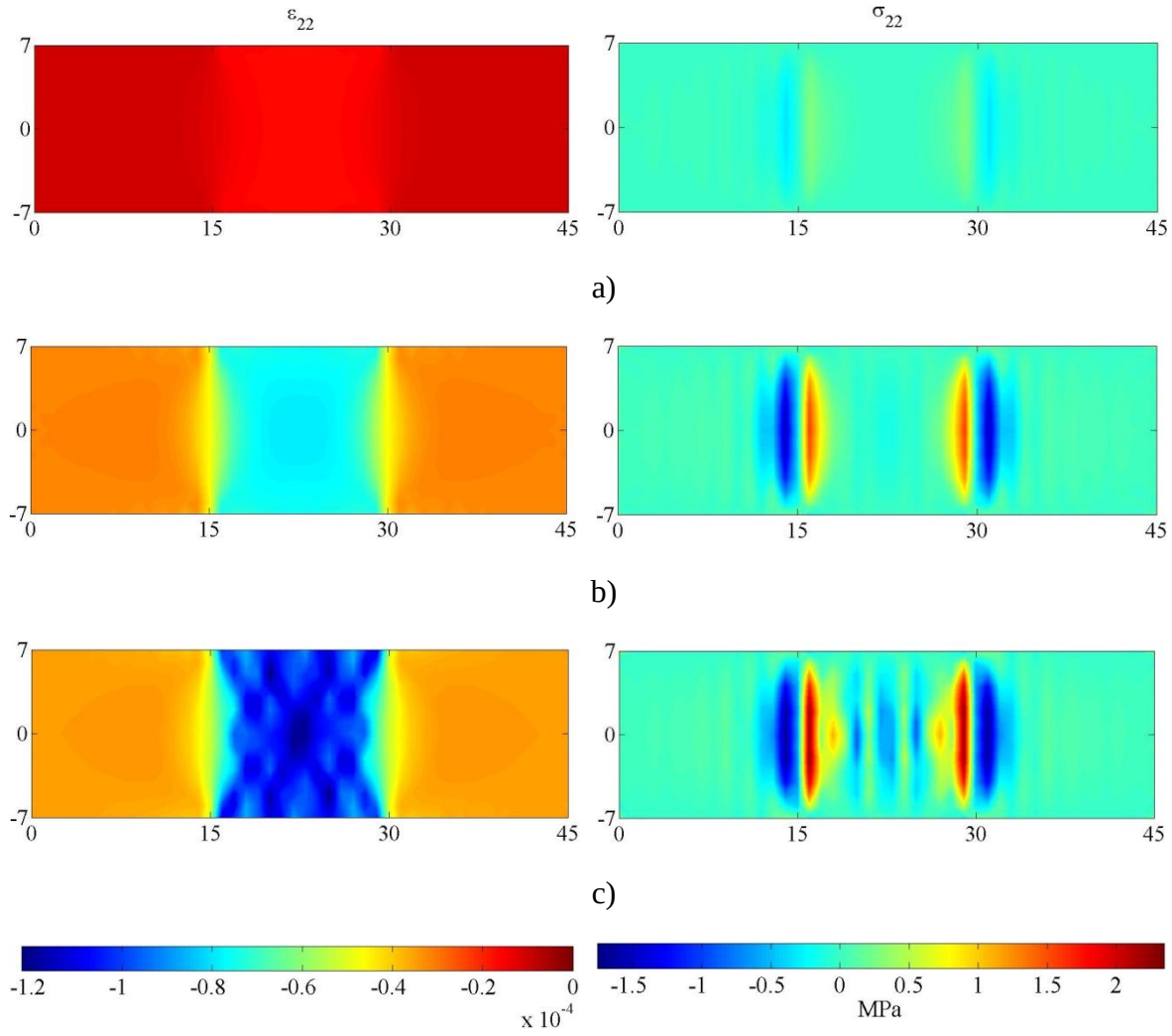

Figure 5.11: Case One – ε_{22} and σ_{22} for Δu= a) 0.0027cm, b) 0.0101 cm, and c) 0.0127 cm.

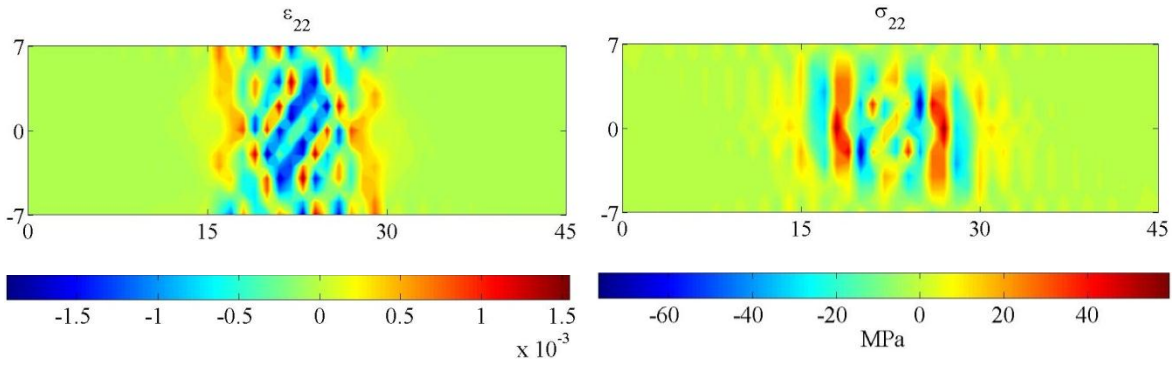

Figure 5.12: Case One – ε_{22} and σ_{22} for Δu= 0.01274 cm.

Figures 5.13 and 5.14 describe the strain and stress response of the structure in the 12-direction at the four loading stages afore mentioned. Strain and stress response shows concentrations at the upper and lower corners of the inclusion. As the load increases, these concentrations become more severe and expand in a lesser magnitude by reflecting themselves in a diagonal-zigzag manner.

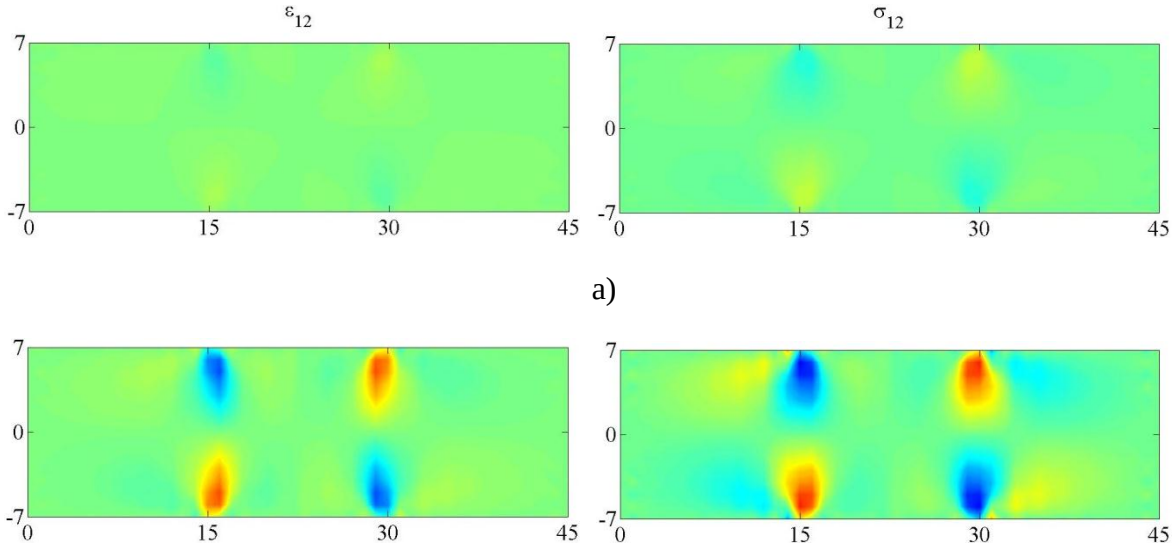

a)

b)

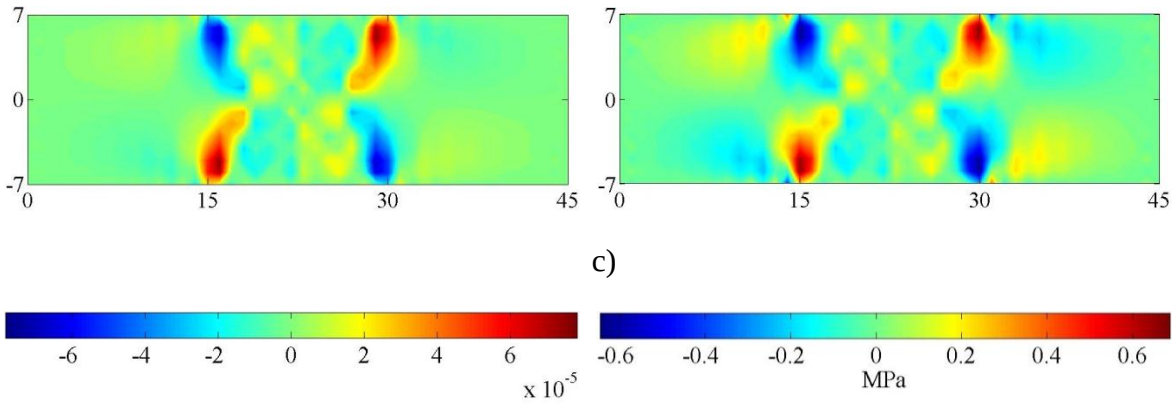

Figure 5.13: Case One – ε_{12} and σ_{12} for Δu= a) 0.0027cm, b) 0.0101 cm, and c) 0.0127 cm.

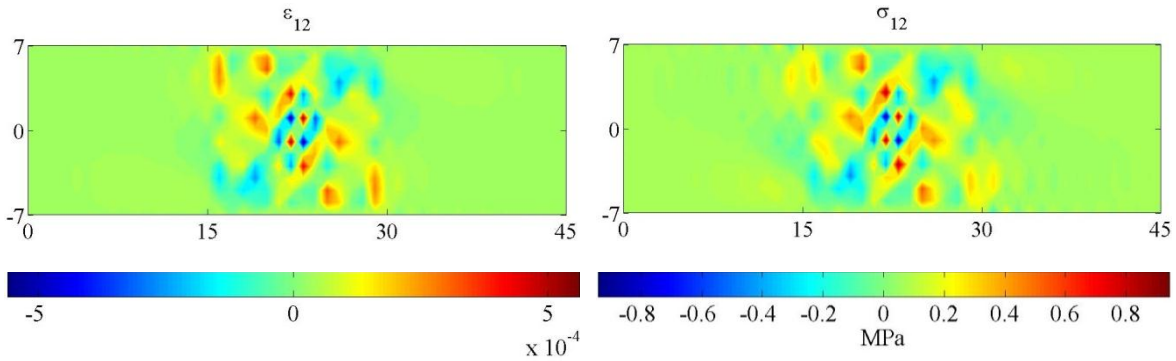

Figure 5.14: Case One – ε_{12} and σ_{12} for Δu= 0.01274 cm.

Figures 5.15-5.16 describe the effective strain and stress response within the structure at the four loading stages afore mentioned. Stress response shows uniform stress distribution along the structure. Reduction on stress magnitude is observed after the peak-load is reached indicating failure of the structure. Strain response show higher strains within the inclusion and strain concentrations at the peak and post-peak stage. At the latter stage, these concentrations become more severe suggesting the presence of fractures within the inclusion that are normal to the load.

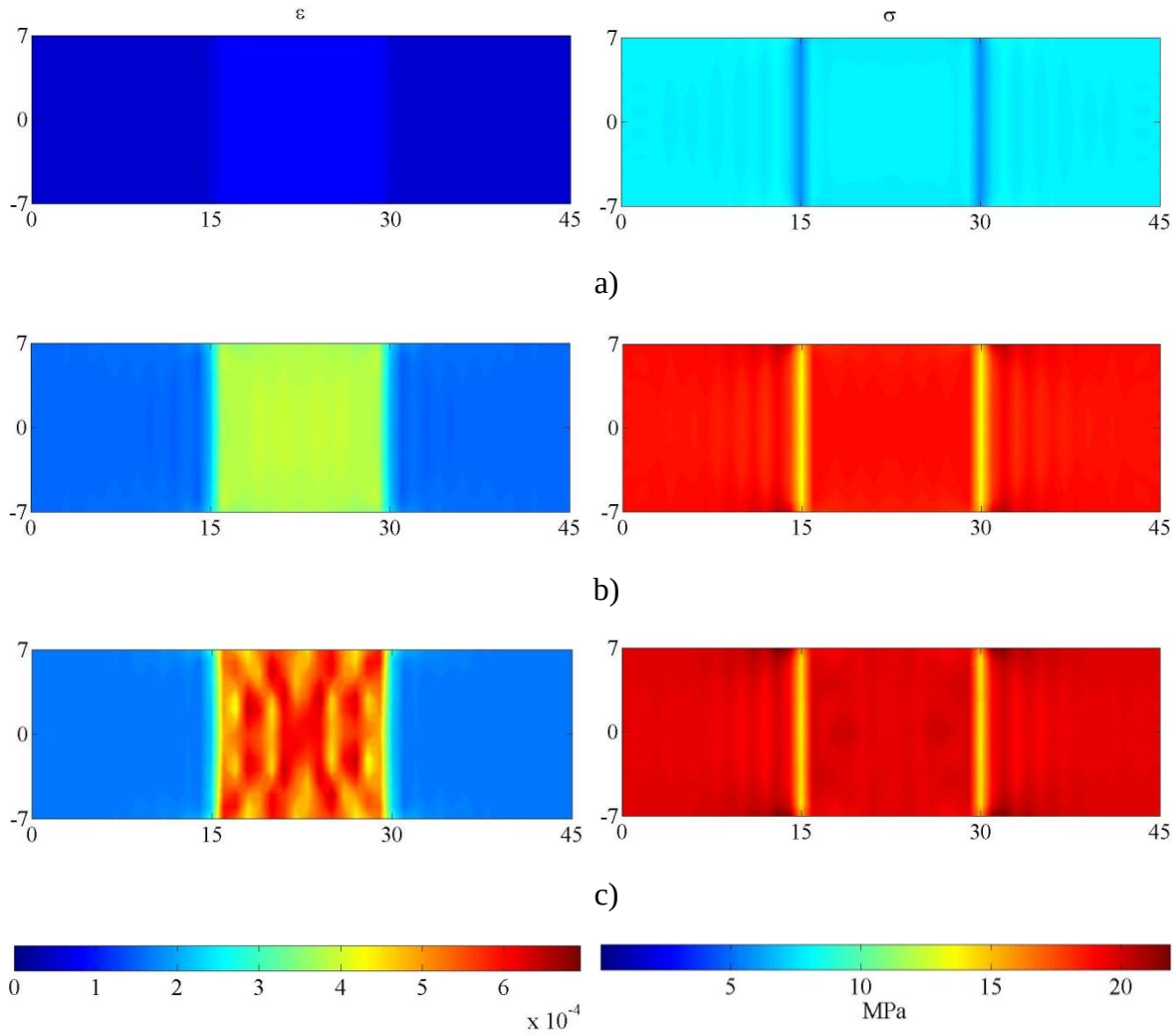

Figure 5.15: Case One – ε and σ for Δu= a) 0.0027cm, b) 0.0101 cm, and c) 0.0127 cm.

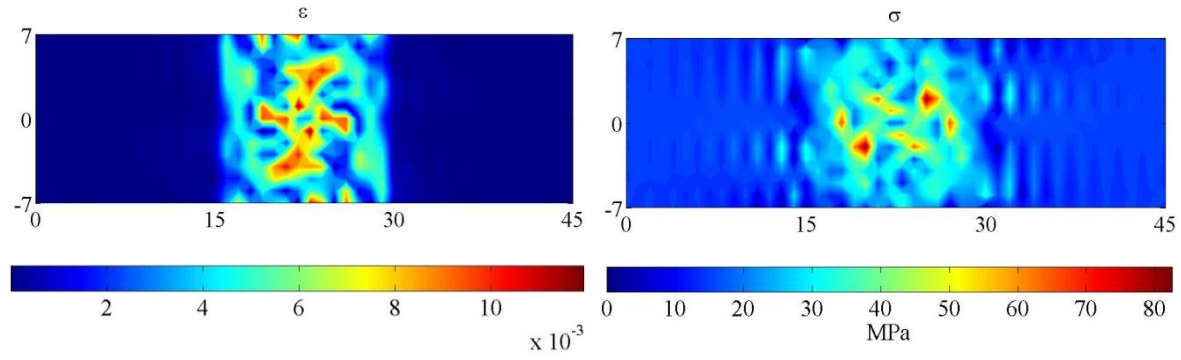

Figure 5.16: Case One – ε and σ for Δu= 0.01274 cm.

Figures 5.17-5.24 describe the gradient strain – double stress response of the structure at the four loading stages afore mentioned. Strain gradient results describe, at the peak and post-peak stages, high tensile and compressive concentrations suggesting the presence of fractures that are aligned vertically. These fractures describe a fracture zone that is mainly normal to the load.

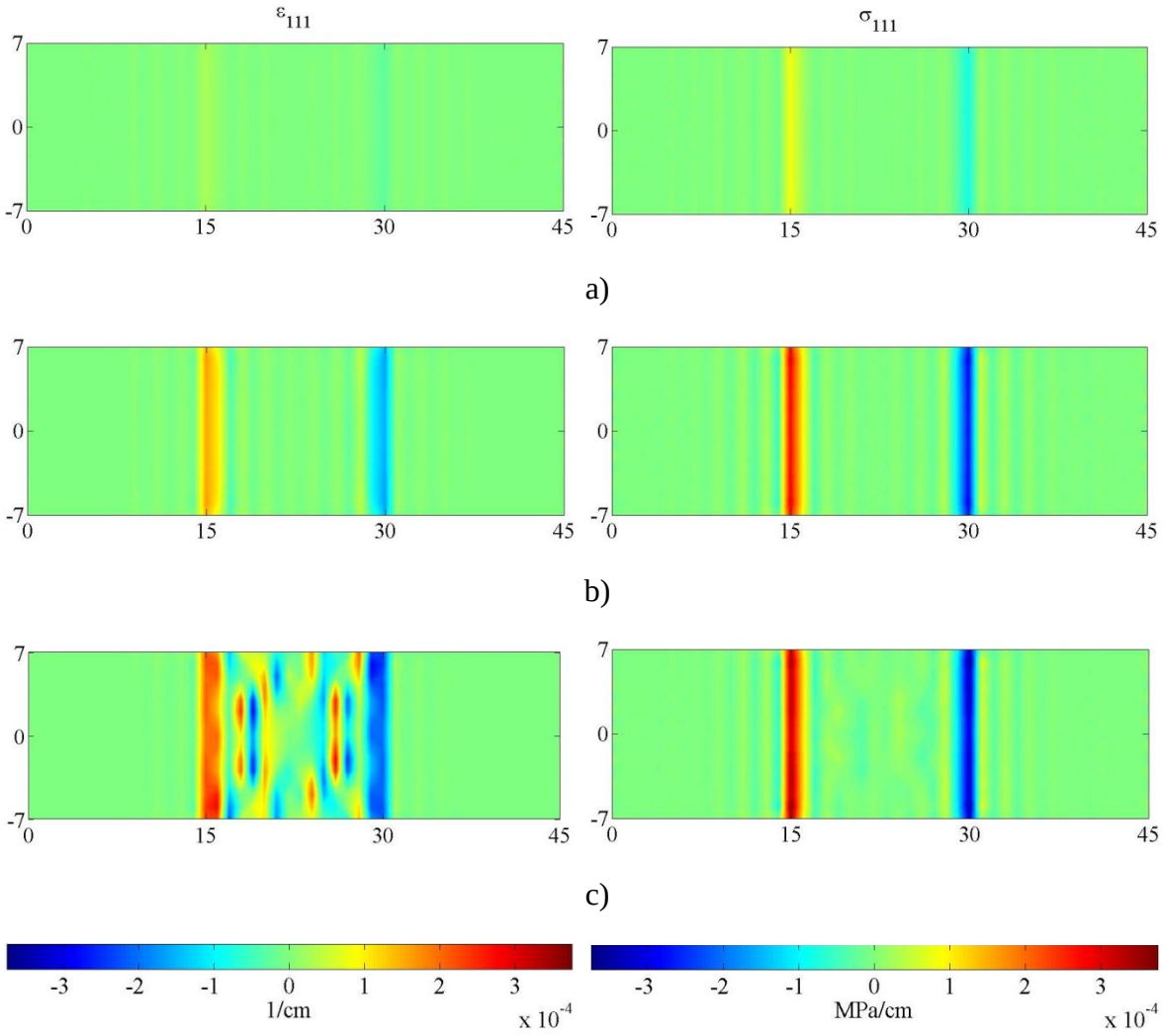

Figure 5.17: Case One – ε_{111} and σ_{111} for Δu= a) 0.0027cm, b) 0.0101 cm, and c) 0.0127 cm.

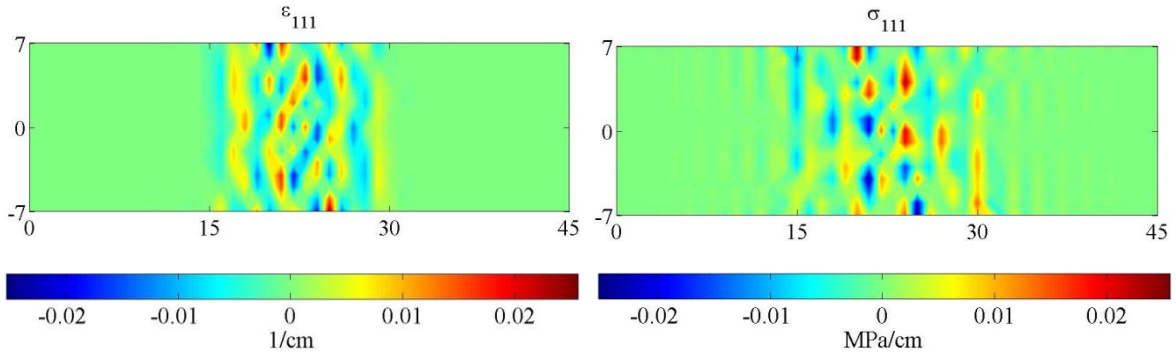

Figure 5.18: Case One – ε_{111} and σ_{111} for Δu= 0.01274 cm.

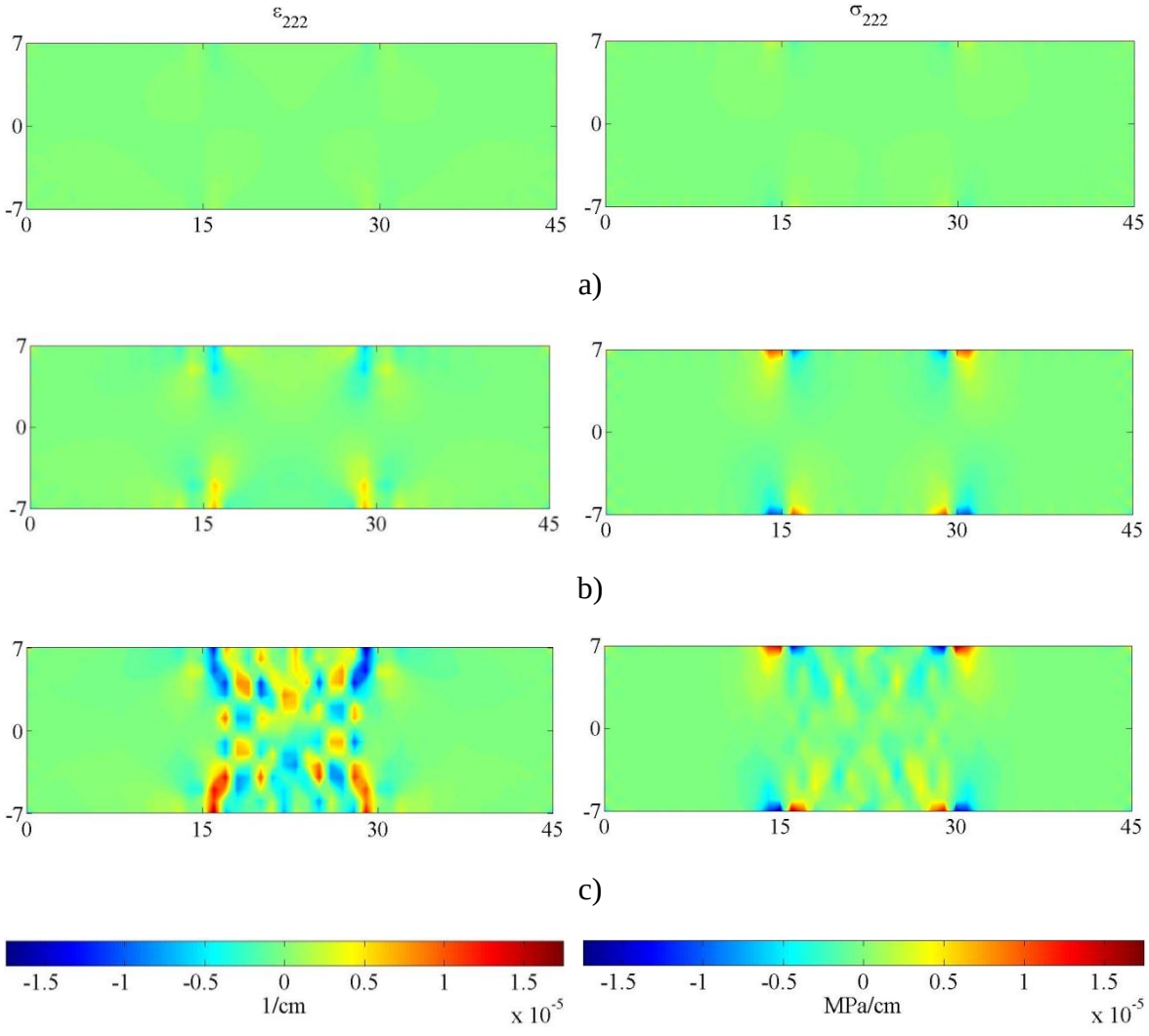

Figure 5.19: Case One – ε_{222} and σ_{222} for Δu= a) 0.0027cm, b) 0.0101 cm, and c) 0.0127 cm.

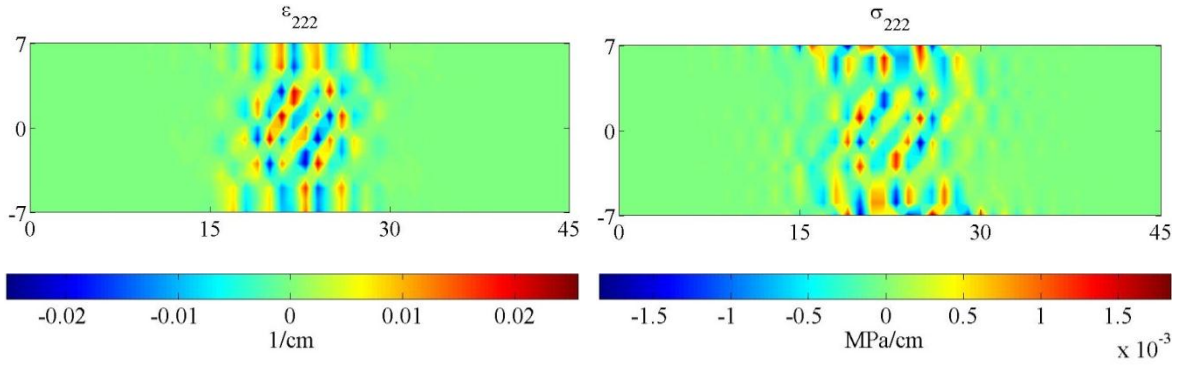

Figure 5.20: Case One – ε_{222} and σ_{222} for Δu= 0.01274 cm.

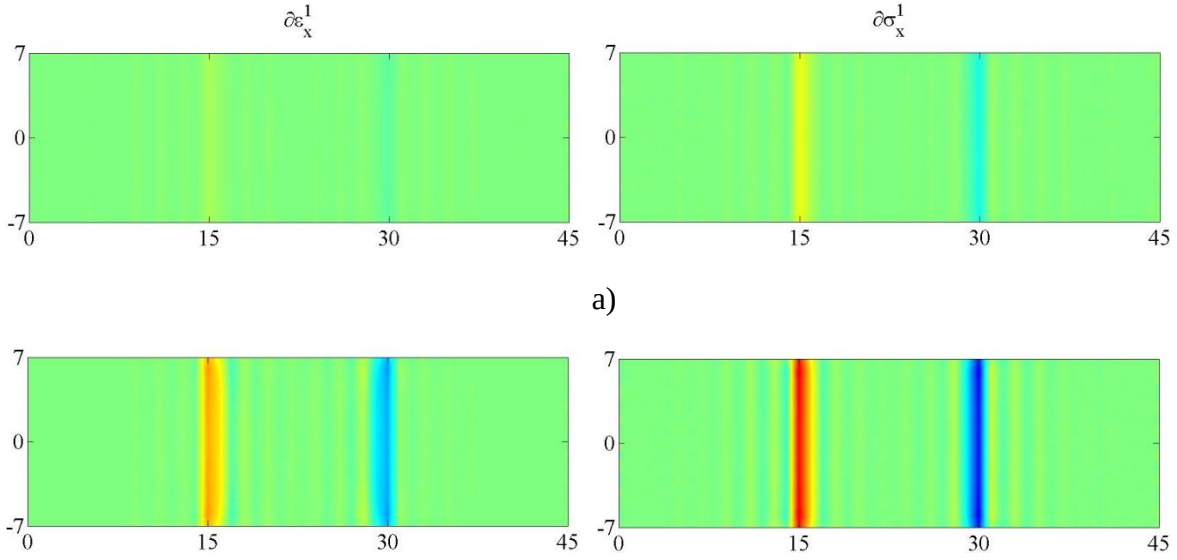

a)

b)

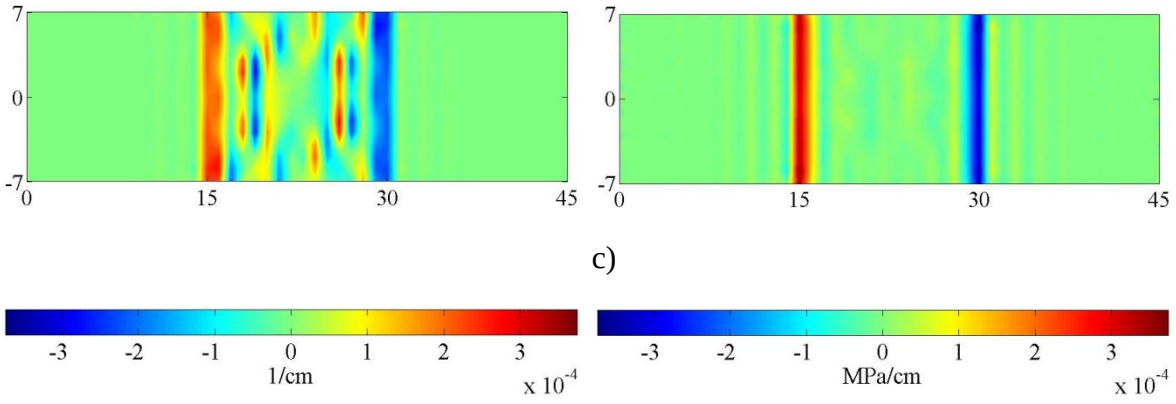

c)

Figure 5.21: Case One – Effective gradient strain and double stress in the 1-direction for Δu= a) 0.0027cm, b) 0.0101 cm, and c) 0.0127 cm.

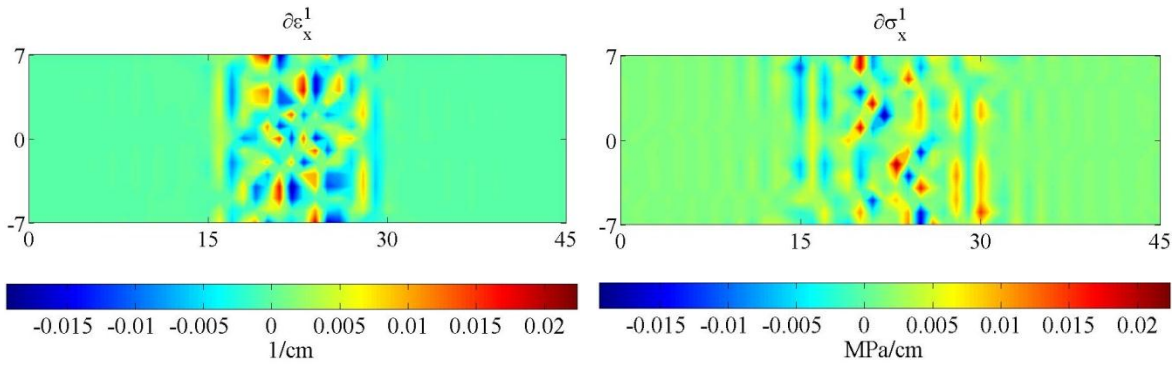

Figure 5.22: Case One – Effective gradient strain and double stress in the 1-direction for Δu= 0.01274 cm.

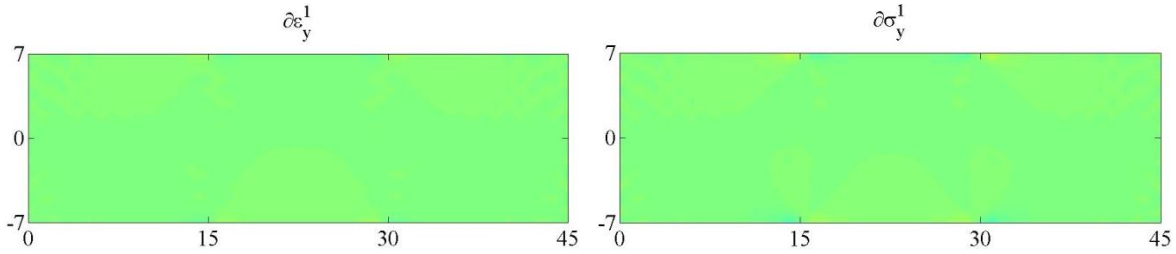

a)

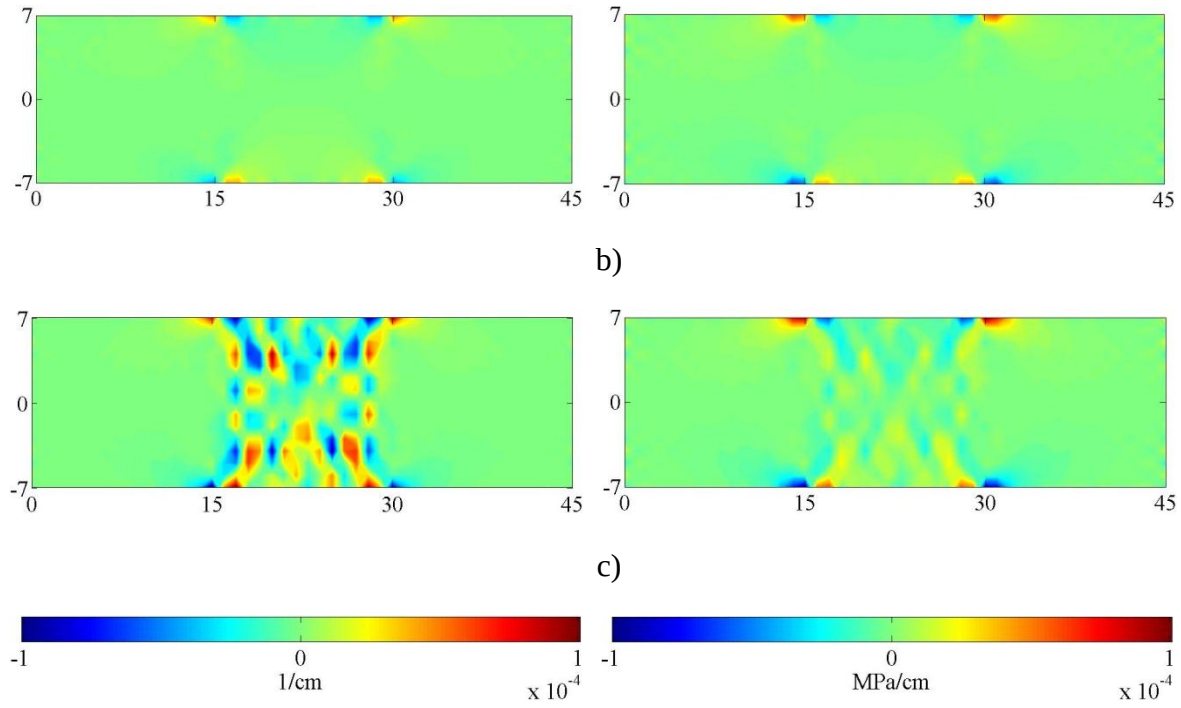

Figure 5.23: Case One – Effective gradient strain and double stress in the 2-direction for Δu= a) 0.0027cm, b) 0.0101 cm, and c) 0.0127 cm.

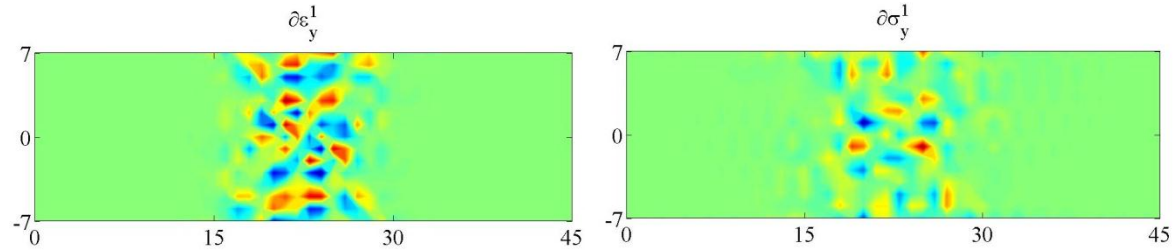

Figure 5.24: Case One – Effective gradient strain and double stress in the 2-direction for Δu= 0.01274 cm.

5.4.2. Case Two: Tensile loading with band inclusion and transverse constraints (L_0=1 mm).

In this simulation, the 2D plate is subjected to tension by applying stretch displacements along its right side. In addition, the plate has a centered band inclusion that is forty percent softer than the plate material and it is modeled with a particle size of L_0=1 mm. The length and height

of the plate and the inclusion are 45 cm×14 cm and 15 cm×14 cm, respectively. The plate is constrained in the 1-direction along its left border while the top and bottom are constrained from vertical translation (See Figure 5.5).

The response of the structure is shown in Figures 5.25-5.33 at four loading stages: initial, pre-peak, peak, and post-peak stages. Figure 5.25 shows the overall stress-strain response in the '11' and '22' directions. Figures 5.26-5.28 show the strain and stress responses in the '11', '22', and '12' directions, and their effective magnitudes are shown in Figure 5.29. Strain gradient and double stress responses are shown in Figures 5.30-5.31, and their effective magnitudes are described in Figures 5.32-5.33.

The overall stress-strain response of the plate in the '11' and '22' directions, is described in Figure 5.25, shows a biaxial stress state with non-linear softening behavior. Past the peak-load failure is described by a reduction in the stress response values.

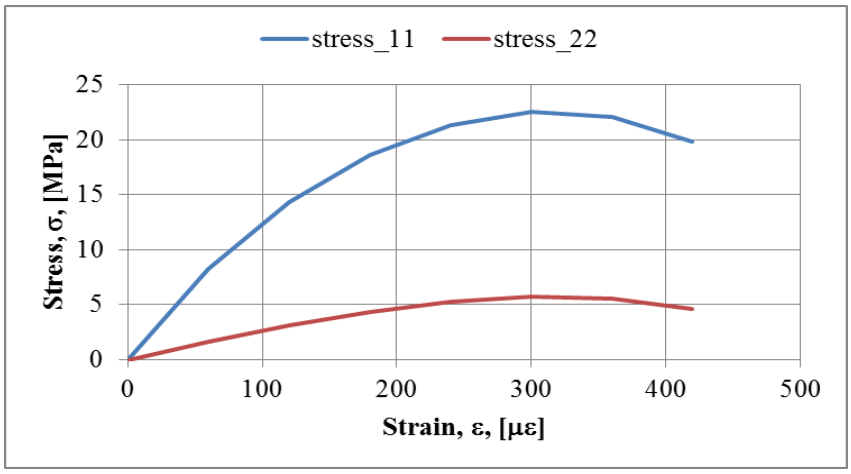

Figure 5.25: Case Two – Overall stress-strain behavior of the plate.

Figure 5.26 describes the strain and stress response of the structure in the 11-direction at the four loading stages afore mentioned. Stress response shows overall uniform stress distribution along the structure. Reduction on stress magnitude is observed after the peak-load is reached indicating failure of the structure. Strain responses show higher strains within the inclusion and strain concentrations at the peak and post-peak stages. At the latter stage, these concentrations become more severe suggesting the presence of micro shear fractures within the inclusion.

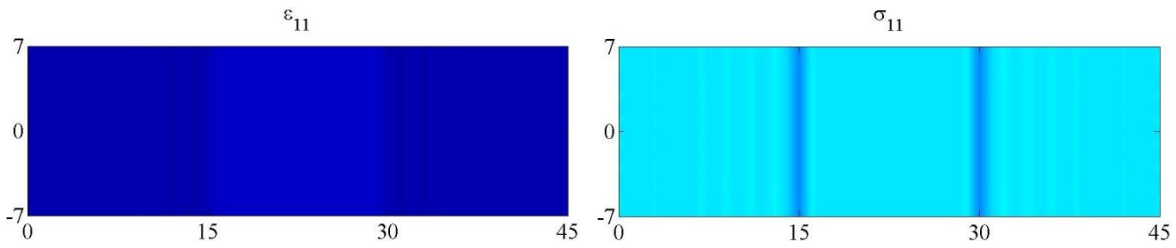

a)

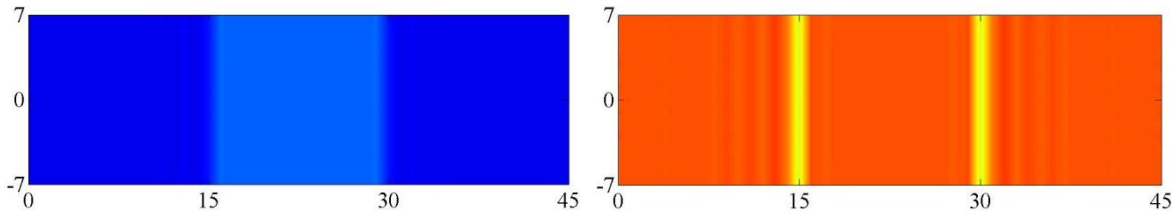

b)

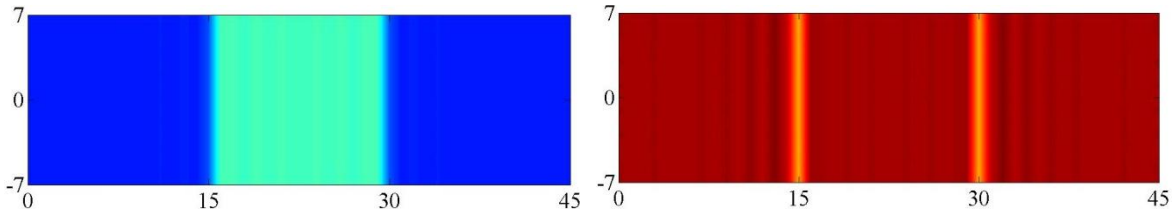

c)

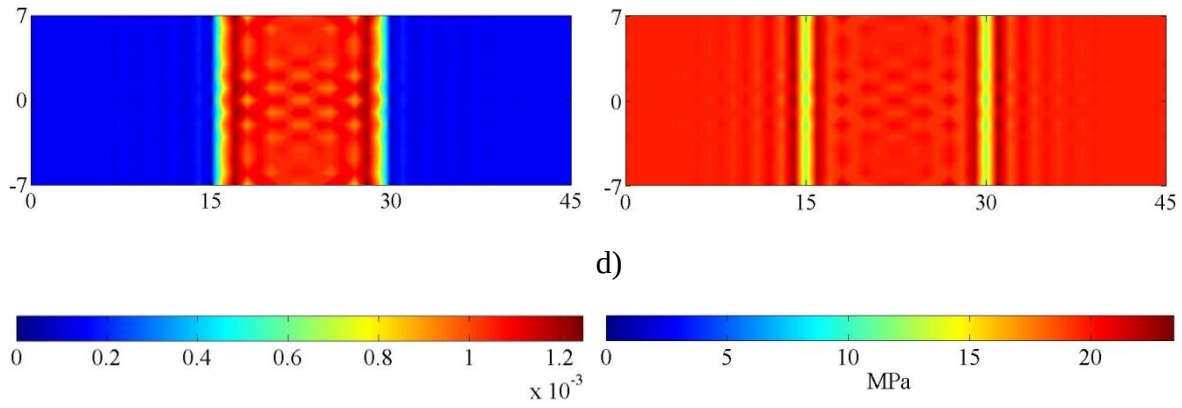

Figure 5.26: Case Two – ε_{11} and σ_{11} for Δu= a) 0.0027cm, b) 0.0081 cm, c) 0.0135 cm, and d) 0.0189 cm.

Figure 5.27 describes the strain and stress response of the structure in the 22-direction at the four loading stages afore mentioned. Stress response show uniform stress distribution with higher magnitudes along the inclusion. Reduction on stress magnitude is observed along the plate outside the inclusion after the peak-load is reached, which indicates failure of the structure. Strain response shows zero strain magnitudes up to the post-peak stage in which compression and tension bands are observed, this is attributed to the loading induced heterogeneity of the material that is captured by the model.

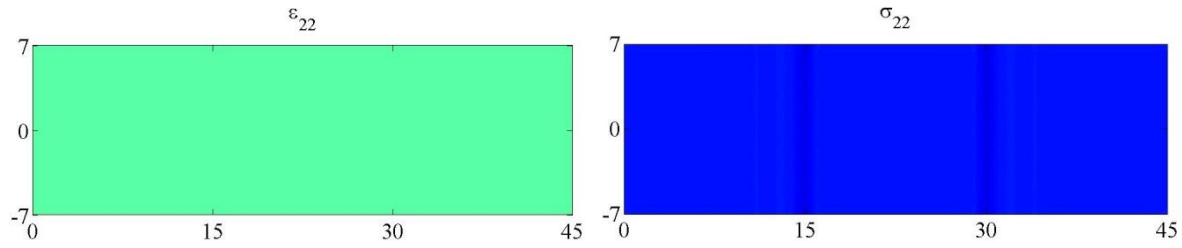

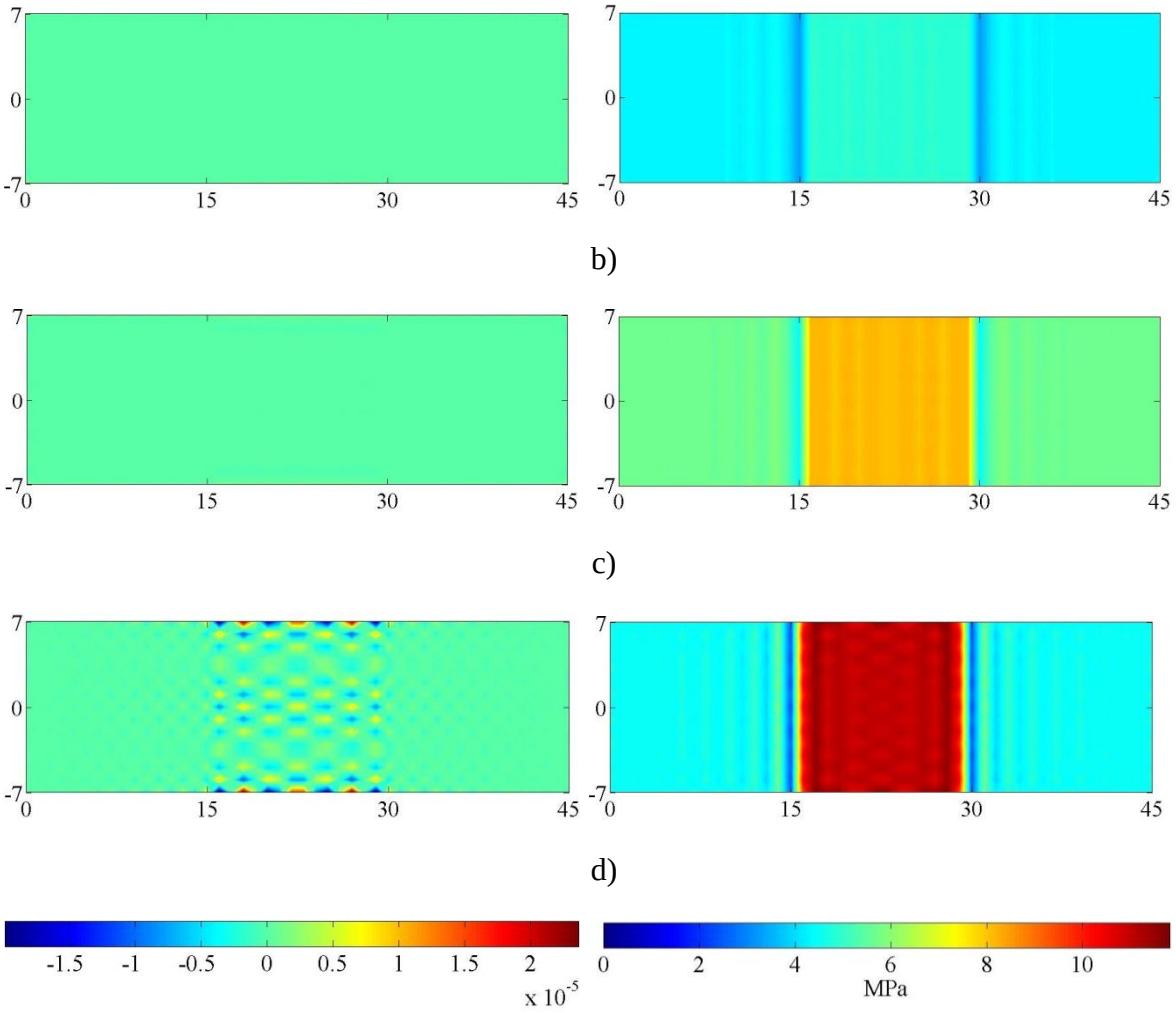

Figure 5.27: Case Two – ε_{22} and σ_{22} for Δu= a) 0.0027cm, b) 0.0081 cm, c) 0.0135 cm, and d) 0.0189 cm.

Figure 5.28 describes the strain and stress response of the structure in the 12-direction at the four loading stages afore mentioned. Strain and stress results show zero magnitudes up to the post-peak stage where compression and tension bands are observed. This is attributed to the loading induced heterogeneity of the material, which is captured by the model.

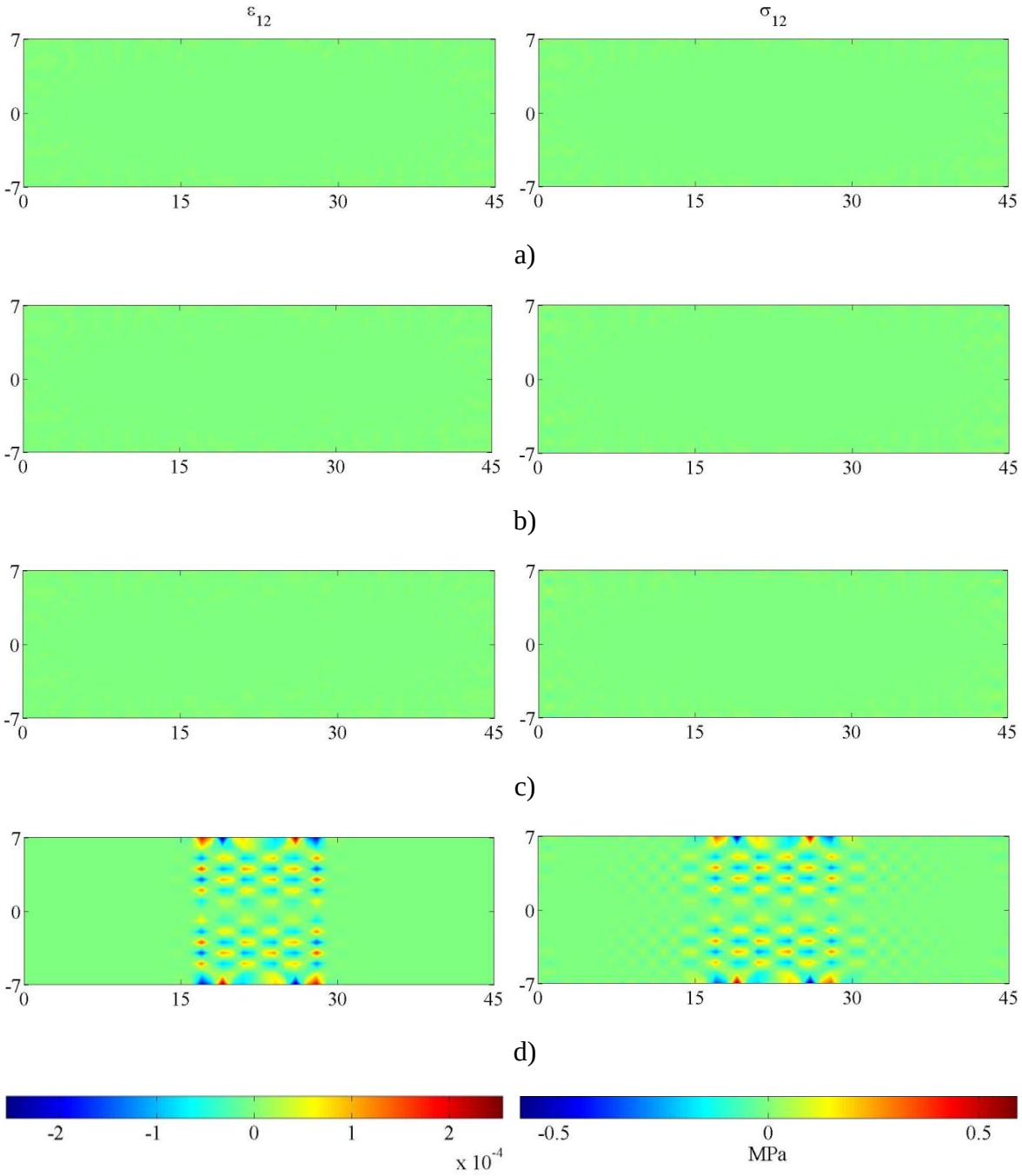

Figure 5.28: Case Two – ε_{12} and σ_{12} for Δu= a) 0.0027cm, b) 0.0081 cm, c) 0.0135 cm, and d) 0.0189 cm.

Figure 5.29 describes the effective strain and stress response within the structure at the four loading stages afore mentioned. Stress response shows overall uniform stress distribution along the structure. Reduction on stress magnitude along the plate and outside the inclusion is observed after the peak-load is reached indicating failure of the structure. Strain response show higher strains within the inclusion and strain concentrations at the peak and post-peak stage. At the latter stage, these concentrations become more severe suggesting the presence shear micro fractures within the inclusion.

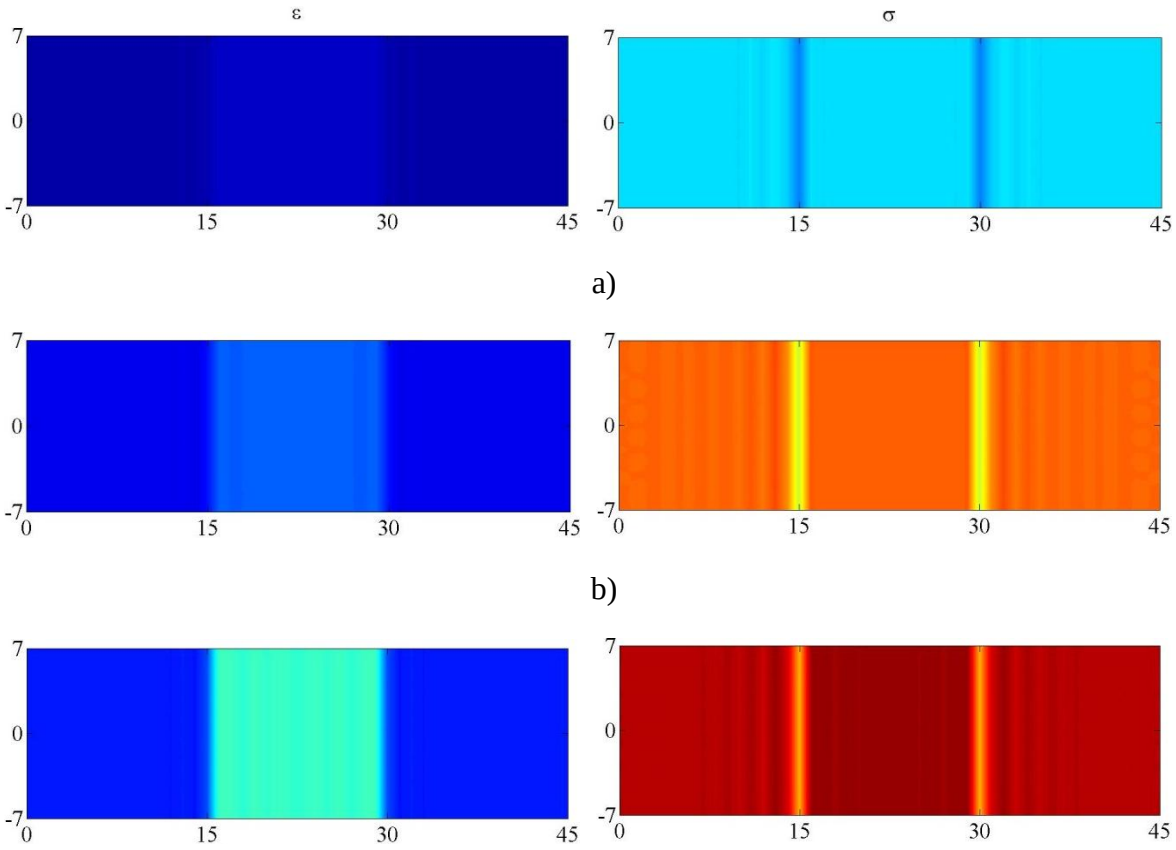

a)

b)

c)

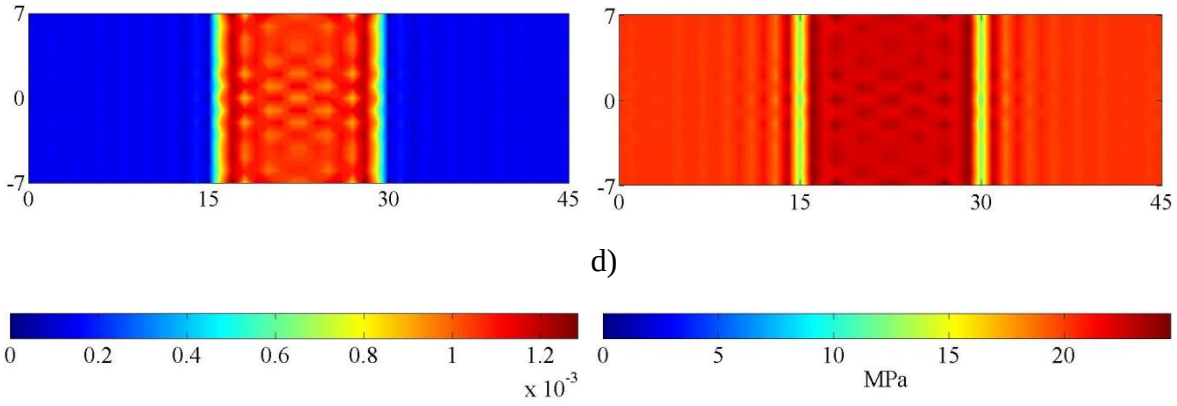

d)

Figure 5.29: Case Two – ε and σ for Δu= a) 0.0027cm, b) 0.0081 cm, c) 0.0135 cm, and d) 0.0189 cm.

Figures 5.30-5.33 describe the gradient strain –double stress response of the structure at the four loading stages afore mentioned. Strain gradient results describe at the peak and post-peak stages tensile and compressive concentrations that are located beside each other suggesting the presence of very small fractures. These fractures describe a fracture zone normal to the load.

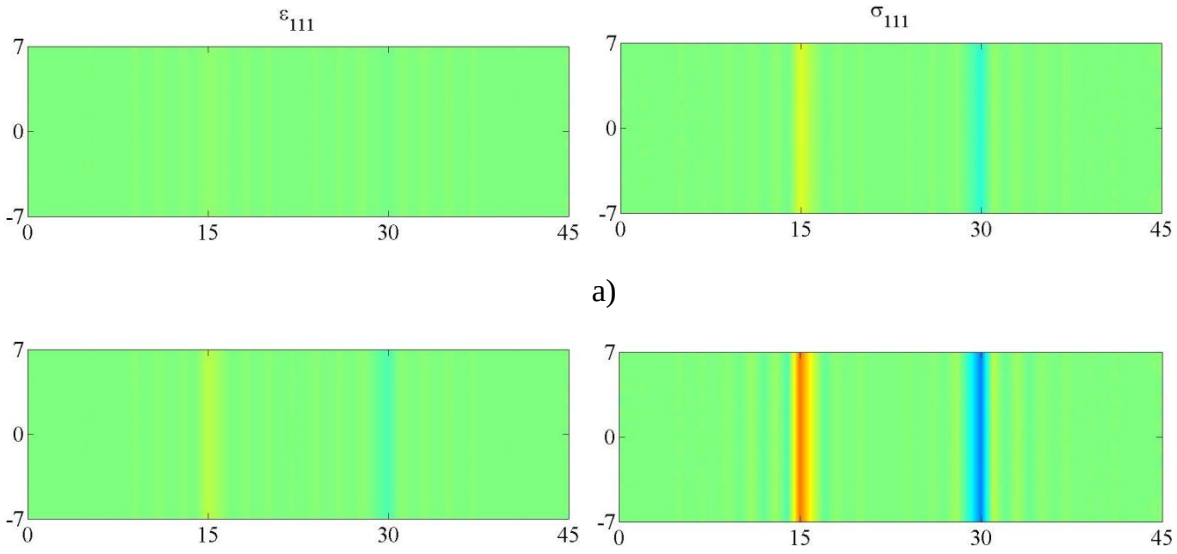

a)

b)

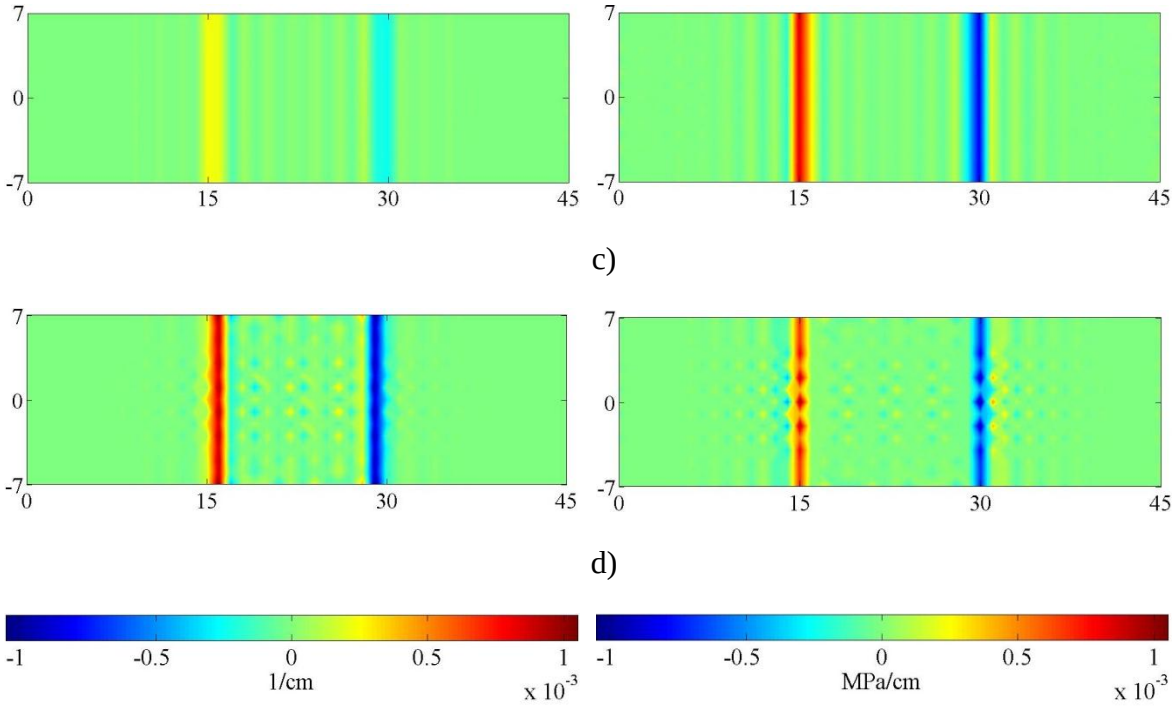

Figure 5.30: Case Two – ε_{111} and σ_{111} for Δu= a) 0.0027cm, b) 0.0081 cm, c) 0.0135 cm, and d) 0.0189 cm.

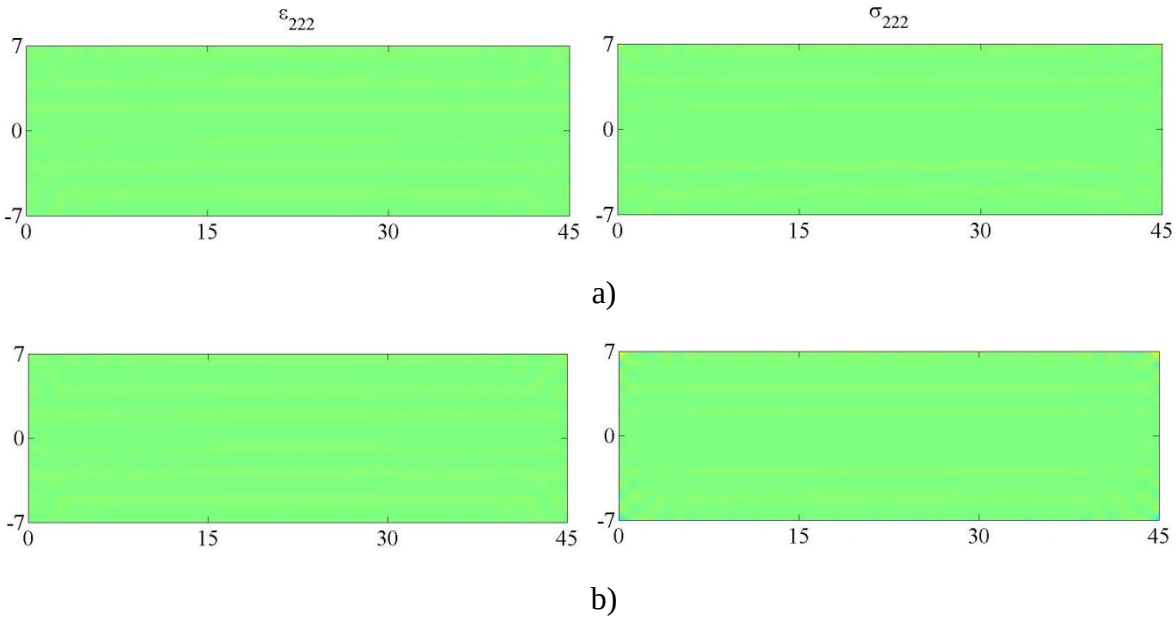

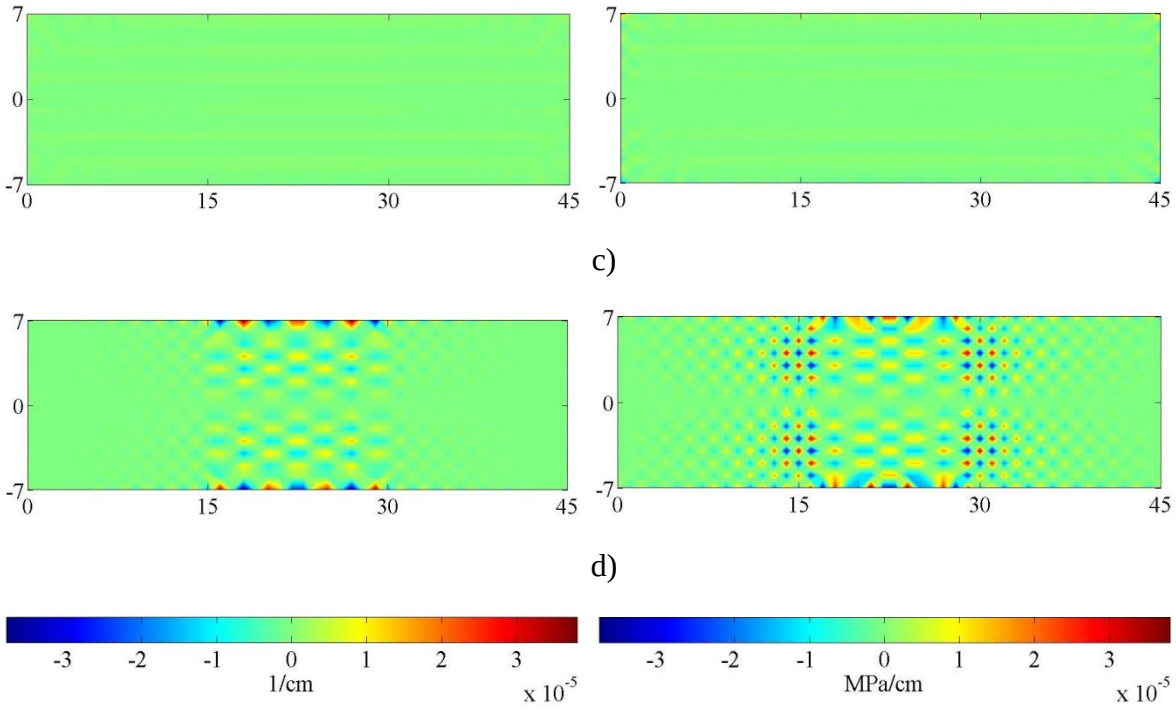

Figure 5.31: Case Two – ε_{222} and σ_{222} for Δu= a) 0.0027cm, b) 0.0081 cm, c) 0.0135 cm, and d) 0.0189 cm.

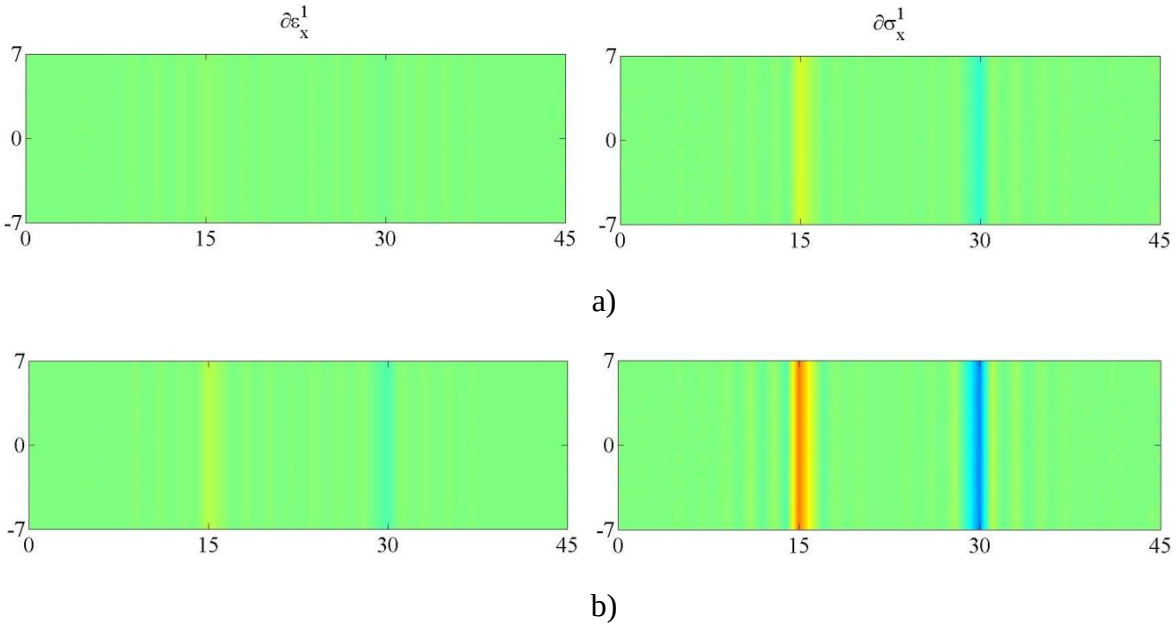

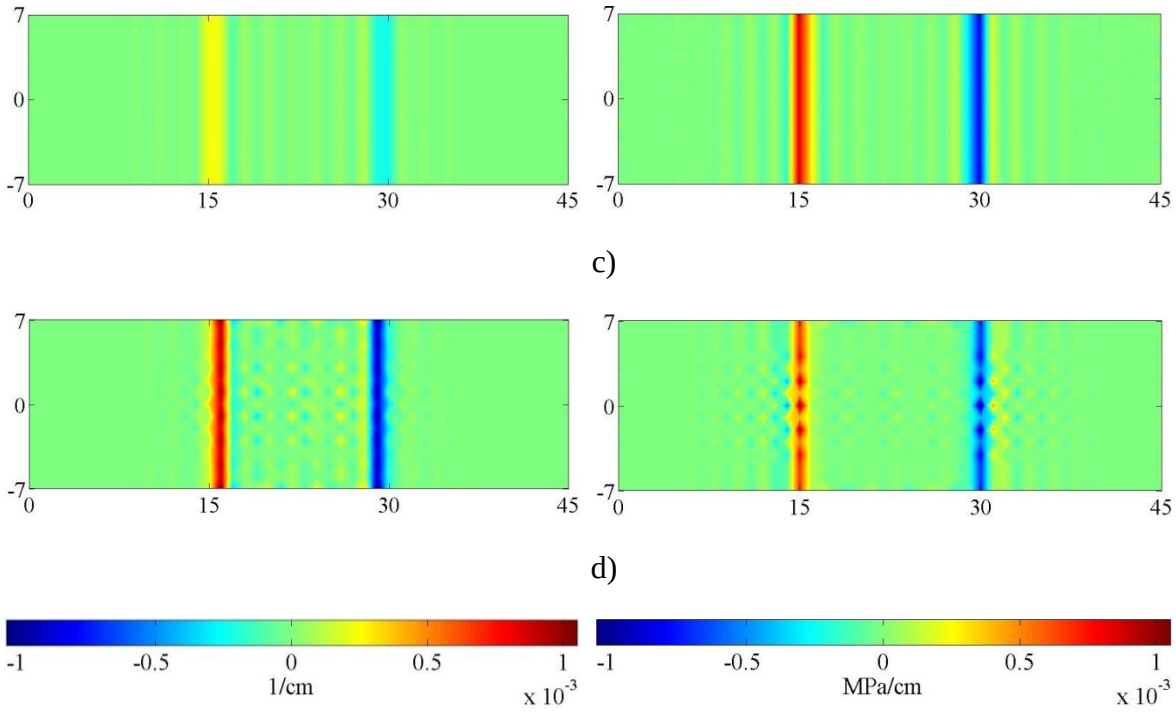

Figure 5.32: Case Two –Effective gradient strains and double stresses in the 1-direction for Δu= a) 0.0027cm, b) 0.0081 cm, c) 0.0135 cm, and d) 0.0189 cm.

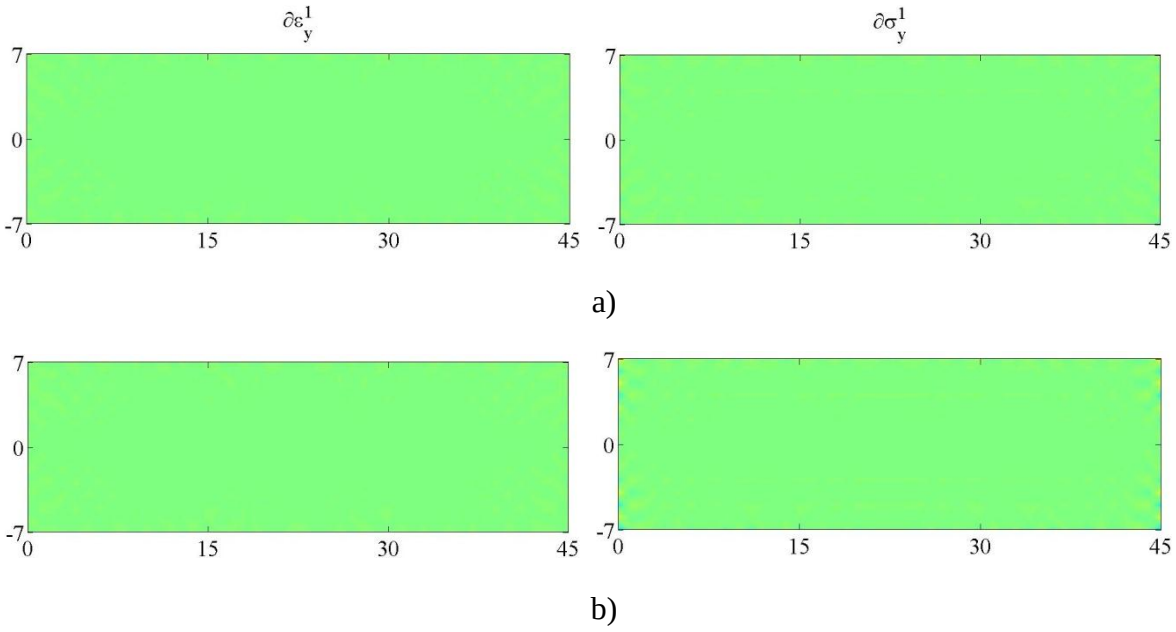

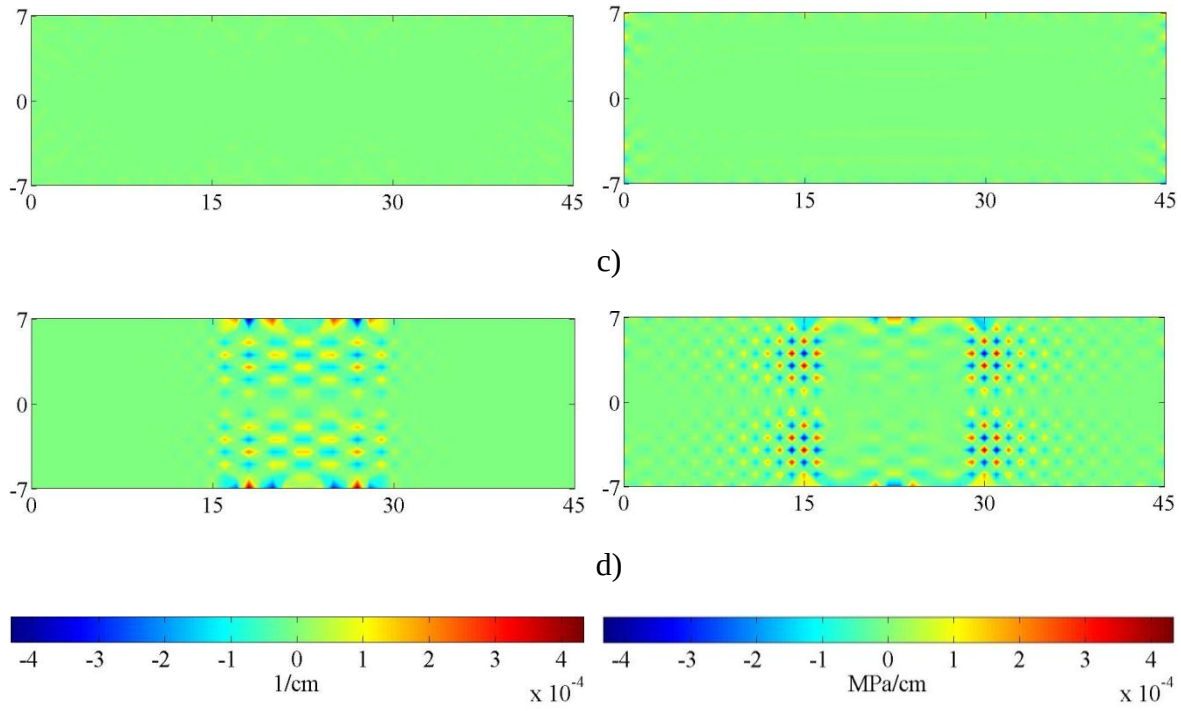

Figure 5.33: Case Two –Effective gradient strains and double stresses in the 2-direction for Δu= a) 0.0027cm, b) 0.0081 cm, c) 0.0135 cm, and d) 0.0189 cm.

5.4.3. Case Three: Tensile loading with square inclusion and no constraints (L_0=1 mm).

In this simulation, the 2D plate is subjected to tension by applying stretch displacements along its right side. In addition, the plate has a centered square inclusion that is forty percent softer than the plate material and it is modeled with a particle size of L_0=1 mm. The length and height of the plate and the inclusion are 45 cm×14 cm and 4cm×4cm, respectively. The plate is constrained in the 1-direction along its left border while the top and bottom have no constraints (See Figure 5.6).

The response of the structure is shown in Figures 5.34-5.50 at four loading stages: initial, pre-peak, peak, and post-peak stage. Figure 5.34 shows the overall stress-strain response in the '11' and '22' directions. Figures 5.35-5.40 show the strain and stress responses in the '11', '22',

and ‘12’ directions, and the effective magnitudes are shown in Figures 5.41-5.42. Strain gradient and double stress responses are shown in Figures 5.43-5.46, and its effective magnitudes are described in Figures 5.47-5.50.

The overall stress-strain response of the plate in the ‘11’ and ‘22’ directions is described in Figure 5.34 and shows a uniaxial stress state with non-linear softening behavior. Failure of the structure is described past the peak-load with a sudden drop in the stress response.

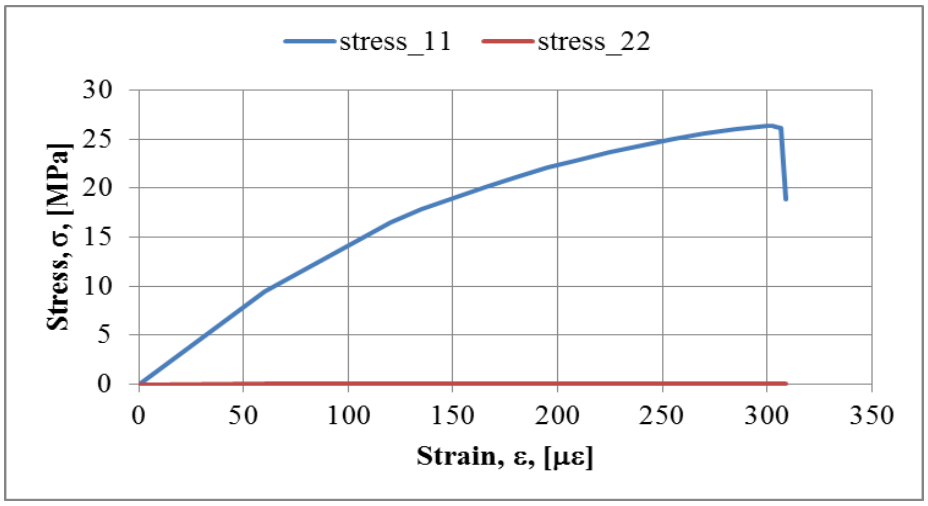

Figure 5.34: Case Three – Overall stress-strain behavior of the plate.

Figures 5.35-5.36 describe the stress strain response of the structure in the 11-direction at the four loading stages afore mentioned. Stress response shows uniform stress distribution with stress concentrations around the top and bottom of the inclusion and lower stresses inside the inclusion. Reduction on the stress magnitude is observed after the peak-load is reached indicating failure of the structure. Strain response show higher strains within the inclusion with high strain concentrations at the peak and post-peak-stage. At the latter stage, these concentrations become more severe suggesting the presence of vertical fractures that are normal to the load.

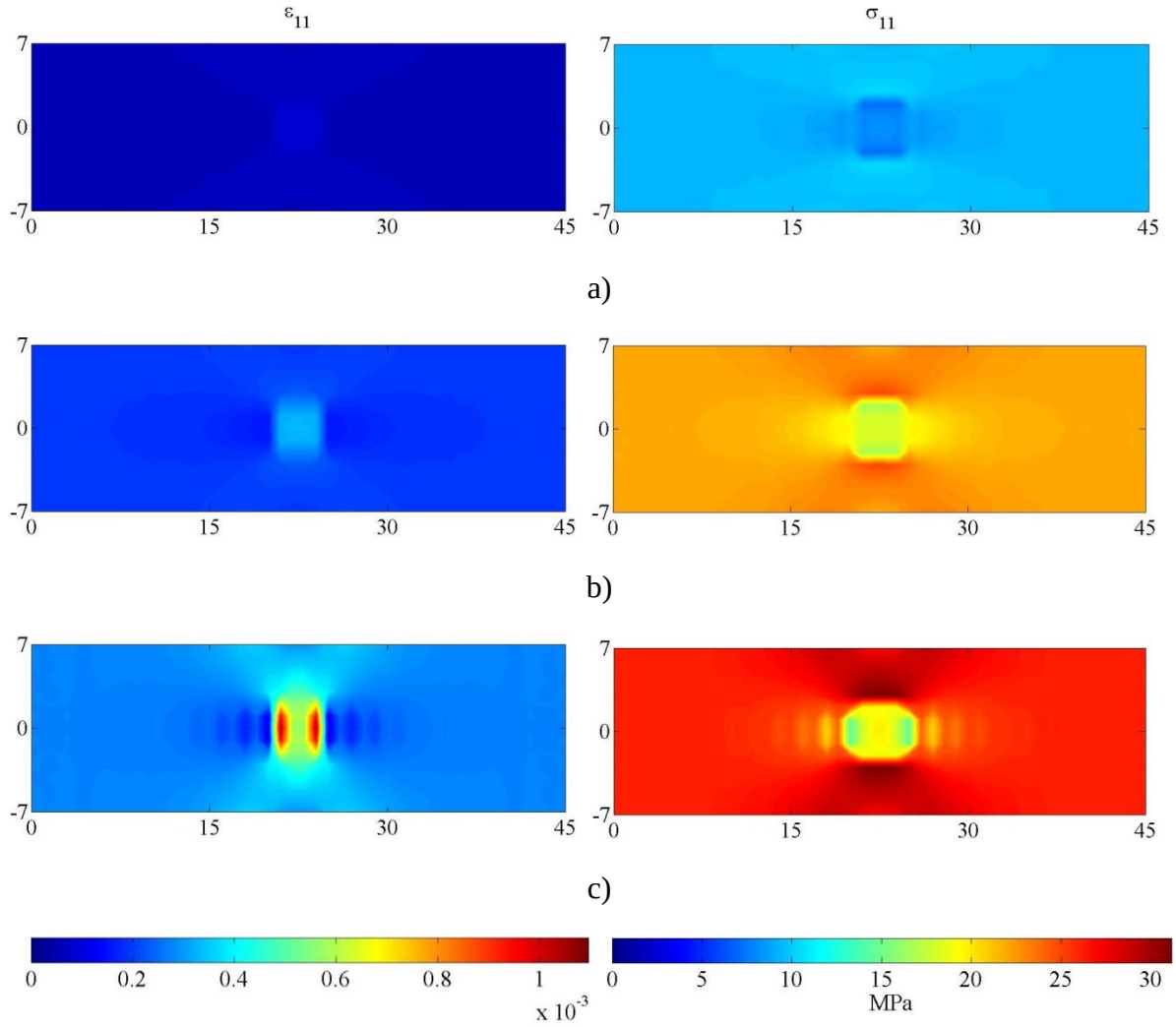

Figure 5.35: Case Three – ε_{11} and σ_{11} for Δu= a) 0.0027cm, b) 0.0088 cm, and c) 0.0135 cm.

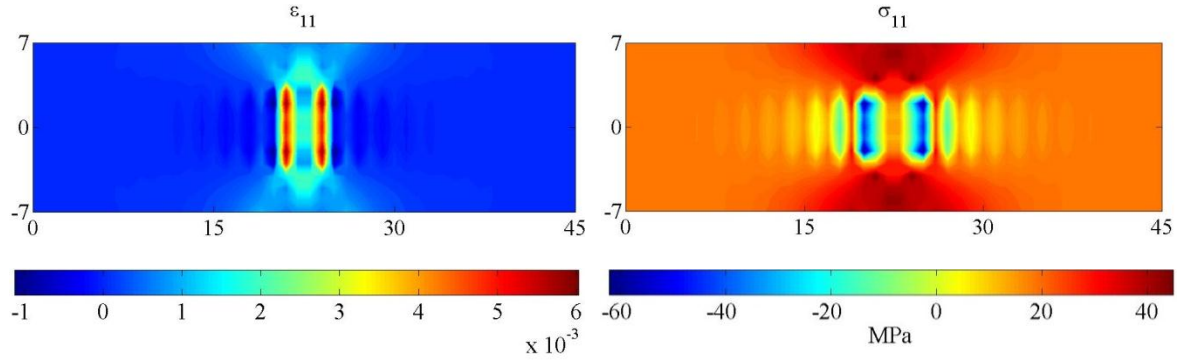

Figure 5.36: Case Three – ε_{11} and σ_{11} for Δu= 0.0139 cm.

Figures 5.37-5.38 describe the stress strain response of the structure in the 22-direction at the four loading stages afore mentioned. Stress response shows uniform zero stress distribution with compressive stress concentrations around the sides of the inclusion that are normal to the load. Strain response show higher contracting strains within the inclusion and strain concentrations that branch out diagonally from the corners of the inclusion at the peak and post-peak stage.

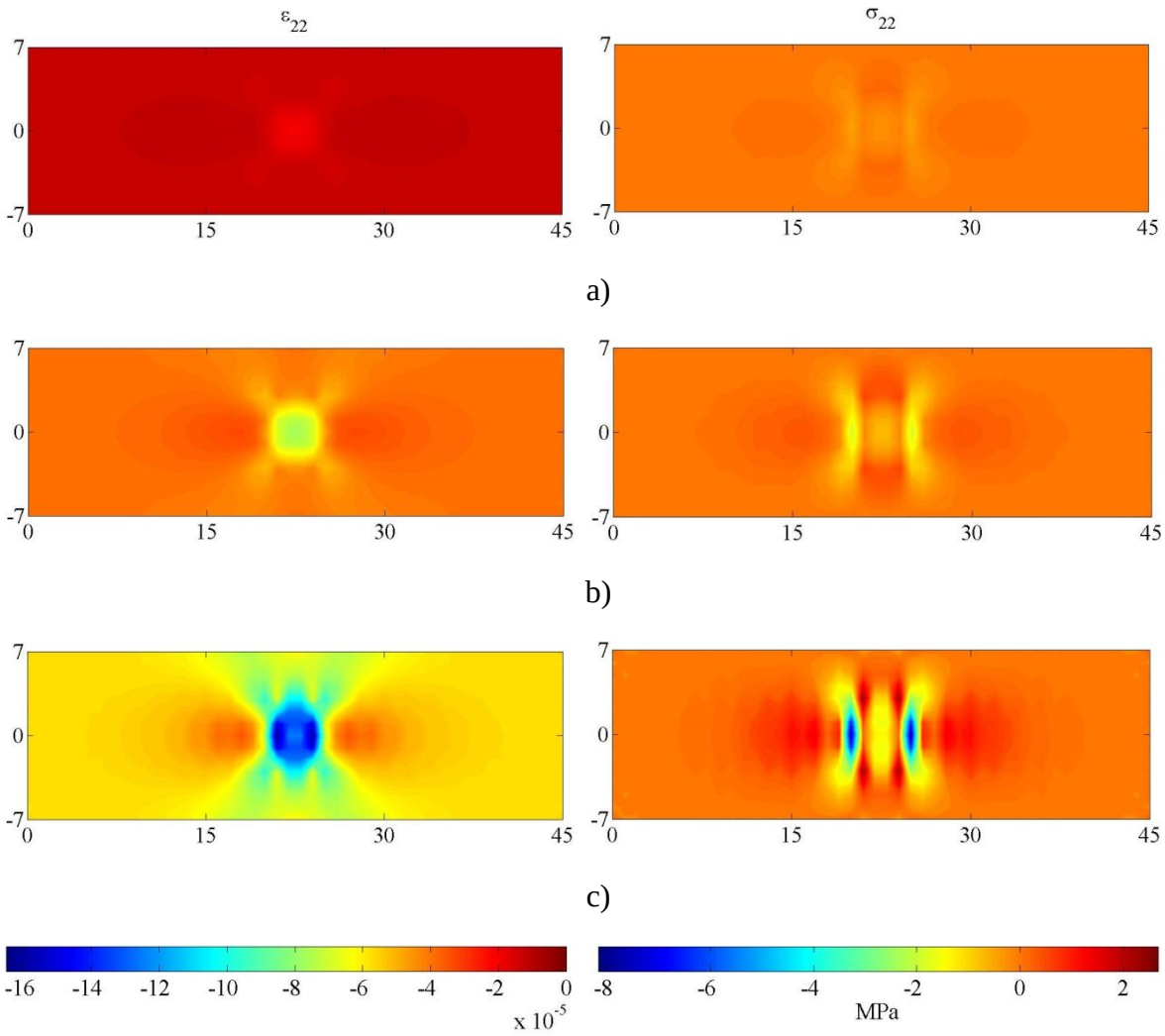

Figure 5.37: Case Three – ε_{22} and σ_{22} for Δu= a) 0.0027cm, b) 0.0088 cm, and c) 0.0135 cm.

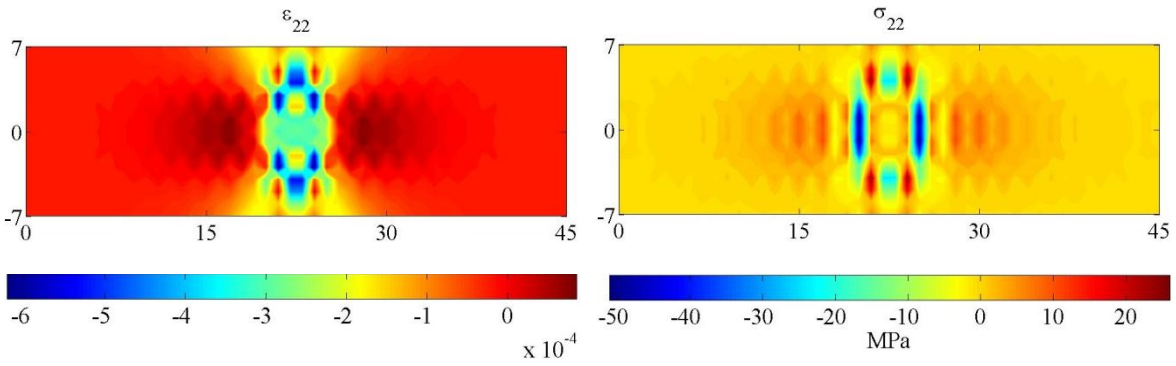

Figure 5.38: Case Three – ε_{22} and σ_{22} for Δu= 0.0139 cm.

Figures 5.39-5.40 describe the stress and strain response of the structure in the 12-direction at the four loading stages afore mentioned. Strain and stress response show concentrations at the corners of the inclusion that becomes more severe as the load increases.

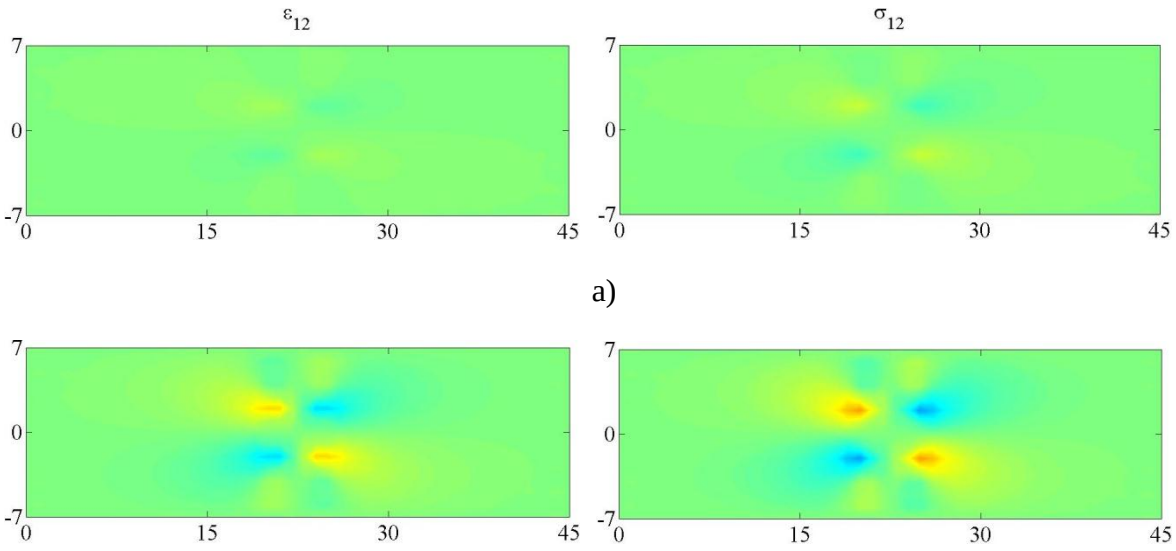

a)

b)

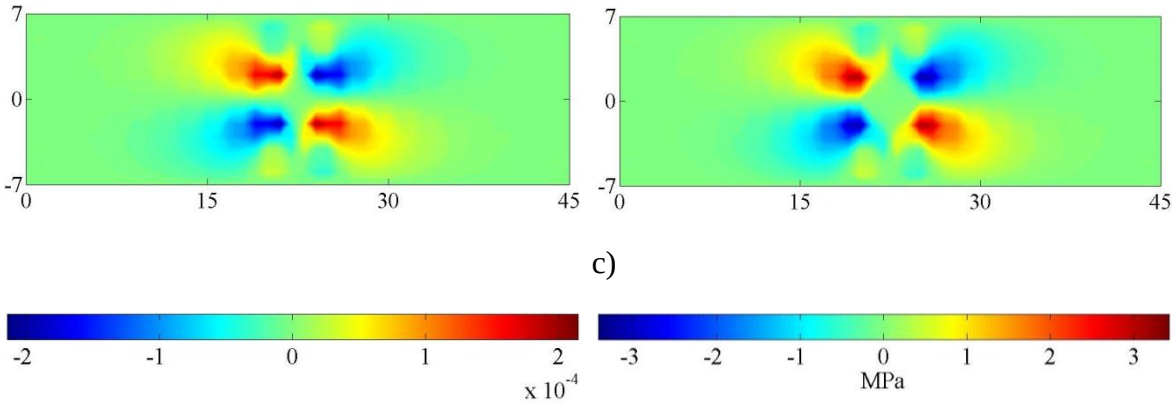

Figure 5.39: Case Three – ε_{12} and σ_{12} for Δu= a) 0.0027cm, b) 0.0088 cm, and c) 0.0135 cm.

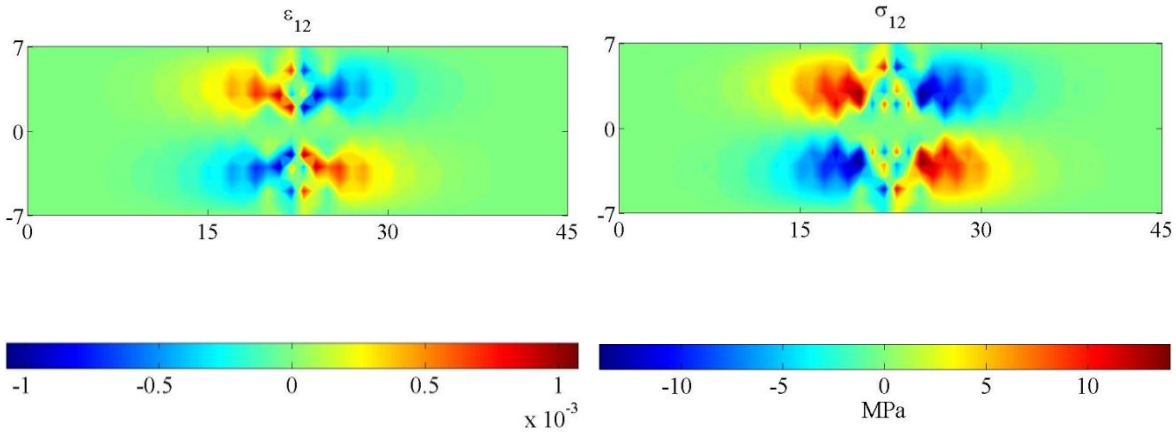

Figure 5.40: Case Three – ε_{12} and σ_{12} for Δu= 0.0139 cm.

Figures 5.41-5.42 describe the effective stress strain results within the structure at the four loading stages afore mentioned. Stress response shows uniform stress distribution with stress concentrations at the top and bottom edges of the inclusion and lower magnitude stresses inside the inclusion. Reduction on stress magnitude is observed after the peak-load is reached indicating failure of the structure. Strain response show higher strains within the inclusion and strain concentrations at the peak and post-peak stage. At the latter stage, these concentrations become more severe suggesting the presence of vertical fractures that are normal to the load.

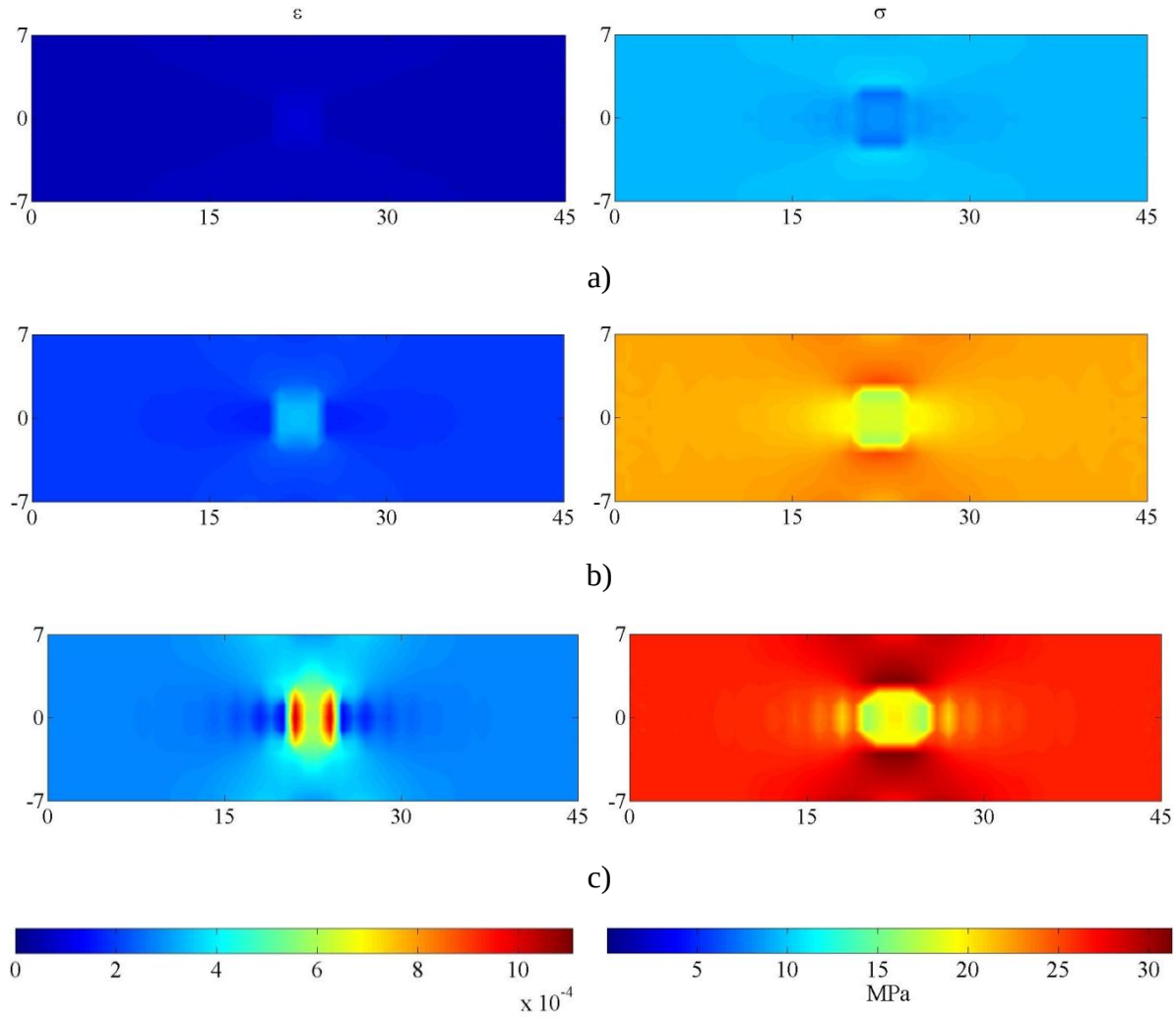

Figure 5.41: Case Three – ε and σ for Δu= a) 0.0027cm, b) 0.0088 cm, and c) 0.0135 cm.

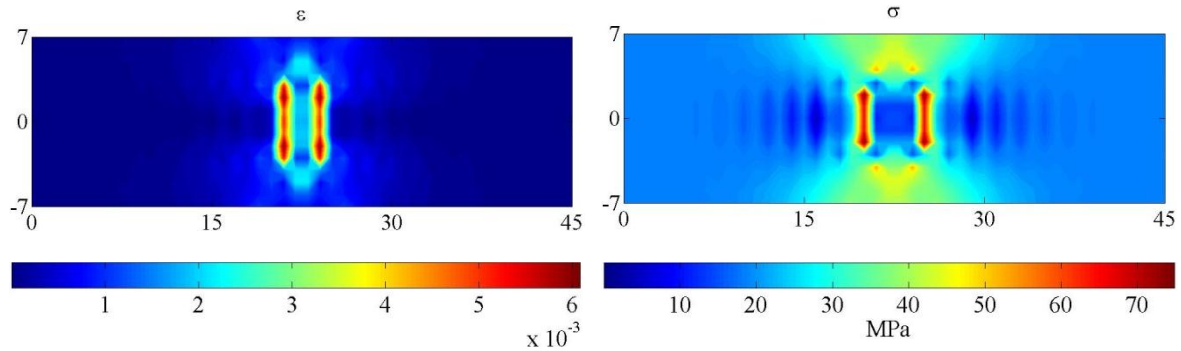

Figure 5.42: Case Three – ε and σ for Δu= 0.0139 cm.

Figures 5.43-5.50 describe the gradient strain–double stress responses of the structure at the four loading stages afore mentioned. Strain gradient results describe, at the peak and post-peak stages, high tensile and compressive concentrations that are located beside each other and suggest the presence of vertical fractures that are normal to the load.

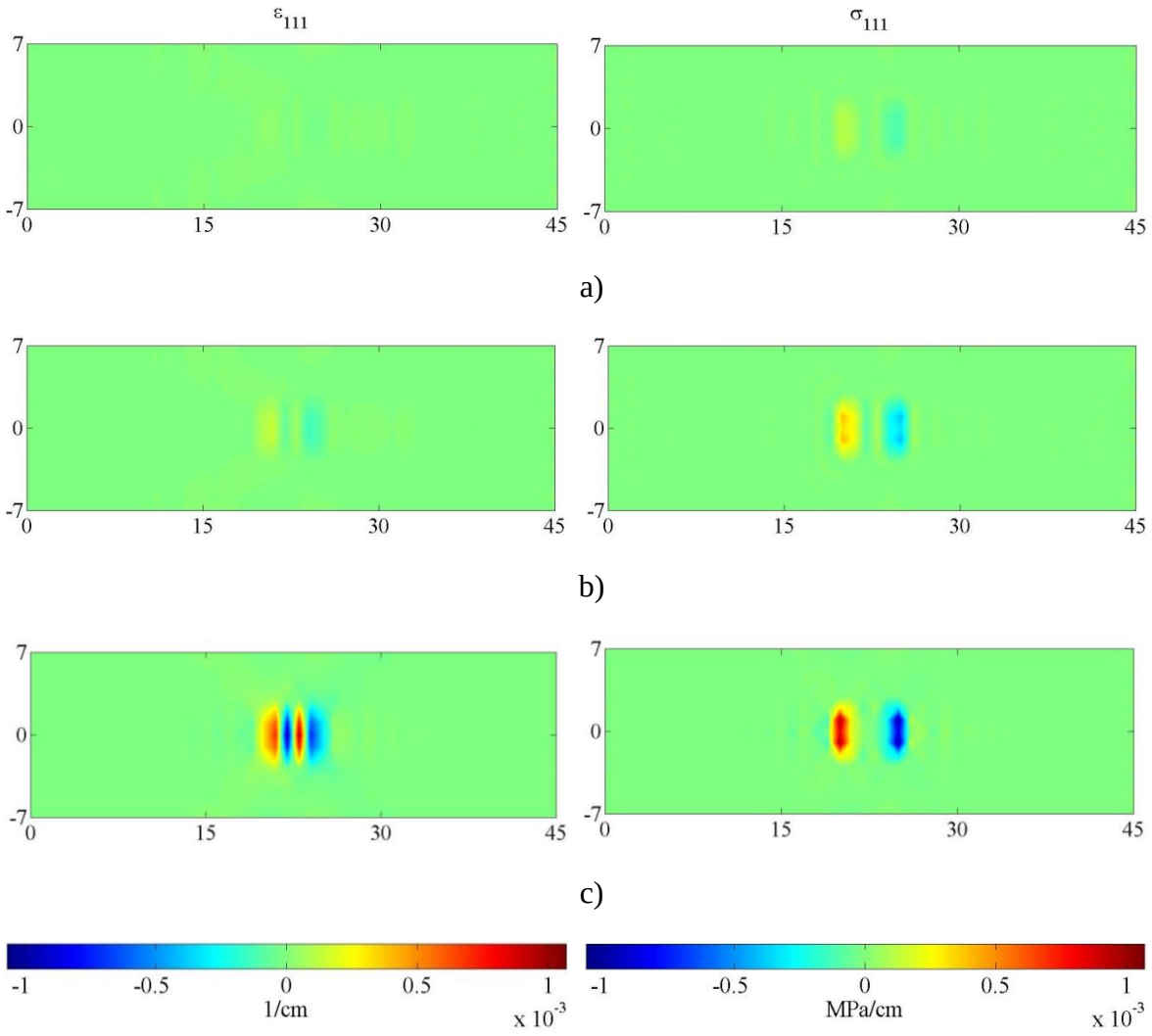

Figure 5.43: Case Three – ε_{111} and σ_{111} for Δu= a) 0.0027cm, b) 0.0088 cm, and c) 0.0135 cm.

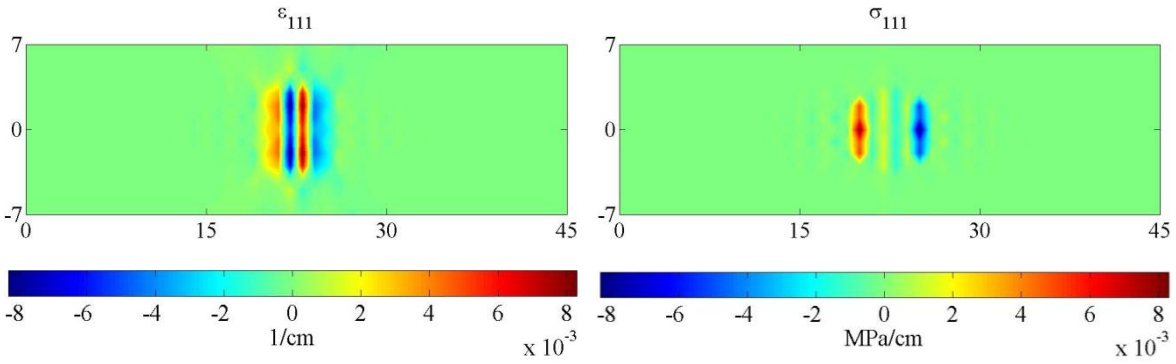

Figure 5.44: Case Three – ε_{111} and σ_{111} for Δu= 0.0139 cm.

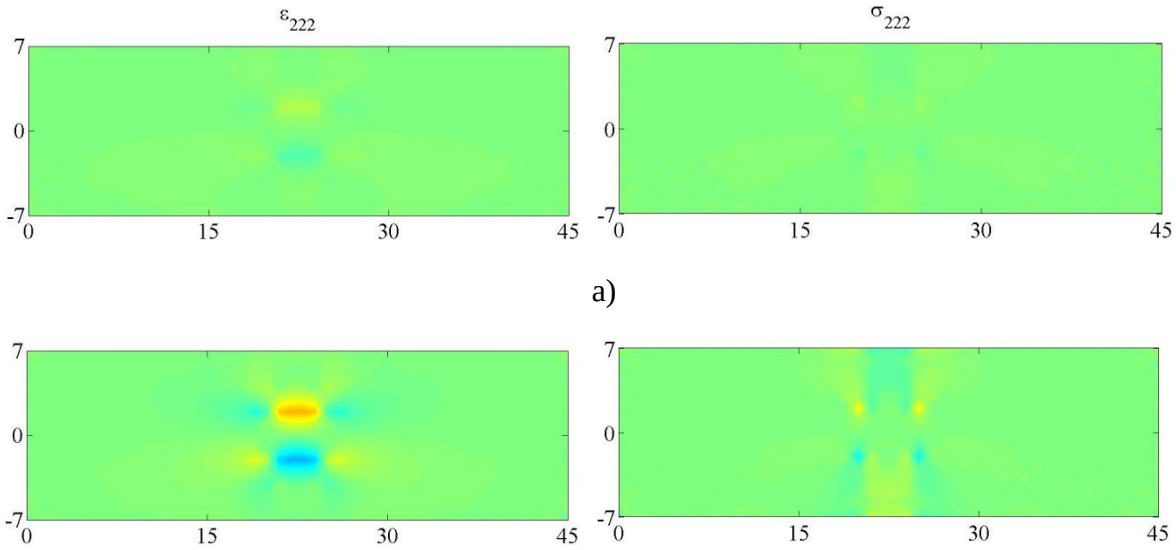

a)

b)

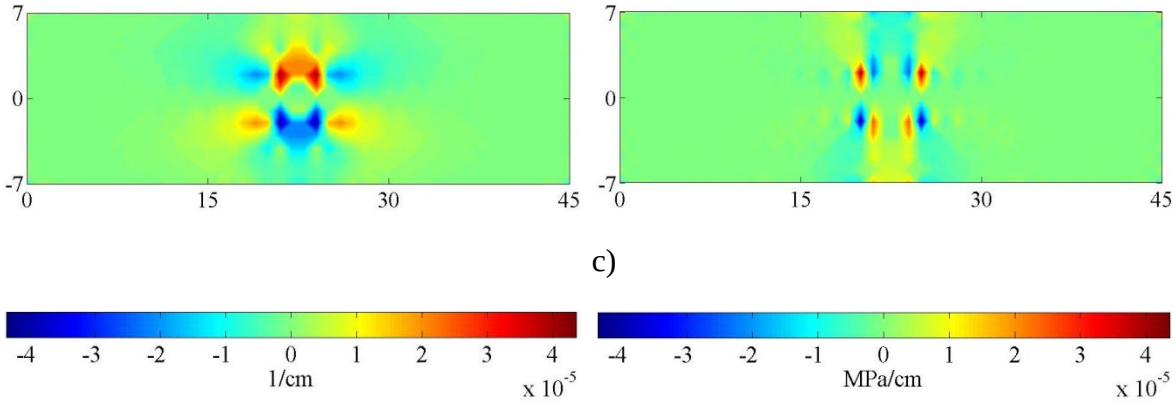

c)

Figure 5.45: Case Three – ε_{222} and σ_{222} for Δu= a) 0.0027cm, b) 0.0088 cm, and c) 0.0135 cm.

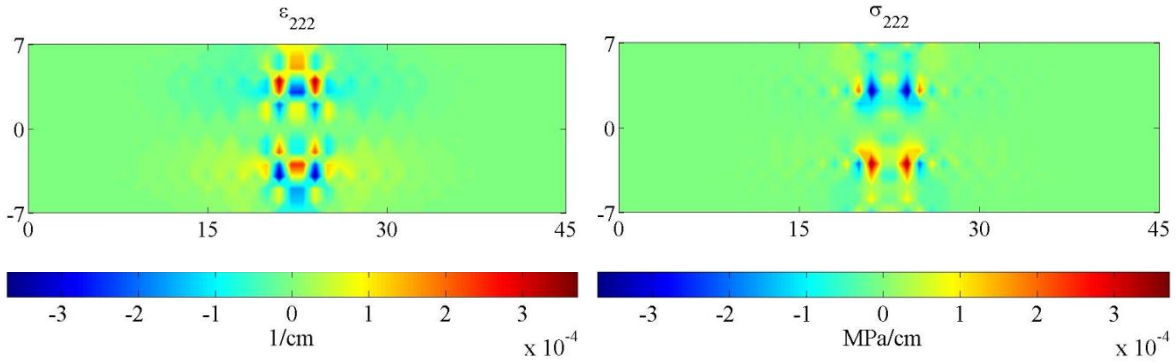

Figure 5.46: Case Three – ε_{222} and σ_{222} for Δu= 0.0139 cm.

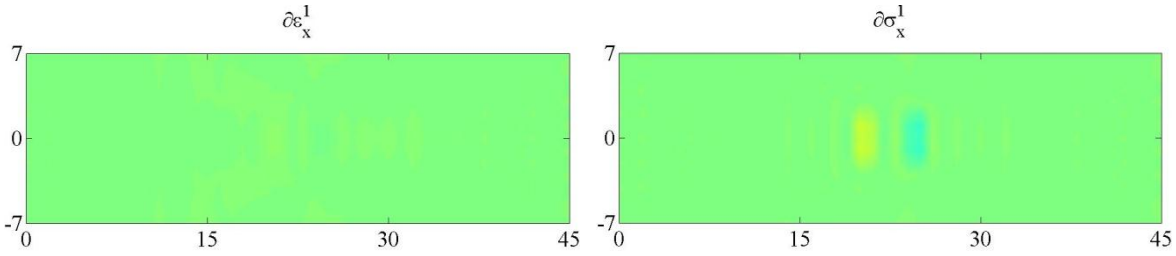

a)

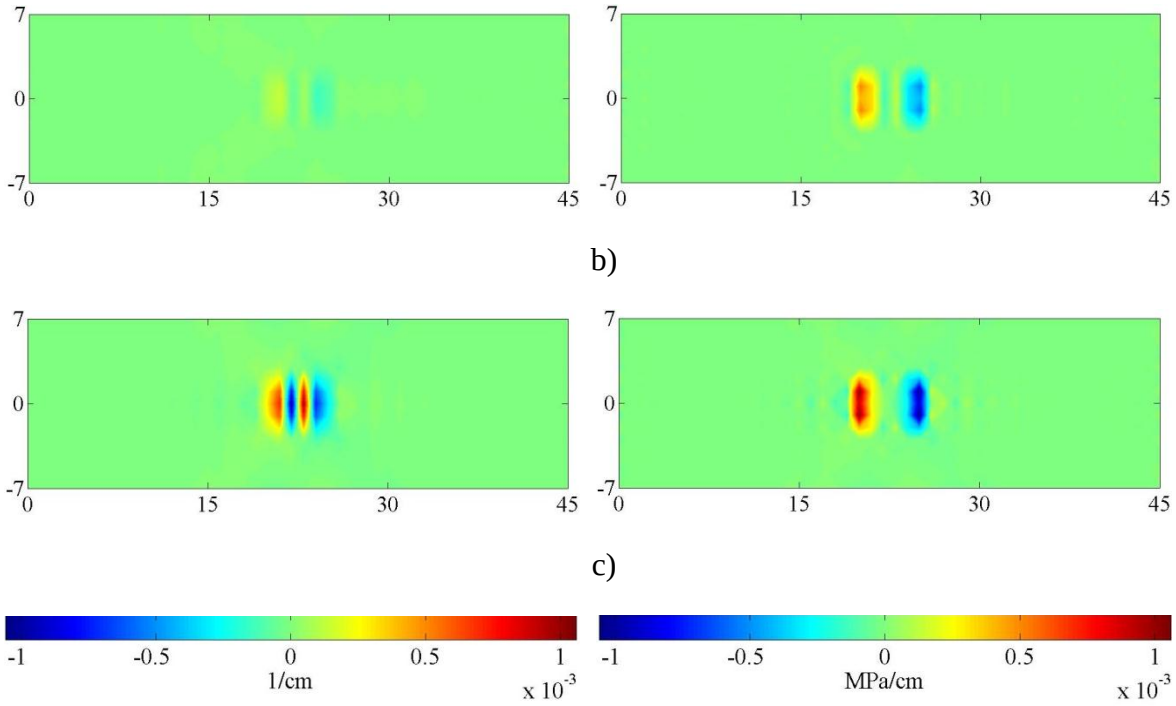

Figure 5.47: Case Three –Effective gradient strains and double stresses in the 1-direction for Δu= a) 0.0027cm, b) 0.0088 cm, and c) 0.0135 cm.

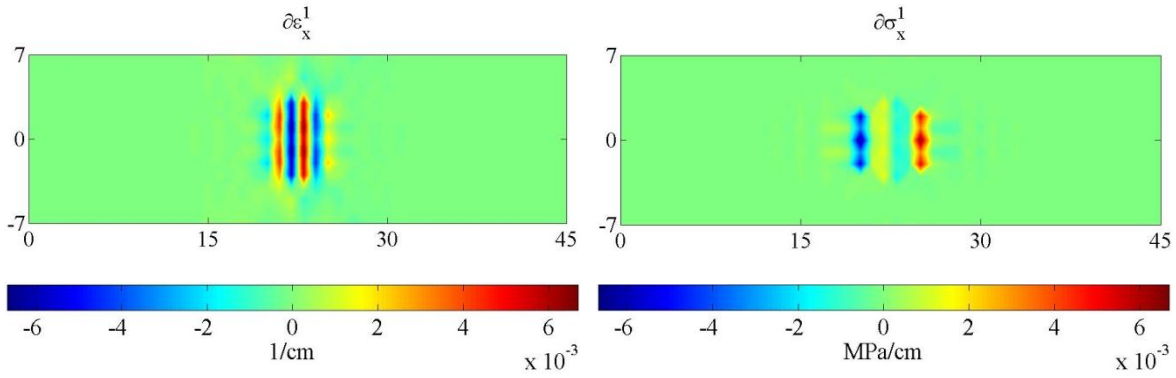

Figure 5.48: Case Three –Effective gradient strains and double stresses in the 1-direction for Δu= 0.0139 cm.

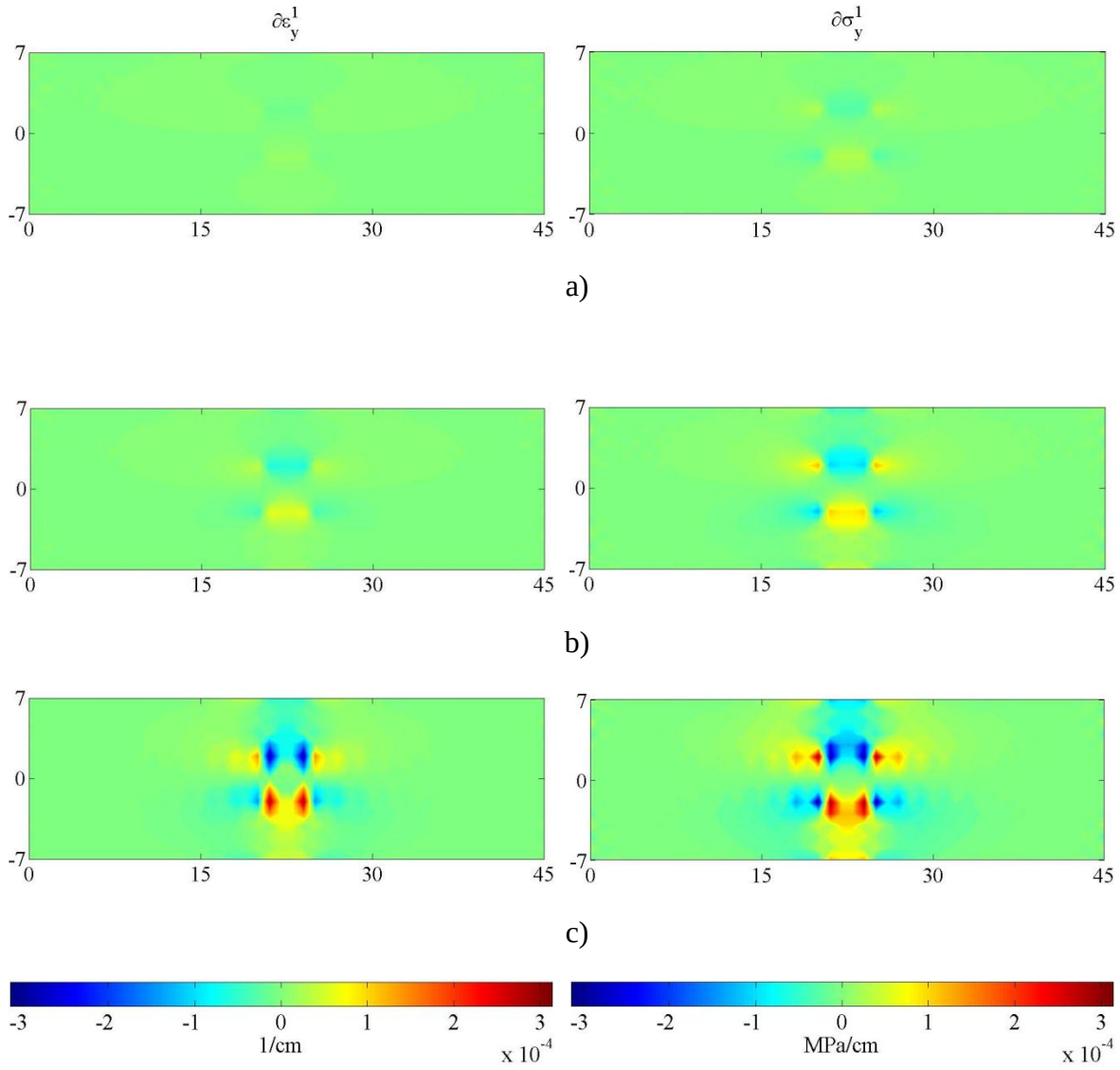

Figure 5.49: Case Three –Effective gradient strains and double stresses in the 2-direction for Δu= a) 0.0027cm, b) 0.0088 cm, and c) 0.0135 cm.

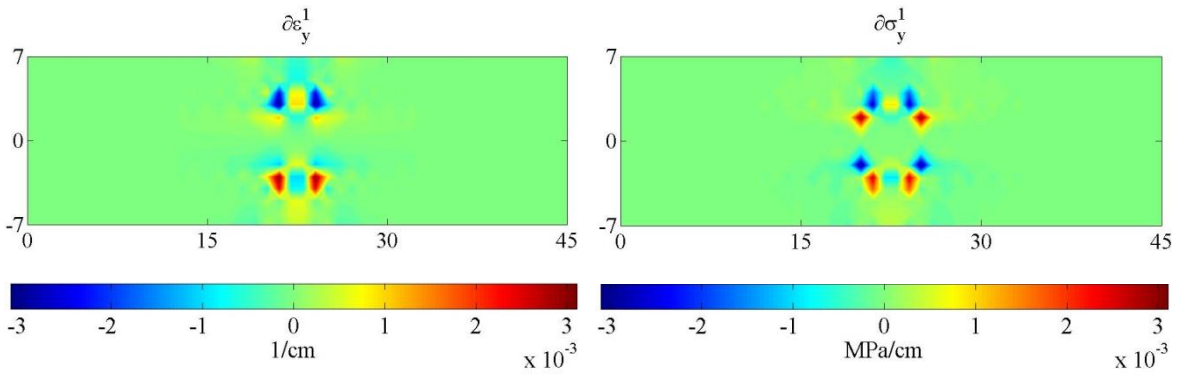

Figure 5.50: Case Three –Effective gradient strains and double stresses in the 2-direction for Δu= 0.0139 cm.

5.4.4. Case Four: Tensile loading with square inclusion and transverse constraints (L_0=1 mm).

In this simulation, the 2D plate is subjected to tension by applying stretch displacements along its right side. In addition, the plate has a centered square inclusion that is forty percent softer than the plate material and it is modeled with a particle size of L_0=1 mm. The length and height of the plate and the inclusion are 45 cm×14 cm and 4 cm×4 cm, respectively. The plate is constrained in the 1-direction along its left border while the top and bottom are constrained from vertical translation (See Figure 5.7).

The response of the structure is shown in Figures 5.51-5.53 at four loading stages: initial, pre-peak, peak, and post-peak stage. Figure 5.51 shows the overall stress-strain response in the '11' and '22' directions. Figures 5.52-5.54 show the strain and stress responses in the '11', '22', and '12' directions, and their effective magnitudes are shown in Figure 5.55. Strain gradient and double stress responses are shown in Figures 5.56-5.57, and their effective magnitudes are described in Figures 5.58-5.59.

The overall stress-strain response of the plate in the '11' and '22' directions is described in Figure 5.51 and shows a biaxial stress state with a non-linear softening behavior. Failure of the structure is described past the peak-load with a reduction in the stress response values.

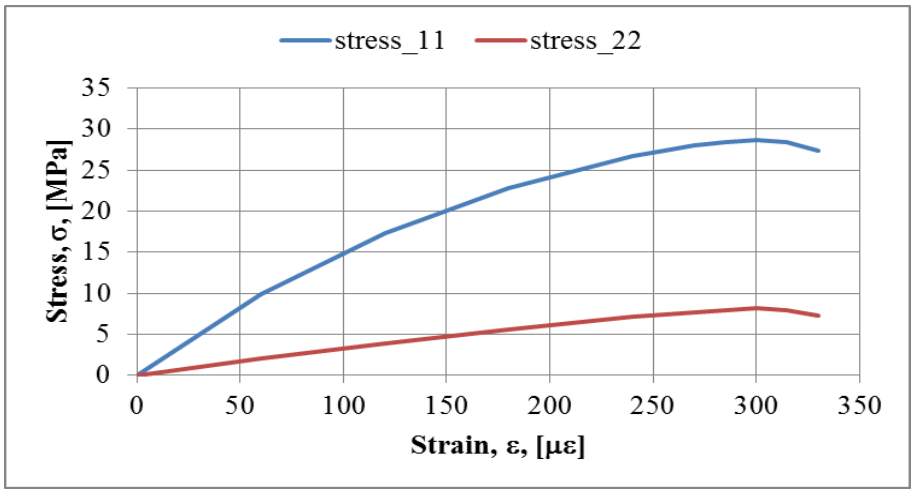

Figure 5.51: Case Four – Overall stress-strain behavior of the plate.

Figure 5.52 describes the strain and stress response of the structure in the '11' direction at the four loading stages afore mentioned. Stress response shows overall uniform stress distribution with stress concentrations at the top and bottom of the inclusion and with lower magnitudes inside the inclusion. Reduction on stress magnitude is observed after the peak-load is reached indicating failure of the structure. Strain response show higher strains within the inclusion and strain concentrations at the peak and post-peak stage. At the latter stage, these concentrations become more severe suggesting the presence of large vertical fractures normal to the load and smaller ones parallel to the load.

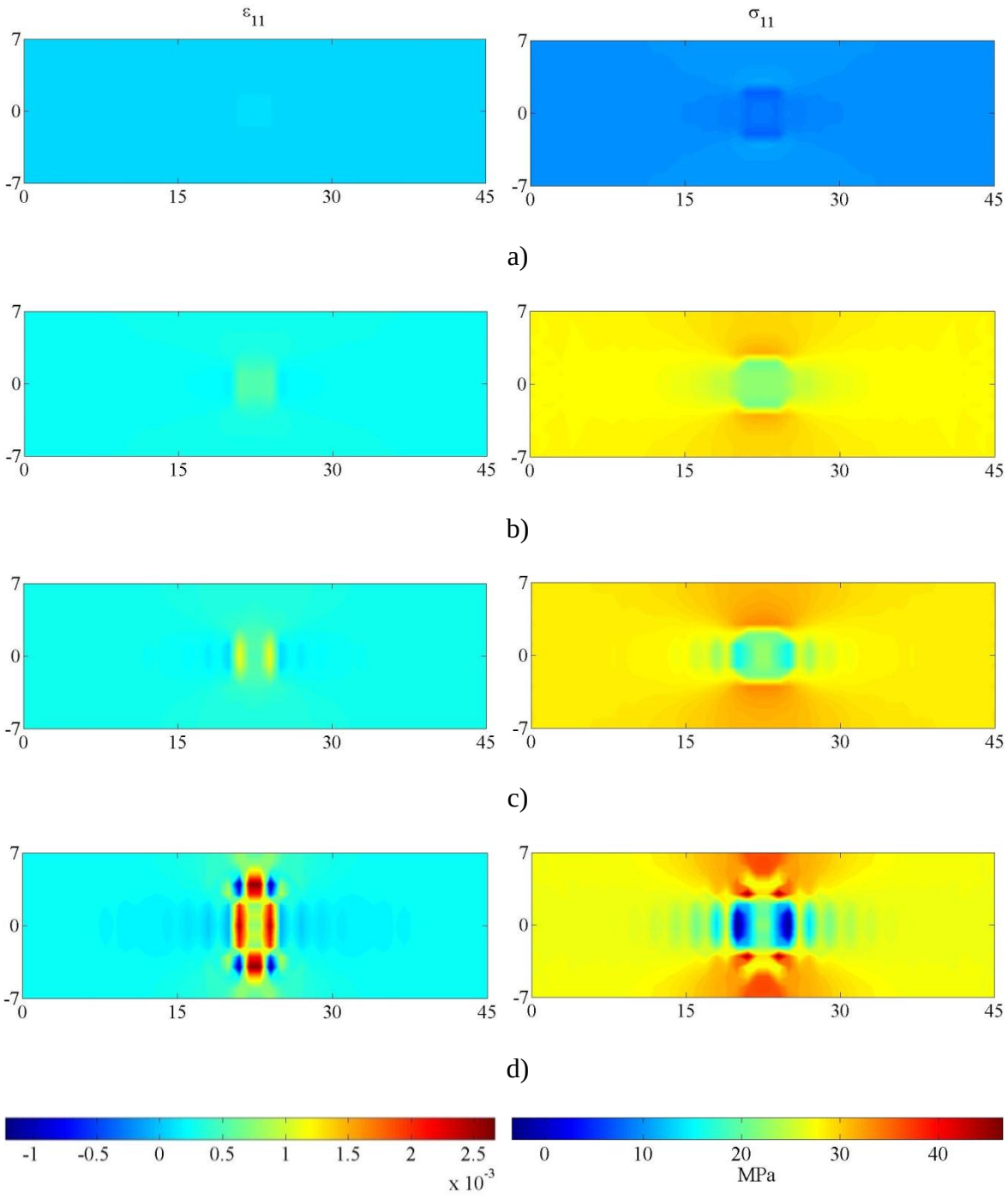

Figure 5.52: Case Four – ε_{11} and σ_{11} for Δu= a) 0.0027cm, b) 0.0122 cm, c) 0.0135 cm, and d) 0.0149 cm.

Figure 5.53 describes the strain and stress response of the structure in the ‘22’ direction at the four loading stages afore mentioned. Stress response shows uniform stress distribution at the initial stage followed by stress concentrations around the sides of the inclusion. Reduction on stress magnitude is observed after the peak-load is reached indicating failure of the. Strain response show tensile strain concentrations at the post-peak stage located at the corners and center of the inclusion.

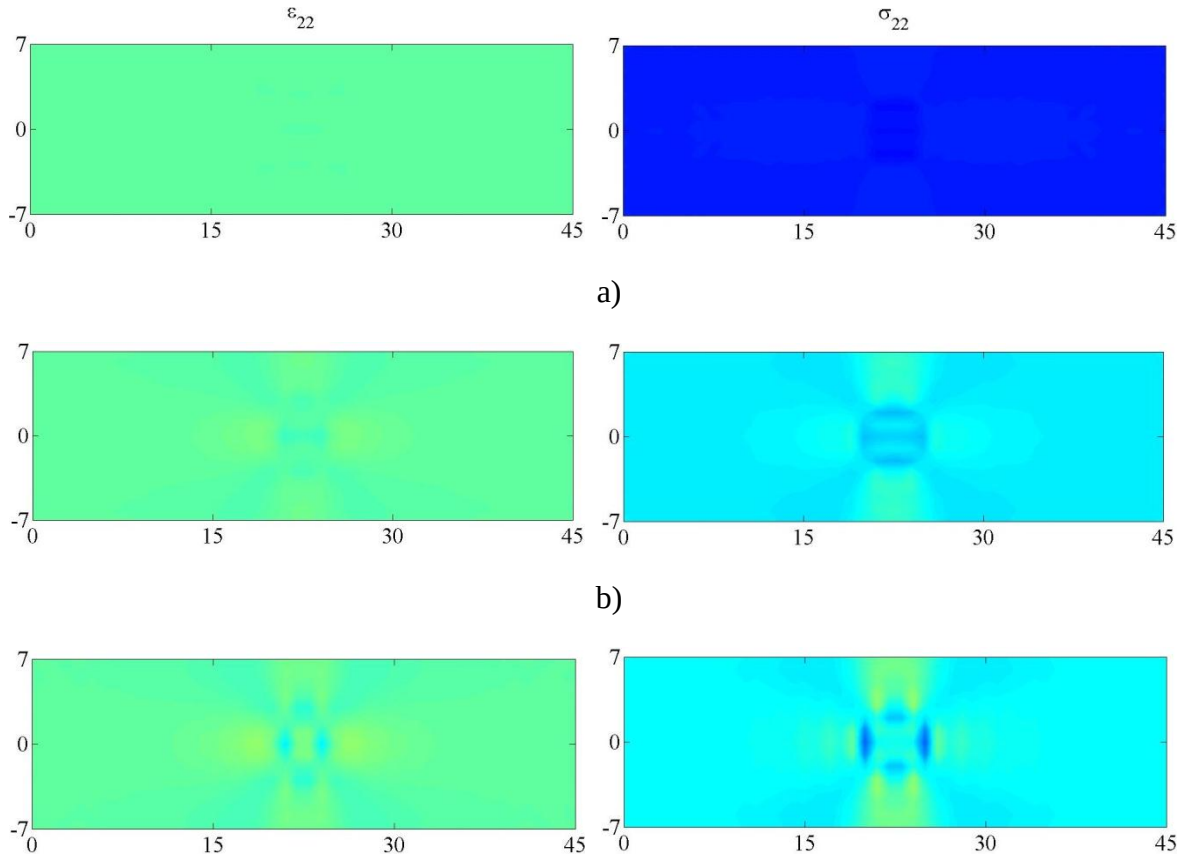

a)

b)

c)

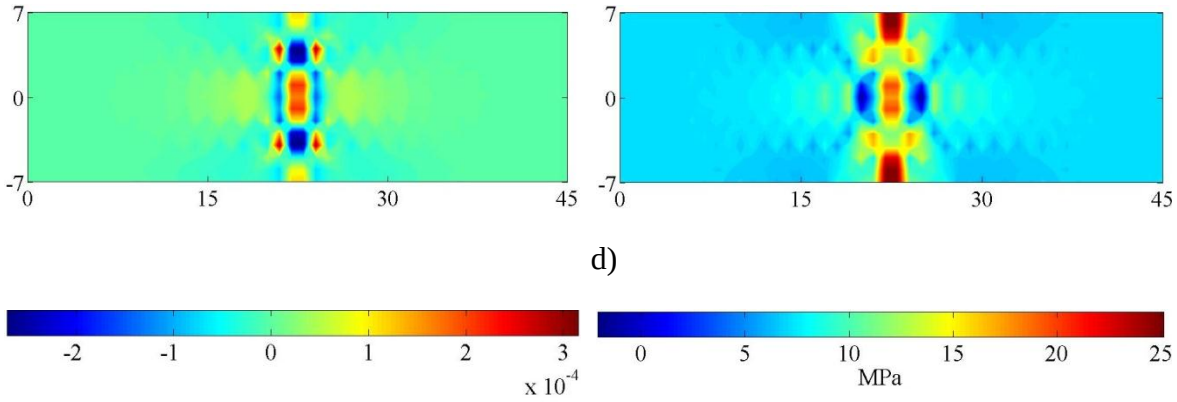

Figure 5.53: Case Four – ε_{22} and σ_{22} for Δu= a) 0.0027cm, b) 0.0122 cm, c) 0.0135 cm, and d) 0.0149 cm.

Figure 5.54 describes the stress and strain response of the structure in the '12' direction at the four loading stages afore mentioned. Strain and stress response show concentrations at the corners of the inclusion that becomes more severe as the load increases.

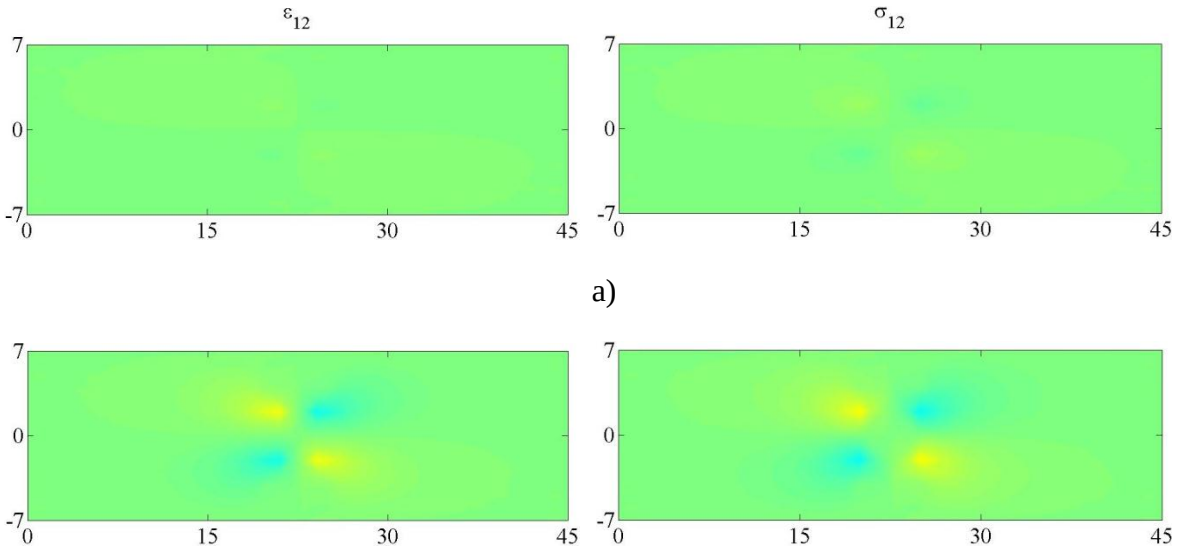

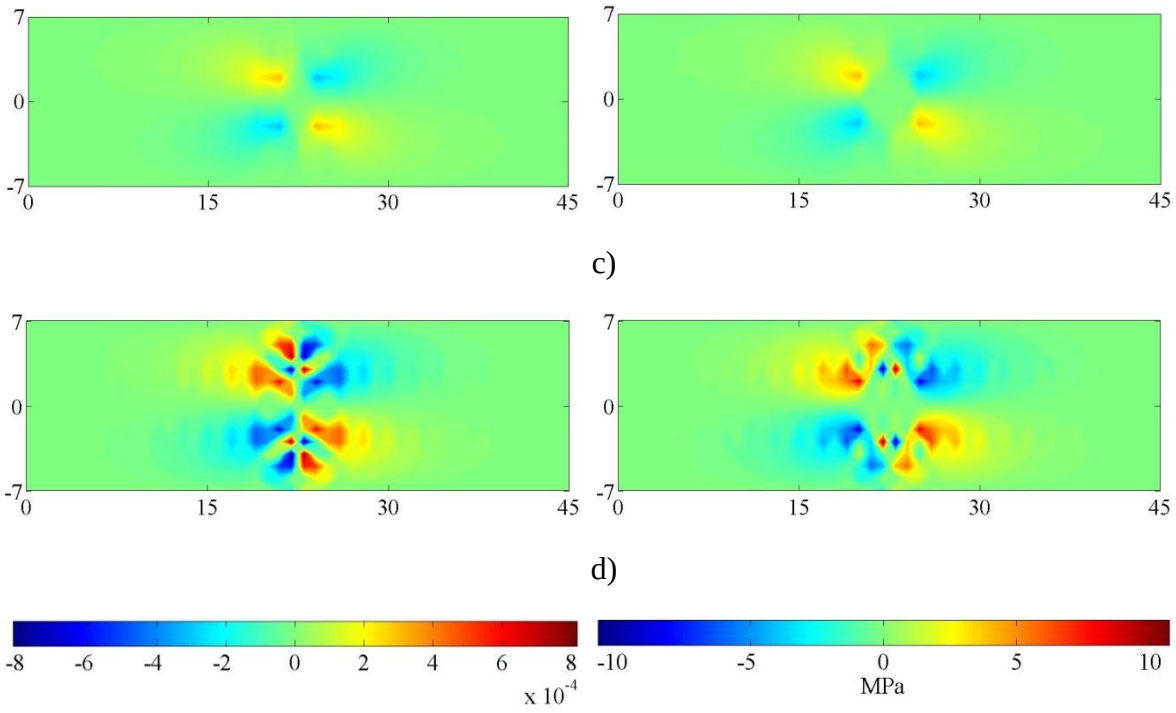

Figure 5.54: Case Four – ε_{12} and σ_{12} for Δu= a) 0.0027cm, b) 0.0122 cm, c) 0.0135 cm, and d) 0.0149 cm.

Figure 5.55 describes the effective strain and stress response within the structure at the four loading stages afore mentioned. Stress response shows overall uniform stress distribution with stress concentrations around the top and bottom of the inclusion and with lower stresses within the inclusion. Reduction on stress magnitude is observed after the peak-load is reached indicating failure of the structure. Strain response show higher strains within the inclusion and strain concentrations at the peak and post-peak stage. At the latter stage, these concentrations become more severe suggesting the presence of fractures around the inclusion that are normal to the load and parallel to the load, being the latter ones smaller.

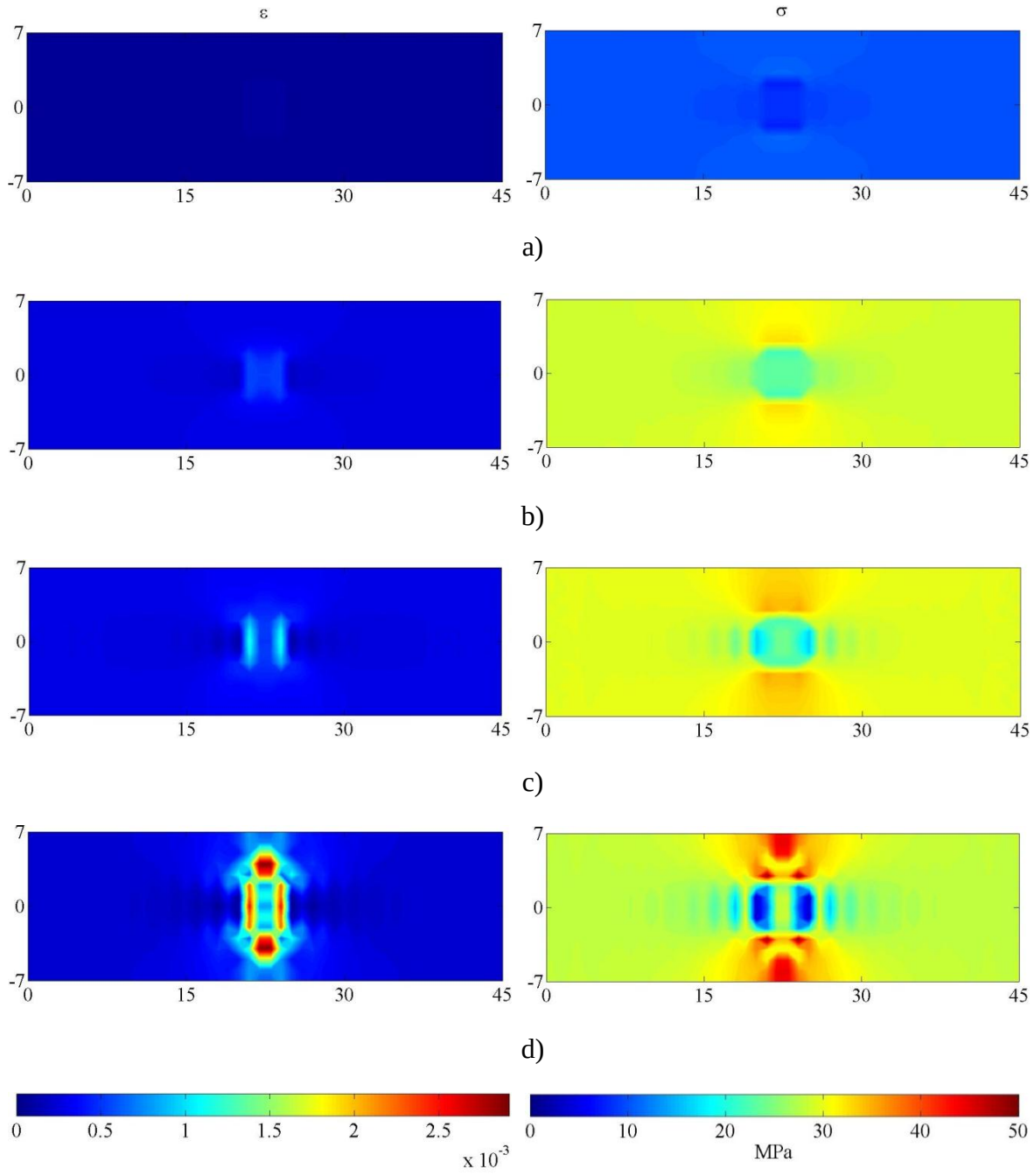

Figure 5.55: Case Four – ε and σ for Δu= a) 0.0027cm, b) 0.0122 cm, c) 0.0135 cm, and d) 0.0149 cm.

Figures 5.56-5.59 describe the gradient strain –double stress response of the structure at the four loading stages afore mentioned. Strain gradient results describe, at the peak and post-peak

stage, high tensile and compressive concentrations that are located beside each other suggesting the presence of fractures around the inclusion that are normal to the load (larger size) and parallel to the load (smaller size).

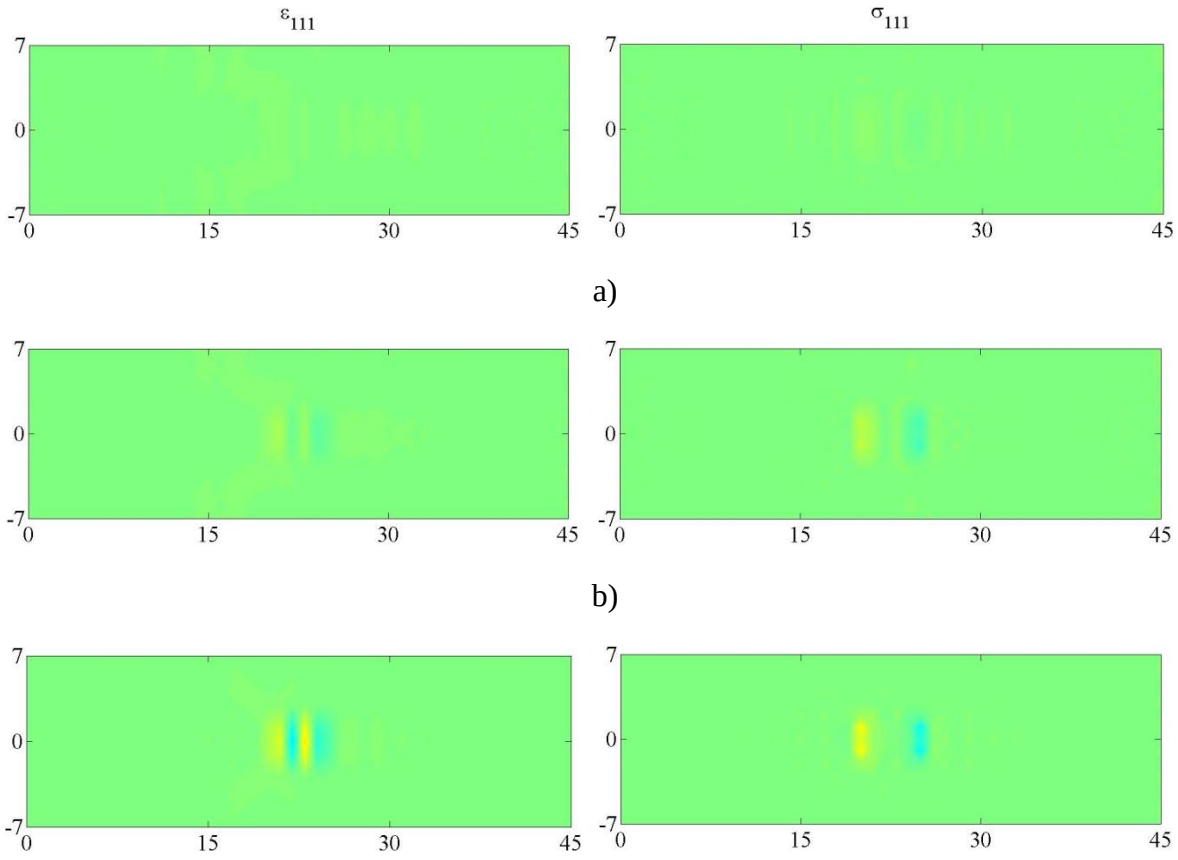

a)

b)

c)

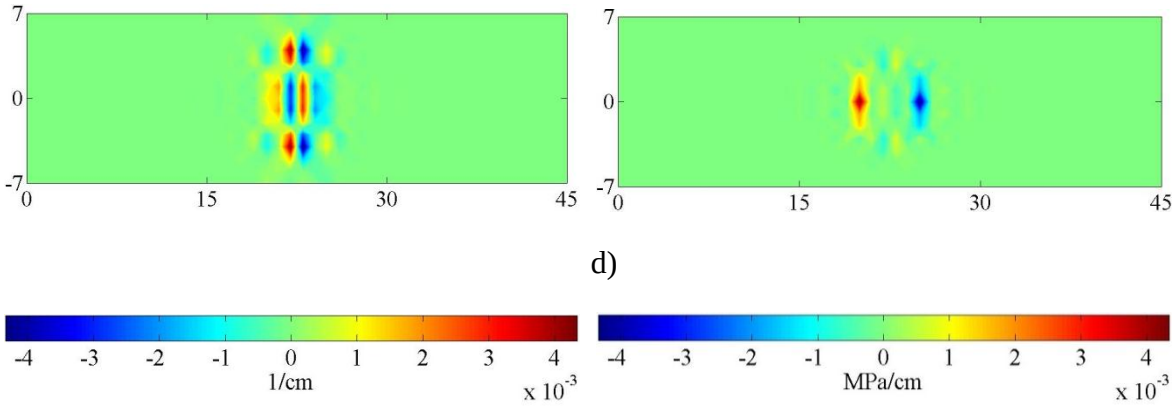

d)

Figure 5.56: Case Four – ε_{111} and σ_{111} for Δu= a) 0.0027cm, b) 0.0122 cm, c) 0.0135 cm, and d) 0.0149 cm.

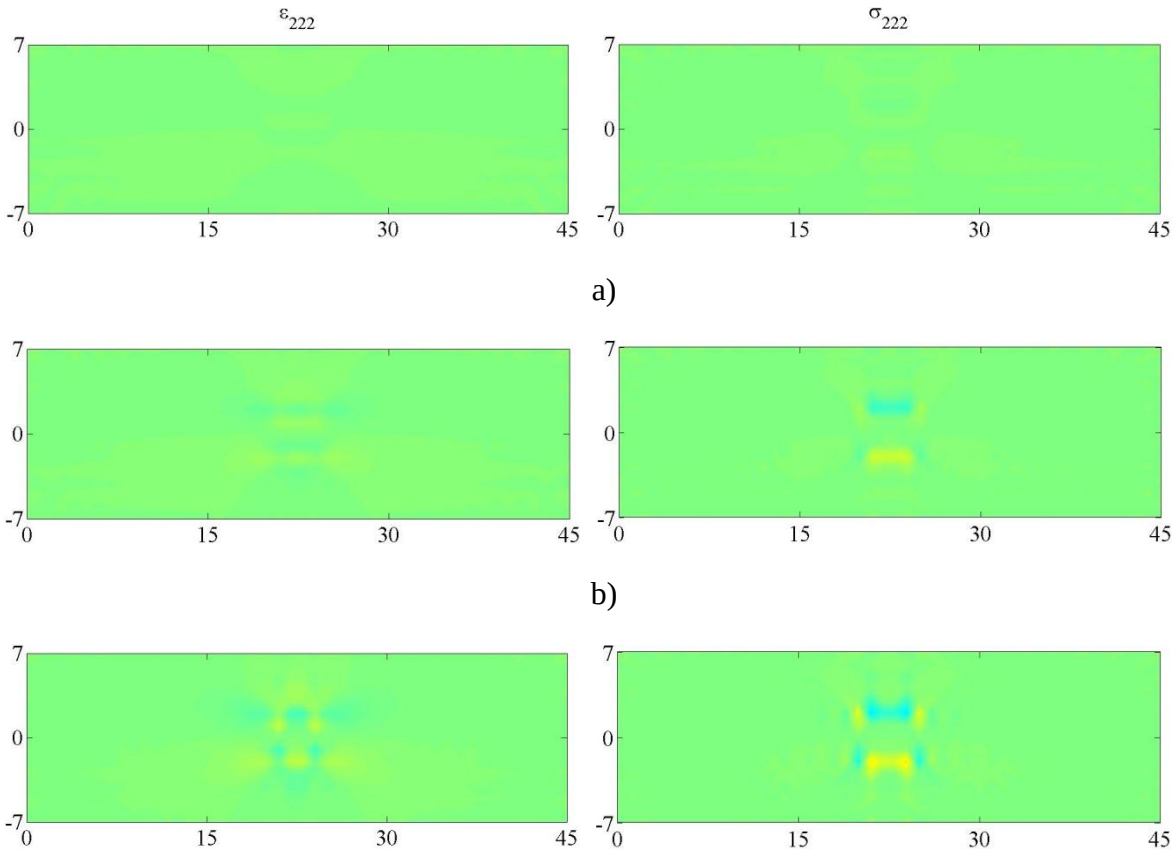

a)

b)

c)

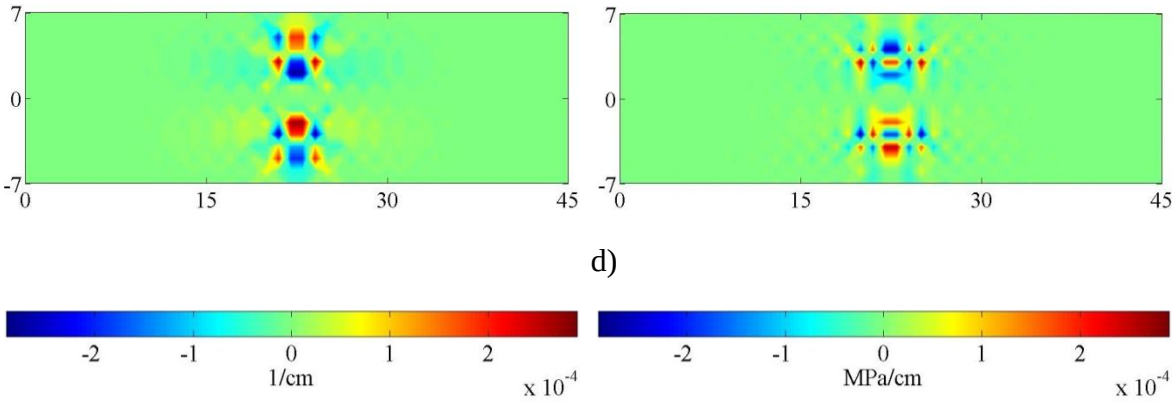

d)

Figure 5.57: Case Four – ε_{222} and σ_{222} for Δu= a) 0.0027cm, b) 0.0122 cm, c) 0.0135 cm, and d) 0.0149 cm.

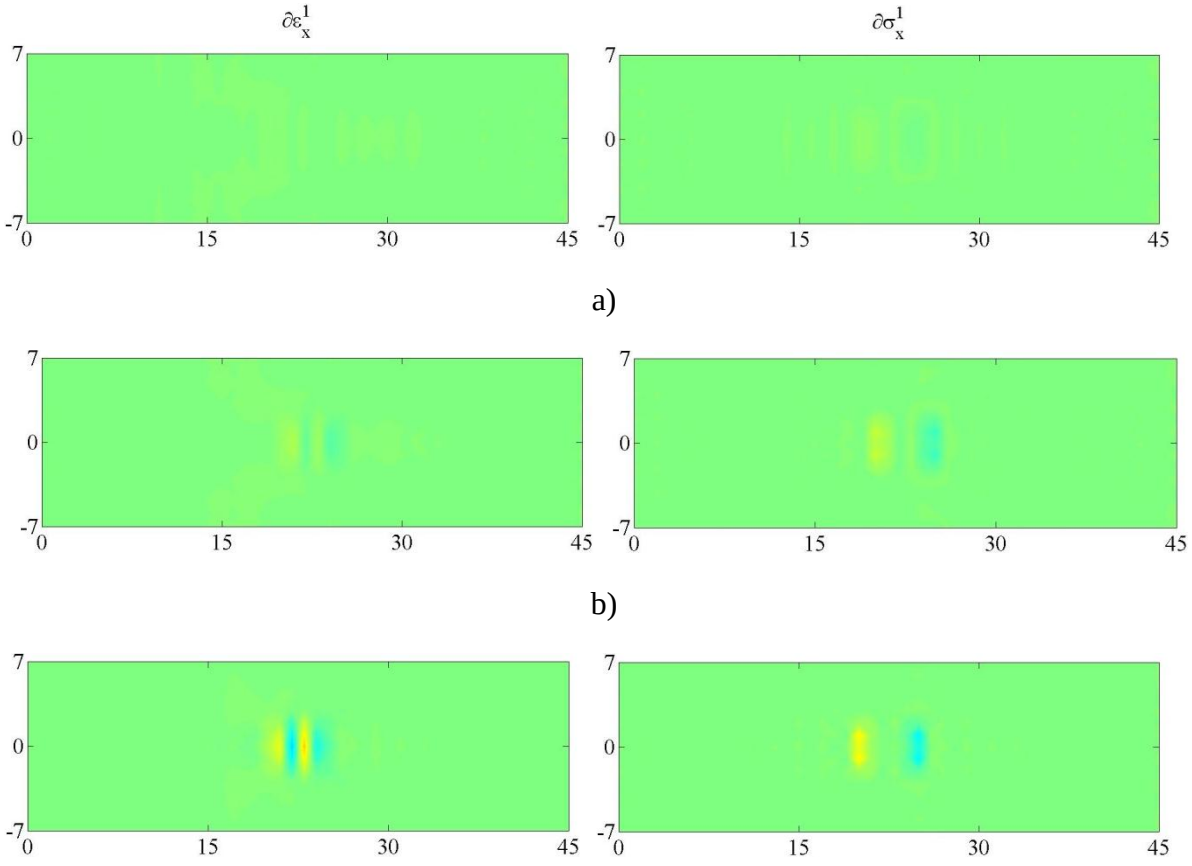

a)

b)

c)

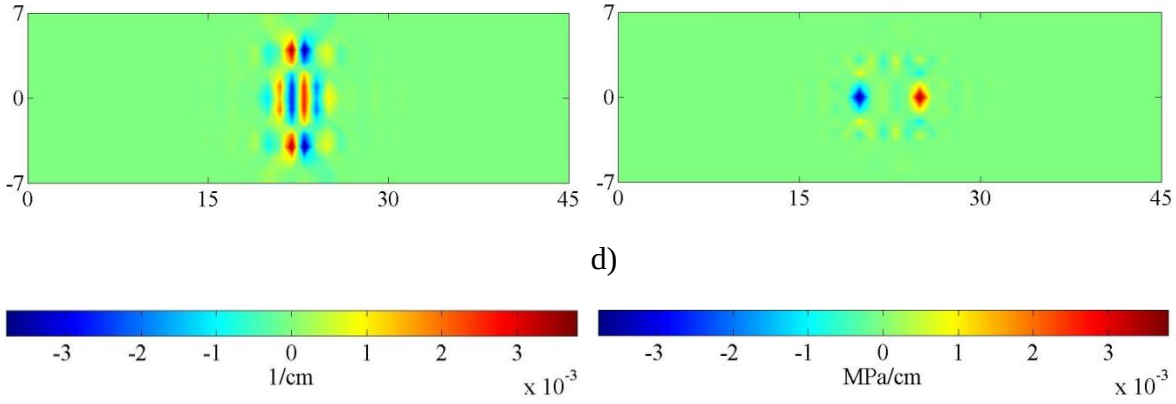

d)

Figure 5.58: Case Four –Effective gradient strains and double stresses in the 1-direction for Δu= a) 0.0027cm, b) 0.0122 cm, c) 0.0135 cm, and d) 0.0149 cm.

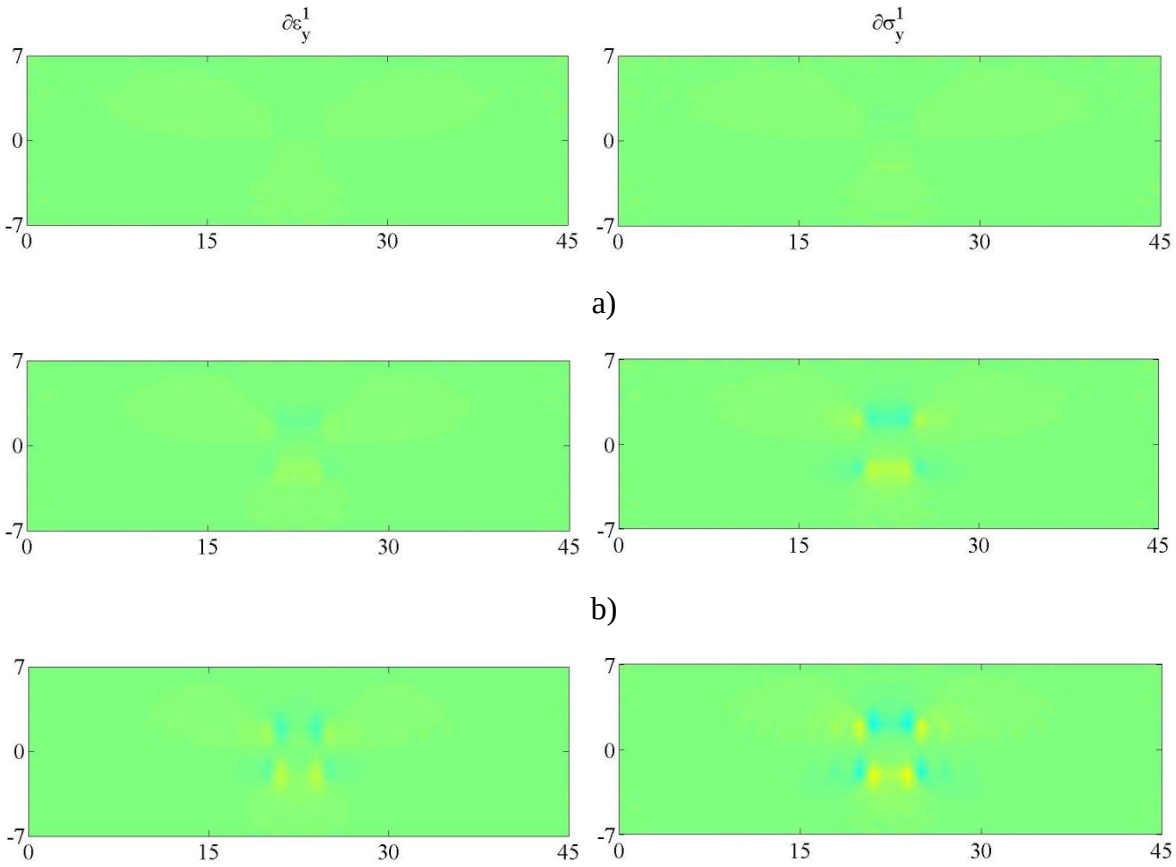

a)

b)

c)

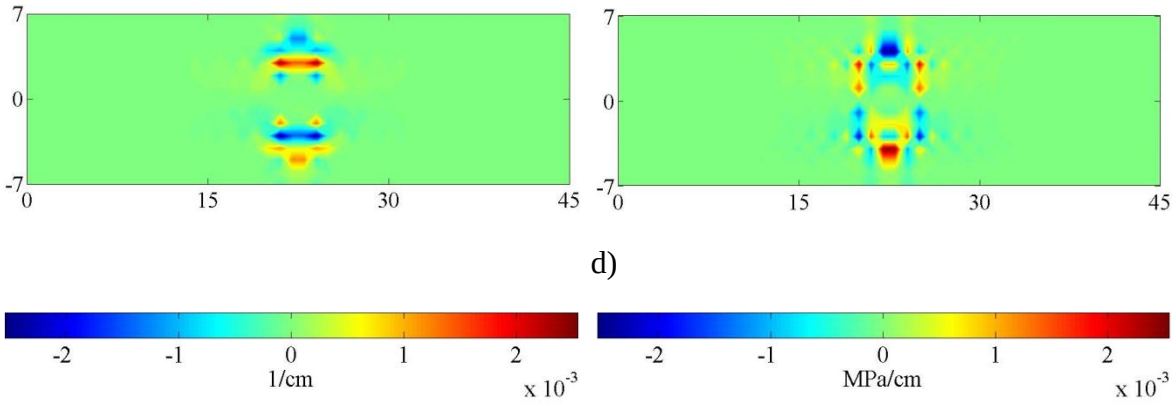

Figure 5.59: Case Four –Effective gradient strains and double stresses in the 2-direction for Δu= a) 0.0027cm, b) 0.0122 cm, c) 0.0135 cm, and d) 0.0149 cm.

5.4.5. Case Five: Tensile loading with square inclusion and no constraints (L_0=10 mm).

In this simulation, the 2D plate is subjected to tension by applying stretch displacements along its right side. In addition, the plate has a centered square inclusion that is forty percent softer than the plate material and it is modeled with a particle size of L_0=10 mm. The length and height of the plate and the inclusion are 45 cm×14 cm and 4 cm×4 cm, respectively. The plate is constrained in the 1-direction along its left border while the top and bottom have no constraints (See Figure 5.6).

The response of the structure is shown in Figures 5.60-5.68 at four loading stages: initial, pre-peak, peak, and post-peak stage. Figure 5.60 shows the overall stress-strain response in the '11' and '22' directions. Figures 5.61-5.63 show the strain and stress responses in the '11', '22', and '12' directions, and their effective magnitudes are shown in Figure 5.64. Strain gradient and double stress responses are shown in Figures 5.65-5.66, and their effective magnitudes are described in Figures 5.67-5.68.

The overall stress-strain response of the plate in the '11' and '22' directions is described in Figure 5.60 and shows a uniaxial stress state with a non-linear softening behavior. Failure of the structure is described past the peak-load with a drop in the stress response.

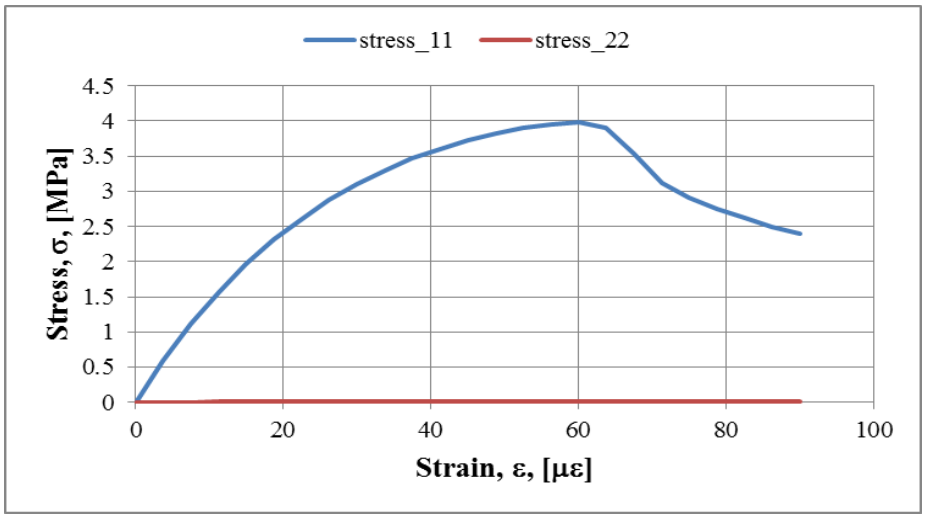

Figure 5.60: Case Five – Overall stress-strain behavior of the plate.

Figure 5.61 describes the strain and stress response of the structure in the '11' direction at the four loading stages afore mentioned. Stress response shows overall uniform stress distribution with stress concentrations at the top and bottom of the inclusion and smaller stresses within the inclusion. Reduction on stress magnitude is observed after the peak-load is reached indicating failure of the structure. Strain response shows higher strains within the inclusion and strain concentrations at the peak and post-peak stage. At the latter stage, these concentrations become more severe suggesting the presence of two vertical fractures along the sides of the inclusion that are normal to the load; these fractures expand throughout the height of the plate.

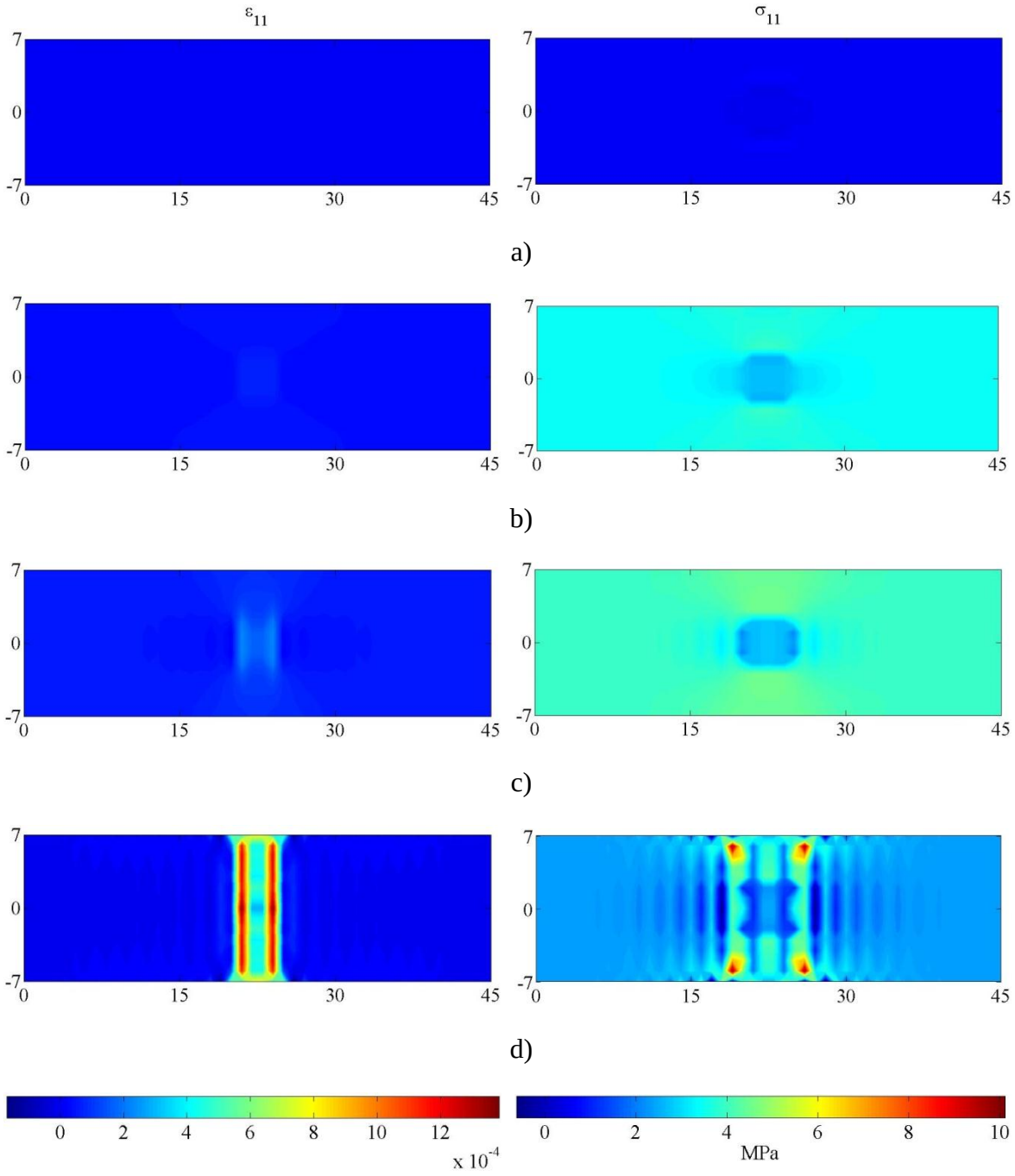

Figure 5.61: Case Five – ε_{11} and σ_{11} for Δu= a) 0.0002cm, b) 0.0017 cm, c) 0.0027 cm, and d) 0.0040 cm.

Figure 5.62 describes the strain and stress response of the structure in the '22' direction at the four loading stages afore mentioned. Stress response shows overall uniform zero stress

distribution along the structure with stress tensile concentrations inside the inclusion at the post-peak stage, which expand diagonally from the corners of the inclusion. Strain response show overall contracting strains with tensile strain concentrations within the inclusion at the post-peak stage.

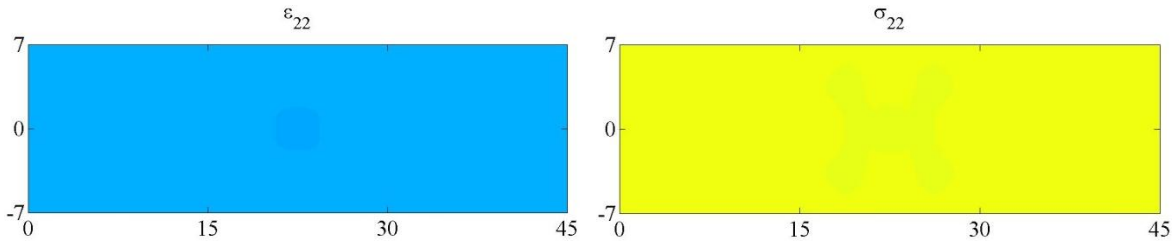

a)

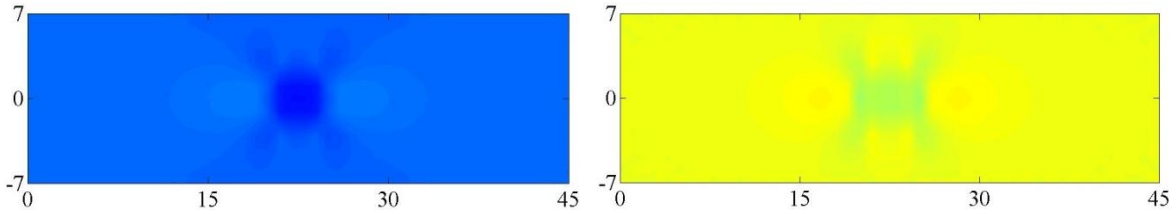

b)

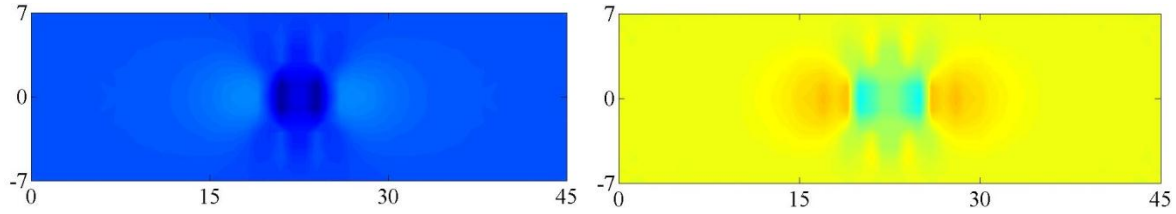

c)

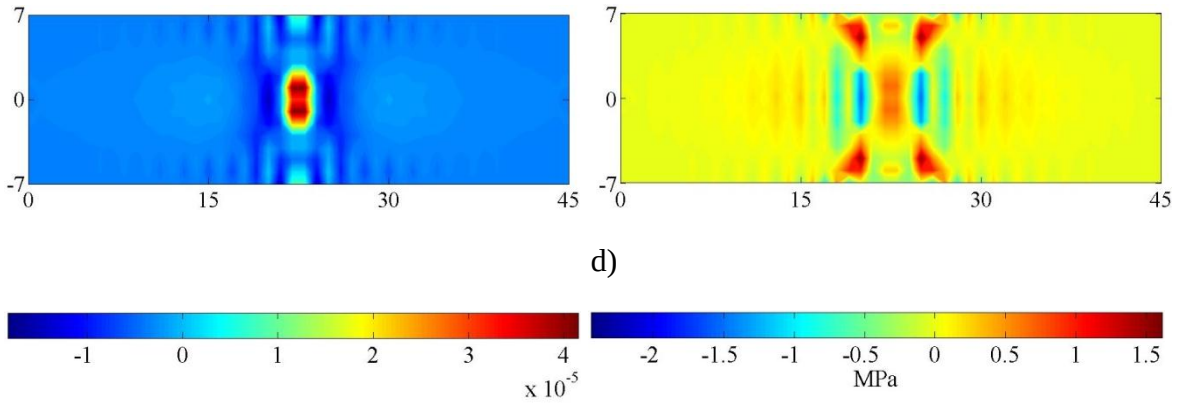

d)

Figure 5.62: Case Five – ε_{22} and σ_{22} for Δu= a) 0.0002cm, b) 0.0017 cm, c) 0.0027 cm, and d) 0.0040 cm.

Figure 5.63 describes the strain and stress response of the structure in the '12' direction at the four loading stages afore mentioned. Strain and stress response show concentrations at the corners of the inclusion that increase and expand as the load increases.

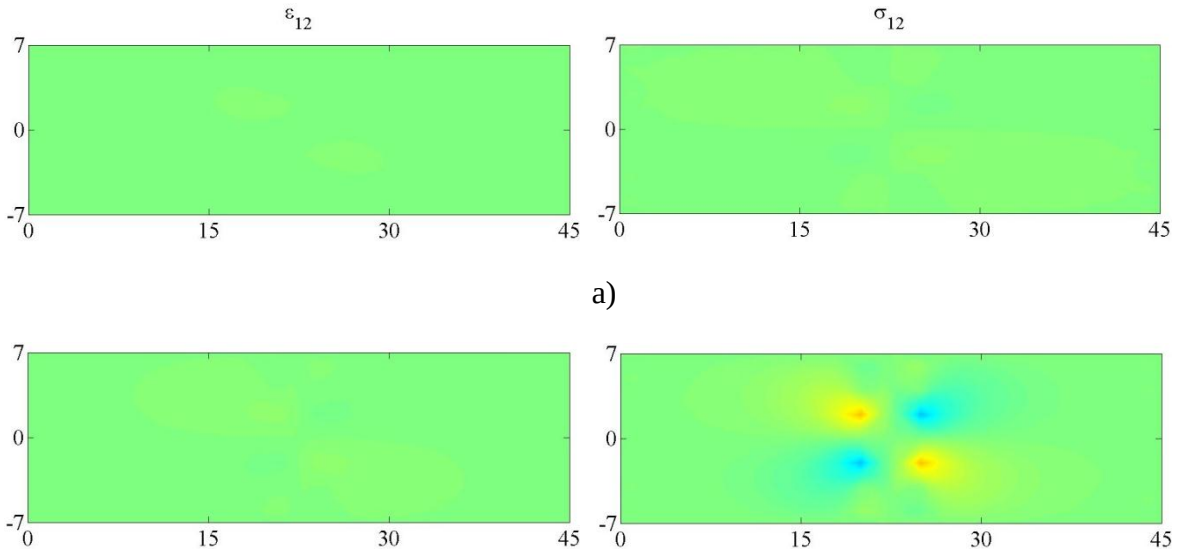

a)

b)

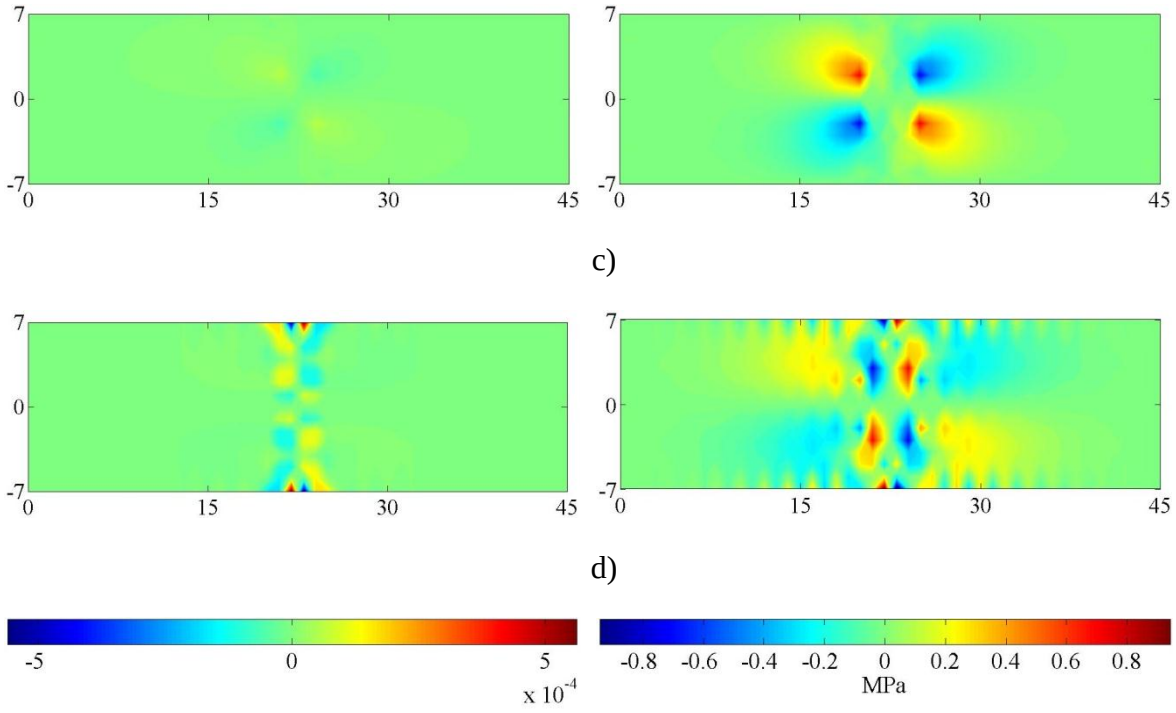

Figure 5.63: Case Five – ε_{12} and σ_{12} for Δu= a) 0.0002cm, b) 0.0017 cm, c) 0.0027 cm, and d) 0.0040 cm.

Figure 5.64 describes the effective strain and stress responses within the structure at the four loading stages afore mentioned. Stress response shows uniform stress distribution with stress concentrations at the top and bottom of the inclusion. Reduction on stress magnitude is observed after the peak-load is reached indicating failure of the structure. Strain response show higher strains within the inclusion and strain concentrations at the peak and post-peak stage. At the latter stage, these concentrations become more severe suggesting the presence of vertical fractures along the sides of the inclusion that expand throughout the height of the plate.

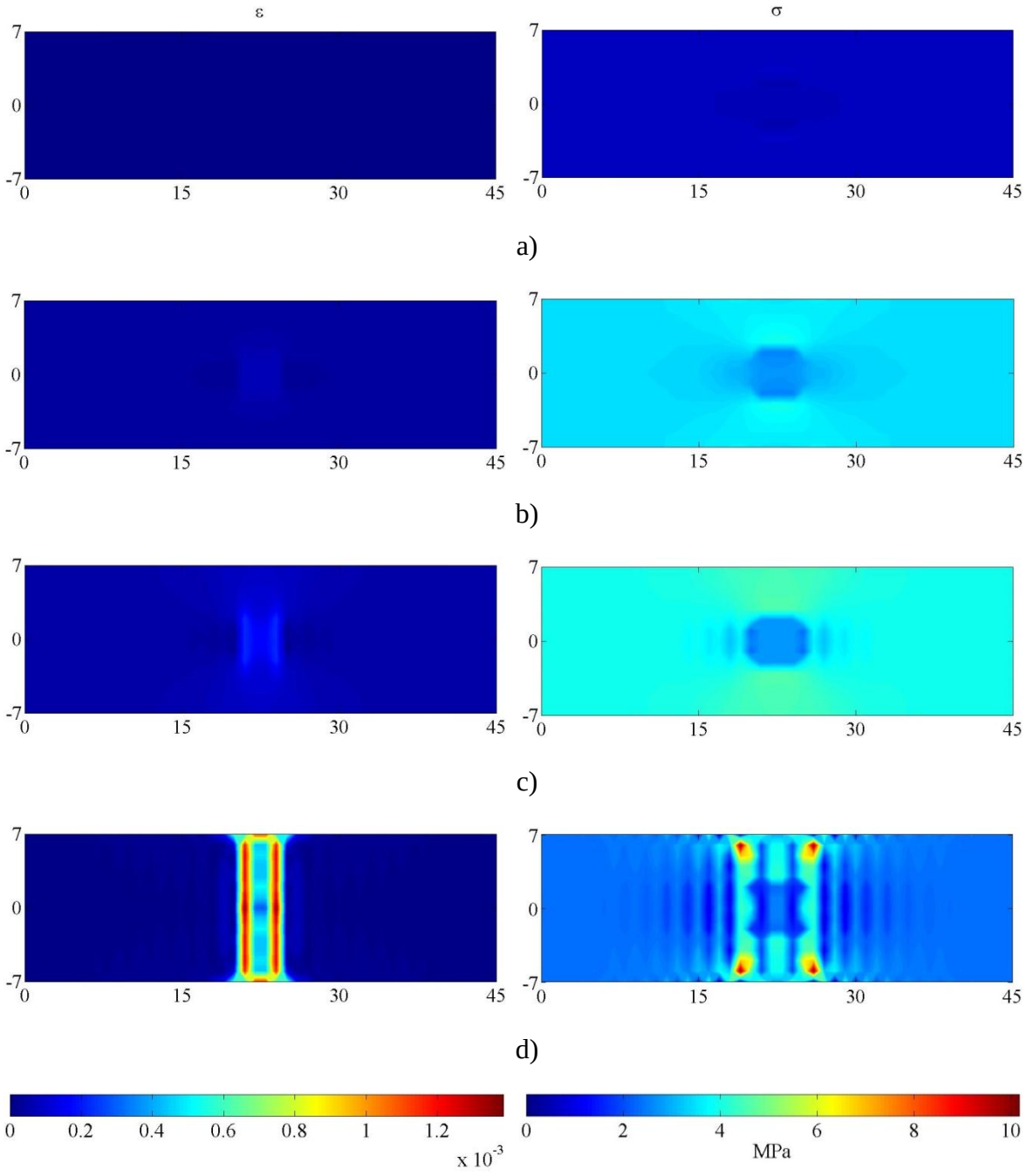

Figure 5.64: Case Five – ε and σ for Δu= a) 0.0002cm, b) 0.0017 cm, c) 0.0027 cm, and d) 0.0040 cm.

Figures 5.65-5.68 describe the gradient strain –double stress responses of the structure at the four loading stages afore mentioned. Strain gradient results describe at the peak and post-peak

stage high tensile and compressive concentrations that are located beside each other suggesting the presence of vertical fractures that are initiated within the inclusion and propagate throughout the height of the plate. These fractures describe the presence of a fracture zone that is normal to the load.

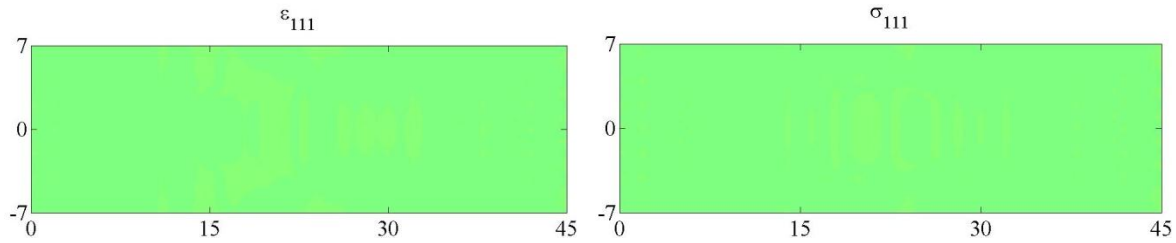

a)

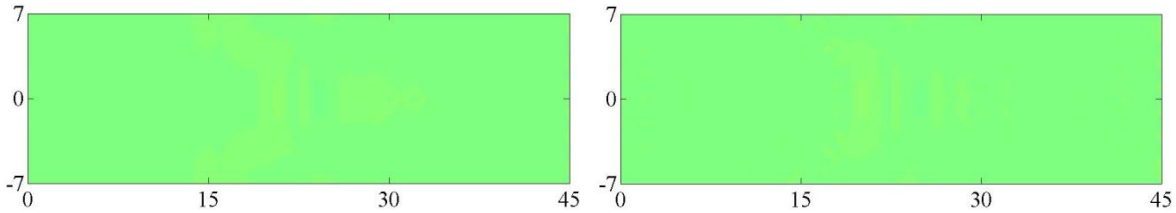

b)

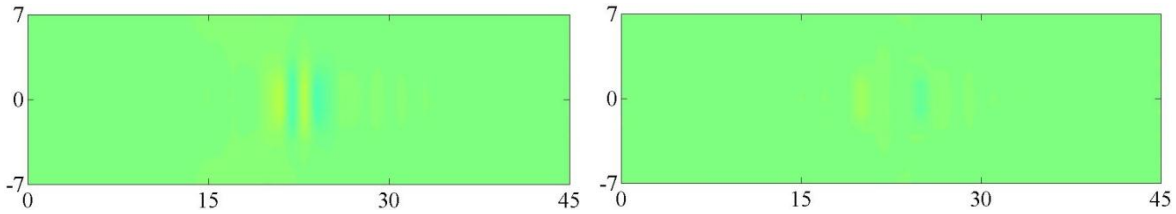

c)

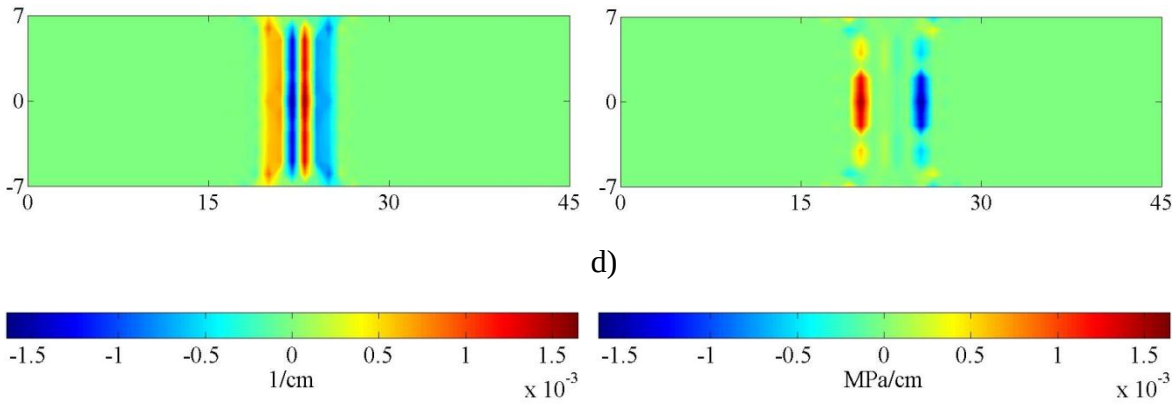

Figure 5.65: Case Five – ε_{111} and σ_{111} for Δu= a) 0.0002cm, b) 0.0017 cm, c) 0.0027 cm, and d) 0.0040 cm.

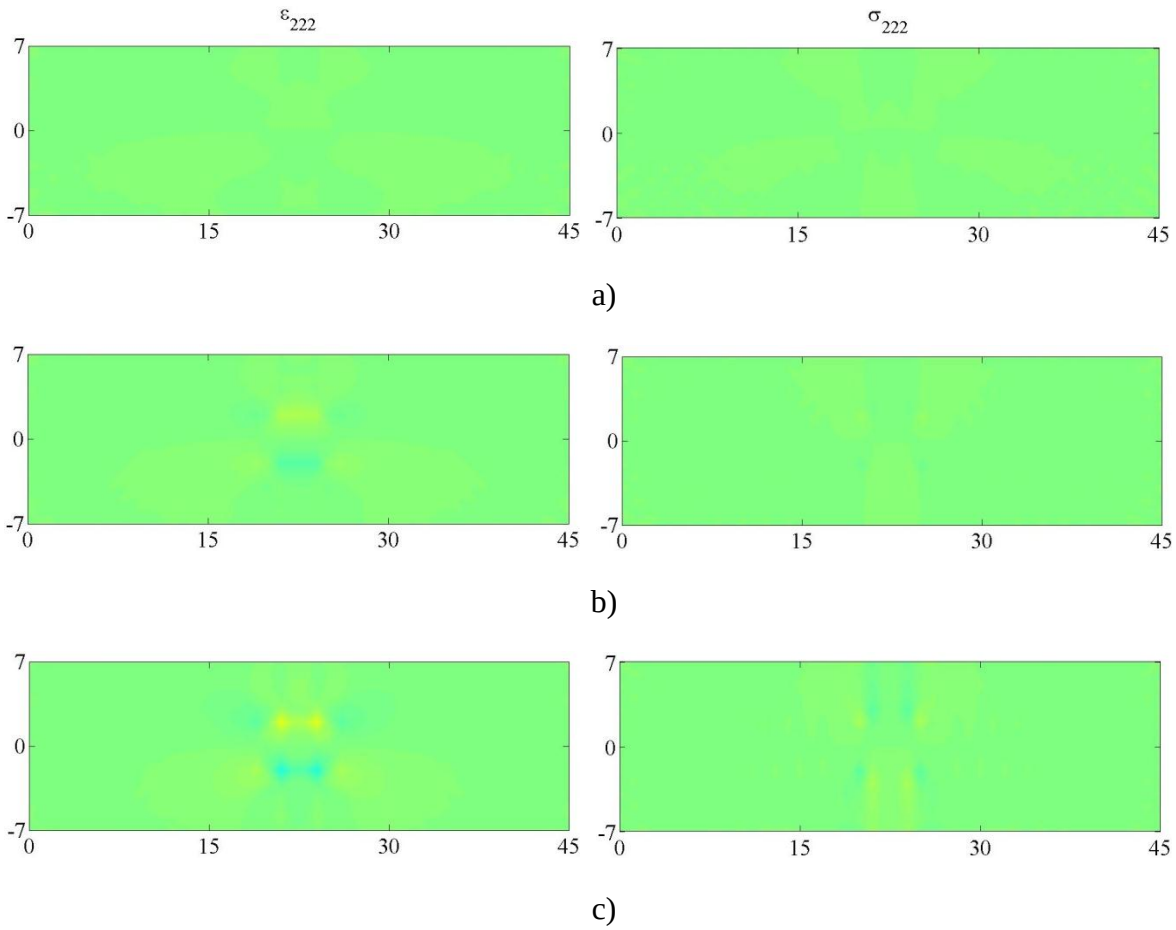

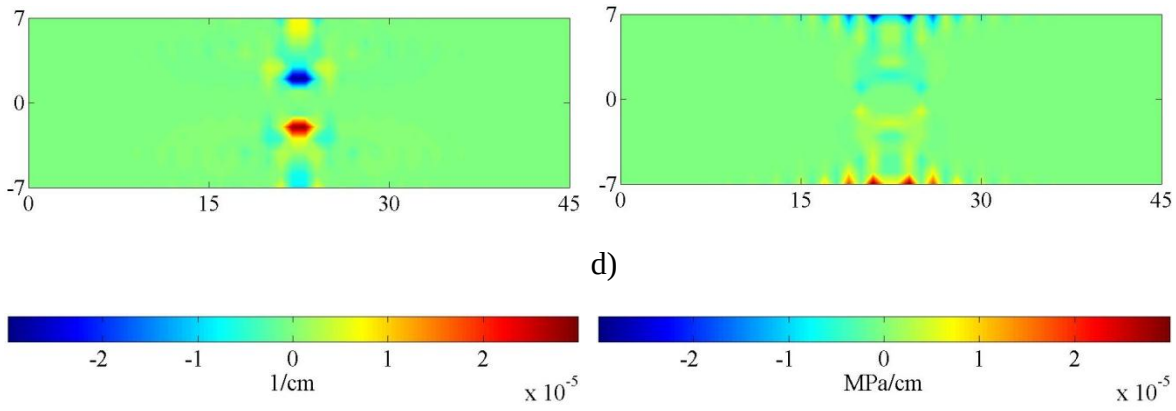

d)

Figure 5.66: Case Five – ε_{222} and σ_{222} for Δu= a) 0.0002cm, b) 0.0017 cm, c) 0.0027 cm, and d) 0.0040 cm.

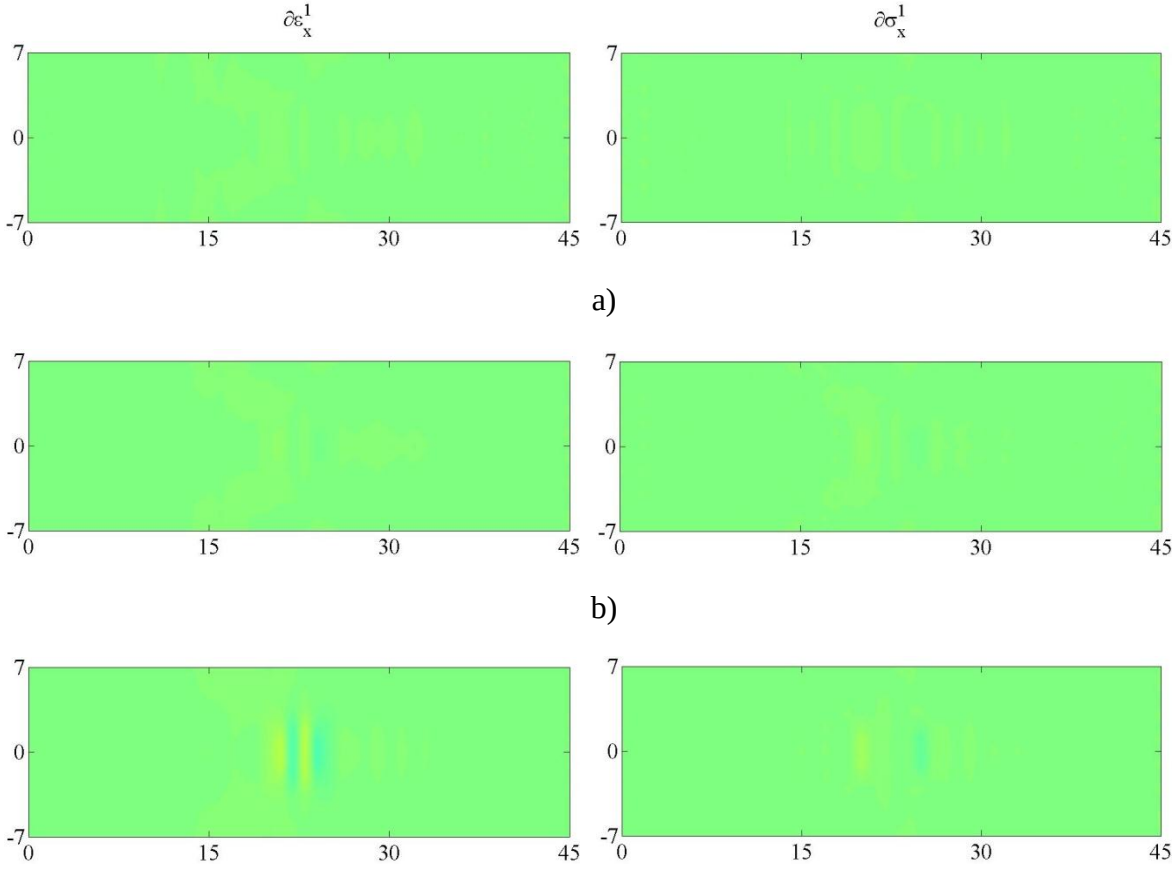

a)

b)

c)

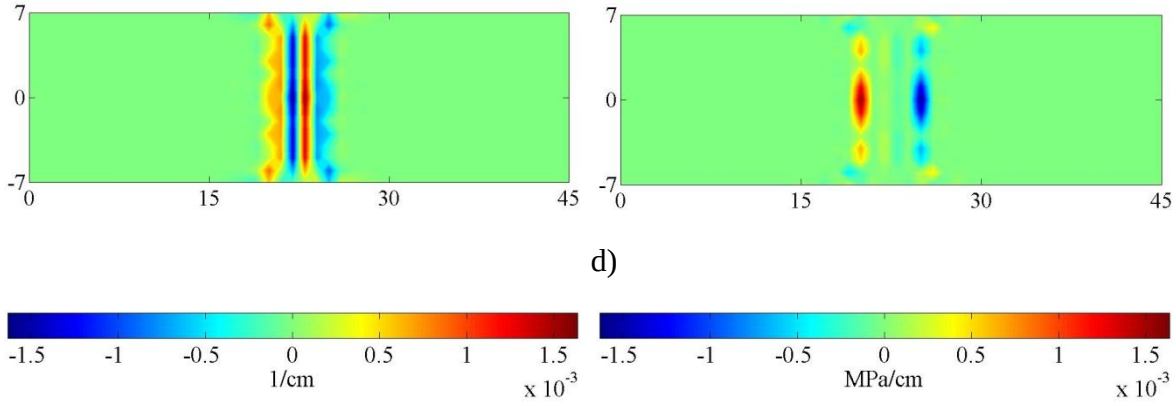

d)

Figure 5.67: Case Five –Effective gradient strains and double stresses in the 1-direction for Δu= a) 0.0002cm, b) 0.0017 cm, c) 0.0027 cm, and d) 0.0040 cm.

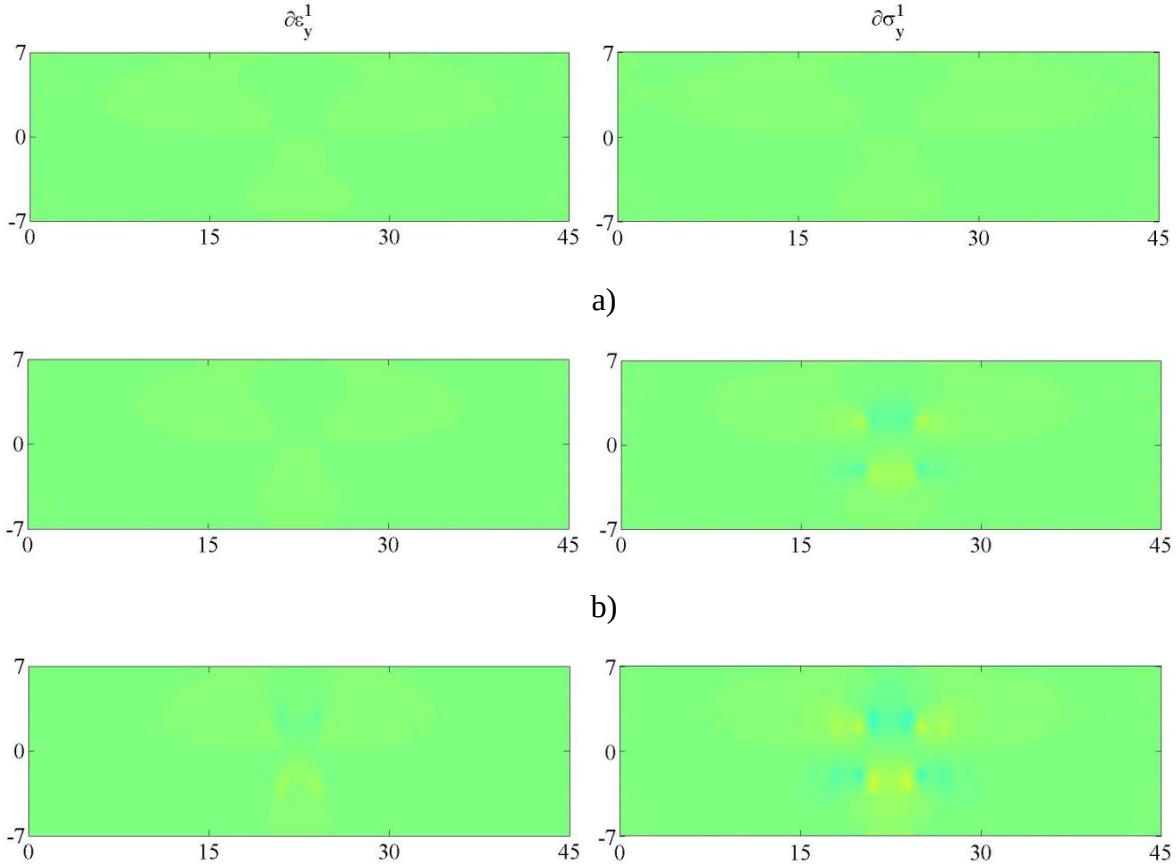

a)

b)

c)

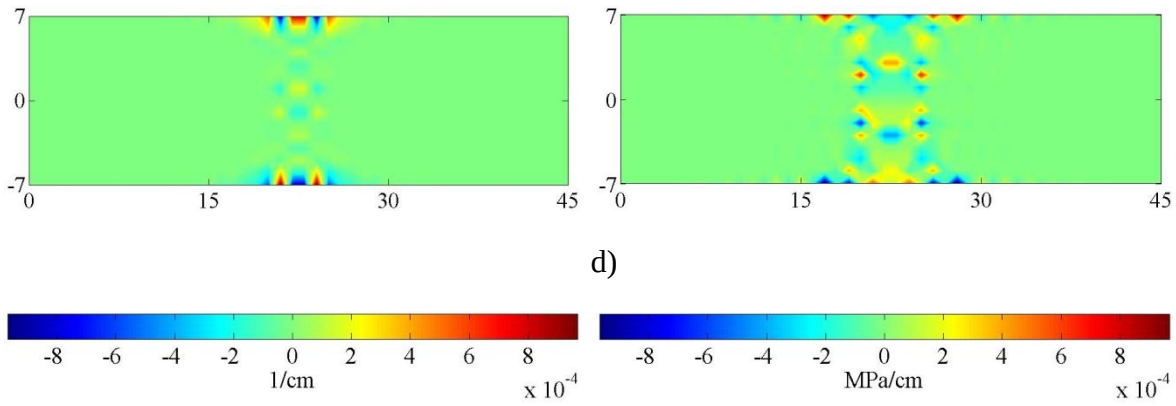

Figure 5.68: Case Five –Effective gradient strains and double stresses in the 2-direction for Δu= a) 0.0002cm, b) 0.0017 cm, c) 0.0027 cm, and d) 0.0040 cm.

5.4.6. Case Six: Tensile loading with square inclusion and transverse constraints (L_0=10 mm).

In this simulation, the 2D plate is subjected to tension by applying stretch displacements along its right side. In addition, the plate has a centered square inclusion that is forty percent softer than the plate material and it is modeled with a particle size of L_0=10 mm. The length and height of the plate and the inclusion are 45 cm×14 cm and 4 cm×4 cm, respectively. The plate is constrained in the 1-direction along its left border while the top and bottom are constrained from vertical translation (See Figure 5.7).

The response of the structure is shown in Figures 5.69-5.77 at four loading stages: initial, pre-peak, peak, and post-peak stage. Figure 5.69 shows the overall stress-strain response in the '11' and '22' directions. Figures 5.70-5.72 show the strain and stress responses in the '11', '22', and '12' directions, and their effective magnitudes are shown in Figure 5.73. Strain gradient and double stress response are shown in Figures 5.74-5.75, and their effective magnitudes are described in Figures 5.76-5.77.

The overall stress-strain response of the plate in the '11' and '22' directions is described in Figure 5.69 and shows a biaxial stress state with non-linear softening behavior. Failure of the structure is described past the peak-load with a reduction in the stress response values.

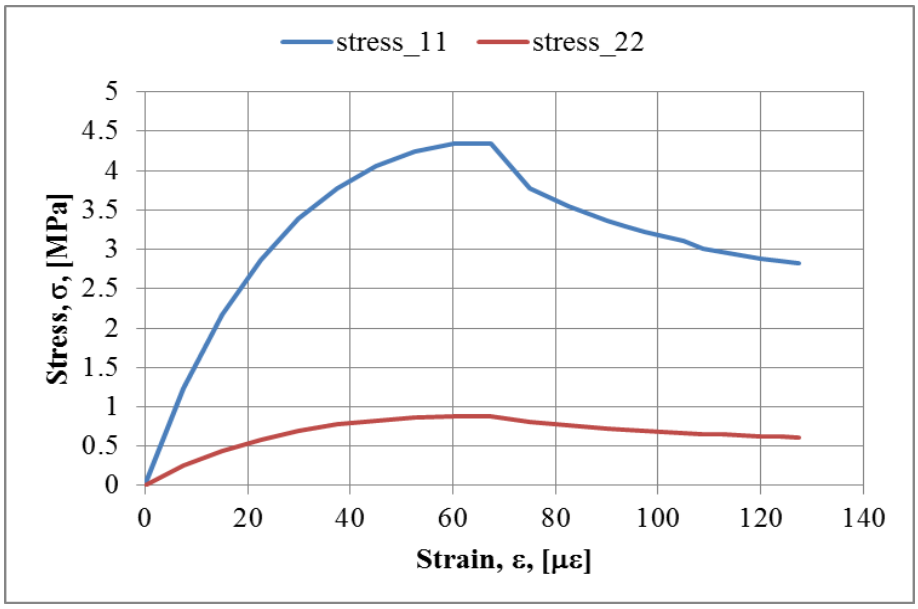

Figure 5.69: Case Six – Overall stress-strain behavior of the plate.

Figure 5.70 describes the strain and stress response of the structure in the '11' direction at the four loading stages afore mentioned. Stress response shows uniform stress distribution with stress concentrations at the top and bottom of the inclusion and smaller stresses within the inclusion. Reduction on stress magnitude is observed after the peak-load is reached indicating failure of the structure. Strain response show higher strains within the inclusion and strain concentrations at the peak and post-peak stage. At the latter stage, these concentrations become more severe and expand vertically suggesting the presence of long vertical fractures along the sides of the inclusion and fractures at the top and bottom of the plate. These fractures suggest the presence of a fracture zone that is normal to the load.

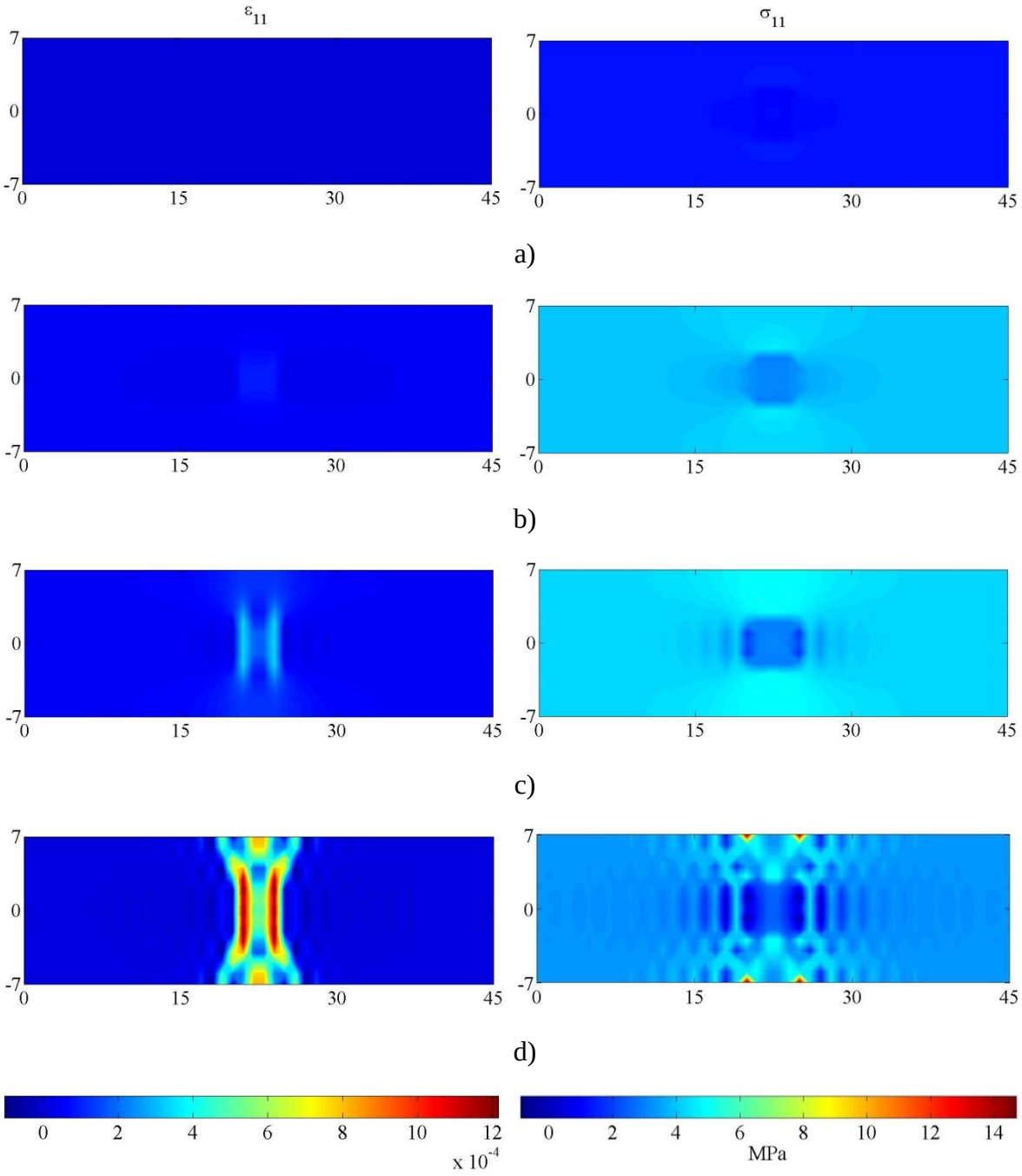

Figure 5.70: Case Six – ε_{11} and σ_{11} for Δu= a) 0.0003 cm, b) 0.0020 cm, c) 0.0030 cm, and d) 0.0041 cm.

Figure 5.71 describes the strain and stress response of the structure in the ‘22’ direction at the four loading stages afore mentioned. Stress response shows overall uniform stress distribution with lower stresses within the inclusion and compressive stress concentrations around the inclusion as the load increases. Reduction on stress magnitude is observed after the peak-load is reached indicating failure of the structure. Strain response show tensile strain concentrations in the center of the inclusion that branch out diagonally from the corners, and compressive strain concentrations around the inclusion.

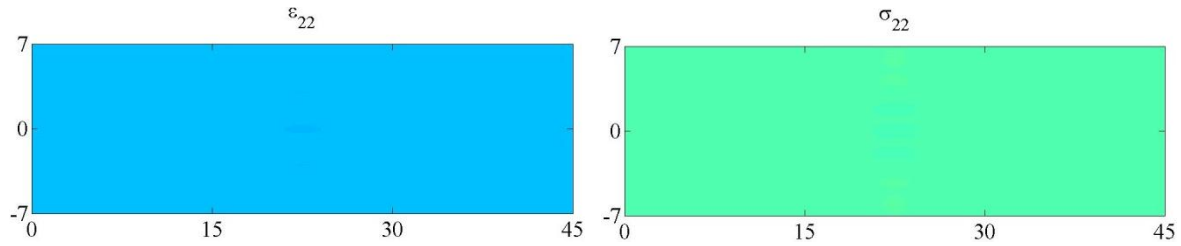

a)

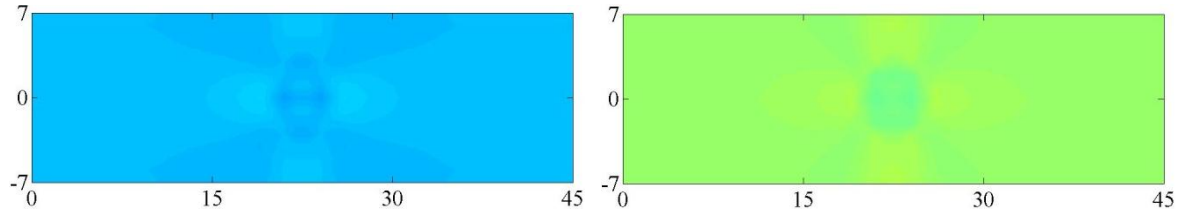

b)

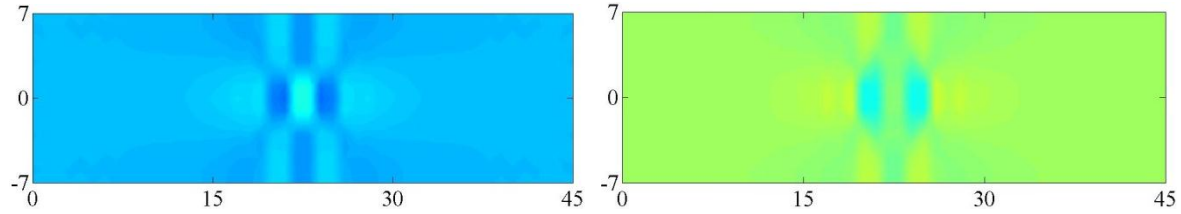

c)

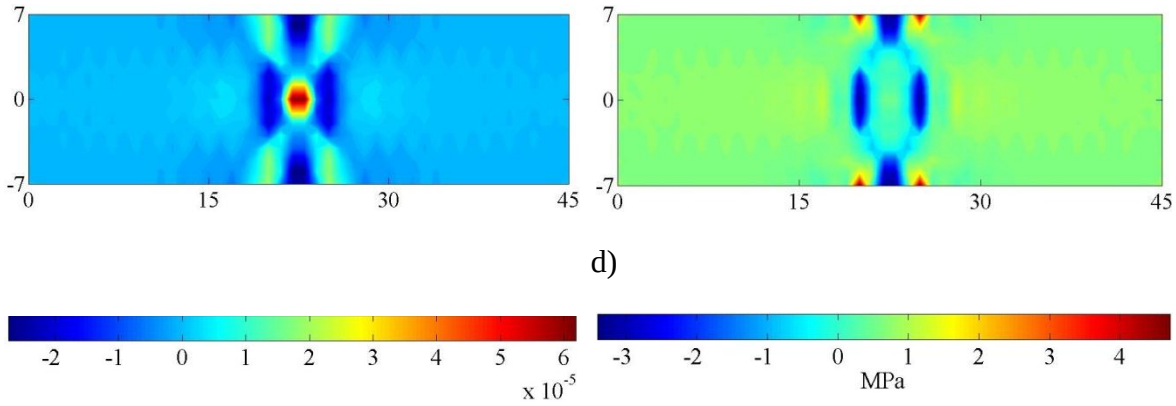

Figure 5.71: Case Six – ε_{22} and σ_{22} for Δu= a) 0.0003 cm, b) 0.0020 cm, c) 0.0030 cm, and d) 0.0041 cm.

Figure 5.72 describes the strain and stress response of the structure in the '12' direction at the four loading stages afore mentioned. Strain and stress responses show concentrations at corners of the inclusion that become higher as the load increases.

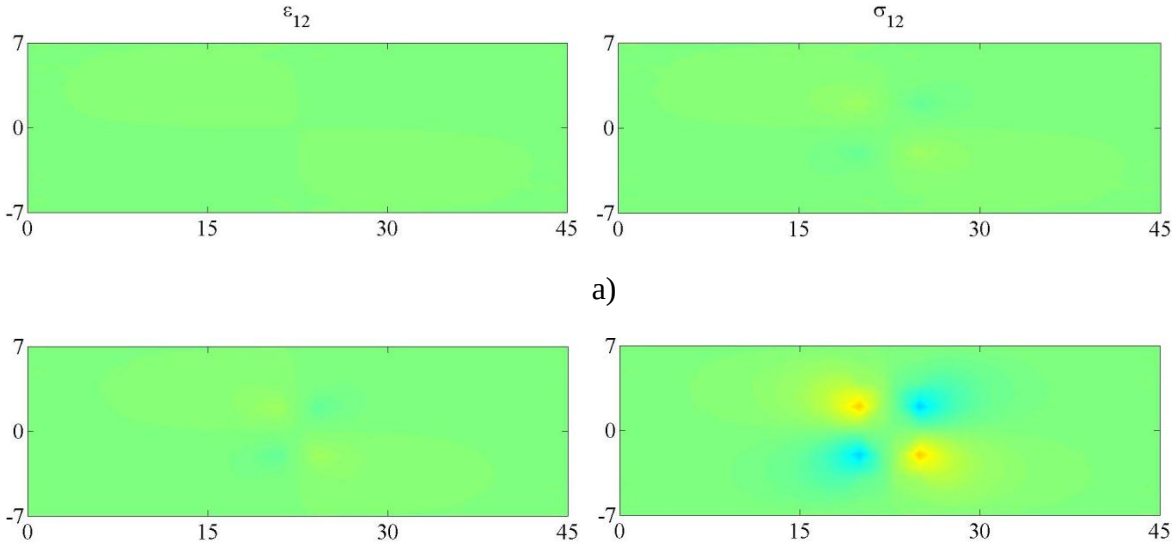

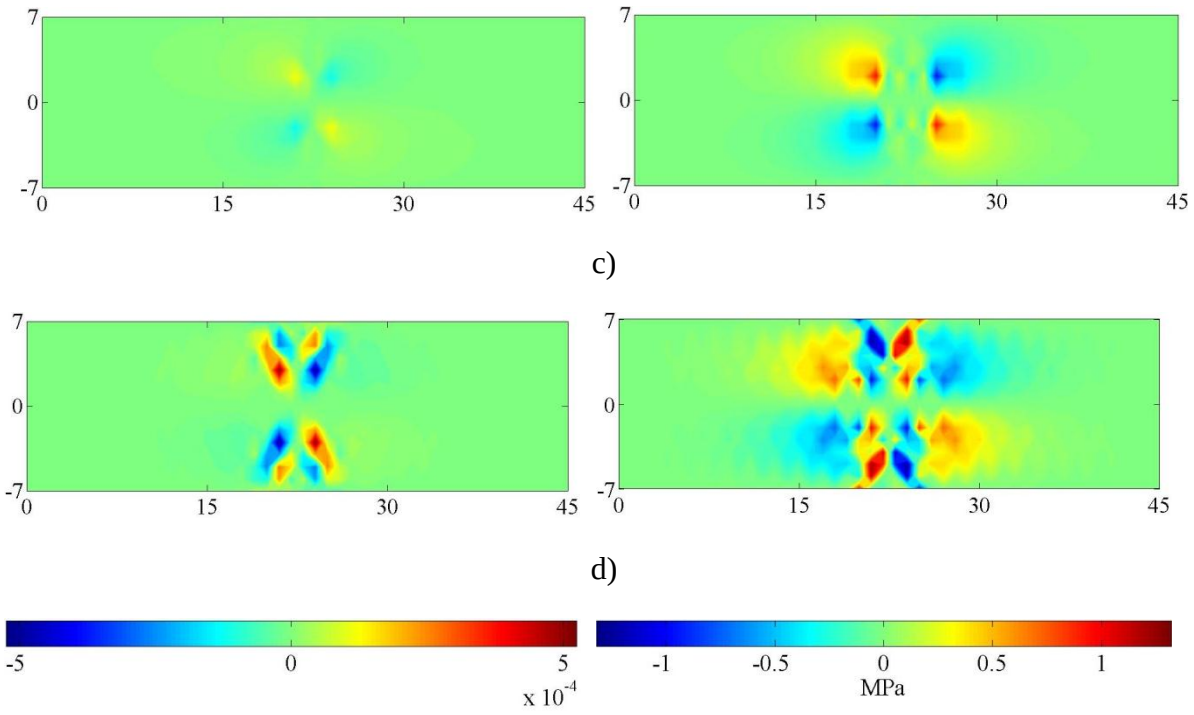

Figure 5.72: Case Six – ε_{12} and σ_{12} for Δu= a) 0.0003 cm, b) 0.0020 cm, c) 0.0030 cm, and d) 0.0041 cm.

Figure 5.73 describes the effective stress strain results within the structure at the four loading stages afore mentioned. Stress response shows uniform stress distribution with stress concentrations at the top and bottom of the inclusion. Reduction on stress magnitude is observed after the peak-load is reached indicating failure of the structure. Strain response show higher strains within the inclusion and strain concentrations at the peak and post-peak stage. At the latter stage, these concentrations become more severe suggesting the presence of large vertical fractures along the sides of the inclusion that are normal to the load and smaller fractures above and below the inclusion. These strain concentrations describe the presence of fracture zone that is mostly normal to the load.

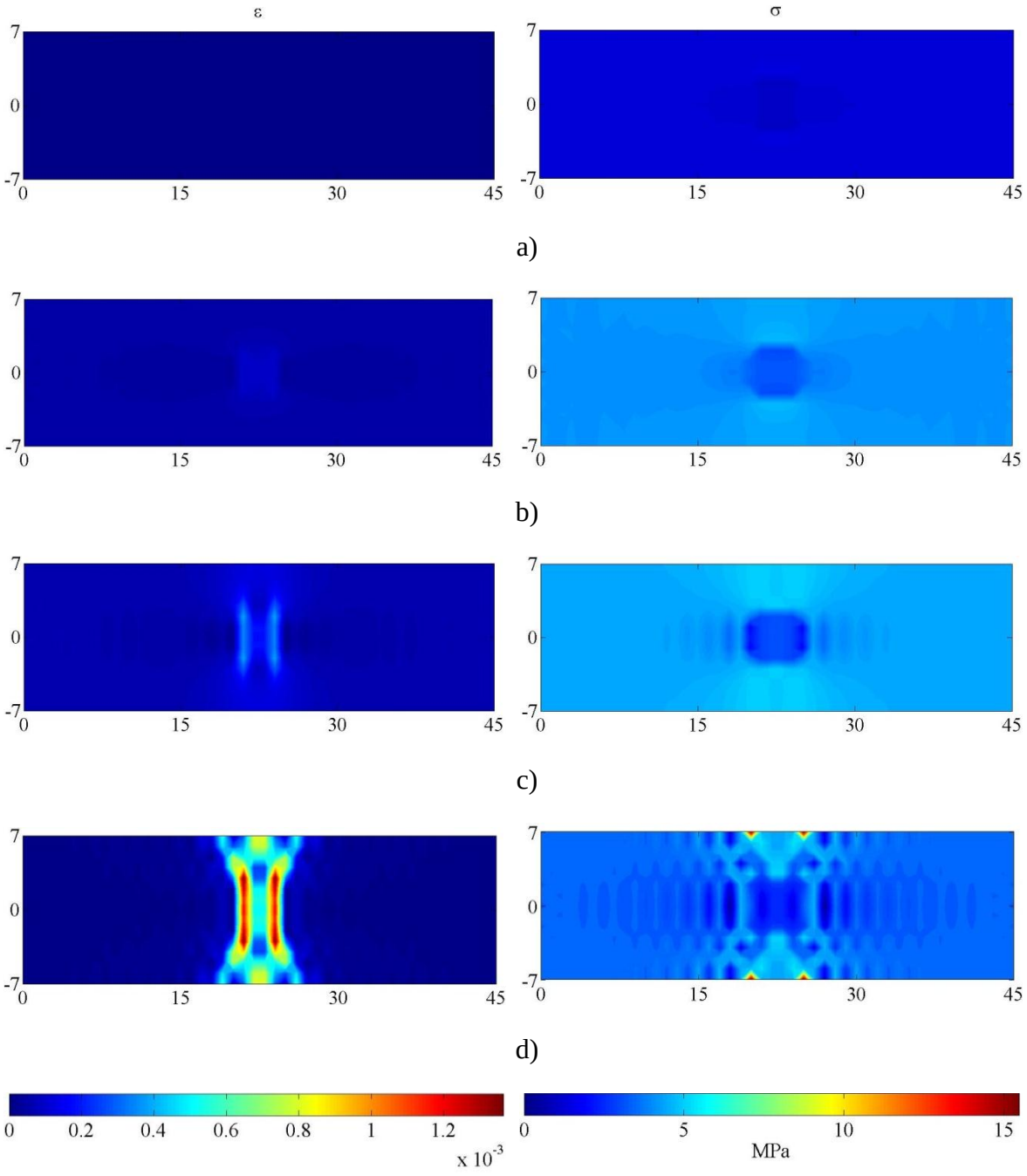

Figure 5.73: Case Six – ε and σ for Δu= a) 0.0003 cm, b) 0.0020 cm, c) 0.0030 cm, and d) 0.0041 cm.

Figures 5.74-5.78 describe the gradient strain –double stress responses of the structure at the four loading stages afore mentioned. Strain gradient results describe at the peak and post-peak stage high tensile and compressive concentrations that are located beside each other suggesting the presence of large vertical fractures along the sides of the inclusion with smaller fracture above and below the inclusion. These fractures describe the presence of a fracture zone that is principally normal to the load.

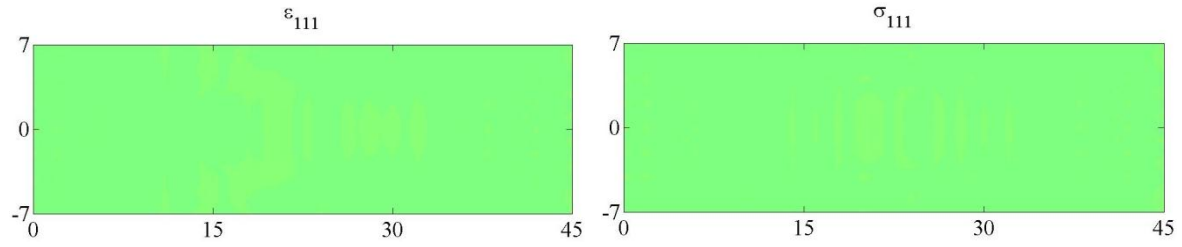

a)

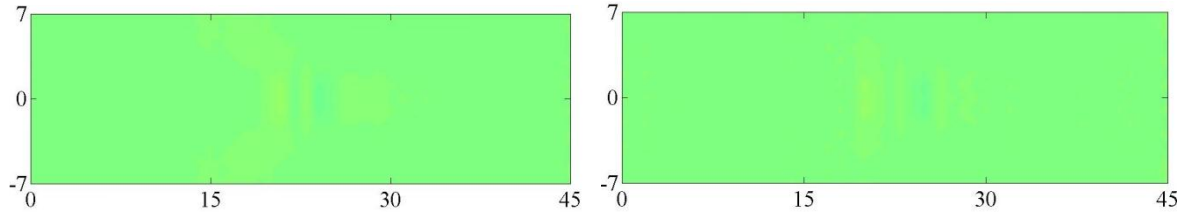

b)

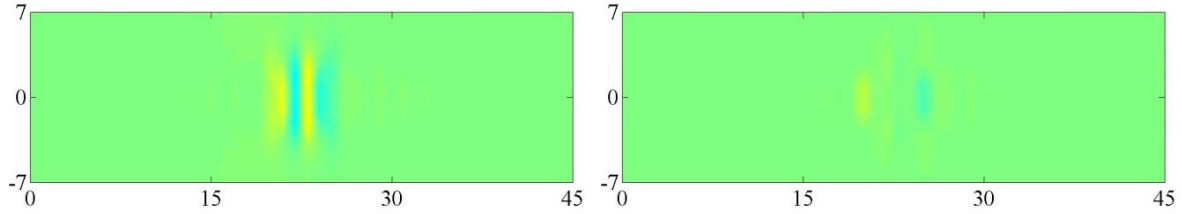

c)

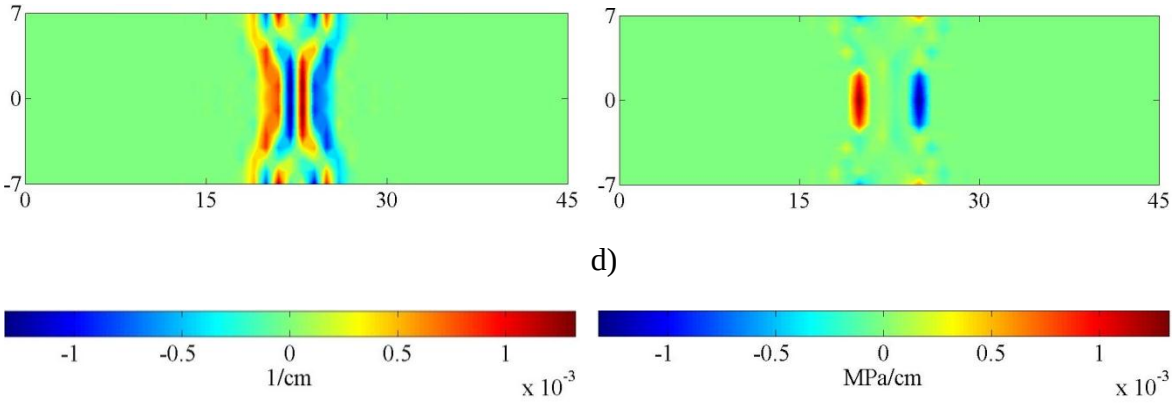

d)

Figure 5.74: Case Six – ε_{111} and σ_{111} for Δu= a) 0.0003 cm, b) 0.0020 cm, c) 0.0030 cm, and d) 0.0041 cm.

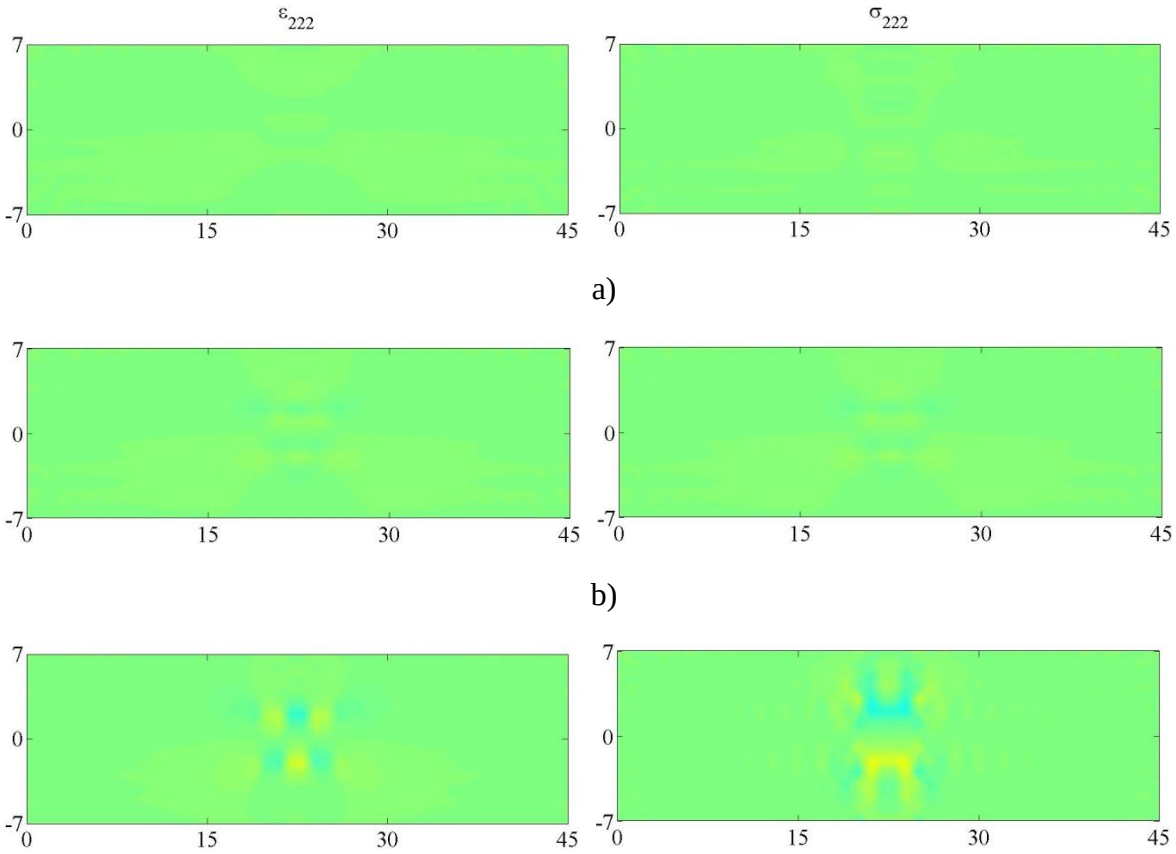

a)

b)

c)

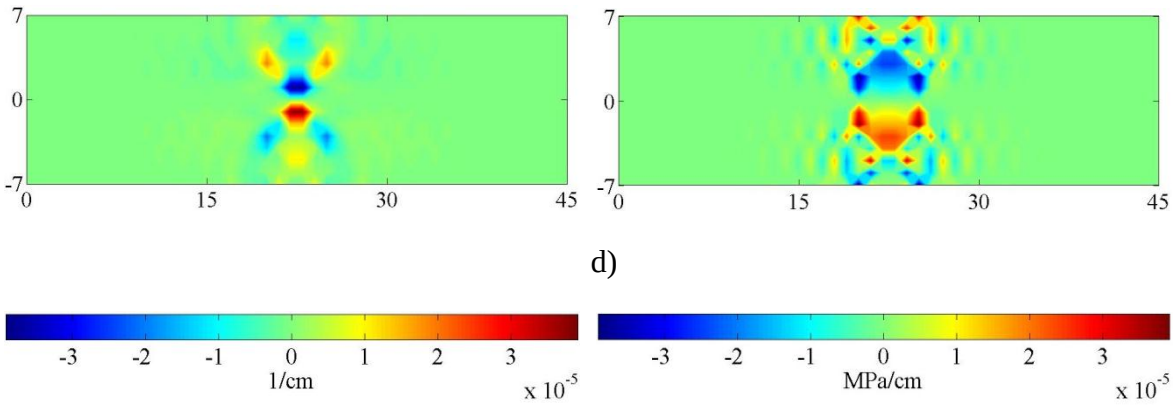

d)

Figure 5.75: Case Six – ε_{222} and σ_{222} for Δu= a) 0.0003 cm, b) 0.0020 cm, c) 0.0030 cm, and d) 0.0041 cm.

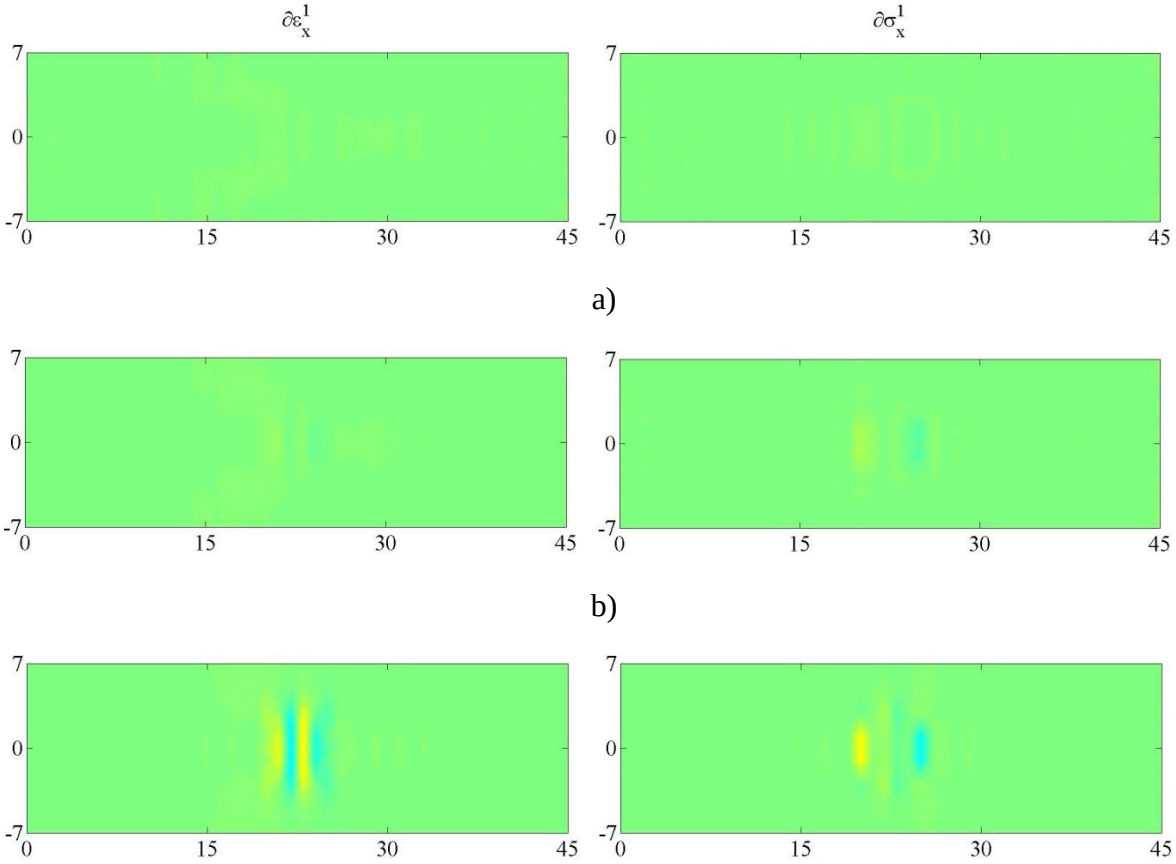

a)

b)

c)

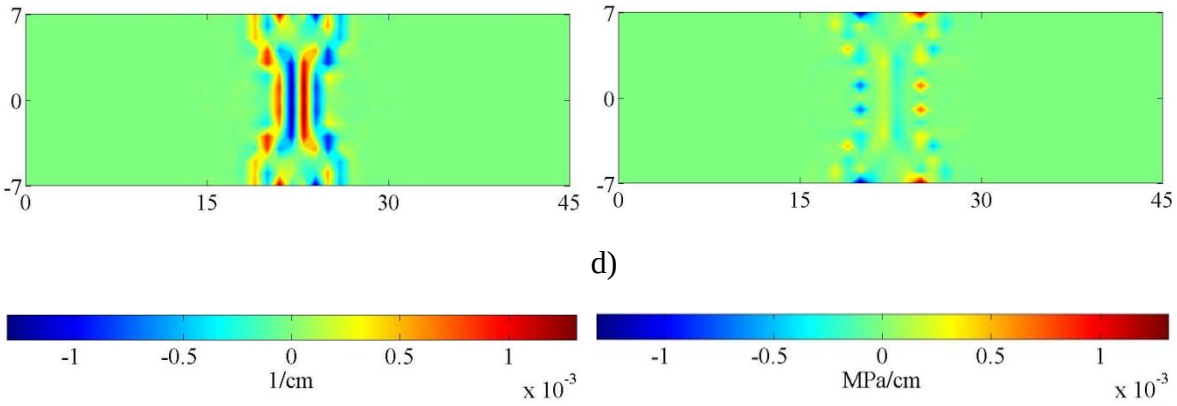

d)

Figure 5.76: Case Six –Effective gradient strains and double stresses in the 1-direction for Δu= a) 0.0003 cm, b) 0.0020 cm, c) 0.0030 cm, and d) 0.0041 cm.

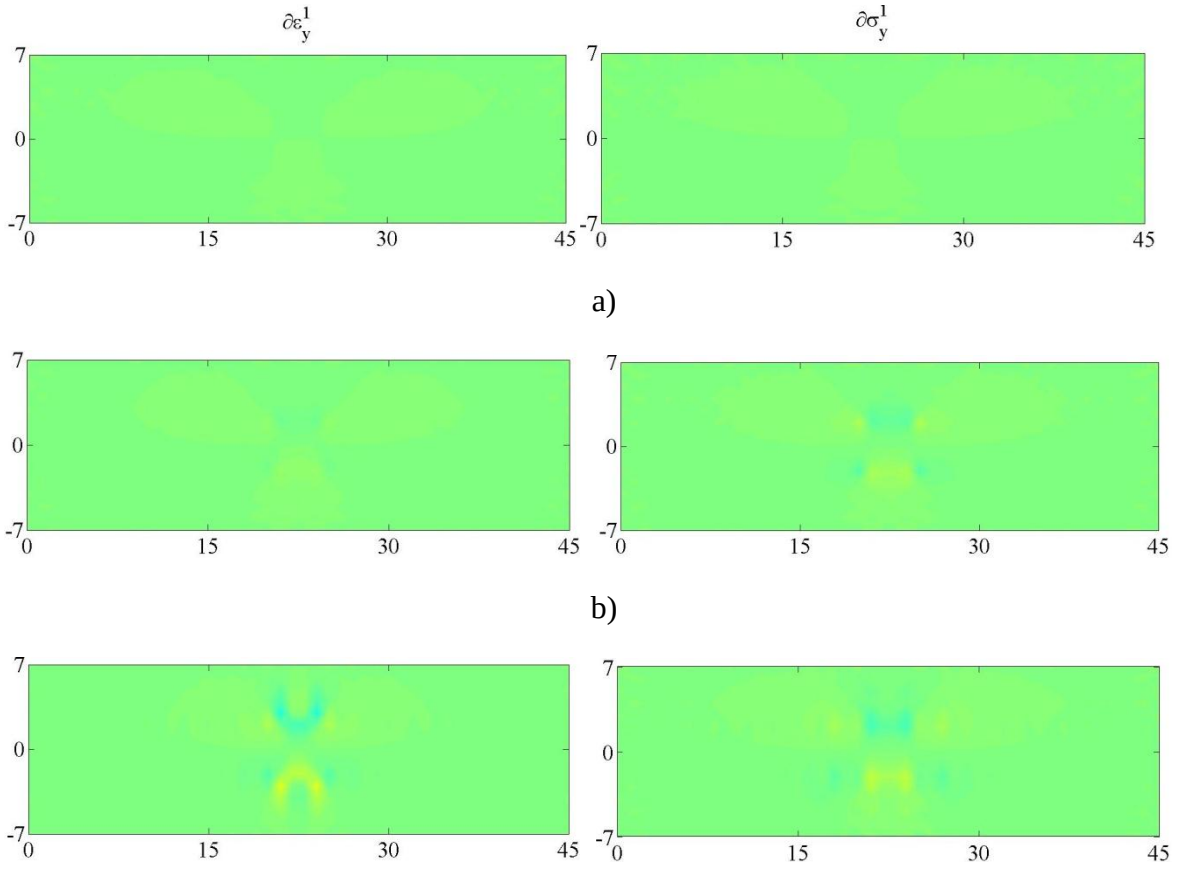

a)

b)

c)

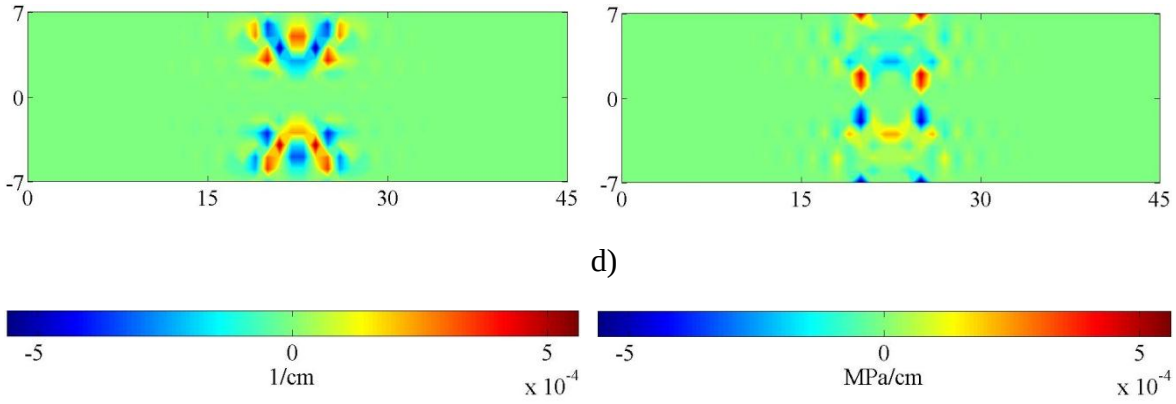

Figure 5.77: Case Six –Effective gradient strains and double stresses in the 2-direction for Δu= a) 0.0003 cm, b) 0.0020 cm, c) 0.0030 cm, and d) 0.0041 cm.

5.4.7. Evaluation of the stress-strain behavior of the structure versus a point within the structure.

The overall tensile stress-strain behavior for a structure and for a point within the structure is analyzed by comparing the results from loading case three (Figure 5.78). The stress-strain response, for the structure and the point, shows similar behavior along the pre-peak curve and differs along the post-peak curve. The post-peak behavior of the structure presents a deep and dramatic drop in the stresses with a very small strain increase. Conversely, the overall stress-strain post-peak results at the point show a gradual (linear) decrease in stress with a large increase in strain deformation. This observation is supported by Gopalaratnam and Shah's (1985) study on the softening response of plain concrete in direct tension (Figures 5.49-5.80).

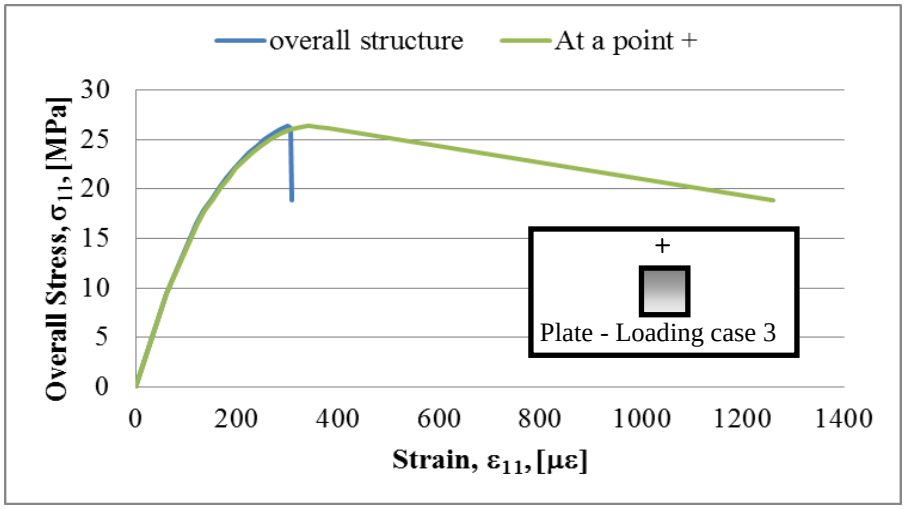

Figure 5.78 Case Three Plate-Overall stress strain behavior versus overall stress-strain behavior at a point

Figure 5.79 shows a schematic drawing of the notched specimen used in Gopalaratnam and Shah's study; the locations of the strain gages and the gage used in their experiment are shown in the figure. Then, Figure 5.80 shows the stress-strain response at the strain-gage locations versus the overall stress strain behavior of the specimen. In this figure, it can be observed that the overall response of the specimen describes a deep drop of the stress response after the peak-load, while the stress-strain behavior of the strain-gages between the notches describe a gradual and linear drop in the stresses after the peak-load.

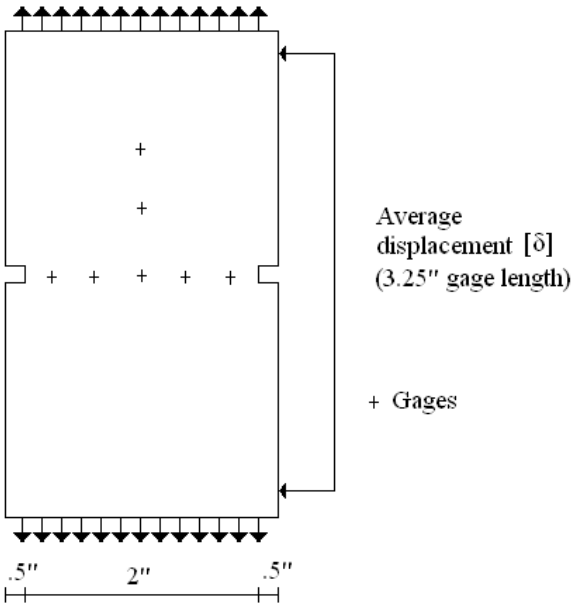

Figure 5.79 Gage location details – schematic drawing of the tensile specimen (Gopalaratnam and Shah, 1985).

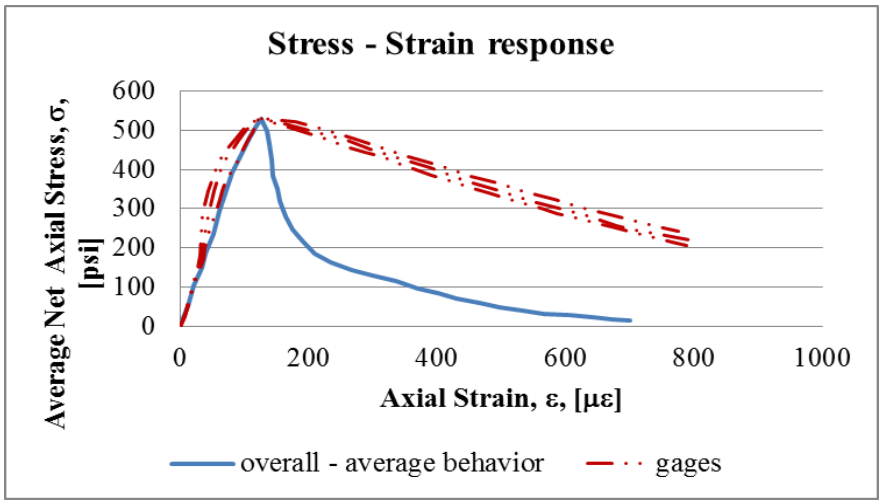

Figure 5.80 Average net axial stress plotted versus axial strain computed from δ and strain gages (Gopalaratnam and Shah, 1985).

5.4.8. Fracture zone comparison.

To evaluate the effect of the particle size on the fracture zone, the normalized effective strains at the peak-stage for the case five and three simulations are compared. A particle size of L_0=10 mm and 1 mm is used on case five and three, respectively. These results are normalized with respect to their corresponding failure strain in the '11' direction. As expected, a larger particle size generates a larger fracture zone. This is described in Figure 5.81.

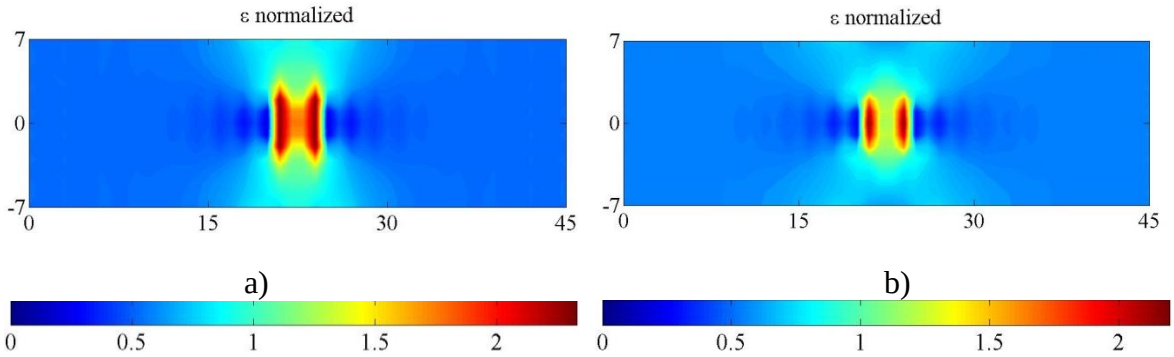

Figure 5.81: Normalized Effective Strain for a) case five with L_0=10 mm, and b) case three with L_0=1 mm.

5.4.9. Case Seven: Compressive loading with band inclusion and no constraints (L_0=10 mm).

In this simulation, the 2D plate is subjected to compression by applying shrink displacements along its right side. In addition, the plate has a centered band inclusion that is forty percent softer than the plate material and it is modeled with a particle size of L_0=10 mm. The length and height of the plate and the inclusion are 45 cm×14 cm and 15 cm×14 cm, respectively. The plate is constrained in the 1-direction along its left border while the top and bottom have no constraints (See Figure 5.4).

The structure responses are shown in Figures 5.82-5.90 at three loading stages: initial, pre-peak, and peak stages. Figure 5.82 shows the overall stress-strain response in the '11' and '22' directions. Figures 5.83-5.85 show the strain and stress responses in the '11', '22', and '12' directions, and their effective magnitudes are shown in Figure 5.86. Strain gradient and double stress responses are shown in Figures 5.87-5.88, and their effective magnitudes are described in Figures 5.89-5.90.

The overall stress-strain response of the plate in the '11' and '22' directions is described in Figure 5.82 and shows a uniaxial stress state with non-linear softening behavior.

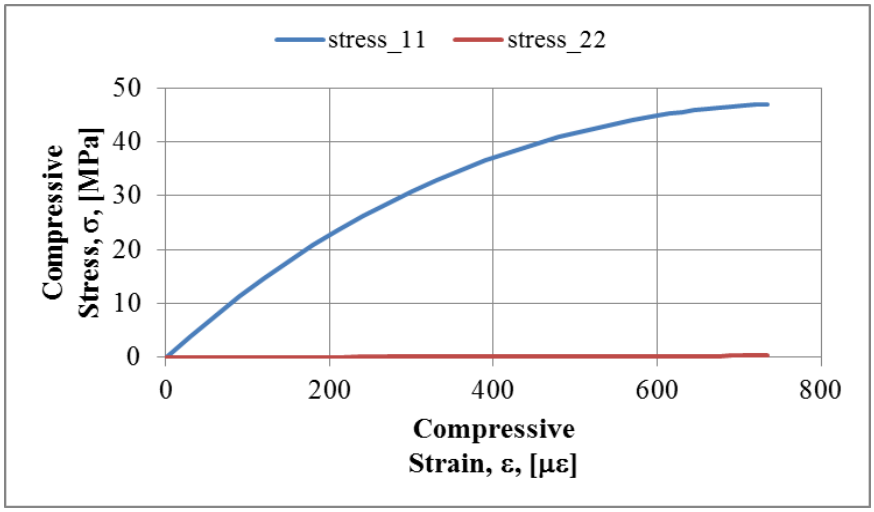

Figure 5.82: Case Seven – Overall stress-strain behavior of the plate.

Figure 5.83 describes the strain and stress response of the structure in the '11' direction at the three loading stages afore mentioned. Stress response shows overall uniform stress distribution with stress bands outside the inclusion that are attributed to the induced load heterogeneity in the material. Strain response show higher strains within the inclusion and strain concentrations at the peak stage. At this stage an 'X' shape shear band is formed.

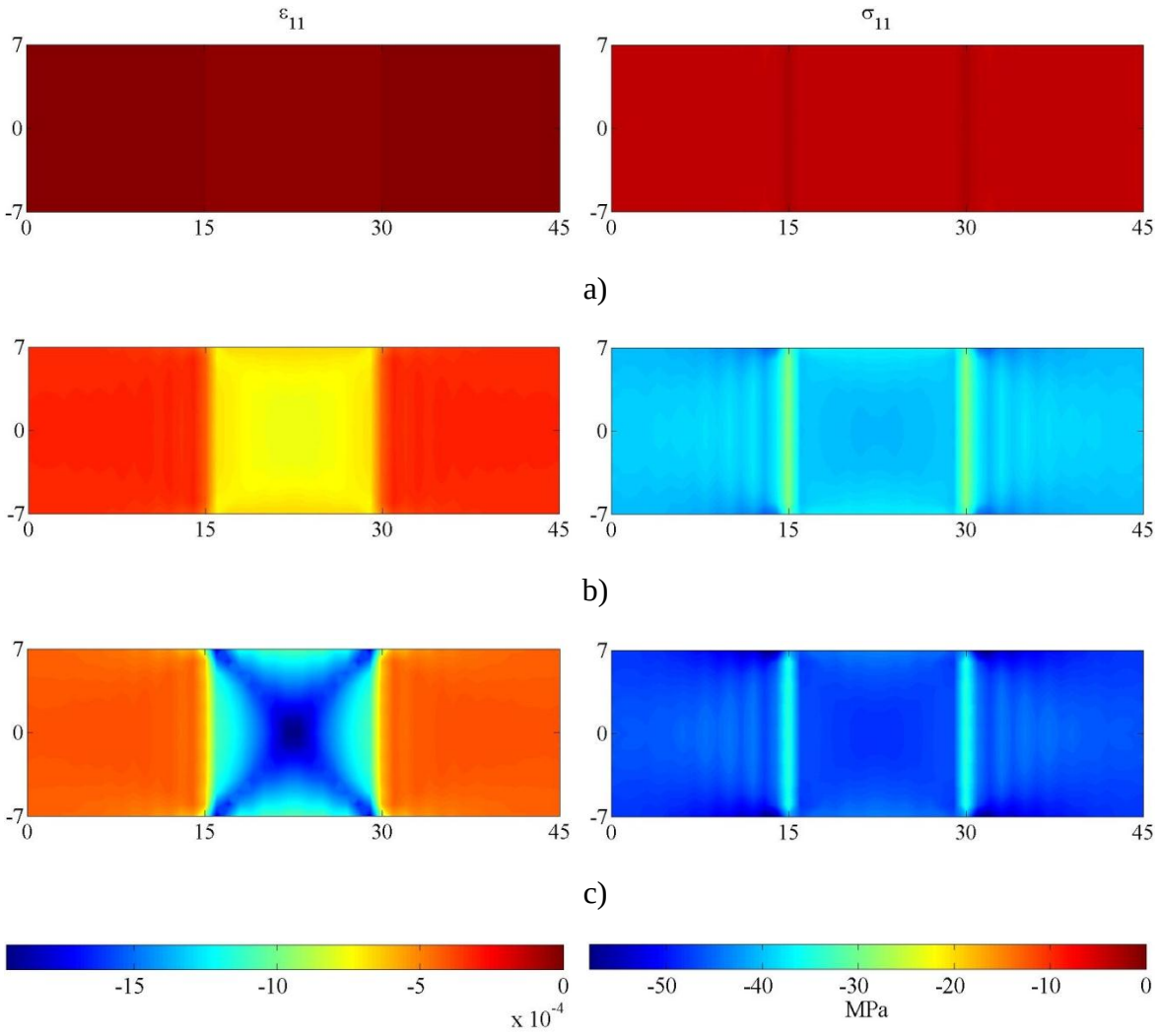

Figure 5.83: Case Seven – ε_{11} and σ_{11} for -Δu= a) 0.0014 cm, b) 0.0203 cm, and c) 0.0331 cm.

Figure 5.84 describes the strain and stress response of the structure in the '22' direction at the three loading stages afore mentioned. Stress response shows overall uniform zero stress distribution with stress compressive concentrations within the inclusion and tensile concentrations on the sides of the inclusion. Strain response shows expansive behavior with higher strains within the inclusion and strain concentrations at the peak stage. At this stage an 'X' shape shear band is formed.

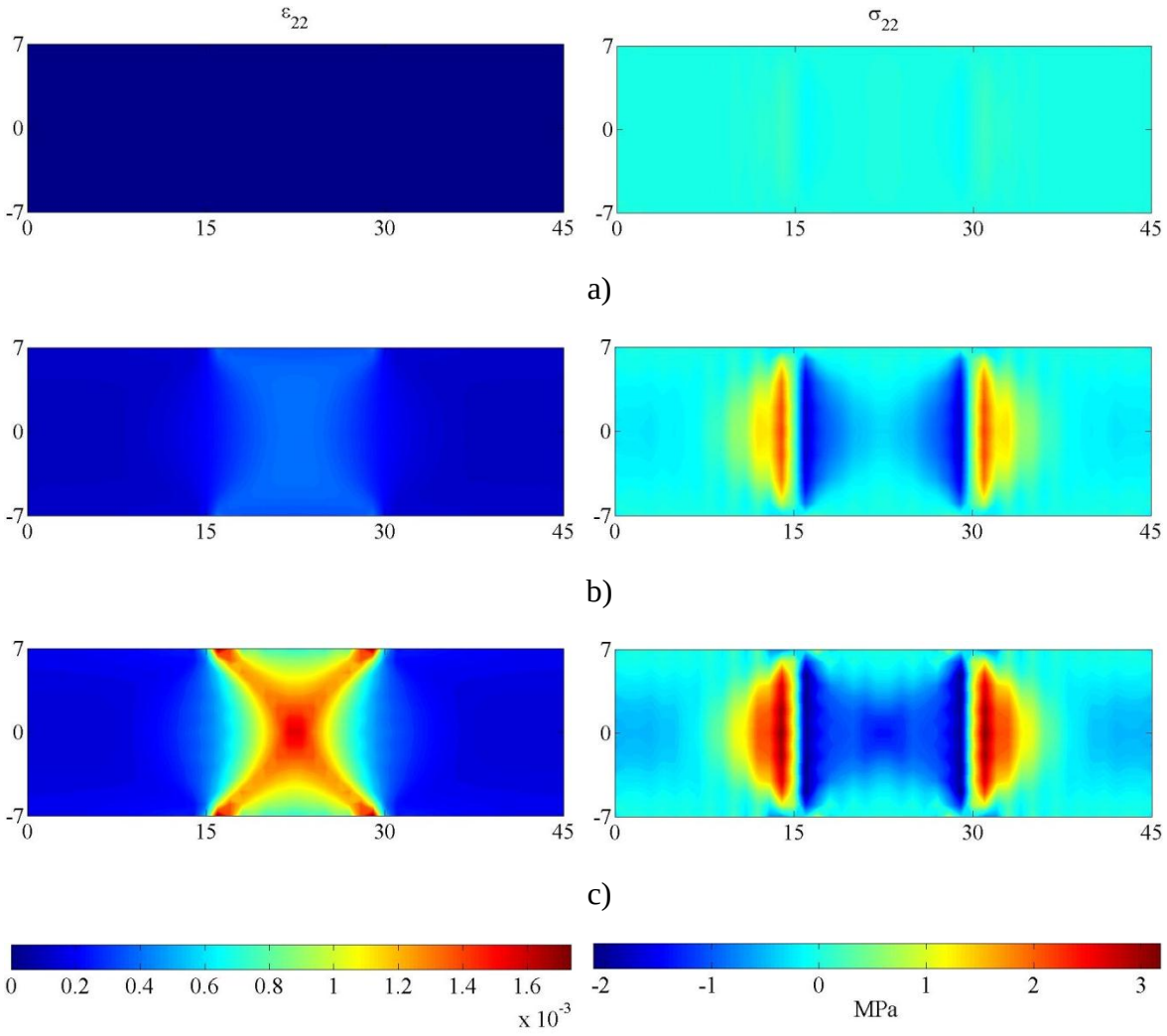

Figure 5.84: Case Seven – ε_{22} and σ_{22} for -Δu= a) 0.0014 cm, b) 0.0203 cm, and c) 0.0331 cm.

Figure 5.85 describes the strain and stress response of the structure in the '12' direction at the three loading stages afore mentioned. Strain and stress response shows concentrations at the corners of the inclusion that become more severe and expand in a zigzag manner as the load increases.

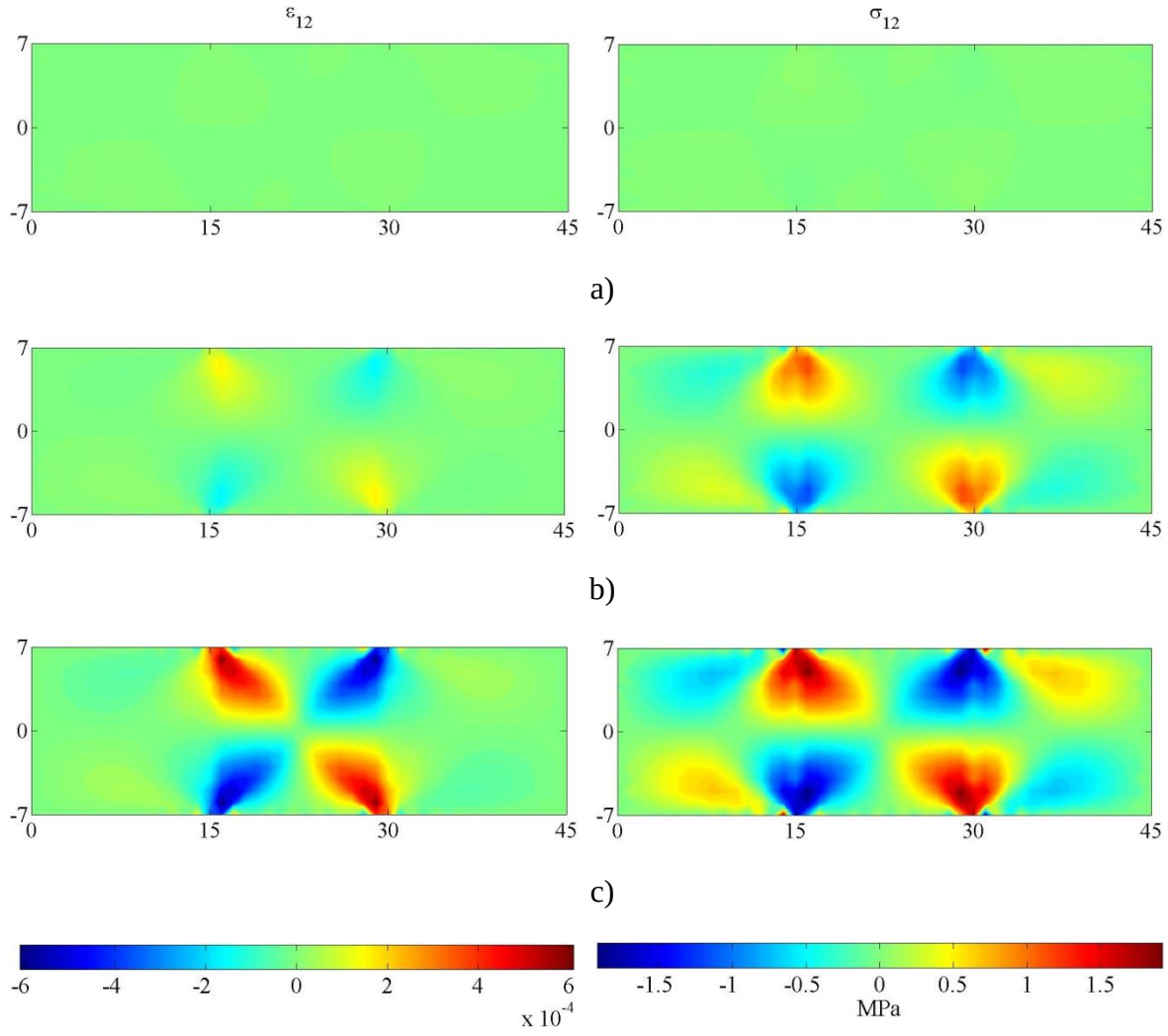

Figure 5.85: Case Seven – ε_{12} and σ_{12} for -Δu= a) 0.0014 cm, b) 0.0203 cm, and c) 0.0331 cm.

Figure 5.86 describes the effective strain and stress response within the structure at the three loading stages afore mentioned. Stress response shows overall uniform stress distribution with stress bands that are attributed to the load induced heterogeneity in the material. Strain response show higher strains within the inclusion and strain concentrations at the peak stage. At this stage an 'X' shape shear band is formed.

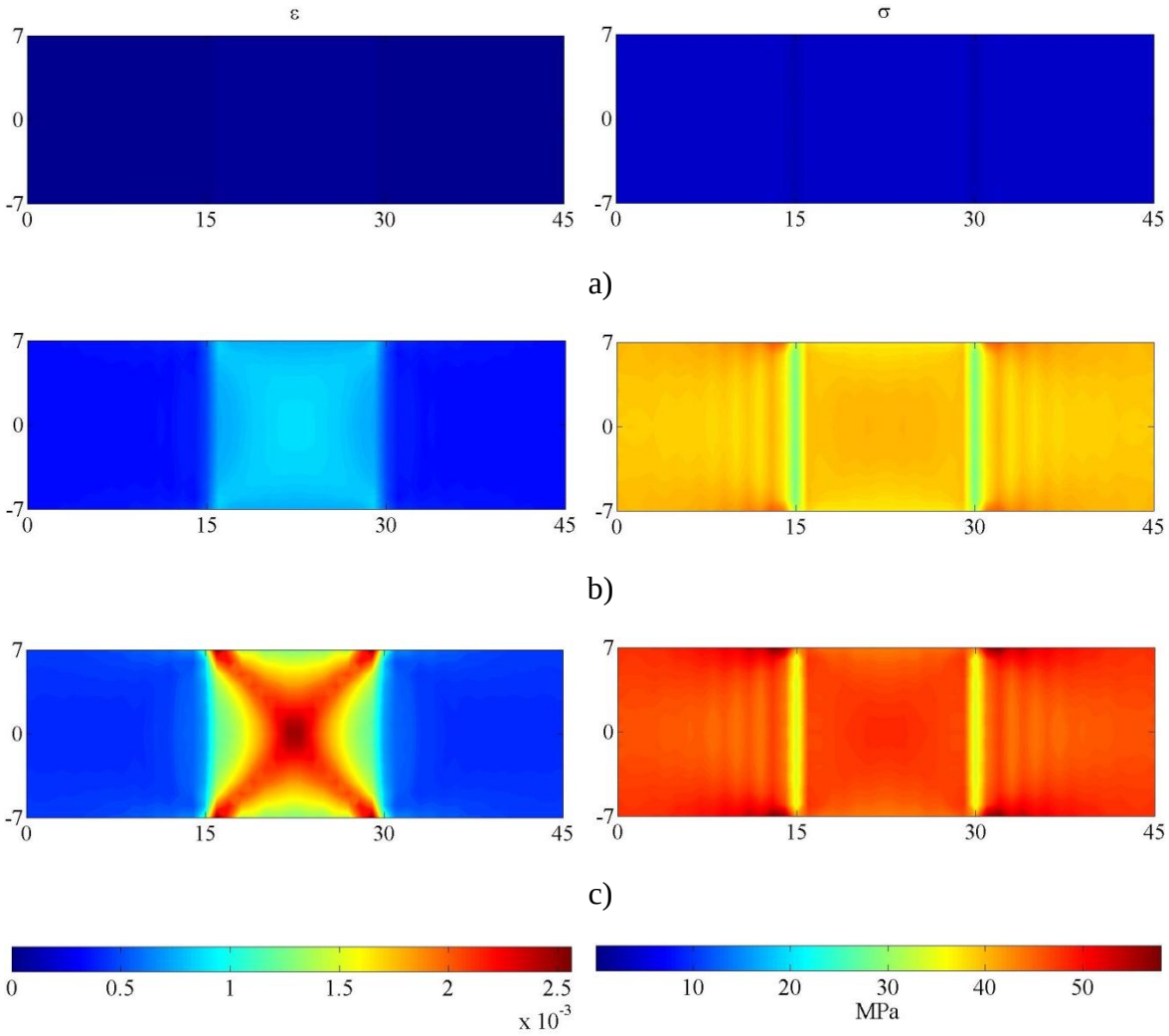

Figure 5.86: Case Seven – ε and σ for -Δu= a) 0.0014 cm, b) 0.0203 cm, and c) 0.0331 cm.

Figures 5.87-5.90 describe the gradient strain –double stress response of the structure at the three loading stages afore mentioned. Strain gradient results describe at the peak stage high tensile and compressive concentrations that suggest an 'X' shear shape fracture.

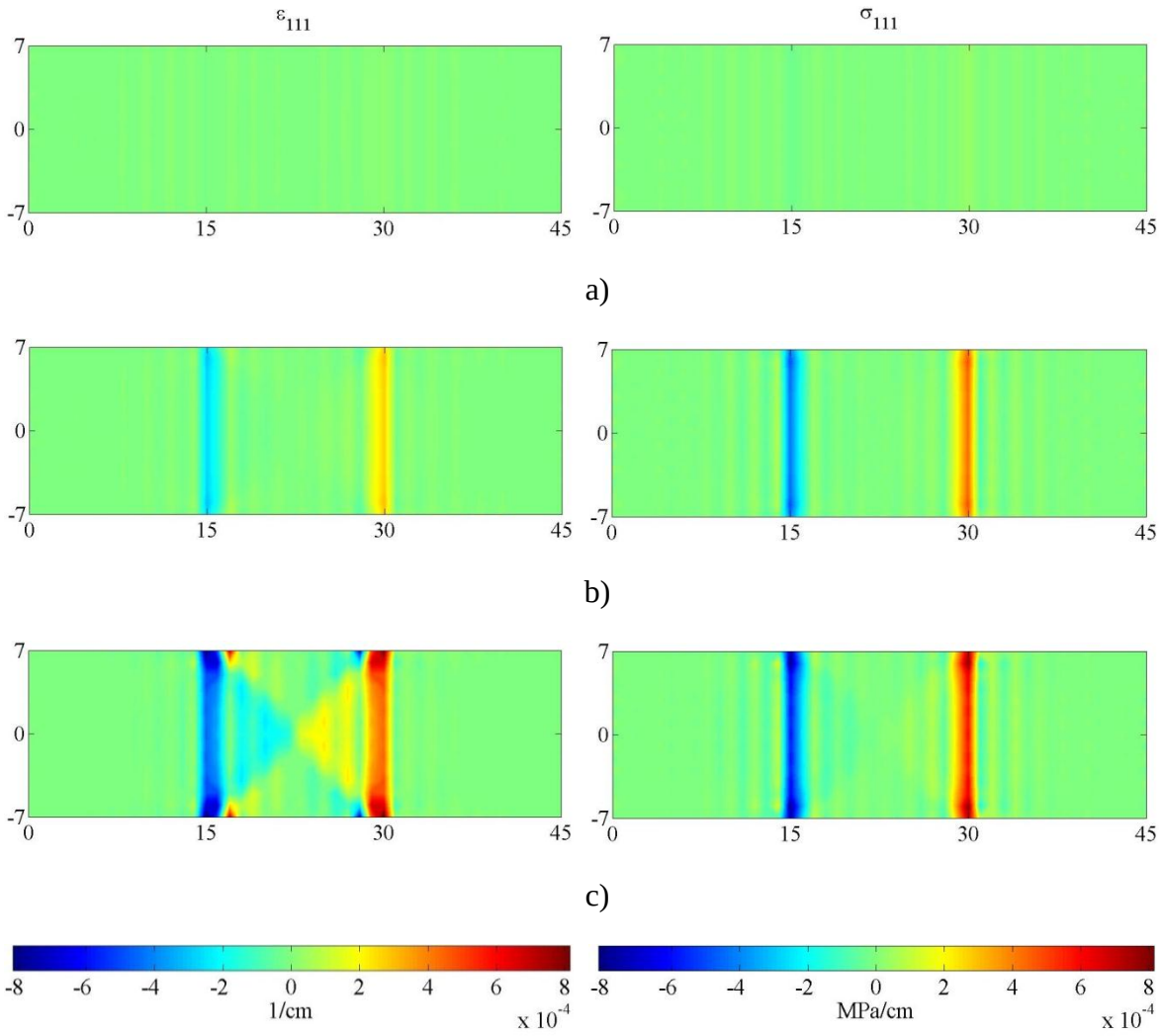

Figure 5.87: Case Seven – ε_{111} and σ_{111} for -Δu= a) 0.0014 cm, b) 0.0203 cm, and c) 0.0331 cm.

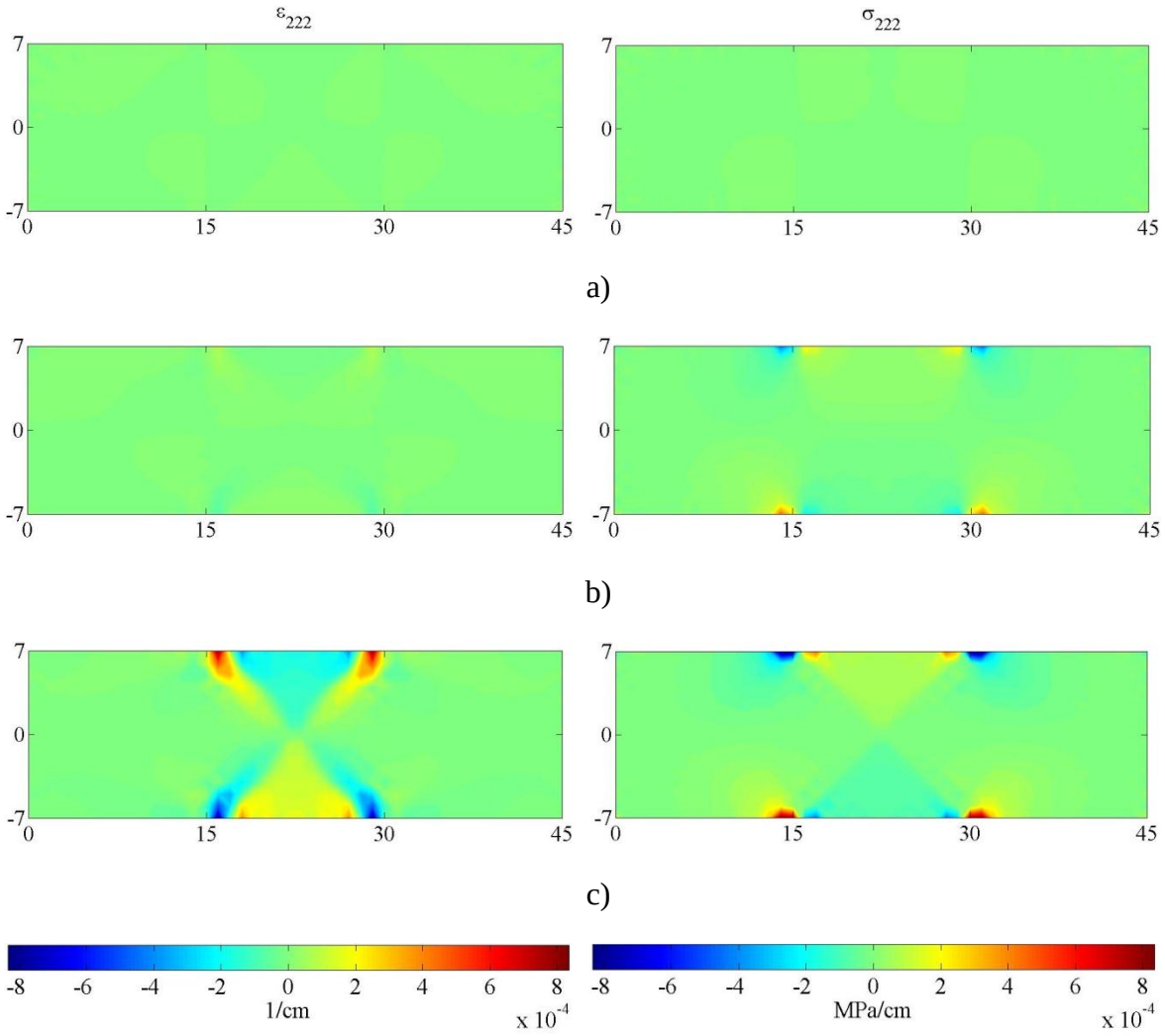

Figure 5.88: Case Seven – ε_{222} and σ_{222} for -Δu= a) 0.0014 cm, b) 0.0203 cm, and c) 0.0331 cm.

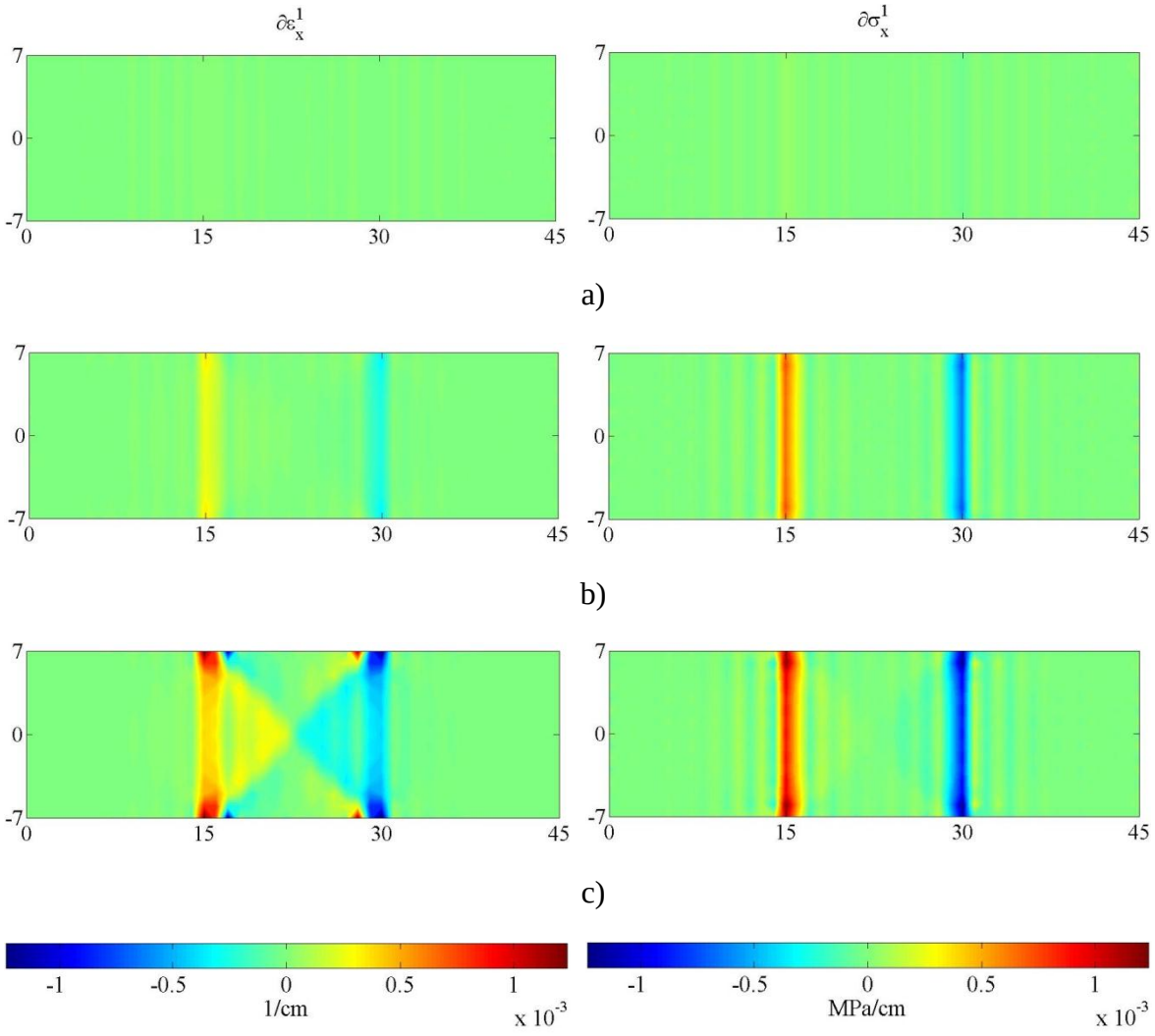

Figure 5.89: Case Seven –Effective gradient strains and double stresses in the 1-direction for -Δu= a) 0.0014 cm, b) 0.0203 cm, and c) 0.0331 cm.

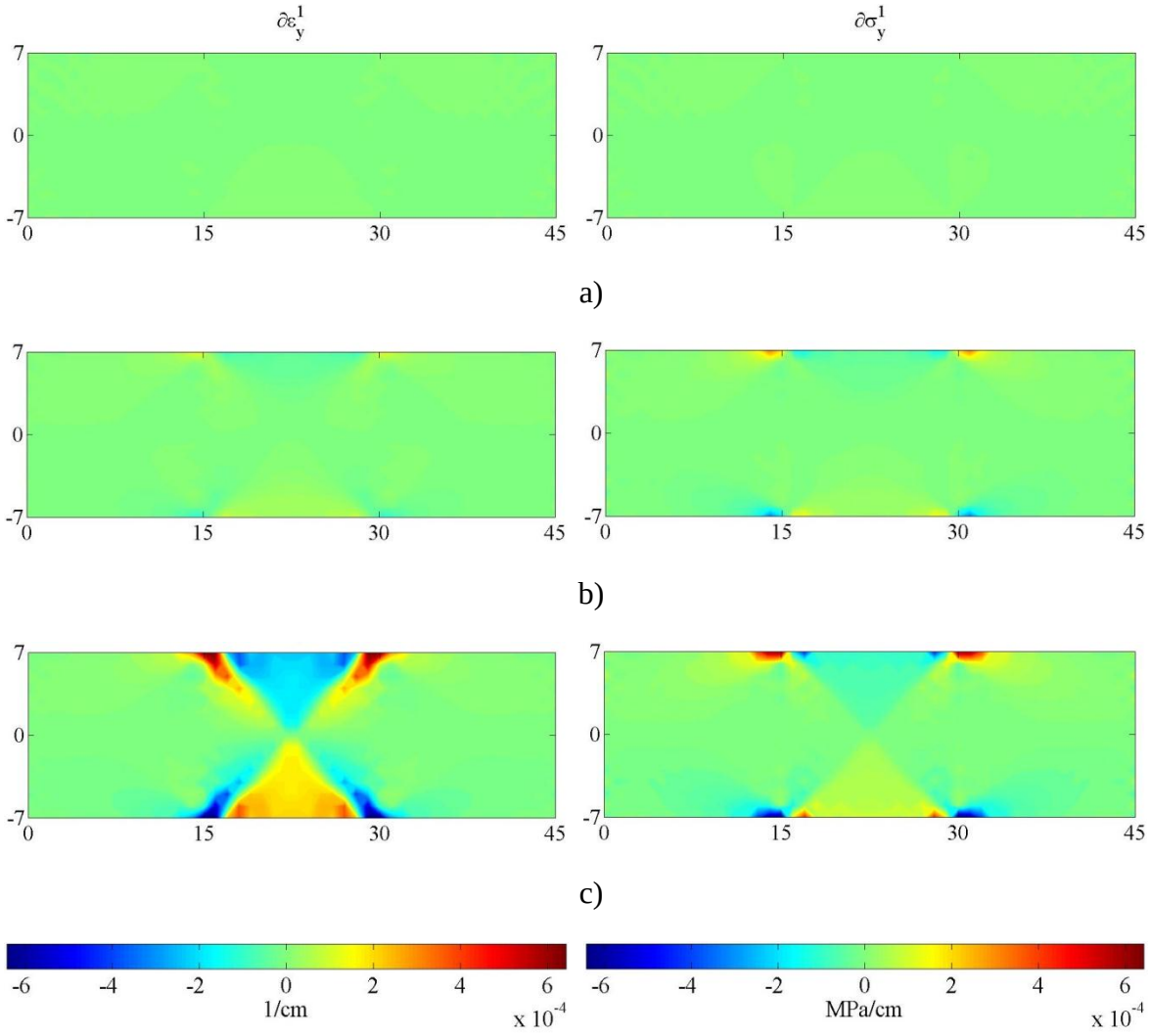

Figure 5.90: Case Seven –Effective gradient strains and double stresses in the 2-direction for -Δu= a) 0.0014 cm, b) 0.0203 cm, and c) 0.0331 cm.

5.4.10. Case Eight: Compressive loading with band inclusion and transverse constraints (L_0=10 mm).

In this simulation, the 2D plate is subjected to compression by applying shrink displacements along its right side. In addition, the plate has a centered band inclusion that is forty percent softer than the plate material and it is modeled with a particle size of L_0=10 mm. The length and height of the plate and the inclusion are 45 cm×14 cm and 15 cm×14 cm, respectively. The plate is

constrained in the horizontal 1-direction along its left border while the top and bottom are constrained from vertical translation (See Figure 5.5).

The response of the structure is shown in Figures 5.91-5.99 at three loading stages: initial, pre-peak, and peak stage. Figure 5.91 shows the overall stress-strain response in the '11' and '22' directions. Figures 5.92-5.94 show the strain and stress responses in the '11', '22', and '12' directions, and the effective magnitudes are shown in Figure 5.95. Strain gradient and double stress response are shown in Figures 5.96-5.97, and its effective magnitudes are described in Figures 5.98-5.99.

The overall stress-strain response of the plate in the '11' and '22' directions is described in Figure 5.91 and shows a biaxial stress state with a non-linear softening behavior.

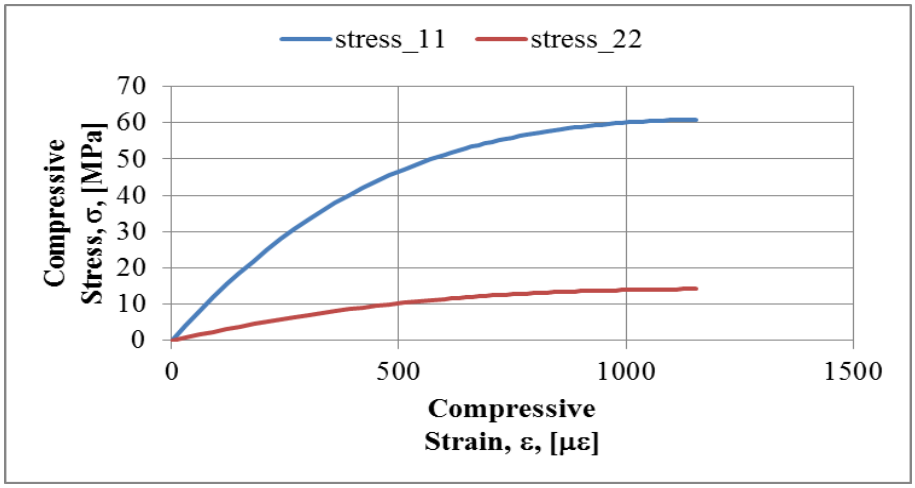

Figure 5.91: Case Eight – Overall stress-strain behavior of the plate.

Figure 5.92 describes the strain and stress response of the structure in the '11' direction at the three loading stages afore mentioned. Stress response shows overall uniform stress distribution with stress bands outside the inclusion that are attributed to the load induced heterogeneity in the

material. Strain response show higher strains within the inclusion illustrating vertical strain concentrations at the peak stage.

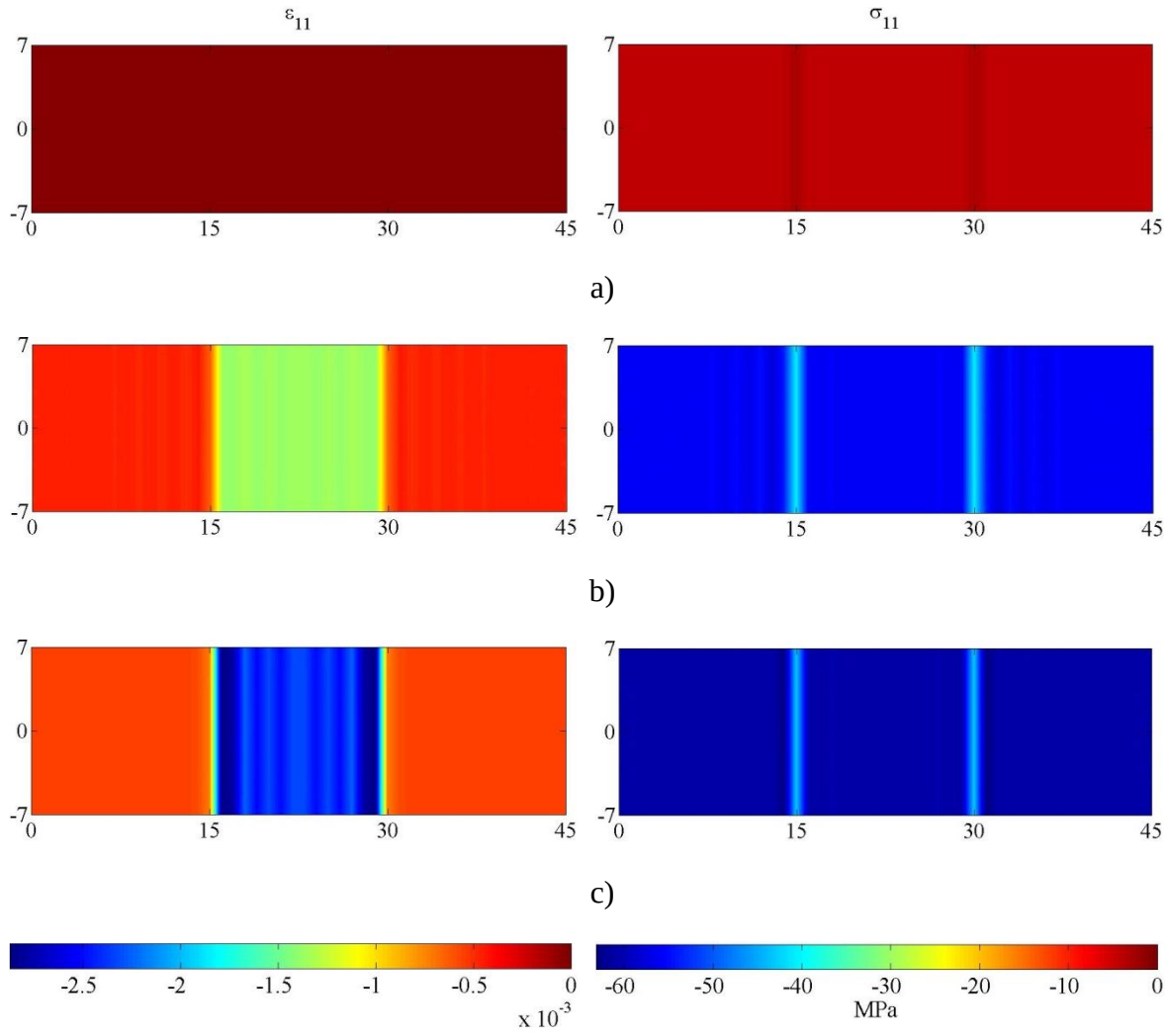

Figure 5.92: Case Eight – ε_{11} and σ_{11} for -Δu= a) 0.0014 cm, b) 0.0338 cm, and c) 0.0520 cm.

Figure 5.93 describes the strain and stress response of the structure in the '22' direction at the three loading stages afore mentioned. Stress response shows overall uniform stress distribution with stress compressive concentrations within the inclusion. Strain response show small

compressive and tensile strain bands along the length of the structure; this is attributed to the load induced heterogeneity in the material.

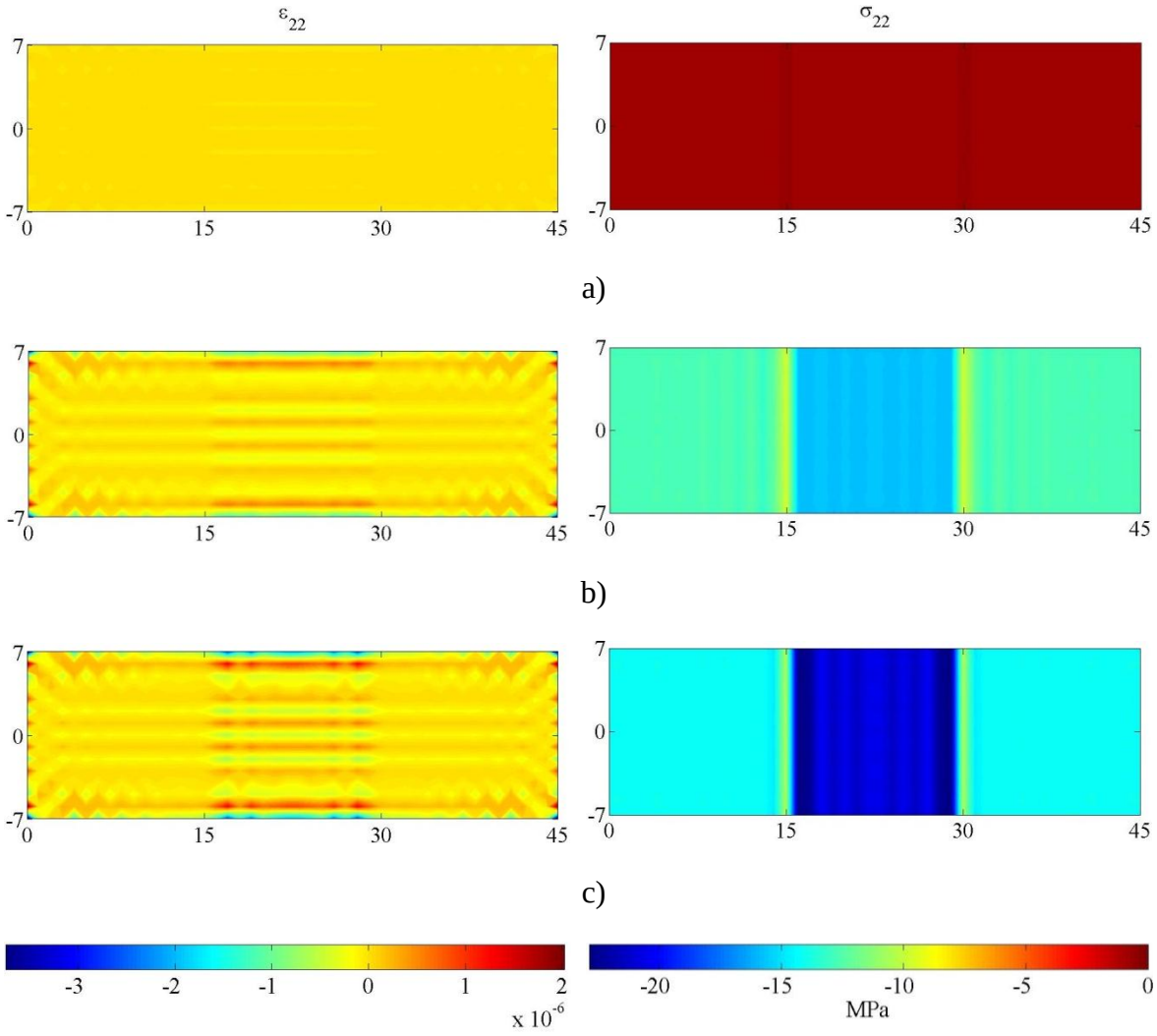

Figure 5.93: Case Eight – ε_{22} and σ_{22} for -Δu= a) 0.0014 cm, b) 0.0338 cm, and c) 0.0520 cm.

Figure 5.94 describes the strain and stress response in the 12 direction within the structure at the three loading stages afore mentioned. Stress and strain response shows overall uniform zero stress distribution with small strain concentrations on top and bottom of the inclusion.

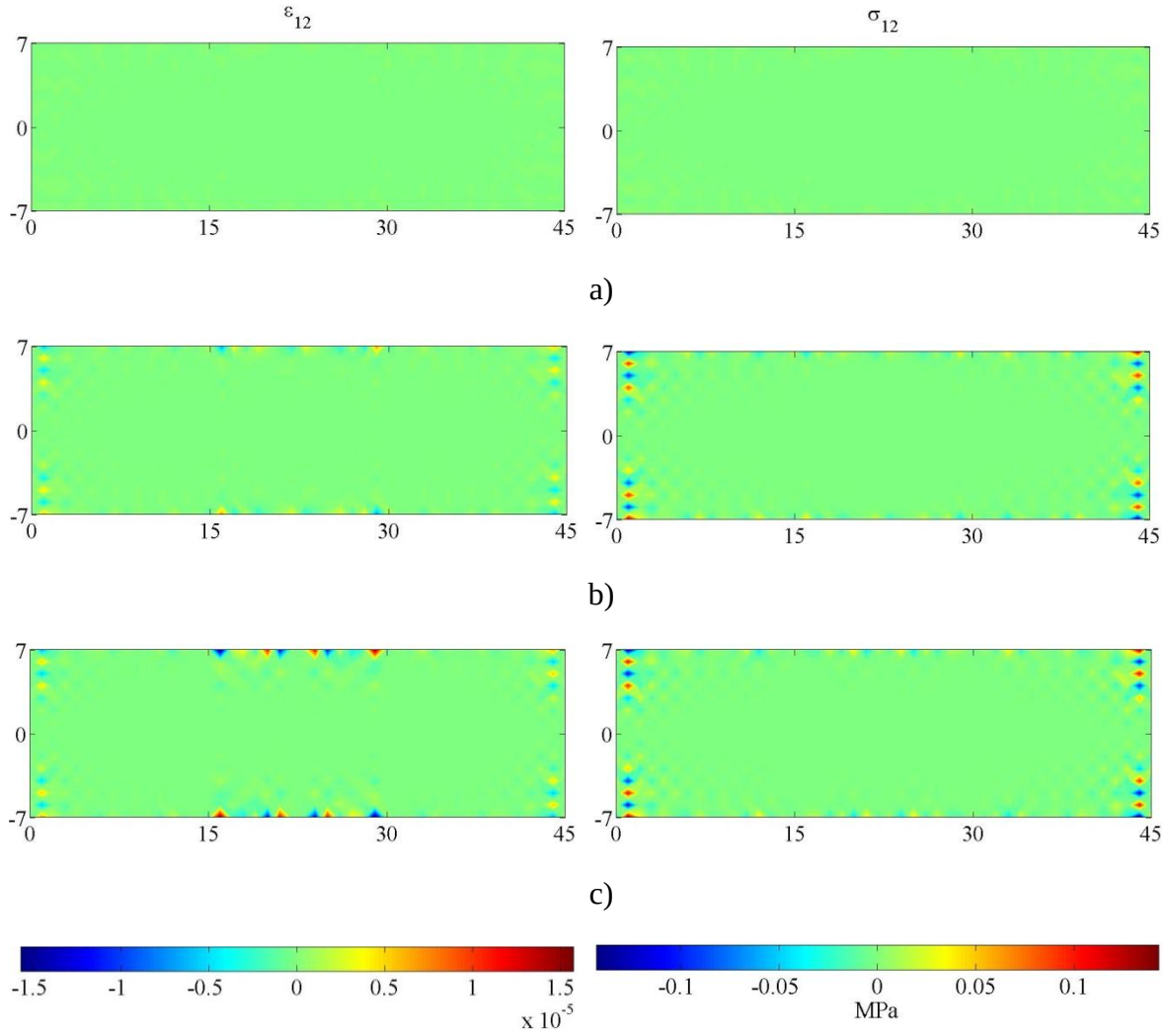

Figure 5.94: Case Eight – ε_{12} and σ_{12} for -Δu= a) 0.0014 cm, b) 0.0338 cm, and c) 0.0520 cm.

Figure 5.95 describes the effective strain and stress response within the structure at the three loading stages afore mentioned. Stress response shows overall uniform stress distribution with stress bands that are attributed to the load induced heterogeneity in the material. Strain response show higher strains within the inclusion and strain concentrations at the peak stage. At this stage vertical bands are formed.

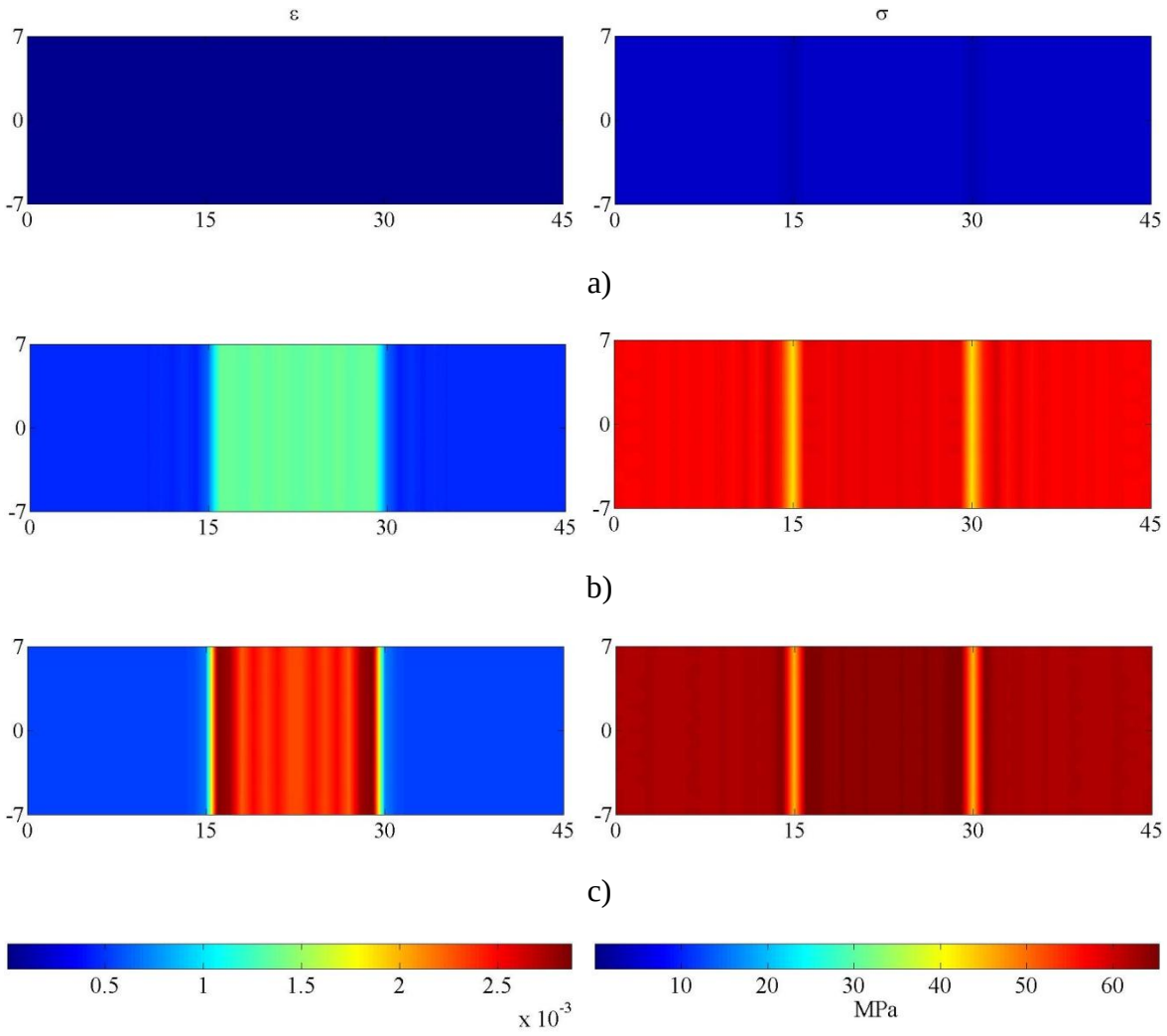

Figure 5.95: Case Eight – ε and σ for -Δu= a) 0.0014 cm, b) 0.0338 cm, and c) 0.0520 cm.

Figures 5.96-5.99 describe the gradient strain –double stress response of the structure at the three loading stages afore mentioned. Strain gradient results illustrate, at the peak stage, high tensile and compressive concentrations that suggest vertical fracture along the sides of the inclusion with less severe vertical fractures within the inclusion.

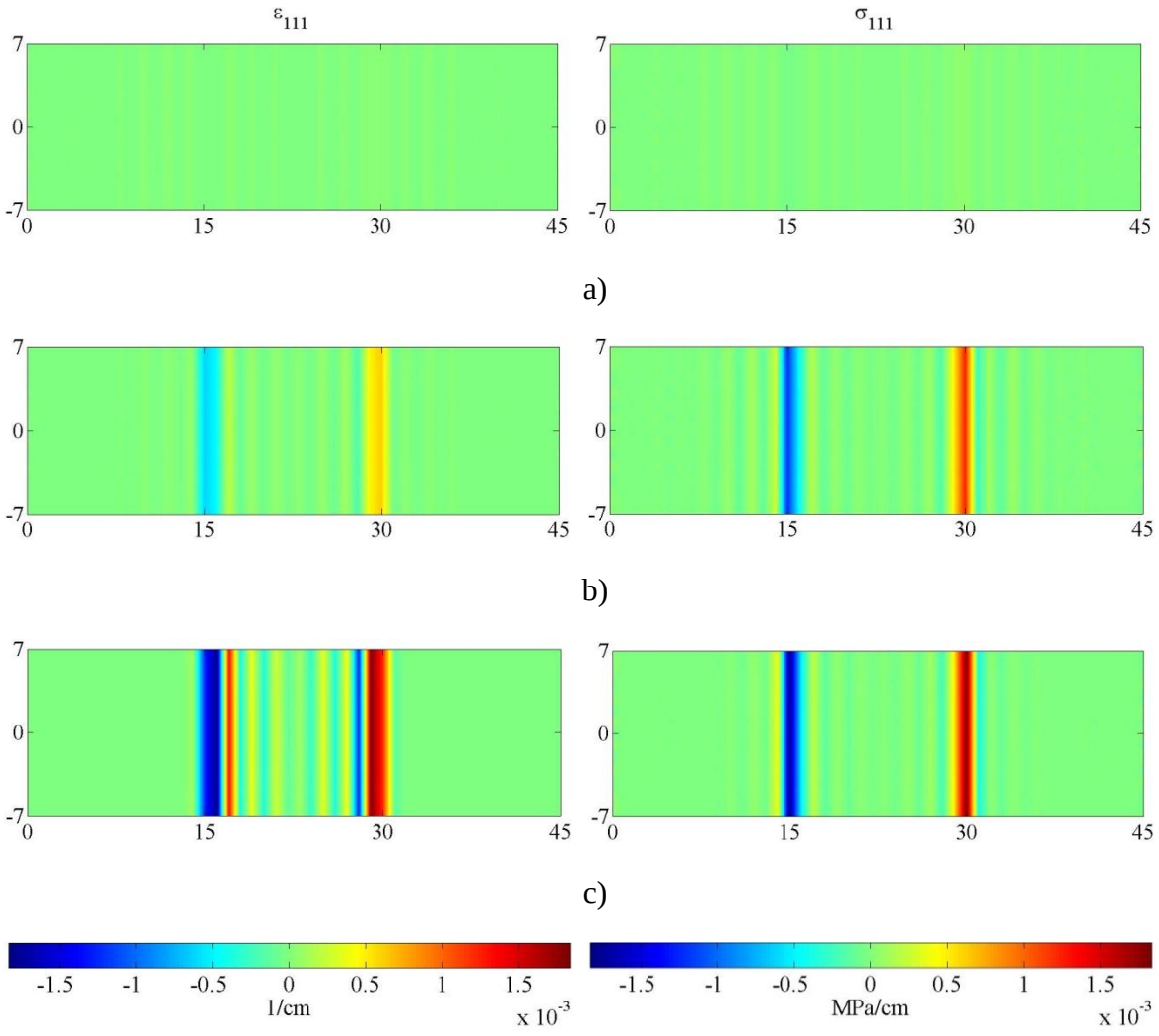

Figure 5.96: Case Eight – ε_{111} and σ_{111} for -Δu= a) 0.0014 cm, b) 0.0338 cm, and c) 0.0520 cm.

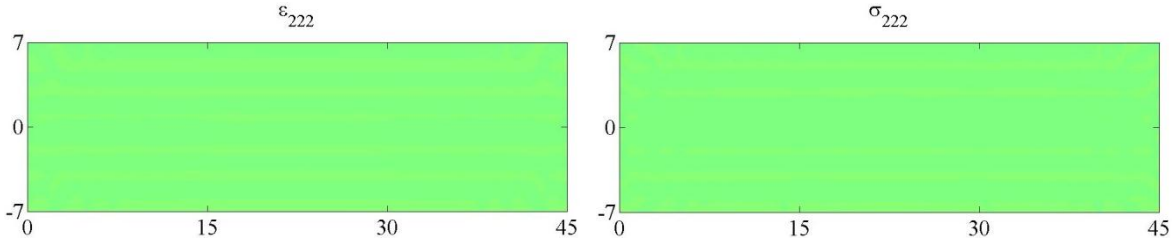

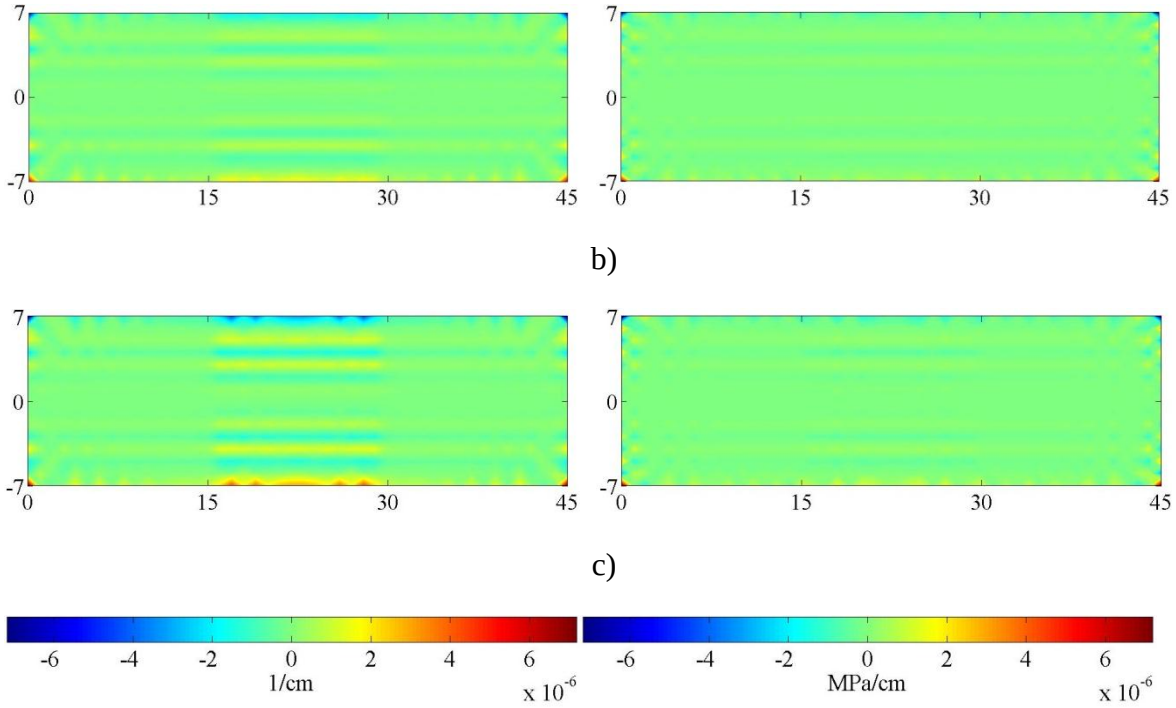

Figure 5.97: Case Eight – ε_{222} and σ_{222} for -Δu= a) 0.0014 cm, b) 0.0338 cm, and c) 0.0520 cm.

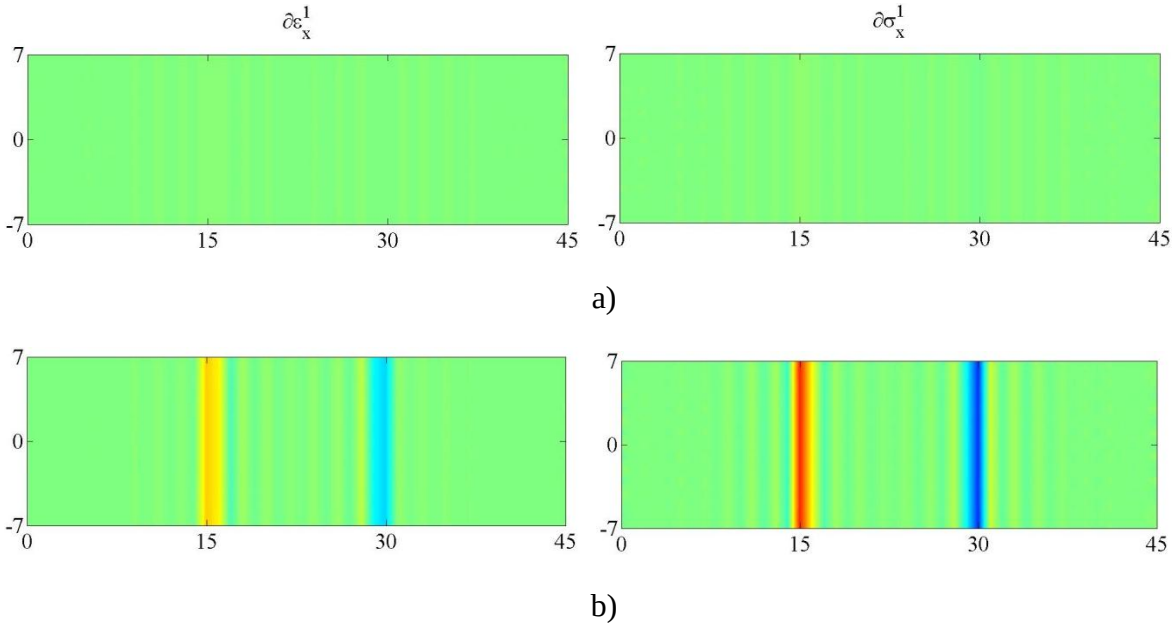

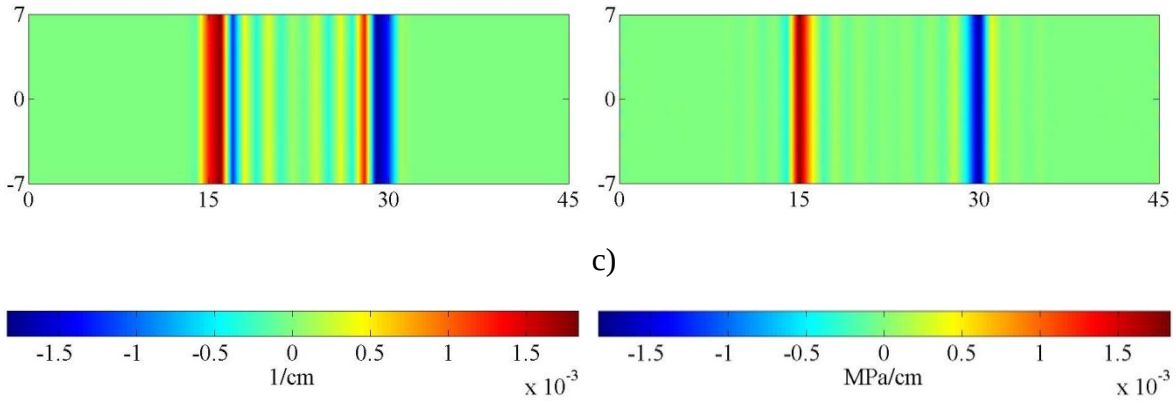

c)

Figure 5.98: Case Eight – Effective gradient strains and double stresses in the 1-direction for -Δu= a) 0.0014 cm, b) 0.0338 cm, and c) 0.0520 cm.

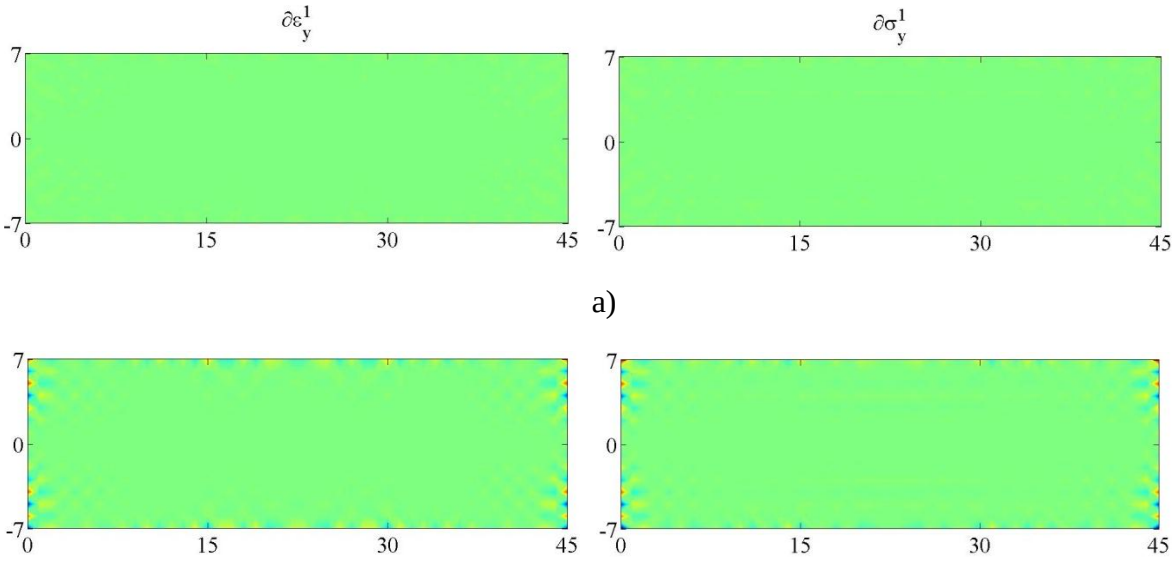

a)

b)

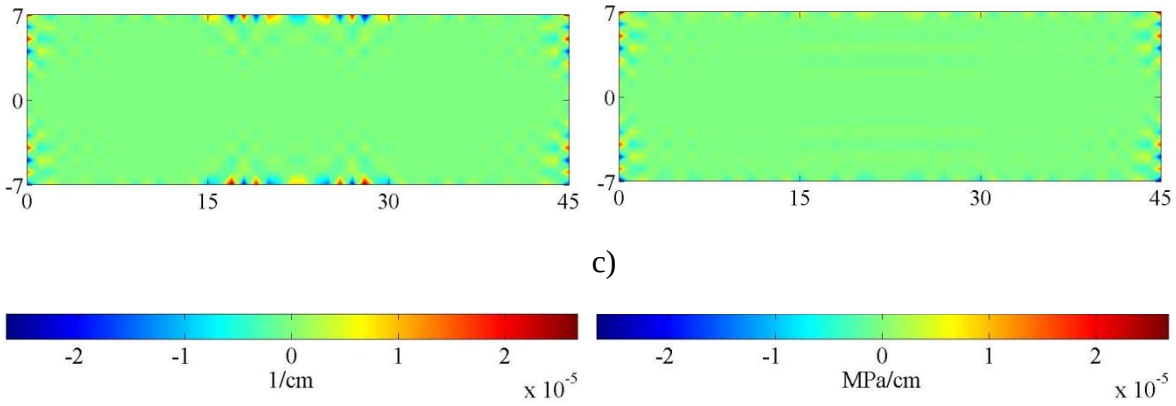

Figure 5.99: Case Eight – Effective gradient strains and double stresses in the 2-direction for -Δu= a) 0.0014 cm, b) 0.0338 cm, and c) 0.0520 cm.

5.4.11. Case Nine: Compressive loading with square inclusion and no constraints (L_0=10 mm).

In this simulation, the 2D plate is subjected to compression by applying shrink displacements along its right side. In addition, the plate has a centered square inclusion that is forty percent softer than the plate material and it is modeled with a particle size of L_0=10 mm. The length and height of the plate and the inclusion are 45 cm×14 cm and 4 cm×4 cm, respectively. The plate is constrained in the 1-direction along its left border while the top and bottom have no constraints (See Figure 5.6).

The response of the structure is shown in Figures 5.100-5.108 at three loading stages: initial, pre-peak, and peak stage. Figure 5.100 shows the overall stress-strain response in the '11' and '22' directions. Figures 5.101-5.103 show the strain and stress responses in the '11', '22', and '12' directions, and their effective magnitudes are shown in Figure 5.104. Strain gradient and double stress response are shown in Figures 5.105-5.106, and their effective magnitudes are described in Figures 5.107-5.108.

The overall stress-strain response of the plate in the '11' and '22' directions is described in Figure 5.100 and shows a uniaxial stress state with non-linear softening behavior.

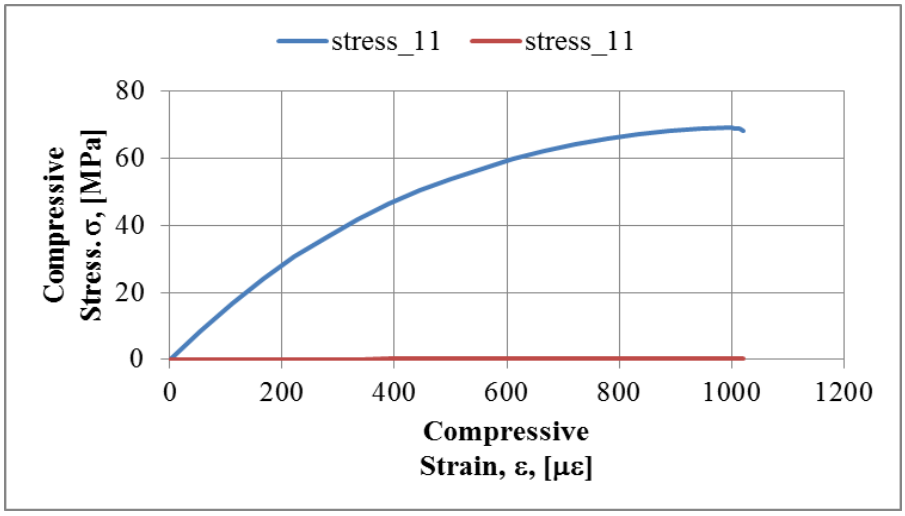

Figure 5.100: Case Nine – Overall stress-strain behavior of the plate.

Figure 5.101 describes the strain and stress response of the structure in the '11' direction at the three loading stages afore mentioned. Stress response shows overall uniform stress distribution with low stresses within the inclusion and high stress concentrations around the top and bottom of the inclusion that branch out in a 'X' shape. Strain response show higher strains within the inclusion and strain concentrations at the peak stage describing an 'X' shear shape band.

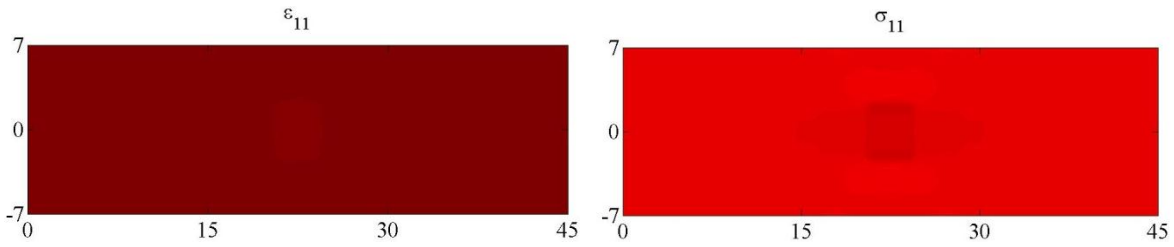

a)

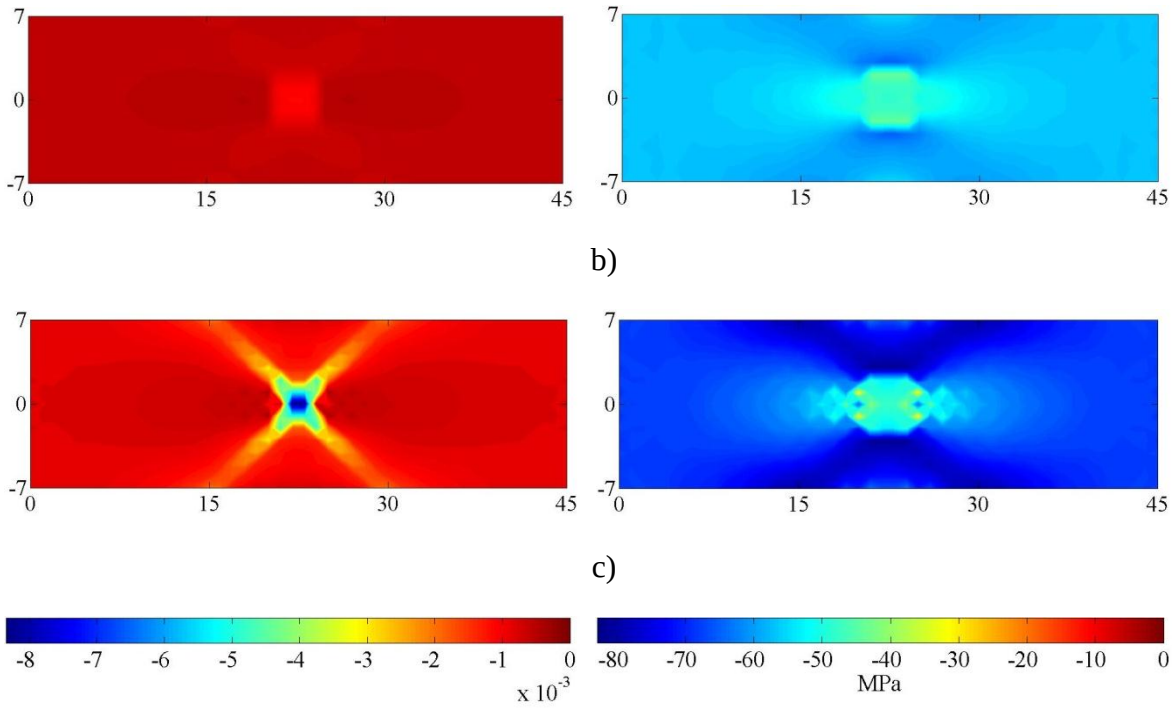

Figure 5.101: Case Nine – ε_{11} and σ_{11} for -Δu= a) 0.0005 cm, b) 0.0106 cm, and c) 0.0191 cm.

Figure 5.102 describes the strain and stress response of the structure in the '22' direction at the three loading stages afore mentioned. Stress response shows overall uniform zero stress distribution with stress compressive concentrations within the inclusion and tensile diagonal concentrations branching out from the sides of the inclusion. Strain response show expansion behavior with higher strains within the inclusion and strain concentrations at the peak stage. At this stage an 'X' shape fine shear band is formed.

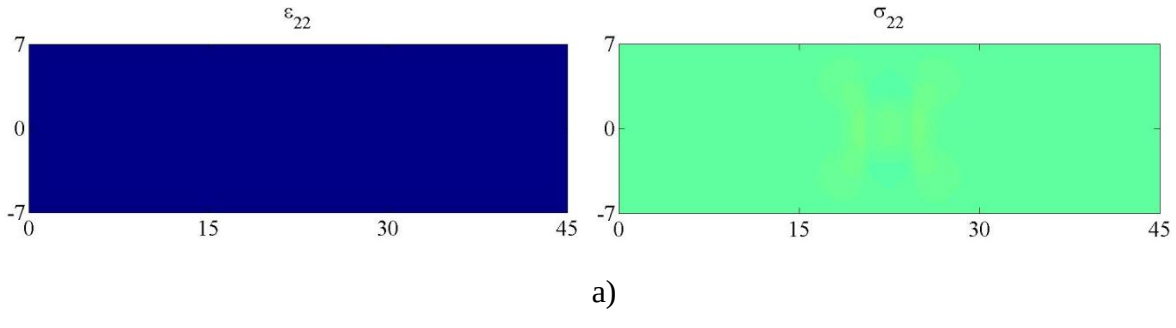

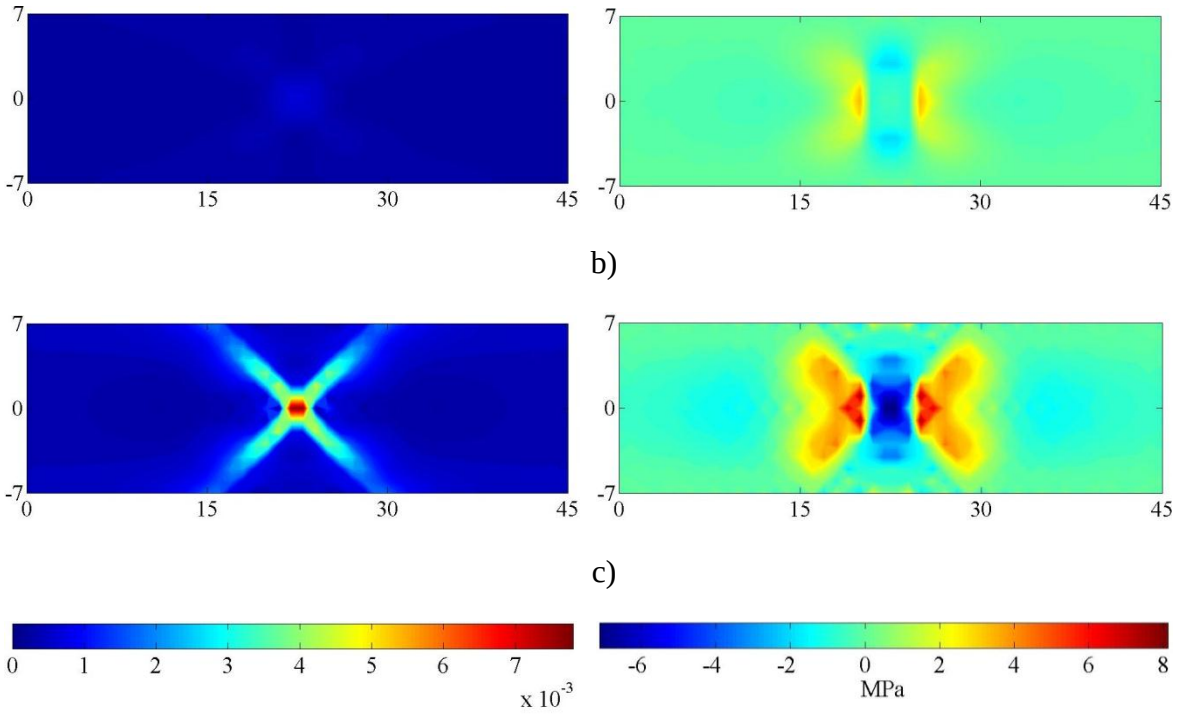

Figure 5.102: Case Nine – ε_{22} and σ_{22} for -Δu= a) 0.0005 cm, b) 0.0106 cm, and c) 0.0191 cm.

Figure 5.103 describes the strain and stress response of the structure in the '12' direction at the three loading stages afore mentioned. Strain and stress response shows concentrations at the corners of the inclusion that become more severe describing two 'X' shear bands.

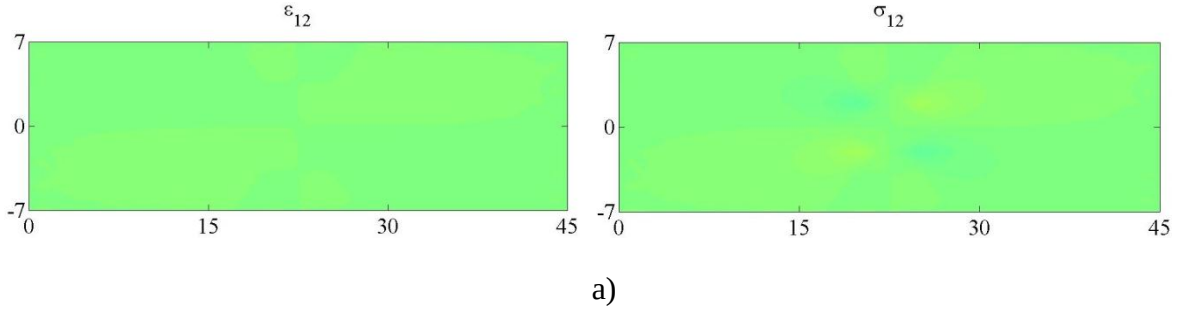

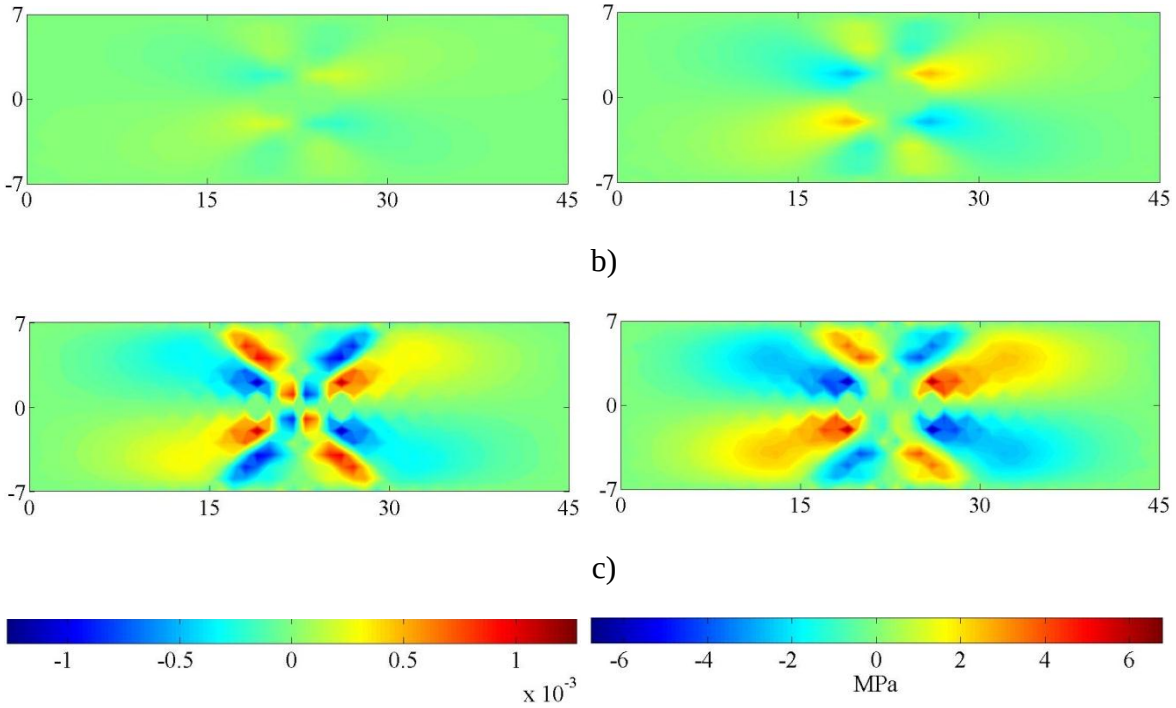

Figure 5.103: Case Nine – ε_{12} and σ_{12} for -Δu= a) 0.0005 cm, b) 0.0106 cm, and c) 0.0191 cm.

Figure 5.104 describes the effective strain and stress response within the structure at the three loading stages afore mentioned. Stress response shows overall uniform stress distribution with stress concentrations on top and bottom of the inclusion that later branch out in an 'X' shape. Strain response shows higher strains within the inclusion and strain concentrations at the peak stage. At this stage an 'X' shape fine shear band is formed.

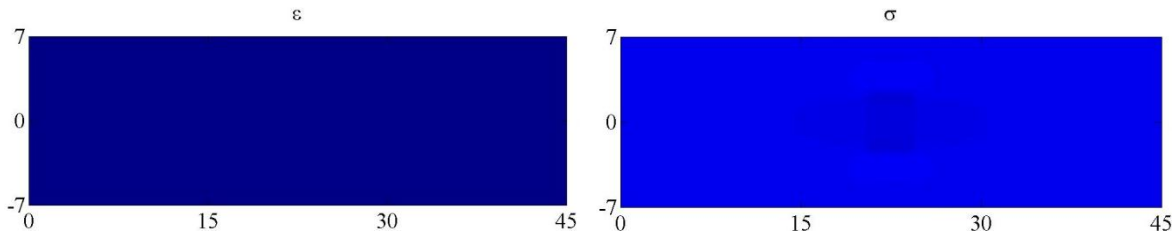

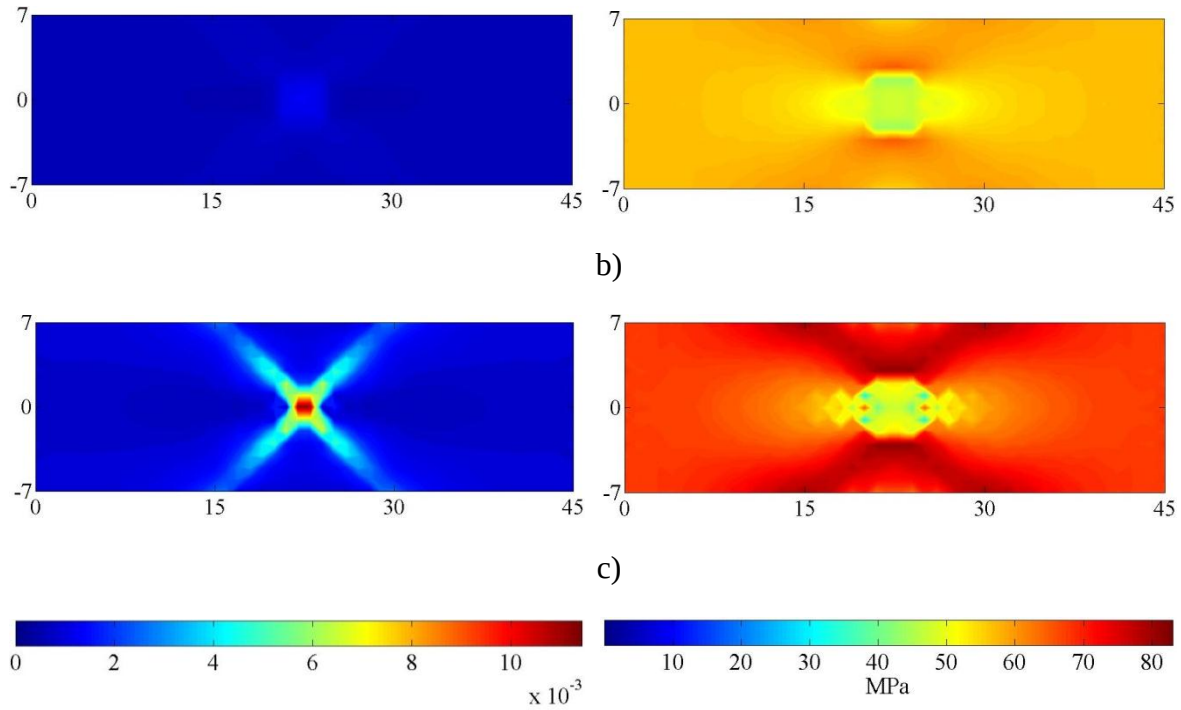

Figure 5.104: Case Nine – ε and σ for -Δu= a) 0.0005 cm, b) 0.0106 cm, and c) 0.0191 cm.

Figures 5.105-5.108 describe the gradient strain –double stress response of the structure at the three loading stages afore mentioned. Strain gradient results describe, at the peak stage, high tensile and compressive concentrations that suggest an 'X' shear shape fracture.

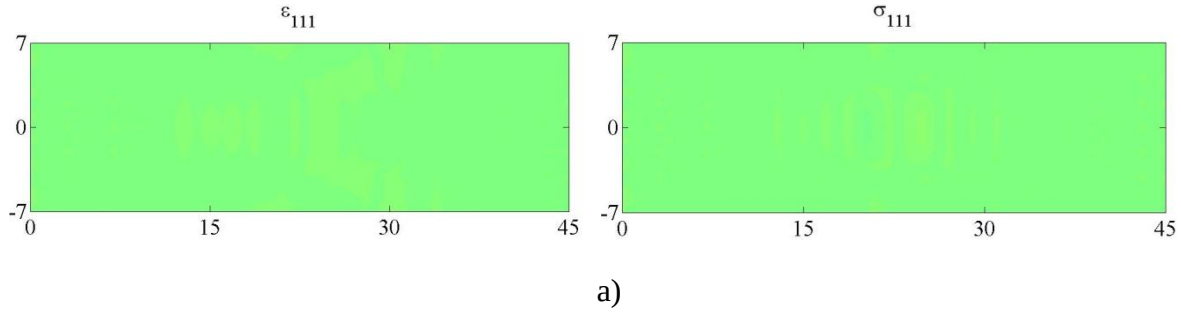

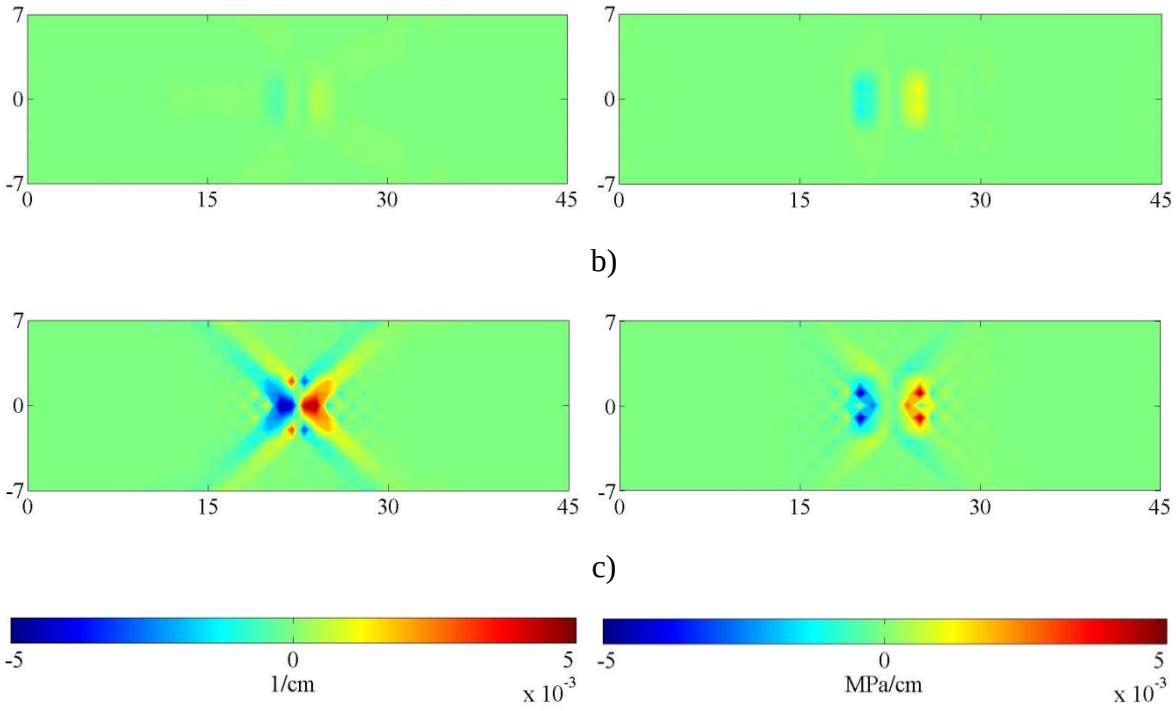

Figure 5.105: Case Nine – ε_{111} and σ_{111} for -Δu= a) 0.0005 cm, b) 0.0106 cm, and c) 0.0191 cm.

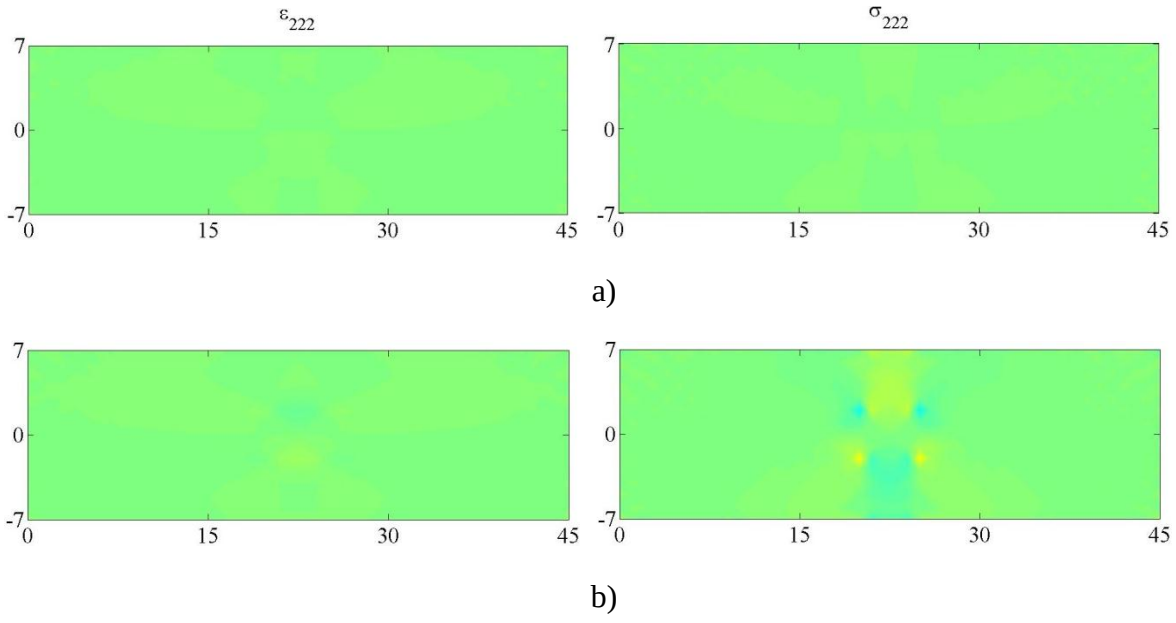

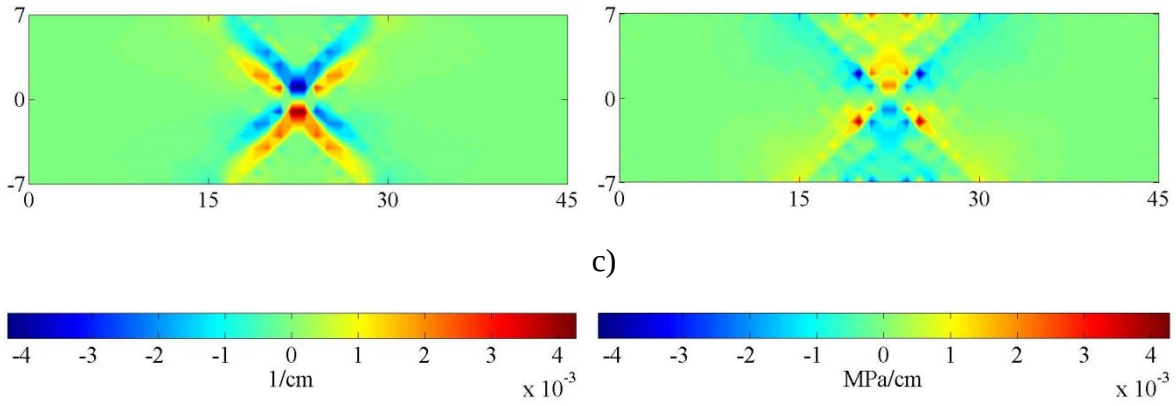

c)

Figure 5.106: Case Nine – ε_{222} and σ_{222} for -Δu= a) 0.0005 cm, b) 0.0106 cm, and c) 0.0191 cm

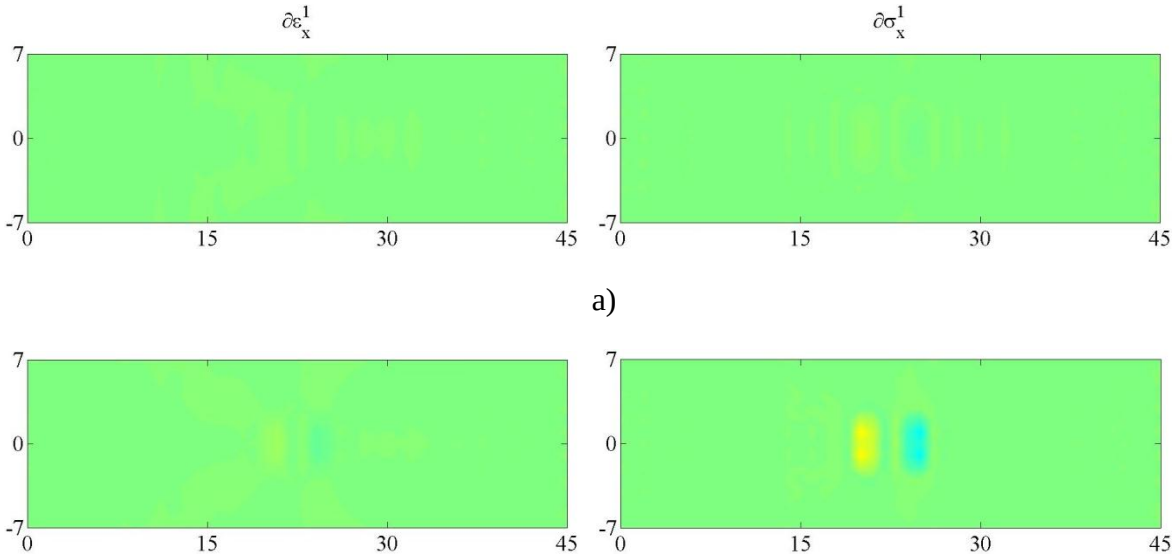

a)

b)

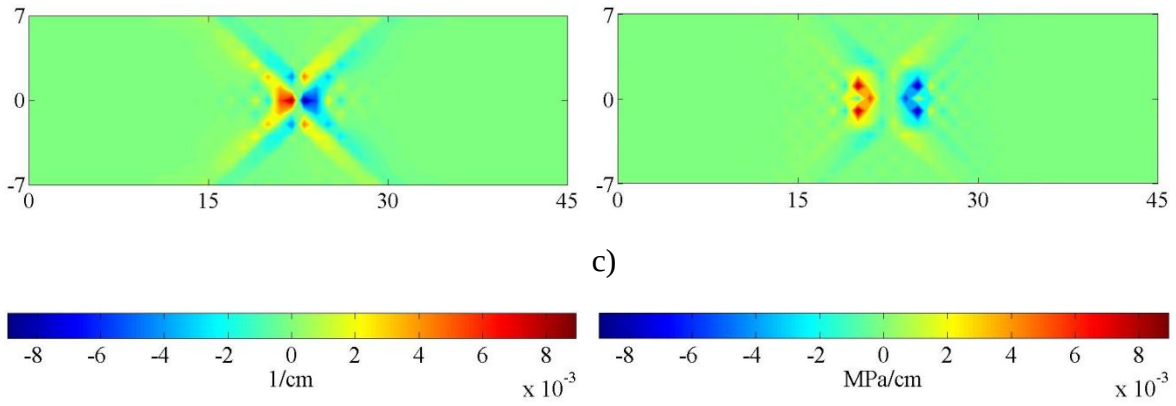

c)

Figure 5.107: Case Nine – Effective gradient strains and double stresses in the 1-direction for -Δu= a) 0.0005 cm, b) 0.0106 cm, and c) 0.0191 cm.

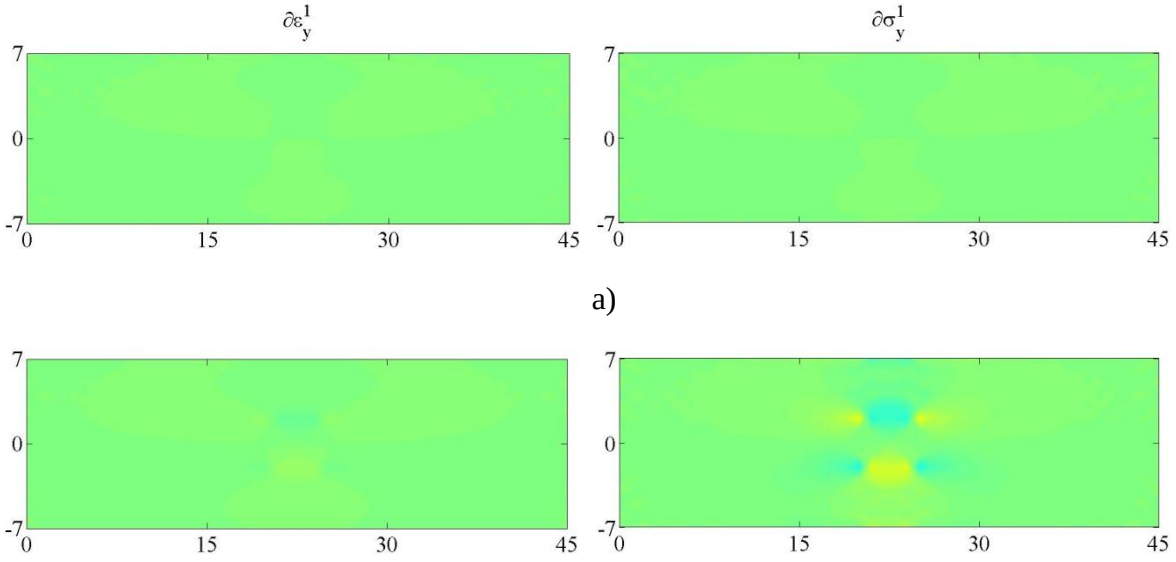

a)

b)

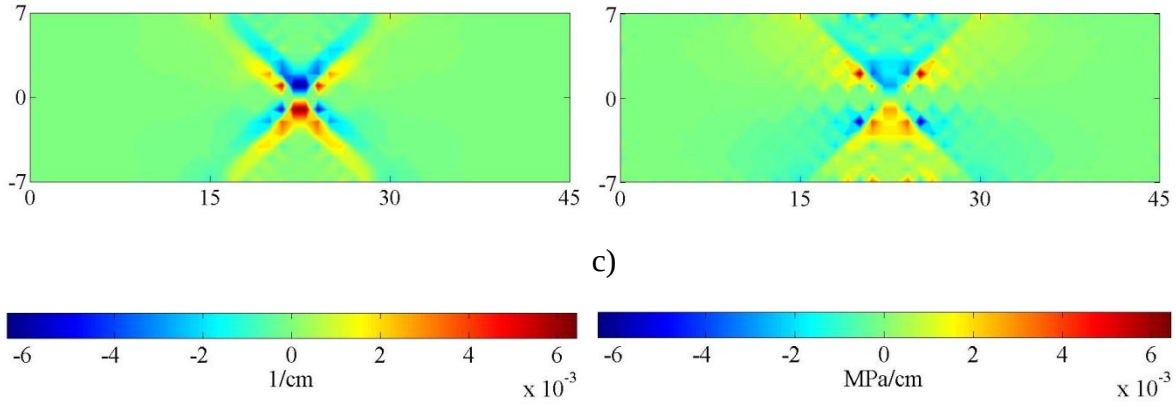

Figure 5.108: Case Nine – Effective gradient strains and double stresses in the 2-direction for -Δu= a) 0.0005 cm, b) 0.0106 cm, and c) 0.0191 cm.

5.4.12. Case Ten: Compressive loading with square inclusion and transverse constraints (L_0=10 mm).

In this simulation, the 2D plate is subjected to compression by applying shrink displacements along its right side. In addition, the plate has a centered square inclusion that is forty percent softer than the plate material and it is modeled with a particle size of L_0=10 mm. The length and height of the plate and the inclusion are 45 cm×14 cm and 4 cm×4 cm, respectively. The plate is constrained in the 1-direction along its left border while the top and bottom are constrained from vertical translation (See Figure 5.7).

The response of the structure is shown in Figures 5.109-5.117 at three loading stages: initial, pre-peak, and peak stage. Figure 5.109 shows the overall stress-strain response in the '11' and '22' directions. Figures 5.110-5.112 show the strain and stress responses in the '11', '22', and '12' directions, and their effective magnitudes are shown in Figure 5.113. Strain gradient and double stress responses are shown in Figures 5.114-5.115, and their effective magnitudes are described in Figures 5.116-5.117.

The overall stress-strain response of the plate in the '11' and '22' directions is described in Figure 5.109 and shows a biaxial stress state with non-linear softening behavior.

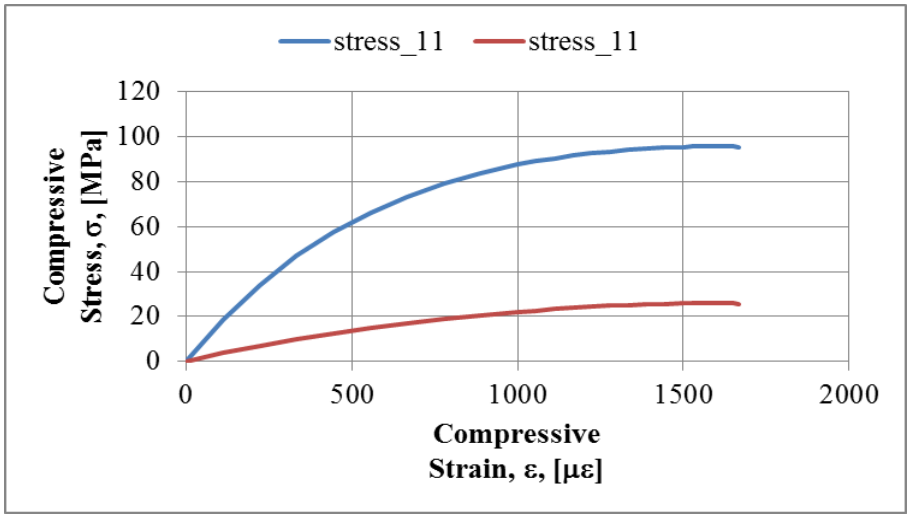

Figure 5.109: Case Ten – Overall stress-strain behavior of the plate.

Figure 5.110 describes the strain and stress response of the structure in the '11' direction at the three loading stages afore mentioned. Stress response shows overall uniform stress distribution with low stresses within the inclusion and high stress concentrations around the top and bottom of the inclusion. Strain response show higher strains within the inclusion and strain concentrations at the peak stage along the sides of the inclusion that expand out from the corners forming an 'X' shape like a shear band with smaller inclination angles.

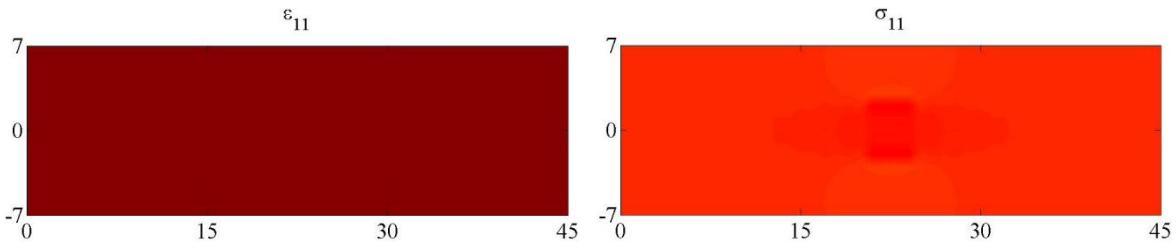

a)

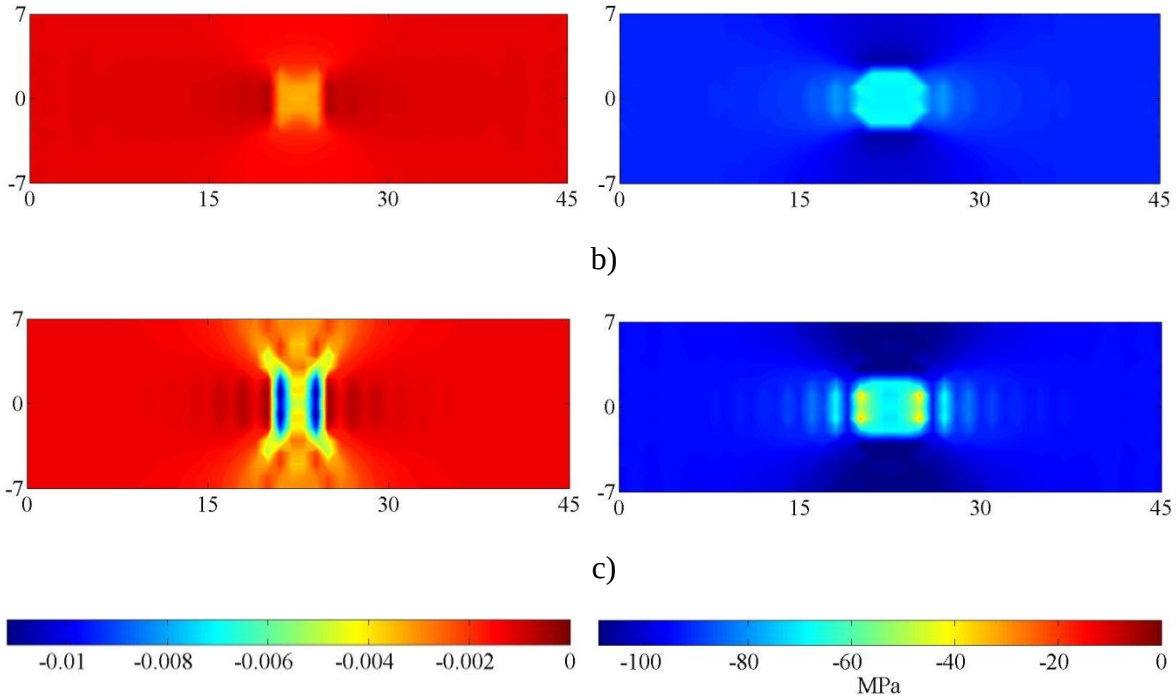

Figure 5.110: Case Ten – ε_{11} and σ_{11} for -Δu= a) 0.0050 cm, b) 0.0550 cm, and c) 0.0750 cm.

Figure 5.111 describes the strain and stress response of the structure in the '22' direction at the three loading stages afore mentioned. Stress response shows overall uniform stress distribution with stress concentrations within the inclusion that branch out from the top and bottom sides. Strain response show compressive strain concentration at the center of the inclusion, and tensile concentrations around the inclusion that become higher and branch out from the top and bottom side of the inclusion describing a 'W' and 'M' like shape.

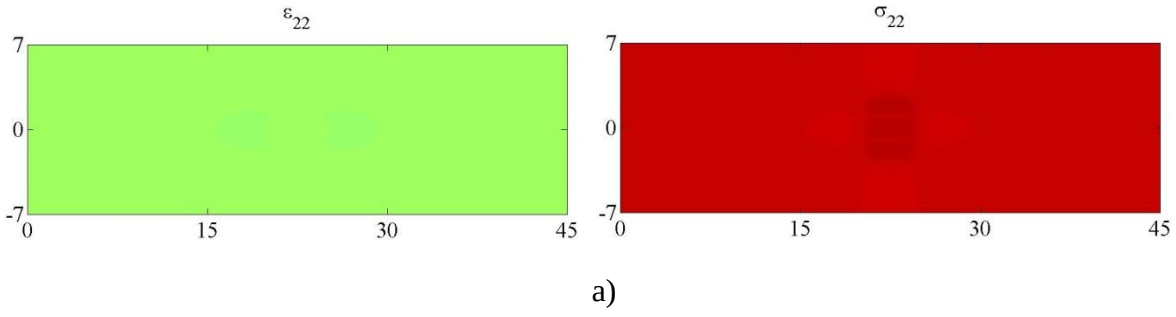

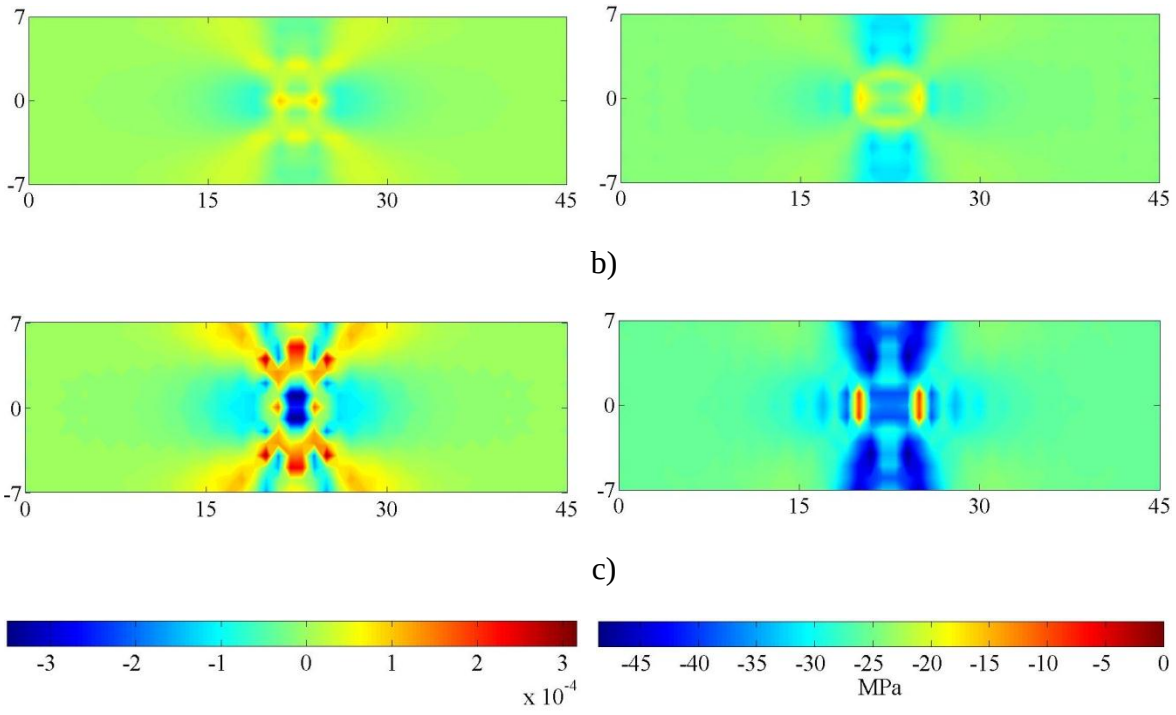

Figure 5.111: Case Ten – ε_{22} and σ_{22} for -Δu= a) 0.0050 cm, b) 0.0550 cm, and c) 0.0750 cm.

Figure 5.112 describes the strain and stress response of the structure in the '12' direction at the three loading stages afore mentioned. Strain and stress response shows concentrations at the corners of the inclusion that become more severe as the load increases.

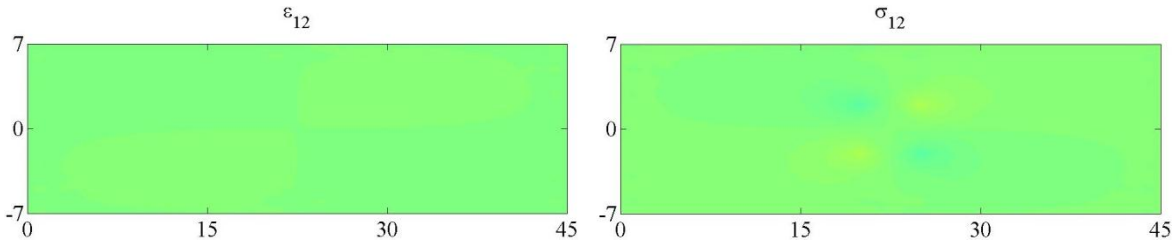

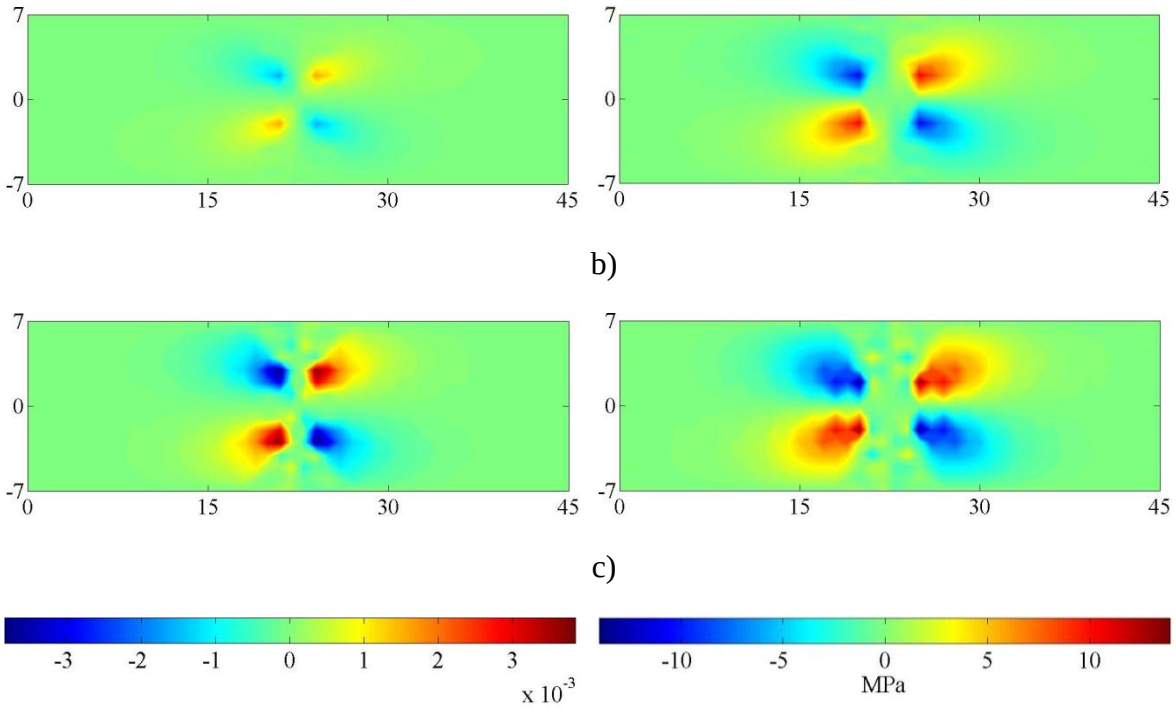

Figure 5.112: Case Ten – ε_{12} and σ_{12} for -Δu= a) 0.0050 cm, b) 0.0550 cm, and c) 0.0750 cm.

Figure 5.113 describes the effective strain and stress response within the structure at the three loading stages afore mentioned. Stress response shows overall uniform stress distribution with stress concentrations on top and bottom of the inclusion. Strain response show higher strains within the inclusion and strain concentrations at the peak stage that expand out from the corners of the inclusion forming an 'X' shape like a shear band with a smaller inclination angle.

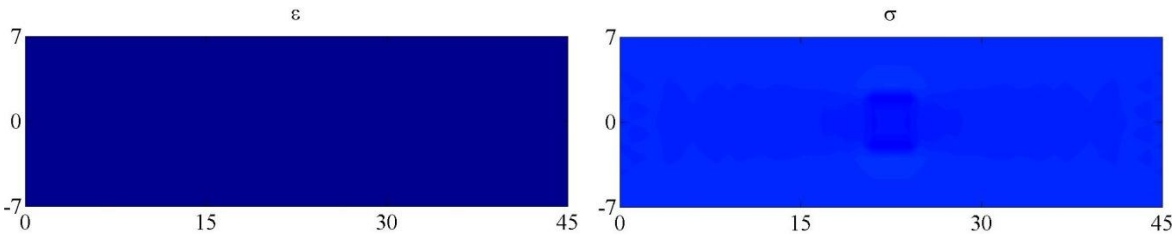

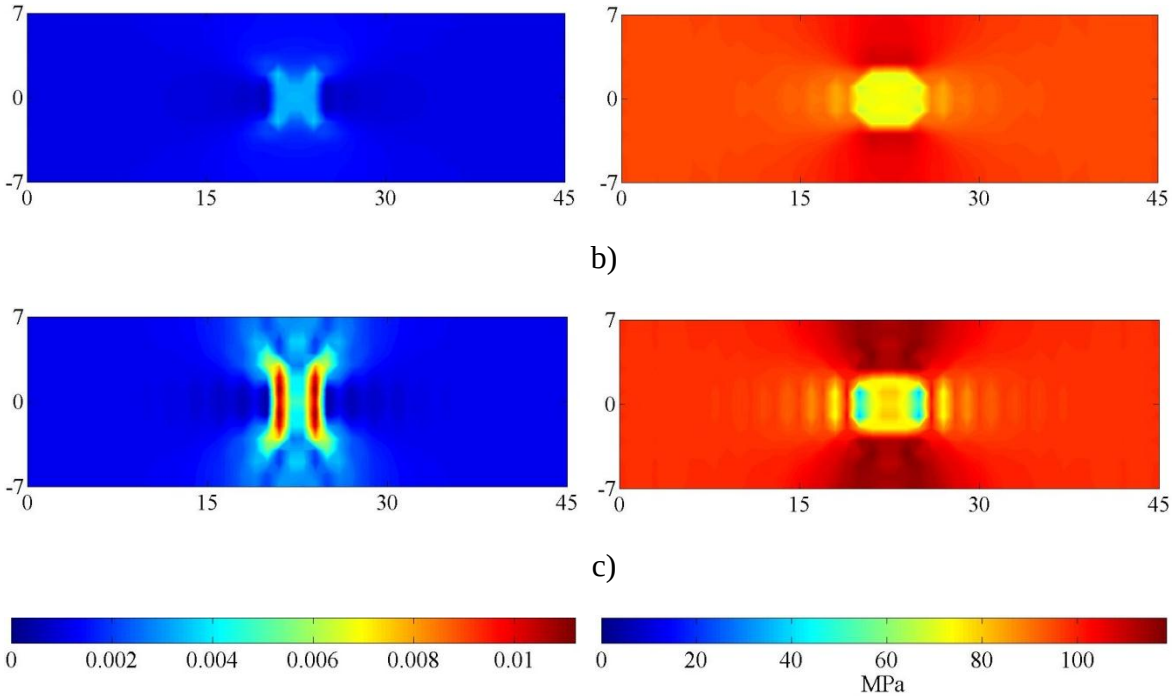

Figure 5.113: Case Ten – ε and σ for -Δu= a) 0.0050 cm, b) 0.0550 cm, and c) 0.0750 cm.

Figures 5.114-5.117 describe the gradient strain –double stress response of the structure at the three loading stages afore mentioned. Strain gradient results describe, at the peak stage, high tensile and compressive concentrations that suggest an 'X' shear shape fracture with vertical fractures within the inclusion.

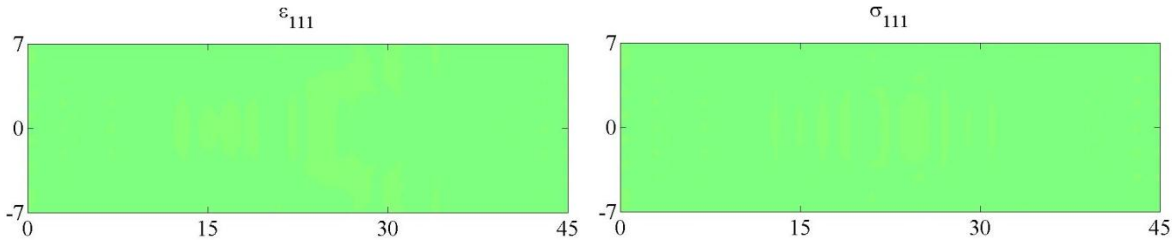

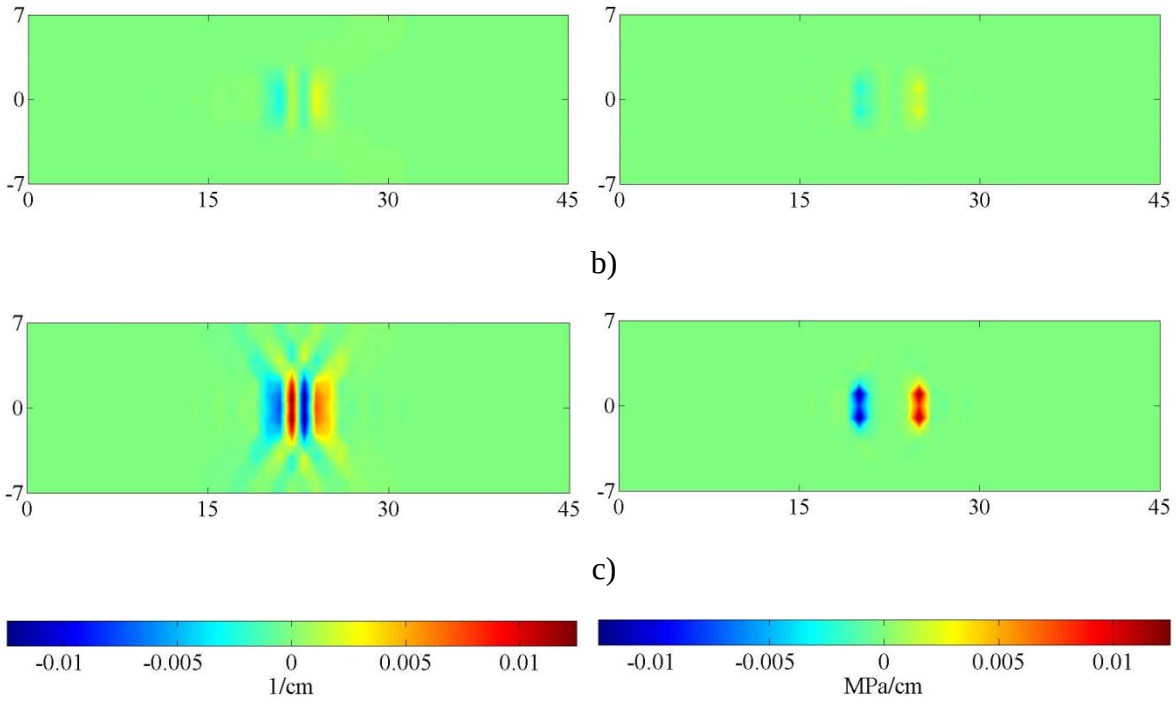

Figure 5.114: Case Ten – ε_{111} and σ_{111} for -Δu= a) 0.0050 cm, b) 0.0550 cm, and c) 0.0750 cm.

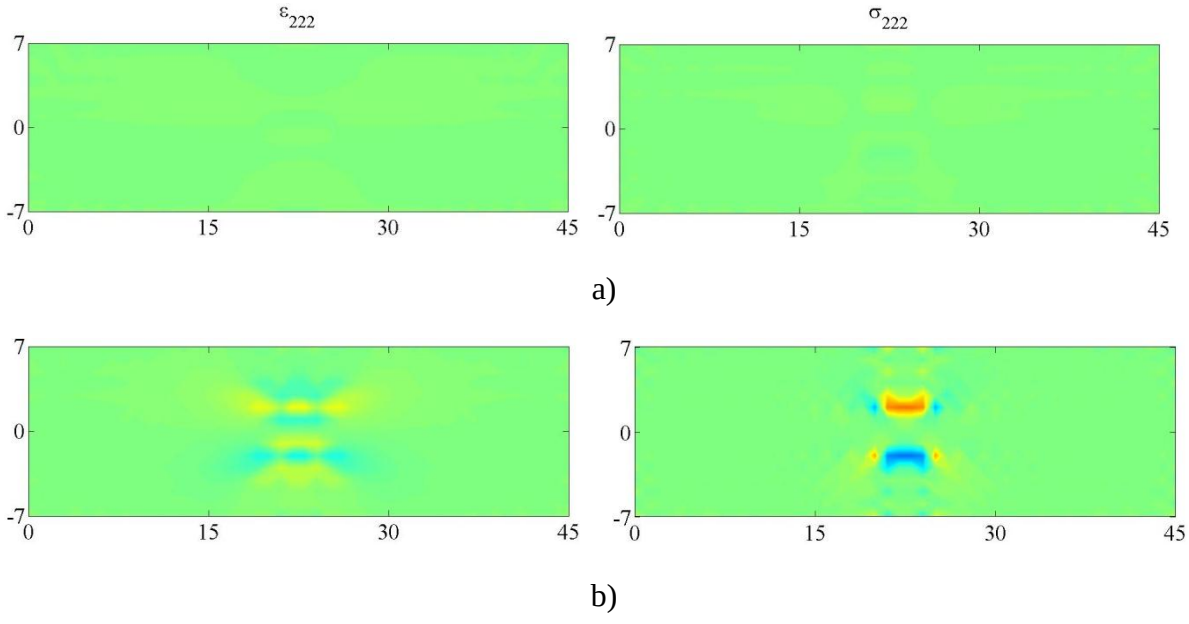

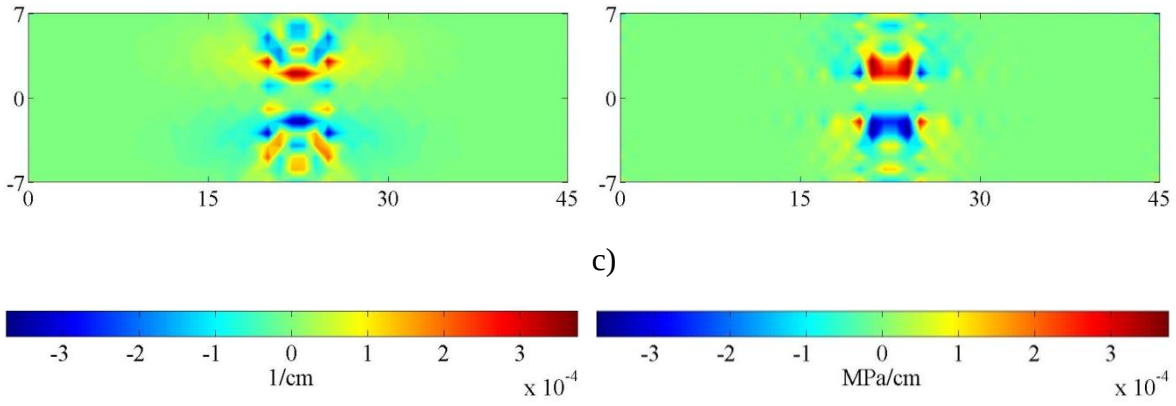

c)

Figure 5.115: Case Ten – ε_{222} and σ_{222} for -Δu= a) 0.0050 cm, b) 0.0550 cm, and c) 0.0750 cm.

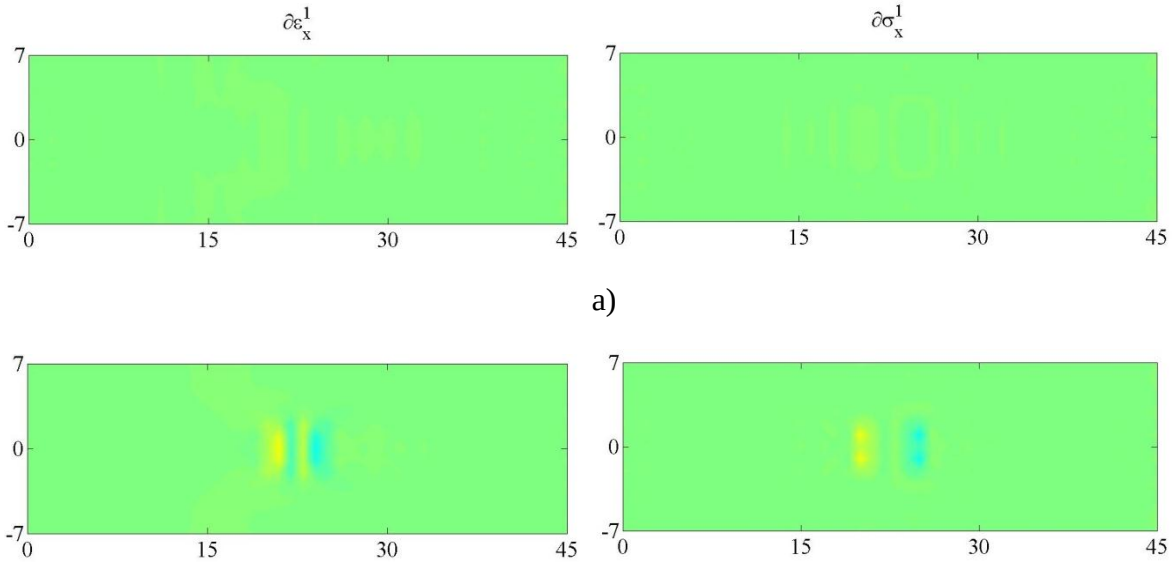

a)

b)

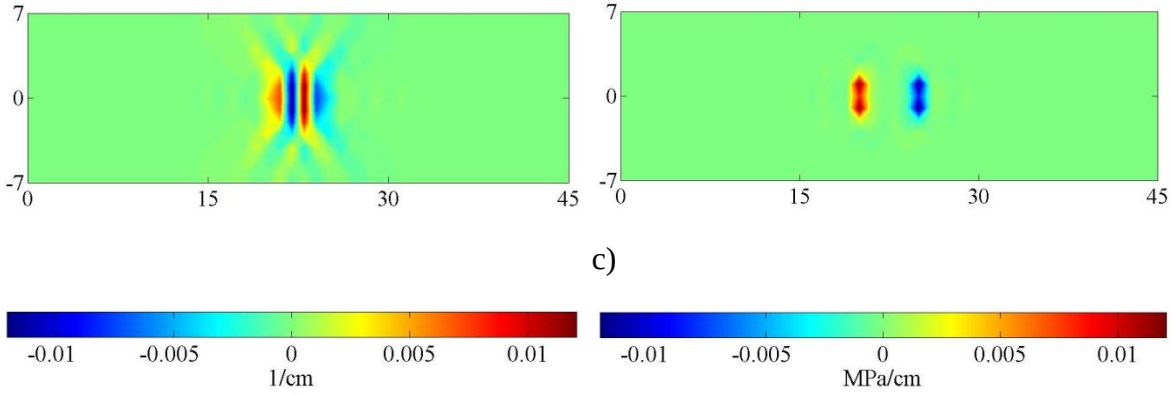

c)

Figure 5.116: Case Ten – Effective gradient strains and double stresses in the 1-direction for -Δu= a) 0.0050 cm, b) 0.0550 cm, and c) 0.0750 cm.

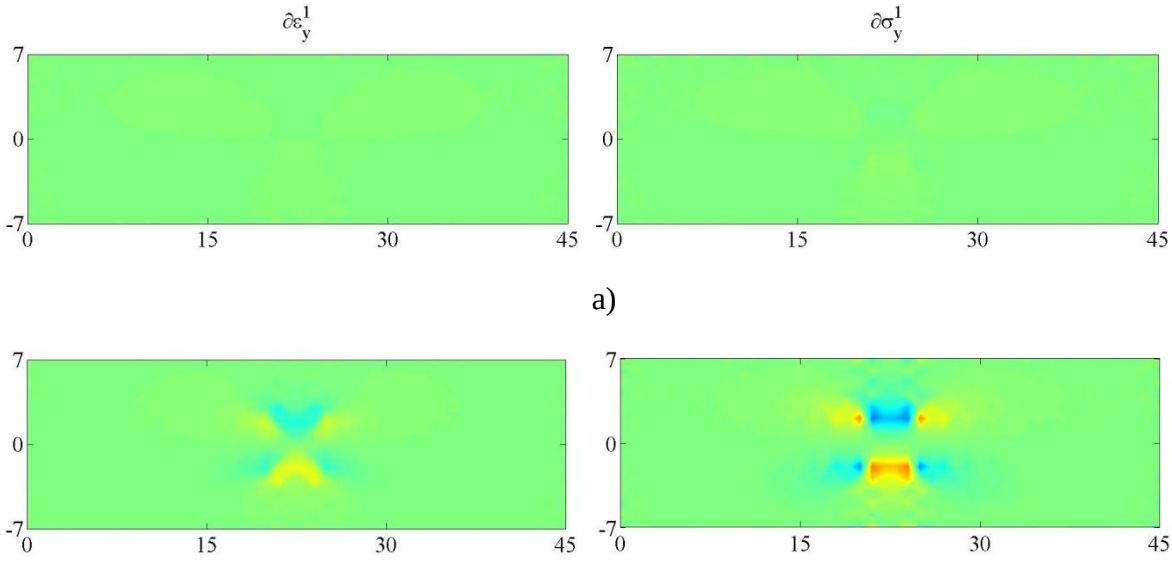

a)

b)

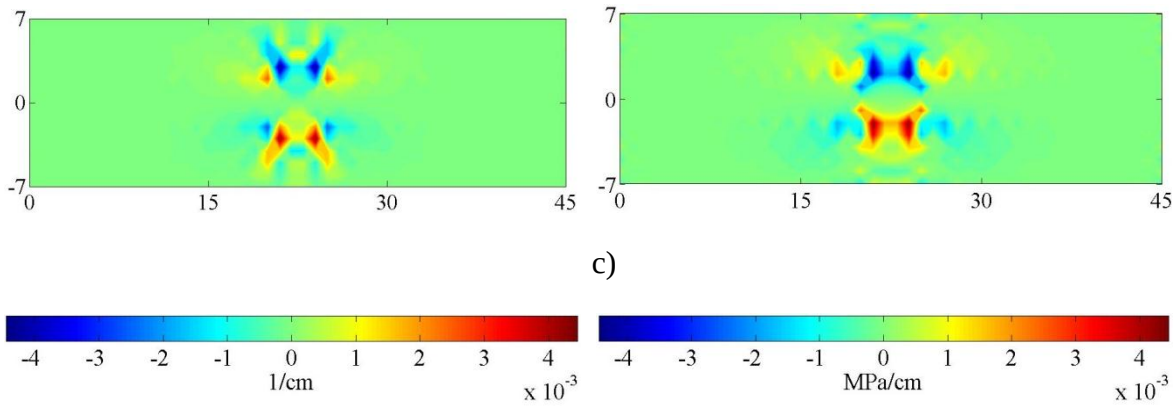

Figure 5.117: Case Ten – Effective gradient strains and double stresses in the 2-direction for -Δu= a) 0.0050 cm, b) 0.0550 cm, and c) 0.0750 cm.

CHAPTER 6. Summary and Conclusions.

6.1. Summary.

The objective of this study is to develop a model that captures and describes the non-linear response of granular solids by developing a constitutive law and a numerical simulation that 1) captures the underlying strain-softening failure mechanisms at the micro level to accurately describe behavior at the macro level and 2) overcomes the deficiencies of finite element by implementing the model into a mesh-free numerical method that captures the structural response and damage development of the material under the presence of pre-existing imperfections . A micromechanics approach and gradient theory is used to derive the constitutive law of the model. The numerical simulation is derived by using a mesh-free method with an element-free-Galerkin formulation. The next sections summarize the sequence used in the derivation of the model.

6.1.1. Idealization and kinematics of the granular system.

The granular system is idealized as a collection of spherical particles connected by pseudo-bonds from which motion equations for the displacement and rotation are described in section 3.1.

6.1.2. Constitutive law.

The local constitutive laws for the force-displacement and moment-rotation of two interacting particles are described in section 3.2. Then, the use of gradient theory, to derive the constitutive laws of the idealized system using 1^{st} and 2^{nd} gradient theory, is described in section

3.4 and section 3.6, respectively. At the local contact surface between particles, the displacement and rotational stiffness are decomposed in the normal and tangential directions, this is described in section 3.2. The force-displacement and moment-rotation potential functions, between two particles for the normal and tangential direction, are described in section 3.3. The displacement and rotational fields are defined using Taylor's expansion and the model's constitutive stress-strain laws are derived by using an energy approach described in sections 3.4 and 3.6.

The global constitutive law is determined by the summation of all the inter-granular interactions over the representative volume. For this integration, an integral form with a density function is used and the global constitutive law is determined and described in sections 3.4 and 3.6.

6.1.3. Derivation of the energy functional and weak-form and its numerical implementation.

For the numerical implementation, the derivation of the energy functional and weak-form using the Galerkin method is described in section 4.1. In this derivation, the natural and essential boundary conditions are determined.

The weak-form equation based on the Galerkin method is used with MLS approximation functions, at the local domain, to obtain the value of the displacements at a specific nodal location, thus discretizing the equations. Derivation of the MLS shape functions is described in section 4.3. Then, the Galerkin weak-form integrals are evaluated by a set of background cells that are defined in section 5.1.

6.2. Conclusions.

This study provides a relatively simple and a realistic method for deriving a model that captures the strain-softening and non-linear failure behavior of granulate materials. The main contributions and findings from this study are described below:

- In Chapter 3, a micromechanical constitutive model with 2nd gradient theory that includes displacement and rotational effects is derived. The model has the capability to compute and describe successfully the failure mechanisms within the material at the contact level. In addition, the model describes the non-linear failure and fracture behavior of the material at the element level for different loading conditions (i.e. uniaxial, biaxial, triaxial, and shear). Furthermore, the model parameters are related to the material geometry and mechanical properties, and therefore, they have physical meaning and can potentially be used to identify/study the properties of the material that need to be enhanced and/or modified for a particular use.
- In Chapter 4, a weak-form equation based on the Galerkin method is derived for the numerical implementation of the model. For this purpose, a mesh-free program is developed where there is no need for meshing the structure, nor having nodal connectivity information, nor adaptive analysis to compute the structure's response. The performed numerical simulation demonstrates that the model successfully describes and captures the fracture process and non-linear failure behavior of the material at the structural level with the presence of pre-existing imperfections and different constraint conditions.
- With this gradient constitutive model and mesh-free program, further simulations under different loading conditions and geometries can potentially be used in the future to describe

the fracture process of concrete and other granular materials. In addition, the derived gradient constitutive model considers displacement and rotational effects, from which the first are evaluated in this study. The latter effects can be studied and implemented into a mesh-free program in future works.

References.

(*1-48*)

1. Askes, H., Pamin, J., and de Borst, R. (2000) Dispersion analysis and element-free Galerkin solutions of second- and fourth-order gradient-enhanced damage models, *International Journal for Numerical Methods in Engineering 49*, 811-832.
2. Bazant, Z. P. (1976) INSTABILITY, DUCTILITY, AND SIZE EFFECT IN STRAIN-SOFTENING CONCRETE, *Journal of the Engineering Mechanics Division-Asce 102*, 331-344.
3. Bazant, Z. P., Belytschko, T. B., and Chang, T. P. (1984) CONTINUUM THEORY FOR STRAIN-SOFTENING, *Journal of Engineering Mechanics-Asce 110*, 1666-1692.
4. Belytschko, T., Bazant, Z. P., Hyun, Y. W., and Chang, T. P. (1986) STRAIN-SOFTENING MATERIALS AND FINITE-ELEMENT SOLUTIONS, *Computers & Structures 23*, 163-180.
5. Belytschko, T., Lu, Y. Y., and Gu, L. (1994) ELEMENT-FREE GALERKIN METHODS, *International Journal for Numerical Methods in Engineering 37*, 229-256.
6. Chang, C. S., and Liao, C. L. (1990) Constitutive Relation for a Particulate Medium with the Effect of Particle Rotation, *International Journal of Solids and Structures 26*, 437-453.
7. Chang, C. S., and Ma, L. (1991) A Micromechanical-Based Micropolar Theory for Deformation of Granular Solids, *International Journal of Solids and Structures 28*, 67-86.

8. Chang, C. S., and Gao, J. (1996) Kinematic and static hypotheses for constitutive modeling of granulates considering particle rotation, *Acta Mechanica 115*, 213-229.

9. Chang, C. S., Askes, H., and Sluys, L. J. (2002) Higher-order strain/higher-order stress gradient models derived from a discrete microstructure, with application to fracture, *Engineering Fracture Mechanics 69*, 1907-1924.

10. Chang, C. S., Wang, T. K., Sluys, L. J., and van Mier, J. G. M. (2002) Fracture modeling using a micro-structural mechanics approach - I. Theory and formulation, *Engineering Fracture Mechanics 69*, 1941-1958.

11. Chang, C. S. W., T. K.; Sluys, L. J. and van Mier, J. G. M. (2002) Fracture modeling using a micro-structural mechanics approach - Finite Element Analysis. , *Engineering Fracture Mechanics 69*, 1959-1976.

12. de Borst, R. S., L. J.; Mühlhaus, H. B.; Pamin, J. . (1993) Fundamental issues in finite element analyses of localization of deformation, *Engineering Computations 10*, 99-121.

13. deBorst, R., Pamin, J., Peerlings, R. H. J., and Sluys, L. J. (1995) On gradient-enhanced damage and plasticity models for failure in quasi-brittle and frictional materials, *Computational Mechanics 17*, 130-141.

14. Devree, J. H. P., Brekelmans, W. A. M., and Vangils, M. A. J. (1995) COMPARISON OF NONLOCAL APPROACHES IN CONTINUUM DAMAGE MECHANICS, *Computers & Structures 55*, 581-588.

15. Frantziskonis, G., and Desai, C. S. (1987) ANALYSIS OF A STRAIN SOFTENING CONSTITUTIVE MODEL, *International Journal of Solids and Structures 23*, 751-767.

16. Gao, H. J., and Klein, P. (1998) Numerical simulation of crack growth in an isotropic solid with randomized internal cohesive bonds, *Journal of the Mechanics and Physics of Solids 46*, 187-218.

17. Gopalaratnam, V. S., and Surendra, P. S. (1985) Softening Response of Plain Concrete in Direct Tension, *American Concrete Institute Journal Proceedings 82*, 310-323.

18. Hughes, B. P., and Chapman, G. P. (1966) The Deformation of Concrete and Micro-Concrete in Compression and Tension with Particular Reference to Agrregate Size, *Magazine of Concrete Research 18*, 19-24.

19. Jia, D., Ramesh, K. T., and Ma, E. (2003) Effects of nanocrystalline and ultrafine grain sizes on constitutive behavior and shear bands in iron, *Acta Materialia 51*, 3495-3509.

20. Karthik, H., Obla, and Haejin, K. (2008) On Aggregate Grading, *Concrete International 30*, 45-50.

21. Komlos, K. (1969) Factors Affecting the Stress-Strain Relation of Concrete in Uniaxial Tension, *American Concrete Institute Journal Proceedings 66*, 111-114.

22. Kroner, E. (1967) Elasticity theory of materials with long range cohesive forces, *International Journal of Solids and Structures 3*, 731-742.

23. Liu, G. R. a. G., Y. T. (2005) *An Introduction to Meshfree Methods and Their Programming*, Springer Dordrecht, New York

24. Mindess, S., Young, J., and Darwin, D. (2003) *Concrete*, 2nd Edition ed., Prentice Hall, c2003., Upper Saddle River, NJ

25. Mindlin, R. D. (1969) Microstructure in linear elasticity, *Archive for Rational Mechanics and Analysis 16*, 51-78.

26. Misra, A., and Yang, Y. (2010) Micromechanical model for cohesive materials based upon pseudo-granular structure, *International Journal of Solids and Structures 47*, 2970-2981.

27. Misra, A. T., G.; and Somboonyanon, P. . (2003) Pseudo particle-potential model for granular materials, *Electronic Proceedings of the 16th ASCE Engineering Mechanics Conference*.

28. Murakami, H., Kendall, D. M., and Valanis, K. C. (1993) A NONLOCAL ELASTIC DAMAGE THEORY - MESH-INSENSITIVITY UNDER STRAIN-SOFTENING, *Computers & Structures 48*, 415-422.

29. Needleman, A. (1988) MATERIAL RATE DEPENDENCE AND MESH SENSITIVITY IN LOCALIZATION PROBLEMS, *Computer Methods in Applied Mechanics and Engineering 67*, 69-85.

30. Nemes, J. A., and Speciel, E. (1996) Use of a rate-dependent continuum damage model to describe strain-softening in laminated composites, *Computers & Structures 58*, 1083-1092.

31. NRMCA, Karthik, O., Haejin, K., and Colin, L. (2007) Effect of Continuous (Well-Graded) Combined Aggregate Grading on Concrete Performance - Phase B: Concrete Performance, p 45, National Ready Mix Concrete Association Research Laboratory.

32. Pamin, J., Askes, H., and de Borst, R. (2003) Two gradient plasticity theories discretized with the element-free Galerkin method, *Computer Methods in Applied Mechanics and Engineering 192*, 2377-2403.

33. Peerlings, R. H. J., deBorst, R., Brekelmans, W. A. M., and deVree, J. H. P. (1996) Gradient enhanced damage for quasi-brittle materials, *International Journal for Numerical Methods in Engineering 39*, 3391-3403.

34. Pietruszczak, S., and Mroz, Z. (1981) FINITE-ELEMENT ANALYSIS OF DEFORMATION OF STRAIN-SOFTENING MATERIALS, *International Journal for Numerical Methods in Engineering 17*, 327-334.

35. Pijaudiercabot, G., and Huerta, A. (1991) FINITE-ELEMENT ANALYSIS OF BIFURCATION IN NONLOCAL STRAIN SOFTENING SOLIDS, *Computer Methods in Applied Mechanics and Engineering 90*, 905-919.

36. Sandler, I. S. (1984) Strain softening for static and dynamic problems, *ASME Winter Annual Meeting, Symp. On constitutive equations: Micro, Macro and Computational Aspects, CEQ, New Orleans*, 217-231.

37. Sluys, L. J., Cauvern, M., and Deborst, R. (1995) DISCRETIZATION INFLUENCE IN STRAIN-SOFTENING PROBLEMS, *Engineering Computations 12*, 209-228.

38. Thiagarajan, G., and Misra, A. (2004) Fracture simulation for anisotropic materials using a virtual internal bond model, *International Journal of Solids and Structures 41*, 2919-2938.

39. Triantafyllidis, N., and Bardenhagen, S. (1993) ON HIGHER-ORDER GRADIENT CONTINUUM-THEORIES IN 1-D NONLINEAR ELASTICITY - DERIVATION FROM AND COMPARISON TO THE CORRESPONDING DISCRETE MODELS, *Journal of Elasticity 33*, 259-293.

40. van Mier, J. G. M. (1986) Multiaxial strain-softening of concrete, *Materials and Structures 19*, 190-200.

41. van Mier, J. G. M. (1997) *Fracture Processes of Concrete - Assesment of Material Parameters for Fracture Models*, CRC Press, Inc., Boca Raton, Florida.

42. van Mier, J. G. M. (2007) Multi-scale interaction potentials (F-r) for describing fracture of brittle disordered materials like cement and concrete, *International Journal of Fracture 143*, 41-78.

43. van Mier, J. G. M., Shah, S. P., Arnaud, M., Balayssac, J. P., Bascoul, A., Choi, S., Dasenbrock, D., Ferrara, G., French, C., Gobbi, M. E., Karihaloo, B. L., Konig, G., Katsovos, M. D., Labuz, J., Lange-Kornbak, D., Markeset, G., Pavlovic, M. N., Simsch, G., Thienel, K. C., Turatsinze, A., Ulmer, M., van Geel, H., van Vliet, M. R. A., and Zissopoulos, D. (1997) Strain-softening of concrete in uniaxial compression - Report of the Round Robin Test carried out by RILEM TC 148-SSC, *Materials and Structures 30*, 195-209.

44. Warda, Bint A., and Munaz, Ahmed N. (2011)
A parametric study for assessing the effects of coarseness factor and workability factor o nconcrete compressive strength,
INTERNATIONAL JOURNAL OF CIVIL AND STRUCTURAL ENGINEERING 1, 740-748.

45. Yang, Y., and Misra, A. (2010) Higher-order stress-strain theory for damage modeling implemented in an element-free Galerkin formulation, *Computer Modeling in Engineering and Sciences 64*, 1-36.

46. Zhang, Z. N., and Ge, X. R. (2005) Micromechanical consideration of tensile crack behavior based on virtual internal bond in contrast to cohesive stress, *Theoretical and Applied Fracture Mechanics 43*, 342-359.

47. Zhang, Z. N., and Ge, X. R. (2006) Micromechanical modelling of elastic continuum with virtual multi-dimensional internal bonds, *International Journal for Numerical Methods in Engineering 65*, 135-146.

48. Zhang, Z. N., Ge, X. R., and Li, Y. H. (2006) A multiscale mechanical model for materials based on virtual internal bond theory, *Acta Mechanica Solida Sinica 19*, 196-202.

Appendix A.1: Derivation of 1st gradient constitutive model.

$$W = \frac{1}{2V}\sum_{c=1}^{N} f_i^c \delta_i^c + m_i^c \theta_i^c$$

$$W = \frac{1}{2V}\sum_{c=1}^{N} f_i^c \left[\varepsilon_{ik}^0 l_k - e_{ijk}\omega_{j,l} J_{kl}^c\right] + m_i^c \left[\gamma_{il}^0 l_l\right]$$

$$W = \frac{1}{2V}\sum_{c=1}^{N} f_i^c \left[\varepsilon_{ik}^0 l_k - e_{ijk}\gamma_{jl}^0 J_{kl}^c\right] + m_i^c \left[\delta_{ij}\gamma_{jl}^0 l_l\right]$$

$$\sigma_{ik}^0 = f_i l_k = K_{iq} l_k \left[\varepsilon_{ql}^0 l_l - e_{qjl}\gamma_{jm}^0 J_{lm}^c\right]$$

$$\mu_{jl}^0 = \delta_{ij} m_i^c l_l - f_i^c e_{ijk} J_{kl}^c = G_{iq} l_l \delta_{ij}\left[\gamma_{qr}^0 l_r\right] - e_{ijk} J_{kl}^c K_{im}\left[\varepsilon_{mp}^0 l_p - e_{mqp}\gamma_{qr}^0 J_{pr}^c\right]$$

or

$$\mu_{jl}^0 = \delta_{ij} m_i^c l_l - f_i^c e_{ijk} r_k l_l = \delta_{ij} m_i^c l_l - e_{ijk} r_k \sigma_{il}^0$$

$$\sigma_{ik}^0 = K_{iq} l_k l_l \varepsilon_{ql}^0 - K_{iq} l_k e_{qjl} J_{lm}^c \gamma_{jm}^0$$

$$\mu_{jl}^0 = -K_{im} l_p e_{ijk} J_{kl}^c \varepsilon_{mp}^0 + \left(G_{iq} l_l \delta_{ij} l_r + e_{ijk} J_{kl}^c K_{im} e_{mqp} J_{pr}^c\right)\gamma_{qr}^0$$

$$\sigma_{ik}^0 = A_{ikql}\varepsilon_{ql}^0 + B_{ikjm}\gamma_{jm}^0$$

$$\mu_{jl}^0 = C_{jlmp}\varepsilon_{mp}^0 + D_{jlqr}\gamma_{qr}^0$$

where B_{ikjm} and C_{jlmp} are zero.

And,

$$A_{ikql} = K_{iq} l_l l_k$$

$$D_{jlqr} = \left(G_{iq} l_l \delta_{ij} l_r + e_{ijk} J_{kl}^c K_{im} e_{mqp} J_{pr}^c\right)$$

Appendix A.2: Derivation of the 2nd gradient constitutive equations.

$$W = \frac{1}{2V}\sum_{c=1}^{N} f_i^c \delta_i^c + m_i^c \theta_i^c$$

$$W = \frac{1}{2V}\sum_{c=1}^{N} f_i^c \left[\varepsilon_{ik}^0 l_k + \varepsilon_{ikl}^I J_{kl}^c\right] + m_i^c \left[\gamma_{il}^0 l_l\right]$$

$$W = \frac{1}{2V}\sum_{c=1}^{N} f_i^c \left[\varepsilon_{ik}^0 l_k + \varepsilon_{ikl}^I J_{kl}^c\right] + m_i^c \left[\gamma_{il}^0 l_l\right]$$

$$\sigma_{ik}^0 = f_i l_k = K_{iq} l_k \left[\varepsilon_{ql}^0 l_l + \varepsilon_{qlm}^I J_{lm}\right]$$

$$\sigma_{ikl}^I = f_i^c J_{kl}^c = K_{iq} J_{kl}^c \left[\varepsilon_{qr}^0 l_r + \varepsilon_{qrm}^I J_{rm}\right]$$

$$\mu_{il}^0 = m_i^c l_l = G_{iq} l_l \left[\gamma_{qr}^0 l_r\right]$$

$$\sigma_{ik}^0 = K_{iq} l_k l_l \varepsilon_{ql}^0 + K_{iq} l_k J_{lm} \varepsilon_{qlm}^I$$

$$\sigma_{ikl}^I = K_{iq} J_{kl}^c l_r \varepsilon_{qr}^0 + K_{iq} J_{kl}^c J_{rm} \varepsilon_{qrm}^I$$

$$\mu_{il}^0 = G_{iq} l_l l_r \gamma_{qr}^0$$

$$\sigma_{ik}^0 = A_{ikql} \varepsilon_{ql}^0 + B_{ikqlm} \varepsilon_{qlm}^I$$

$$\sigma_{ikl}^I = D_{iklqr} \varepsilon_{qr}^0 + E_{iklqrm} \varepsilon_{qrm}^I$$

$$\mu_{il}^0 = G_{ilqr} \gamma_{qr}^0$$

where B_{ikqlm} and D_{iklqr} are zero.

And,

$$A_{ikql} = \frac{1}{2V}\sum_{c=1}^{N} K_{iq} l_k l_l$$

$$E_{iklqrm} = \frac{1}{2V}\sum_{c=1}^{N} K_{iq} J_{kl}^c J_{rm}$$

$$G_{ilqr} = \frac{1}{2V}\sum_{c=1}^{N} G_{iq} l_l l_r$$

Appendix B.1: Derivation of the equilibrium and weak form equations for the 1st gradient constitutive model.

Having:

$$\sigma_{iq}^{0} = A_{iqkl}\varepsilon_{kl}^{0}$$
$$M_{iq}^{0} = D_{iqjl}\gamma_{jl}^{0}$$

where:

$$A_{iqkl} = \frac{1}{2V}\sum_{c=1}^{N} K_{ik} l_l l_q$$
$$D_{iqjl} = \frac{1}{2V}\sum_{c=1}^{N}\left(G_{rj} l_q \delta_{ri} l_l + e_{rik} J_{kq}^{c} K_{rm} e_{mjp} J_{pl}^{c}\right)$$

We write the energy functional in the incremental form as follows:

$$\Delta W = \int_{\varepsilon^0} \Delta\sigma_{iq}^{0} d\varepsilon_{iq} + \int_{\gamma^0} \Delta M_{iq}^{0} d\gamma_{iq}^{0}$$
$$\Delta W = \int_{\varepsilon^0} A_{iqkl}\Delta\varepsilon_{kl}^{0} d\varepsilon_{iq}^{0} + \int_{\gamma^0} D_{iqjl}\Delta\gamma_{jl}^{0} d\gamma_{iq}^{0} \qquad \text{(B1-1)}$$

For the equilibrium condition, the energy functional is minimized as follows:

$$\frac{\partial \Delta W}{\partial \varepsilon_{iq}^{0}} = 0 \qquad \text{(B1-2)}$$

$$\frac{\partial \Delta W}{\partial \gamma_{iq}^{0}} = 0 \qquad \text{(B1-3)}$$

From equation (B1-2):

$$\frac{\partial \Delta W}{\partial \varepsilon_{iq}^{0}} = 0 = -\left(\frac{\partial A_{iqkl}}{\partial x_q}\Delta\varepsilon_{kl}^{0} + A_{iqkl}\frac{\partial \Delta\varepsilon_{kl}^{0}}{\partial x_q}\right) \qquad \text{(B1-4)}$$

Applying chain rule:

$$\frac{\partial \Delta W}{\partial \varepsilon_{iq}^0} = 0 = -\left(\frac{\partial A_{iqkl}}{\partial \Delta \varepsilon_{st}^0} \frac{\partial \Delta \varepsilon_{st}^0}{\partial x_q} \Delta \varepsilon_{kl}^0 + A_{iqkl} \frac{\partial \Delta \varepsilon_{kl}^0}{\partial x_q} \right) \tag{B1-5}$$

For further derivation the following substitution is used:

$$\phi_i = \Delta u_i - e_{ijk} \Delta \omega_j x_k; \qquad \Delta \varepsilon_{ik}^0 = \Delta u_{i,k} - e_{ijk} \Delta \omega_j = \frac{\partial \phi_i}{\partial x_k}; \quad \Delta \gamma_{jl}^0 = \frac{\partial \Delta \omega_j}{\partial x_l} \tag{B1-6}$$

Substitution (B1-6) into (B1-4), the equilibrium equation becomes:

$$\frac{\partial \Delta W}{\partial \varepsilon_{iq}^0} = 0 = -\left(\frac{\partial A_{iqkl}}{\partial \varepsilon_{st}^0} \frac{\partial^2 \phi_s}{\partial x_t \partial x_q} \frac{\partial \phi_k}{\partial x_l} + A_{iqkl} \frac{\partial^2 \phi_k}{\partial x_l \partial x_q} \right) \tag{B1-7}$$

Similarly, equilibrium equation (B1-3) becomes:

$$\frac{\partial \Delta W}{\partial \gamma_{iq}^0} = -G_{iqjl} \frac{\partial^2 \Delta \omega_j}{\partial x_l \partial x_q} - \frac{\partial G_{iqjl}}{\partial \Delta \gamma_{st}^0} \frac{\partial \Delta \gamma_{st}^0}{\partial x_q} \frac{\partial \Delta \omega_j}{\partial x_l} = -G_{iqjl} \frac{\partial^2 \Delta \omega_j}{\partial x_l \partial x_q} - \frac{\partial G_{iqjl}}{\partial \Delta \gamma_{st}^0} \frac{\partial^2 \Delta \omega_s}{\partial x_t \partial x_q} \frac{\partial \Delta \omega_j}{\partial x_l} \tag{B1-8}$$

Deriving the weak form

Using Galerkin method, the weak form is derived by pre-multiplying the test functions $\delta\phi_i$ and $\delta\omega_i$ to equations (B1-7) and (B1-8), respectively.

$$\int_\Omega \delta \phi_i \left[-\left(\frac{\partial A_{iqkl}}{\partial \Delta \varepsilon_{st}} \frac{\partial^2 \phi_s}{\partial x_t \partial x_q} \frac{\partial \phi_k}{\partial x_l} + A_{iqkl} \frac{\partial^2 \phi_k}{\partial x_l \partial x_q} \right) \right] d\Omega = 0 \tag{B1-9}$$

The second term is expanded by integrating by parts as follows:

$$-\int_{\Omega}\delta\phi_i\left(A_{iqkl}\frac{\partial^2\phi_k}{\partial x_l\partial x_q}\right)d\Omega=-\int_{\Gamma}\delta\phi_i n_q\left[A_{iqkl}\frac{\partial\phi_k}{\partial x_l}\right]d\Gamma$$
$$+\int_{\Omega}\frac{\partial\delta\phi_i}{\partial x_q}A_{iqkl}\frac{\partial\phi_k}{\partial x_l}d\Omega+\int_{\Omega}\delta\phi_i\frac{\partial A_{iqkl}}{\partial\Delta\varepsilon_{st}}\frac{\partial^2\phi_s}{\partial x_t\partial x_q}\frac{\partial\phi_k}{\partial x_l}d\Omega \tag{B1-10}$$

Substituting equation (B1-10) into (B1-9), the weak form becomes:

$$\int_{\Omega}\frac{\partial\delta\phi_i}{\partial x_q}A_{iqkl}\frac{\partial\phi_k}{\partial x_l}d\Omega=\int_{\Gamma}\delta\phi_i n_q\left[A_{iqkl}\frac{\partial\phi_k}{\partial x_l}\right]d\Gamma \tag{B1-11}$$

Then, recalling the equilibrium equation (B1-8):

$$\frac{\partial\Delta W}{\partial\gamma^0_{iq}}=0=D_{iqjl}\frac{\partial^2\Delta\omega_j}{\partial x_l\partial x_q}-\frac{\partial D_{iqjl}}{\partial\Delta\gamma^0_{st}}\frac{\partial\Delta\gamma^0_{st}}{\partial x_q}\frac{\partial\Delta\omega_j}{\partial x_l}=-D_{iqjl}\frac{\partial^2\Delta\omega_j}{\partial x_l\partial x_q}-\frac{\partial D_{iqjl}}{\partial\Delta\gamma^0_{st}}\frac{\partial^2\Delta\omega_s}{\partial x_t\partial x_q}\frac{\partial\Delta\omega_j}{\partial x_l}$$

Its weak form is written as follows:

$$-\int_{\Omega}\delta\omega_i\left[D_{iqjl}\frac{\partial^2\Delta\omega_j}{\partial x_l\partial x_q}+\frac{\partial D_{iqjl}}{\partial\Delta\gamma^0_{st}}\frac{\partial^2\Delta\omega_s}{\partial x_t\partial x_q}\frac{\partial\Delta\omega_j}{\partial x_l}\right]d\Omega=0=$$
$$-\int_{\Gamma}\delta\omega_i n_q\left[D_{iqjl}\frac{\partial\Delta\omega_j}{\partial x_l}\right]d\Gamma-\int_{\Gamma}\delta\omega_i n_q\left[\frac{\partial D_{iqjl}}{\partial\Delta\gamma^0_{st}}\frac{\partial\Delta\omega_s}{\partial x_t}\frac{\partial\Delta\omega_j}{\partial x_l}\right]d\Gamma+$$
$$\int_{\Omega}\frac{\partial\delta\omega_i}{\partial x_q}\left[D_{iqjl}\frac{\partial\Delta\omega_j}{\partial x_l}\right]d\Omega+\int_{\Omega}\delta\omega_i\left[\frac{\partial D_{iqjl}}{\partial\Delta\gamma^0_{st}}\frac{\partial^2\Delta\omega_s}{\partial x_t\partial x_q}\frac{\partial\Delta\omega_j}{\partial x_l}\right]d\Omega+$$
$$\int_{\Omega}\frac{\partial\delta\omega_i}{\partial x_q}\left[\frac{\partial D_{iqjl}}{\partial\Delta\gamma^0_{st}}\frac{\partial\Delta\omega_s}{\partial x_t}\frac{\partial\Delta\omega_j}{\partial x_l}\right]d\Omega+\int_{\Omega}\delta\omega_i\left[\frac{\partial D_{iqjl}}{\partial\Delta\gamma^0_{st}}\frac{\partial^2\Delta\omega_s}{\partial x_t\partial x_q}\frac{\partial\Delta\omega_j}{\partial x_l}\right]d\Omega \tag{B1-12}$$

where the second term can be written as:

$$\int_{\Omega} \delta\omega_i \left[\frac{\partial D_{iqjl}}{\partial \Delta\gamma^0_{st}} \frac{\partial^2 \Delta\omega_s}{\partial x_t \partial x_q} \frac{\partial \Delta\omega_j}{\partial x_l} \right] d\Omega =$$

$$\int_{\Gamma} \delta\omega_i n_q \left[\frac{\partial D_{iqjl}}{\partial \Delta\gamma^0_{st}} \frac{\partial \Delta\omega_s}{\partial x_t} \frac{\partial \Delta\omega_j}{\partial x_l} \right] d\Gamma - \int_{\Omega} \delta\omega_i \left[\frac{\partial D_{iqjl}}{\partial \Delta\gamma^0_{st}} \frac{\partial^2 \Delta\omega_s}{\partial x_t \partial x_q} \frac{\partial \Delta\omega_j}{\partial x_l} \right] d\Omega - \int_{\Omega} \frac{\partial \delta\omega_i}{\partial x_q} \left[\frac{\partial D_{iqjl}}{\partial \Delta\gamma^0_{st}} \frac{\partial \Delta\omega_s}{\partial x_t} \frac{\partial \Delta\omega_j}{\partial x_l} \right]$$

(B1-13)

Then, by substituting equation (B1-13) into (B1-12), equation (B1-8) becomes:

$$\int_{\Omega} \frac{\partial \delta\omega_i}{\partial x_q} \left[D_{iqjl} \frac{\partial \Delta\omega_j}{\partial x_l} \right] d\Omega = \int_{\Gamma} \delta\omega_i n_q \left[D_{iqjl} \frac{\partial \Delta\omega_j}{\partial x_l} \right] d\Gamma \tag{B1-14}$$

Summarizing, we recall the final weak forms on equations (B1-8) and (B1-14):

$$\left[\int_{\Omega} \frac{\partial \delta\phi_i}{\partial x_q} A_{iqkl} \frac{\partial \phi_k}{\partial x_l} d\Omega \right] = \int_{\Gamma} \left[\delta\phi_i n_q \left[A_{iqkl} \frac{\partial \phi_k}{\partial x_l} \right] \right] d\Gamma$$

$$\int_{\Omega} \frac{\partial \delta\omega_i}{\partial x_q} \left[G_{iqjl} \frac{\partial \Delta\omega_j}{\partial x_l} \right] d\Omega = \int_{\Gamma} \delta\omega_i n_q \left[G_{iqjl} \frac{\partial \Delta\omega_j}{\partial x_l} \right] d\Gamma$$

(B1-15)

where:

$$\Delta\sigma^0_{iq} = A_{iqkl} \Delta\varepsilon^0_{kl} = A_{iqkl} \frac{\partial \phi_k}{\partial x_l}$$

$$\Delta M^0_{iq} = D_{iqjl} \Delta\gamma^0_{jl} = D_{iqjl} \frac{\partial \Delta\omega_j}{\partial x_l}$$

(B1-16)

Then, weak form equations can be rewritten as:

$$\int_{\Omega} \frac{\partial \delta\phi_i}{\partial x_q} A_{iqkl} \frac{\partial \phi_k}{\partial x_l} d\Omega = \int_{\Gamma} \left[\delta\phi_i n_q \left(\Delta\sigma_{iq}^0 \right) \right] d\Gamma \tag{B1-17}$$

$$\int_{\Omega} \frac{\partial \delta\omega_i}{\partial x_q} \left[D_{iqjl} \frac{\partial \Delta\omega_j}{\partial x_l} \right] d\Omega = \int_{\Gamma} \delta\omega_i n_q \Delta M_{iq}^0 d\Gamma \tag{B1-18}$$

Appendix B.2: Derivation of the equilibrium and weak form equations for the 2nd gradient constitutive model.

Having:

$$\sigma_{iq}^{0} = A_{iqkl}\varepsilon_{kl}^{0}$$
$$\sigma_{ipq}^{I} = E_{ipqklm}\varepsilon_{klm}^{I}$$
$$\mu_{iq}^{0} = G_{iqjl}\gamma_{jl}^{0}$$

where:

$$A_{iqkl} = \frac{1}{2V}\sum_{c=1}^{N} K_{ik} l_q l_l$$
$$E_{ipqklm} = \frac{1}{2V}\sum_{c=1}^{N} K_{ik} J_{pq}^{c} J_{lm}$$
$$G_{iqjl} = \frac{1}{2V}\sum_{c=1}^{N} G_{ij} l_q l_l$$

We write the energy functional in the incremental form as follows:

$$\Delta W = \int_{\varepsilon^0} \Delta\sigma_{iq}^{0} d\varepsilon_{iq} + \int_{\varepsilon^I} \Delta\sigma_{ipq}^{I} d\varepsilon_{ipq}^{I} + \int_{\gamma^0} \Delta\mu_{iq}^{0} d\gamma_{iq}^{0}$$
$$\Delta W = \int_{\varepsilon^0} A_{iqkl}\Delta\varepsilon_{kl}^{0} d\varepsilon_{iq}^{0} + \int_{\varepsilon^I} E_{ipqklm}\Delta\varepsilon_{klm}^{I} d\varepsilon_{ipq}^{I} + \int_{\gamma^0} G_{iqjl}\Delta\gamma_{jl}^{0} d\gamma_{iq}^{0} \qquad \text{(B2-1)}$$

Integrating by parts $\int u\,dv = uv - \int v\,du$ and by neglecting the boundary terms:

$$\int_{\varepsilon^I} E_{ipqklm}\Delta\varepsilon_{klm}^{I} d\varepsilon_{ipq}^{I} = -\int_{\varepsilon^0} \left(E_{ipqklm}\frac{\partial^2 \Delta\varepsilon_{km}^{0}}{\partial x_l \partial x_p} + \frac{\partial E_{ipqklm}}{\partial x_p}\frac{\partial \Delta\varepsilon_{km}^{0}}{\partial x_l} \right) d\varepsilon_{iq}^{0}$$
$$\Delta\varepsilon_{ipq}^{I} = \frac{\partial \Delta\varepsilon_{iq}^{0}}{\partial x_p} = d\varepsilon_{iq}^{0} \qquad \text{(B2-2)}$$

Then we substitute (B2-2) into (B2-1):

$$\Delta W = \int_{\varepsilon^0} A_{iqkl}\Delta\varepsilon^0_{kl}\,d\varepsilon^0_{iq} - \int_{\varepsilon^0}\left(E_{ipqklm}\frac{\partial^2\Delta\varepsilon^0_{km}}{\partial x_l\partial x_p} + \frac{\partial E_{ipqklm}}{\partial x_p}\frac{\partial\Delta\varepsilon^0_{km}}{\partial x_l}\right)d\varepsilon^0_{iq} + \int_{\gamma^0} G_{iqjl}\Delta\gamma^0_{jl}\,d\gamma^0_{iq} \tag{B2-3}$$

Further integration by parts and ignoring the boundary terms, the energy functional becomes:

$$\Delta W = -\int_{\varepsilon^0}\left(\frac{\partial A_{iqkl}}{\partial x_q}\Delta\varepsilon^0_{kl} + A_{iqkl}\frac{\partial\Delta\varepsilon^0_{kl}}{\partial x_q}\right)\varepsilon^0_{iq} + \int_{\varepsilon^0}\left(\frac{\partial E_{ipqklm}}{\partial x_q}\frac{\partial^2\Delta\varepsilon^0_{km}}{\partial x_l\partial x_p} + E_{ipqklm}\frac{\partial^3\Delta\varepsilon^0_{km}}{\partial x_l\partial x_p\partial x_q}\right)\varepsilon^0_{iq}$$
$$+\int_{\varepsilon^0}\left(\frac{\partial^2 E_{ipqklm}}{\partial x_p\partial x_q}\frac{\partial\Delta\varepsilon^0_{km}}{\partial x_l} + \frac{\partial E_{ipqklm}}{\partial x_p}\frac{\partial^2\Delta\varepsilon^0_{km}}{\partial x_l\partial x_q}\right)\varepsilon^0_{iq} - \int_{\gamma^0}\left(G_{iqjl}\frac{\gamma^0_{jl}}{\partial x_q} + \frac{G_{iqjl}}{\partial x_q}\gamma^0_{jl}\right)\gamma^0_{iq} \tag{B2-3.a}$$

We minimize equation (B2-3.a) to satisfy the stationery condition of the potential energy as follows:

$$\frac{\partial\Delta W}{\partial\varepsilon^0_{iq}} = 0 \tag{B2-4}$$

$$\frac{\partial\Delta W}{\partial\gamma^0_{iq}} = 0 \tag{B2-5}$$

From equation (B2-4)

$$\frac{\partial\Delta W}{\partial\varepsilon^0_{iq}} = 0 = -\left(\frac{\partial A_{iqkl}}{\partial x_q}\Delta\varepsilon^0_{kl} + A_{iqkl}\frac{\partial\Delta\varepsilon^0_{kl}}{\partial x_q}\right) + \left(\frac{\partial E_{ipqklm}}{\partial x_q}\frac{\partial^2\Delta\varepsilon^0_{km}}{\partial x_l\partial x_p} + E_{ipqklm}\frac{\partial^3\Delta\varepsilon^0_{km}}{\partial x_l\partial x_p\partial x_q}\right)$$
$$+\left(\frac{\partial^2 E_{ipqklm}}{\partial x_p\partial x_q}\frac{\partial\Delta\varepsilon^0_{km}}{\partial x_l} + \frac{\partial E_{ipqklm}}{\partial x_p}\frac{\partial^2\Delta\varepsilon^0_{km}}{\partial x_l\partial x_q}\right) \tag{B2-5.1}$$

Applying chain rule into equation (B2-5.1):

$$\frac{\partial \Delta W}{\partial \varepsilon_{iq}^{0}} = 0 =$$
$$-\left(\frac{\partial A_{iqkl}}{\partial \Delta \varepsilon_{st}^{0}} \frac{\partial \Delta \varepsilon_{st}^{0}}{\partial x_q} \varepsilon_{kl}^{0} + A_{iqkl} \frac{\partial \Delta \varepsilon_{kl}^{0}}{\partial x_q} \right)$$
$$+\left(\frac{\partial E_{ipqklm}}{\partial \Delta \varepsilon_{st}^{0}} \frac{\partial \Delta \varepsilon_{st}^{0}}{\partial x_q} \frac{\partial^2 \Delta \varepsilon_{km}^{0}}{\partial x_l \partial x_p} + E_{ipqklm} \frac{\partial^3 \Delta \varepsilon_{km}^{0}}{\partial x_l \partial x_p \partial x_q} \right)$$
$$+\left(\frac{\partial E_{ipqklm}}{\partial \Delta \varepsilon_{st}^{0}} \frac{\partial^2 \Delta \varepsilon_{st}^{0}}{\partial x_p \partial x_q} \frac{\partial \Delta \varepsilon_{km}^{0}}{\partial x_l} + \frac{\partial E_{ipqklm}}{\partial \Delta \varepsilon_{st}^{0}} \frac{\partial \Delta \varepsilon_{st}^{0}}{\partial x_p} \frac{\partial^2 \Delta \varepsilon_{km}^{0}}{\partial x_l \partial x_q} \right) \quad \text{(B2-5.2)}$$

For further derivation the following substitution is used:

$$\phi_i = \Delta u_i - e_{ijk} \Delta \omega_j x_k; \qquad \Delta \varepsilon_{ik}^{0} = \Delta u_{i,k} - e_{ijk} \Delta \omega_j = \frac{\partial \phi_i}{\partial x_k}; \qquad \Delta \varepsilon_{ikl}^{I} = \Delta u_{i,kl} - e_{ijk} \Delta \omega_{j,l} = \frac{\partial^2 \phi_i}{\partial x_l \partial x_k}$$
$$\Delta \gamma_{jl}^{0} = \frac{\partial \Delta \omega_j}{\partial x_l} \quad \text{(B2-5.3)}$$

Then Equilibrium equation (B2-4) becomes:

$$\frac{\partial \Delta W}{\partial \varepsilon_{iq}^{0}} = 0 = -\left(\frac{\partial A_{iqkl}}{\partial \Delta \varepsilon_{st}^{0}} \frac{\partial^2 \phi_s}{\partial x_t \partial x_q} \frac{\partial \phi_k}{\partial x_l} + A_{iqkl} \frac{\partial^2 \phi_k}{\partial x_l \partial x_q} \right)$$
$$+\left(\frac{\partial E_{ipqklm}}{\partial \Delta \varepsilon_{st}^{0}} \frac{\partial^2 \phi_s}{\partial x_t \partial x_q} \frac{\partial^3 \phi_k}{\partial x_m \partial x_l \partial x_p} + E_{ipqklm} \frac{\partial^4 \phi_k}{\partial x_m \partial x_l \partial x_p \partial x_q} \right)$$
$$+\left(\frac{\partial E_{ipqklm}}{\partial \Delta \varepsilon_{st}^{0}} \frac{\partial^3 \phi_s}{\partial x_t \partial x_p \partial x_q} \frac{\partial^2 \phi_k}{\partial x_m \partial x_l} + \frac{\partial E_{ipqklm}}{\partial \Delta \varepsilon_{st}^{0}} \frac{\partial^2 \phi_s}{\partial x_t \partial x_p} \frac{\partial^3 \phi_k}{\partial x_m \partial x_l \partial x_q} \right) \quad \text{(B2-6)}$$

And equilibrium equation (B2-5) becomes:

$$\frac{\partial \Delta W}{\partial \gamma_{iq}^{0}} = 0 = -G_{iqjl} \frac{\partial^2 \Delta \omega_j}{\partial x_l \partial x_q} - \frac{\partial G_{iqjl}}{\partial \Delta \gamma_{st}^{0}} \frac{\partial \Delta \gamma_{st}^{0}}{\partial x_q} \frac{\partial \Delta \omega_j}{\partial x_l} = -G_{iqjl} \frac{\partial^2 \Delta \omega_j}{\partial x_l \partial x_q} - \frac{\partial G_{iqjl}}{\partial \Delta \gamma_{st}^{0}} \frac{\partial^2 \Delta \omega_s}{\partial x_t \partial x_q} \frac{\partial \Delta \omega_j}{\partial x_l} \quad \text{(B2-7)}$$

Deriving the weak form

Using Galerkin method, the terms from equation (B2-6) are pre-multiplied by a test function $\delta\phi$:

$$\int_{\Omega} \delta\phi_i \left[\begin{array}{l} -\left(\frac{\partial A_{iqkl}}{\partial \Delta\varepsilon_{st}} \frac{\partial^2 \phi_s}{\partial x_t \partial x_q} \frac{\partial \phi_k}{\partial x_l} + A_{iqkl} \frac{\partial^2 \phi_k}{\partial x_l \partial x_q} \right) \\ +\left(\frac{\partial E_{ipqklm}}{\partial \Delta\varepsilon^0_{st}} \frac{\partial^2 \phi_s}{\partial x_t \partial x_q} \frac{\partial^3 \phi_k}{\partial x_m \partial x_l \partial x_p} + E_{ipqklm} \frac{\partial^4 \phi_k}{\partial x_m \partial x_l \partial x_p \partial x_q} \right) \\ +\left(\frac{\partial E_{ipqklm}}{\partial \Delta\varepsilon^0_{st}} \frac{\partial^3 \phi_s}{\partial x_t \partial x_p \partial x_q} \frac{\partial^2 \phi_k}{\partial x_m \partial x_l} + \frac{\partial E_{ipqklm}}{\partial \Delta\varepsilon^0_{st}} \frac{\partial^2 \phi_s}{\partial x_t \partial x_p} \frac{\partial^3 \phi_k}{\partial x_m \partial x_l \partial x_q} \right) \end{array} \right] d\Omega = 0$$

(B2-8)

Integrating by parts, where:

$$-\int_{\Omega} \delta\phi_i \left(A_{iqkl} \frac{\partial^2 \phi_k}{\partial x_l \partial x_q} \right) d\Omega = -\int_{\Gamma} \delta\phi_i n_q \left[A_{iqkl} \frac{\partial \phi_k}{\partial x_l} \right] d\Gamma + \int_{\Omega} \frac{\partial \delta\phi_i}{\partial x_q} A_{iqkl} \frac{\partial \phi_k}{\partial x_l} d\Omega$$

$$+\int_{\Omega} \delta\phi_i \frac{\partial A_{iqkl}}{\partial \Delta\varepsilon_{st}} \frac{\partial^2 \phi_s}{\partial x_t \partial x_q} \frac{\partial \phi_k}{\partial x_l} d\Omega$$

And

$$\int_{\Omega} \delta\phi_i \left(E_{ipqklm} \frac{\partial^4 \phi_k}{\partial x_m \partial x_l \partial x_p \partial x_q} \right) d\Omega = \int_{\Gamma} \delta\phi_i n_q \left[E_{ipqklm} \frac{\partial^3 \phi_k}{\partial x_m \partial x_l \partial x_p} \right] d\Gamma$$

$$-\int_{\Omega} \frac{\partial \delta\phi_i}{\partial x_q} \left[E_{ipqklm} \frac{\partial^3 \phi_k}{\partial x_m \partial x_l \partial x_p} \right] d\Omega - \int_{\Omega} \delta\phi_i \left[\frac{\partial E_{ipqklm}}{\partial \Delta\varepsilon_{st}} \frac{\partial^2 \phi_s}{\partial x_t \partial x_q} \frac{\partial^3 \phi_k}{\partial x_m \partial x_l \partial x_p} \right] d\Omega$$

(B2-8.1)

The weak form on equation (B2-8) becomes:

$$\int_{\Omega}\delta\phi_i\left[\left(\frac{\partial E_{ipqklm}}{\partial\Delta\varepsilon_{st}^0}\frac{\partial^3\phi_s}{\partial x_t\partial x_p\partial x_q}\frac{\partial^2\phi_k}{\partial x_m\partial x_l}+\frac{\partial E_{ipqklm}}{\partial\Delta\varepsilon_{st}^0}\frac{\partial^2\phi_s}{\partial x_t\partial x_p}\frac{\partial^3\phi_k}{\partial x_m\partial x_l\partial x_q}\right)\right]d\Omega+\int_{\Omega}\frac{\partial\delta\phi_i}{\partial x_q}A_{iqkl}\frac{\partial\phi_k}{\partial x_l}d\Omega$$
$$-\int_{\Omega}\frac{\partial\delta\phi_i}{\partial x_q}\left[E_{ipqklm}\frac{\partial^3\phi_k}{\partial x_m\partial x_l\partial x_p}\right]d\Omega=\int_{\Gamma}\delta\phi_i n_q\left[A_{iqkl}\frac{\partial\phi_k}{\partial x_l}\right]d\Gamma-\int_{\Gamma}\delta\phi_i n_q\left[E_{ipqklm}\frac{\partial^3\phi_k}{\partial x_m\partial x_l\partial x_p}\right]d\Gamma$$

(B2-8.2)

where we proceed to integrate by parts:

Term one:

$$\int_{\Omega}\delta\phi_i\left[\frac{\partial E_{ipqklm}}{\partial\Delta\varepsilon_{st}^0}\frac{\partial^3\phi_s}{\partial x_t\partial x_p\partial x_q}\frac{\partial^2\phi_k}{\partial x_m\partial x_l}\right]d\Omega=\int_{\Gamma}\delta\phi_i n_q\left[\frac{\partial E_{ipqklm}}{\partial\Delta\varepsilon_{st}^0}\frac{\partial^2\phi_s}{\partial x_t\partial x_p}\frac{\partial^2\phi_k}{\partial x_m\partial x_l}\right]d\Gamma$$
$$-\int_{\Omega}\frac{\partial\delta\phi_i}{\partial x_q}\left[\frac{\partial E_{ipqklm}}{\partial\Delta\varepsilon_{st}^0}\frac{\partial^2\phi_s}{\partial x_t\partial x_p}\frac{\partial^2\phi_k}{\partial x_m\partial x_l}\right]d\Omega-\int_{\Omega}\delta\phi_i\left[\frac{\partial E_{ipqklm}}{\partial\Delta\varepsilon_{st}^0}\frac{\partial^3\phi_s}{\partial x_t\partial x_p\partial x_q}\frac{\partial^2\phi_k}{\partial x_m\partial x_l}\right]d\Omega$$
$$=$$
$$\int_{\Gamma}\delta\phi_i n_q\left[\frac{\partial E_{ipqklm}}{\partial\Delta\varepsilon_{st}^0}\frac{\partial^2\phi_s}{\partial x_t\partial x_p}\frac{\partial^2\phi_k}{\partial x_m\partial x_l}\right]d\Gamma-\int_{\Gamma}\frac{\partial\delta\phi_i}{\partial x_q}n_p\left[\frac{\partial E_{ipqklm}}{\partial\Delta\varepsilon_{st}^0}\frac{\partial\phi_s}{\partial x_t}\frac{\partial^2\phi_k}{\partial x_m\partial x_l}\right]d\Gamma$$
$$+\int_{\Omega}\frac{\partial^2\delta\phi_i}{\partial x_q\partial x_p}\left[\frac{\partial E_{ipqklm}}{\partial\Delta\varepsilon_{st}^0}\frac{\partial\phi_s}{\partial x_t}\frac{\partial^2\phi_k}{\partial x_m\partial x_l}\right]d\Omega+\int_{\Omega}\frac{\partial\delta\phi_i}{\partial x_q}\left[\frac{\partial E_{ipqklm}}{\partial\Delta\varepsilon_{st}^0}\frac{\partial^2\phi_s}{\partial x_t\partial x_p}\frac{\partial^2\phi_k}{\partial x_m\partial x_l}\right]d\Omega$$
$$-\int_{\Omega}\delta\phi_i\left[\frac{\partial E_{ipqklm}}{\partial\Delta\varepsilon_{st}^0}\frac{\partial^3\phi_s}{\partial x_t\partial x_p\partial x_q}\frac{\partial^2\phi_k}{\partial x_m\partial x_l}\right]d\Omega$$

(B2-8.3)

Term two:

$$\int_{\Omega} \delta\phi_i \left[\frac{\partial E_{ipqklm}}{\partial \Delta\varepsilon_{st}^0} \frac{\partial^2 \phi_s}{\partial x_t \partial x_p} \frac{\partial^3 \phi_k}{\partial x_m \partial x_l \partial x_q} \right] d\Omega = \int_{\Gamma} \delta\phi_i n_q \left[\frac{\partial E_{ipqklm}}{\partial \Delta\varepsilon_{st}^0} \frac{\partial^2 \phi_s}{\partial x_t \partial x_p} \frac{\partial^2 \phi_k}{\partial x_m \partial x_l} \right] d\Gamma$$
$$- \int_{\Omega} \frac{\partial \delta\phi_i}{\partial x_q} \left[\frac{\partial E_{ipqklm}}{\partial \Delta\varepsilon_{st}^0} \frac{\partial^2 \phi_s}{\partial x_t \partial x_p} \frac{\partial^2 \phi_k}{\partial x_m \partial x_l} \right] d\Omega - \int_{\Omega} \delta\phi_i \left[\frac{\partial E_{ipqklm}}{\partial \Delta\varepsilon_{st}^0} \frac{\partial^3 \phi_s}{\partial x_t \partial x_p \partial x_q} \frac{\partial^2 \phi_k}{\partial x_m \partial x_l} \right] d\Omega$$
=
$$\int_{\Gamma} \delta\phi_i n_q \left[\frac{\partial E_{ipqklm}}{\partial \Delta\varepsilon_{st}^0} \frac{\partial^2 \phi_s}{\partial x_t \partial x_p} \frac{\partial^2 \phi_k}{\partial x_m \partial x_l} \right] d\Gamma - \int_{\Gamma} \frac{\partial \delta\phi_i}{\partial x_q} n_p \left[\frac{\partial E_{ipqklm}}{\partial \Delta\varepsilon_{st}^0} \frac{\partial \phi_s}{\partial x_t} \frac{\partial^2 \phi_k}{\partial x_m \partial x_l} \right] d\Gamma$$
$$+ \int_{\Omega} \frac{\partial^2 \delta\phi_i}{\partial x_q \partial x_p} \left[\frac{\partial E_{ipqklm}}{\partial \varepsilon_{st}^0} \frac{\partial \phi_s}{\partial x_t} \frac{\partial^2 \phi_k}{\partial x_m \partial x_l} \right] d\Omega + \int_{\Omega} \frac{\partial \delta\phi_i}{\partial x_q} \left[\frac{\partial E_{ipqklm}}{\partial \varepsilon_{st}^0} \frac{\partial^2 \phi_s}{\partial x_t \partial x_p} \frac{\partial^2 \phi_k}{\partial x_m \partial x_l} \right]$$
$$- \int_{\Omega} \delta\phi_i \left[\frac{\partial E_{ipqklm}}{\partial \Delta\varepsilon_{st}^0} \frac{\partial^3 \phi_s}{\partial x_t \partial x_p \partial x_q} \frac{\partial^2 \phi_k}{\partial x_m \partial x_l} \right] d\Omega \qquad \text{(B2-8.4)}$$

Term three:

$$\int_{\Omega} \frac{\partial \delta\phi_i}{\partial x_q} A_{iqkl} \frac{\partial \phi_k}{\partial x_l} d\Omega \qquad \text{(B2-8.5)}$$

Term four:

$$-\int_{\Omega}\frac{\partial\delta\phi_i}{\partial x_q}\left[E_{ipqklm}\frac{\partial^3\phi_k}{\partial x_m\partial x_l\partial x_p}\right]d\Omega =$$
$$-\int_{\Gamma}\frac{\partial\delta\phi_i}{\partial x_q}n_p\left[E_{ipqklm}\frac{\partial^2\phi_k}{\partial x_m\partial x_l}\right]d\Gamma+\int_{\Omega}\frac{\partial^2\delta\phi_i}{\partial x_q\partial x_p}\left[E_{ipqklm}\frac{\partial^2\phi_k}{\partial x_m\partial x_l}\right]d\Omega$$
$$+\int_{\Omega}\frac{\partial\delta\phi_i}{\partial x_q}\left[\frac{\partial E_{ipqklm}}{\partial\Delta\varepsilon_{st}}\frac{\partial^2\phi_s}{\partial x_t\partial x_p}\frac{\partial^2\phi_k}{\partial x_m\partial x_l}\right]d\Omega$$

(B2-8.6)

Recalling equation (B2-8.2):

$$\int_{\Omega}\delta\phi_i\left[\left(\frac{\partial E_{ipqklm}}{\partial\Delta\varepsilon^0_{st}}\frac{\partial^3\phi_s}{\partial x_t\partial x_p\partial x_q}\frac{\partial^2\phi_k}{\partial x_m\partial x_l}+\frac{\partial E_{ipqklm}}{\partial\Delta\varepsilon^0_{st}}\frac{\partial^2\phi_s}{\partial x_t\partial x_p}\frac{\partial^3\phi_k}{\partial x_m\partial x_l\partial x_q}\right)\right]d\Omega+\int_{\Omega}\frac{\partial\delta\phi_i}{\partial x_q}A_{iqkl}\frac{\partial\phi_k}{\partial x_l}d\Omega$$
$$-\int_{\Omega}\frac{\partial\delta\phi_i}{\partial x_q}\left[E_{ipqklm}\frac{\partial^3\phi_k}{\partial x_m\partial x_l\partial x_p}\right]d\Omega=\int_{\Gamma}\delta\phi_i n_q\left[A_{iqkl}\frac{\partial\phi_k}{\partial x_l}\right]d\Gamma-\int_{\Gamma}\delta\phi_i n_q\left[E_{ipqklm}\frac{\partial^3\phi_k}{\partial x_m\partial x_l\partial x_p}\right]d\Gamma$$

(B2-8.2)

By substituting (B2-8.3), (B2-8.4), (B2-8.5), (B2-8.6) into (B2-8.2) we obtain:

$$\left[\begin{array}{l}
+2\int\limits_{\Omega}\frac{\partial^2\delta\phi_i}{\partial x_q\partial x_p}\left[\frac{\partial E_{ipqklm}}{\partial\Delta\varepsilon^0_{st}}\frac{\partial\phi_s}{\partial x_t}\frac{\partial^2\phi_k}{\partial x_m\partial x_l}\right]d\Omega \\
+2\int\limits_{\Omega}\frac{\partial\delta\phi_i}{\partial x_q}\left[\frac{\partial E_{ipqklm}}{\partial\Delta\varepsilon^0_{st}}\frac{\partial^2\phi_s}{\partial x_t\partial x_p}\frac{\partial^2\phi_k}{\partial x_m\partial x_l}\right]d\Omega \\
-2\int\limits_{\Omega}\delta\phi_i\left[\frac{\partial E_{ipqklm}}{\partial\Delta\varepsilon^0_{st}}\frac{\partial^3\phi_s}{\partial x_t\partial x_p\partial x_q}\frac{\partial^2\phi_k}{\partial x_m\partial x_l}\right]d\Omega \\
+\int\limits_{\Omega}\frac{\partial\delta\phi_i}{\partial x_q}A_{iqkl}\frac{\partial\phi_k}{\partial x_l}d\Omega \\
+\int\limits_{\Omega}\frac{\partial^2\delta\phi_i}{\partial x_q\partial x_p}\left[E_{ipqklm}\frac{\partial^2\phi_k}{\partial x_m\partial x_l}\right]d\Omega \\
+\int\limits_{\Omega}\frac{\partial\delta\phi_i}{\partial x_q}\left[\frac{\partial E_{ipqklm}}{\partial\Delta\varepsilon_{st}}\frac{\partial^2\phi_s}{\partial x_t\partial x_p}\frac{\partial^2\phi_k}{\partial x_m\partial x_l}\right]d\Omega
\end{array}\right] = \int\limits_{\Gamma}\left[\begin{array}{l}
\delta\phi_i n_q\left[A_{iqkl}\frac{\partial\phi_k}{\partial x_l}\right] \\
-\delta\phi_i n_q\left[E_{ipqklm}\frac{\partial^3\phi_k}{\partial x_m\partial x_l\partial x_p}\right] \\
-2\delta\phi_i n_q\left[\frac{\partial E_{ipqklm}}{\partial\Delta\varepsilon^0_{st}}\frac{\partial^2\phi_s}{\partial x_t\partial x_p}\frac{\partial^2\phi_k}{\partial x_m\partial x_l}\right] \\
+2\frac{\partial\delta\phi_i}{\partial x_q}n_p\left[\frac{\partial E_{ipqklm}}{\partial\Delta\varepsilon^0_{st}}\frac{\partial\phi_s}{\partial x_t}\frac{\partial^2\phi_k}{\partial x_m\partial x_l}\right] \\
+\frac{\partial\delta\phi_i}{\partial x_q}n_p\left[E_{ipqklm}\frac{\partial^2\phi_k}{\partial x_m\partial x_l}\right]
\end{array}\right]d\Gamma \qquad \text{(B2-8.7)}$$

where:

$$+2\int\limits_{\Omega}\frac{\partial\delta\phi_i}{\partial x_q}\left[\frac{\partial E_{ipqklm}}{\partial\Delta\varepsilon^0_{st}}\frac{\partial^2\phi_s}{\partial x_t\partial x_p}\frac{\partial^2\phi_k}{\partial x_m\partial x_l}\right]d\Omega =$$
$$\int\limits_{\Gamma}2\frac{\partial\delta\phi_i}{\partial x_q}n_p\left[\frac{\partial E_{ipqklm}}{\partial\Delta\varepsilon^0_{st}}\frac{\partial\phi_s}{\partial x_t}\frac{\partial^2\phi_k}{\partial x_m\partial x_l}\right]d\Gamma - 2\int\limits_{\Omega}\frac{\partial^2\delta\phi_i}{\partial x_q\partial x_p}\left[\frac{\partial E_{ipqklm}}{\partial\Delta\varepsilon^0_{st}}\frac{\partial\phi_s}{\partial x_t}\frac{\partial^2\phi_k}{\partial x_m\partial x_l}\right]d\Omega$$
$$-2\int\limits_{\Omega}\frac{\partial\delta\phi_i}{\partial x_q}\left[\frac{\partial E_{ipqklm}}{\partial\Delta\varepsilon^0_{st}}\frac{\partial^2\phi_s}{\partial x_t\partial x_p}\frac{\partial^2\phi_k}{\partial x_m\partial x_l}\right]d\Omega \qquad \text{(B2-8.8)}$$

By substituting (B2-8.8) into (B2-8.7):

$$\begin{bmatrix} -2\int_{\Omega}\frac{\partial\delta\phi_i}{\partial x_q}\left[\frac{\partial E_{ipqklm}}{\partial\Delta\varepsilon^0_{st}}\frac{\partial^2\phi_s}{\partial x_t\partial x_p}\frac{\partial^2\phi_k}{\partial x_m\partial x_l}\right]d\Omega \\ -2\int_{\Omega}\delta\phi_i\left[\frac{\partial E_{ipqklm}}{\partial\Delta\varepsilon^0_{st}}\frac{\partial^3\phi_s}{\partial x_t\partial x_p\partial x_q}\frac{\partial^2\phi_k}{\partial x_m\partial x_l}\right]d\Omega \\ +\int_{\Omega}\frac{\partial\delta\phi_i}{\partial x_q}A_{iqkl}\frac{\partial\phi_k}{\partial x_l}\,d\Omega \\ +\int_{\Omega}\frac{\partial^2\delta\phi_i}{\partial x_q\partial x_p}\left[E_{ipqklm}\frac{\partial^2\phi_k}{\partial x_m\partial x_l}\right]d\Omega \\ +\int_{\Omega}\frac{\partial\delta\phi_i}{\partial x_q}\left[\frac{\partial E_{ipqklm}}{\partial\Delta\varepsilon_{st}}\frac{\partial^2\phi_s}{\partial x_t\partial x_p}\frac{\partial^2\phi_k}{\partial x_m\partial x_l}\right]d\Omega \end{bmatrix} = \int_{\Gamma}\begin{bmatrix} \delta\phi_i n_q\left[A_{iqkl}\frac{\partial\phi_k}{\partial x_l}\right] \\ -\delta\phi_i n_q\left[E_{ipqklm}\frac{\partial^3\phi_k}{\partial x_m\partial x_l\partial x_p}\right] \\ -\delta\phi_i n_q\left[\frac{\partial E_{ipqklm}}{\partial\varepsilon^0_{st}}\frac{\partial^2\phi_s}{\partial x_t\partial x_p}\frac{\partial^2\phi_k}{\partial x_m\partial x_l}\right] \\ -\delta\phi_i n_q\left[\frac{\partial E_{ipqklm}}{\partial\varepsilon^0_{st}}\frac{\partial^2\phi_s}{\partial x_t\partial x_p}\frac{\partial^2\phi_k}{\partial x_m\partial x_l}\right] \\ +\frac{\partial\delta\phi_i}{\partial x_q}n_p\left[E_{ipqklm}\frac{\partial^2\phi_k}{\partial x_m\partial x_l}\right] \end{bmatrix}.d\Gamma \qquad \text{(B2-8.9)}$$

where:

$$-\int_{\Omega}\delta\phi_i\left[\frac{\partial E_{ipqklm}}{\partial\Delta\varepsilon^0_{st}}\frac{\partial^3\phi_s}{\partial x_t\partial x_p\partial x_q}\frac{\partial^2\phi_k}{\partial x_m\partial x_l}\right]d\Omega = -\int_{\Gamma}\delta\phi_i n_q\left[\frac{\partial E_{ipqklm}}{\partial\Delta\varepsilon^0_{st}}\frac{\partial^2\phi_s}{\partial x_t\partial x_p}\frac{\partial^2\phi_k}{\partial x_m\partial x_l}\right]d\Gamma$$
$$+\int_{\Omega}\frac{\partial\delta\phi_i}{\partial x_q}\left[\frac{\partial E_{ipqklm}}{\partial\Delta\varepsilon^0_{st}}\frac{\partial^2\phi_s}{\partial x_t\partial x_p}\frac{\partial^2\phi_k}{\partial x_m\partial x_l}\right]d\Omega+\int_{\Omega}\delta\phi_i\left[\frac{\partial E_{ipqklm}}{\partial\Delta\varepsilon^0_{st}}\frac{\partial^3\phi_s}{\partial x_t\partial x_p\partial x_q}\frac{\partial^2\phi_k}{\partial x_m\partial x_l}\right] \qquad \text{(B2-8.10)}$$

By substituting (B2-7.10) into (B2-7.9), equation (B2-7.2) becomes:

$$\left[\begin{array}{l} +\int_{\Omega}\frac{\partial\delta\phi_i}{\partial x_q}A_{iqkl}\frac{\partial\phi_k}{\partial x_l}\,d\Omega \\ +\int_{\Omega}\frac{\partial^2\delta\phi_i}{\partial x_q\partial x_p}\left[E_{ipqklm}\frac{\partial^2\phi_k}{\partial x_m\partial x_l}\right]d\Omega \end{array}\right]=\int_{\Gamma}\left[\begin{array}{l} \delta\phi_i n_q\left[A_{iqkl}\frac{\partial\phi_k}{\partial x_l}\right] \\ -\delta\phi_i n_q\left[E_{ipqklm}\frac{\partial^3\phi_k}{\partial x_m\partial x_l\partial x_p}\right] \\ -\delta\phi_i n_q\left[\frac{\partial E_{ipqklm}}{\partial\Delta\varepsilon^0_{st}}\frac{\partial^2\phi_s}{\partial x_t\partial x_p}\frac{\partial^2\phi_k}{\partial x_m\partial x_l}\right] \\ +\frac{\partial\delta\phi_i}{\partial x_q}n_p\left[E_{ipqklm}\frac{\partial^2\phi_k}{\partial x_m\partial x_l}\right] \end{array}\right]d\Gamma \qquad \text{(B2-9)}$$

Then, recalling the equilibrium equation (B2-7):

$$\frac{\partial\Delta W}{\partial\gamma^0_{iq}}=G_{iqjl}\Delta\gamma^0_{jl}=0=$$

$$-G_{iqjl}\frac{\partial^2\Delta\omega_j}{\partial x_l\partial x_q}-\frac{\partial G_{iqjl}}{\partial\Delta\gamma^0_{st}}\frac{\partial\Delta\gamma^0_{st}}{\partial x_q}\frac{\partial\Delta\omega_j}{\partial x_l}=-G_{iqjl}\frac{\partial^2\Delta\omega_j}{\partial x_l\partial x_q}-\frac{\partial G_{iqjl}}{\partial\Delta\gamma^0_{st}}\frac{\partial^2\Delta\omega_s}{\partial x_t\partial x_q}\frac{\partial\Delta\omega_j}{\partial x_l}$$

Its weak form is derived as follows:

$$-\int_{\Omega}\delta\omega_i\left[G_{iqjl}\frac{\partial^2\Delta\omega_j}{\partial x_l\partial x_q}+\frac{\partial G_{iqjl}}{\partial\Delta\gamma^0_{st}}\frac{\partial^2\Delta\omega_s}{\partial x_t\partial x_q}\frac{\partial\Delta\omega_j}{\partial x_l}\right]d\Omega=0=$$

$$-\int_{\Gamma}\delta\omega_i n_q\left[G_{iqjl}\frac{\partial\Delta\omega_j}{\partial x_l}\right]d\Gamma-\int_{\Gamma}\delta\omega_i n_q\left[\frac{\partial G_{iqjl}}{\partial\Delta\gamma^0_{st}}\frac{\partial\Delta\omega_s}{\partial x_t}\frac{\partial\Delta\omega_j}{\partial x_l}\right]d\Gamma+$$

$$\int_{\Omega}\frac{\partial\delta\omega_i}{\partial x_q}\left[G_{iqjl}\frac{\partial\Delta\omega_j}{\partial x_l}\right]d\Omega+\int_{\Omega}\delta\omega_i\left[\frac{\partial G_{iqjl}}{\partial\Delta\gamma^0_{st}}\frac{\partial^2\Delta\omega_s}{\partial x_t\partial x_q}\frac{\partial\Delta\omega_j}{\partial x_l}\right]d\Omega+$$

$$\int_{\Omega}\frac{\partial\delta\omega_i}{\partial x_q}\left[\frac{\partial G_{iqjl}}{\partial\Delta\gamma^0_{st}}\frac{\partial\Delta\omega_s}{\partial x_t}\frac{\partial\Delta\omega_j}{\partial x_l}\right]d\Omega+\int_{\Omega}\delta\omega_i\left[\frac{\partial G_{iqjl}}{\partial\Delta\gamma^0_{st}}\frac{\partial^2\Delta\omega_s}{\partial x_t\partial x_q}\frac{\partial\Delta\omega_j}{\partial x_l}\right]d\Omega$$

(B2-10)

where

$$\int_{\Omega} \delta\omega_i \left[\frac{\partial G_{iqjl}}{\partial \Delta\gamma_{st}^0} \frac{\partial^2 \Delta\omega_s}{\partial x_t \partial x_q} \frac{\partial \Delta\omega_j}{\partial x_l} \right] d\Omega =$$

$$\int_{\Gamma} \delta\omega_i n_q \left[\frac{\partial G_{iqjl}}{\partial \Delta\gamma_{st}^0} \frac{\partial \Delta\omega_s}{\partial x_t} \frac{\partial \Delta\omega_j}{\partial x_l} \right] d\Gamma - \int_{\Omega} \delta\omega_i \left[\frac{\partial G_{iqjl}}{\partial \Delta\gamma_{st}^0} \frac{\partial^2 \Delta\omega_s}{\partial x_t \partial x_q} \frac{\partial \Delta\omega_j}{\partial x_l} \right] d\Omega - \int_{\Omega} \frac{\partial \delta\omega_i}{\partial x_q} \left[\frac{\partial G_{iqjl}}{\partial \Delta\gamma_{st}^0} \frac{\partial \Delta\omega_s}{\partial x_t} \frac{\partial \Delta\omega_j}{\partial x_l} \right]$$

(B2-10.1)

By substituting (B2-10.1) into (B2-10):

$$-\int_{\Omega} \delta\omega_i \left[G_{iqjl} \frac{\partial^2 \Delta\omega_j}{\partial x_l \partial x_q} + \frac{\partial G_{iqjl}}{\partial \Delta\gamma_{st}^0} \frac{\partial^2 \Delta\omega_s}{\partial x_t \partial x_q} \frac{\partial \Delta\omega_j}{\partial x_l} \right] d\Omega = 0$$

$$\int_{\Omega} \frac{\partial \delta\omega_i}{\partial x_q} \left[G_{iqjl} \frac{\partial \Delta\omega_j}{\partial x_l} \right] d\Omega = \int_{\Gamma} \delta\omega_i n_q \left[G_{iqjl} \frac{\partial \Delta\omega_j}{\partial x_l} \right] d\Gamma \qquad \text{(B2-11)}$$

Summarizing, we recall the final weak forms described on equations (B2-9) and (B2-10):

$$\begin{bmatrix} +\int_{\Omega} \frac{\partial \delta\phi_i}{\partial x_q} A_{iqkl} \frac{\partial \phi_k}{\partial x_l} d\Omega \\ +\int_{\Omega} \frac{\partial^2 \delta\phi_i}{\partial x_q \partial x_p} \left[E_{ipqklm} \frac{\partial^2 \phi_k}{\partial x_m \partial x_l} \right] d\Omega \end{bmatrix} = \int_{\Gamma} \begin{bmatrix} \delta\phi_i n_q \left[A_{iqkl} \frac{\partial \phi_k}{\partial x_l} \right] \\ -\delta\phi_i n_q \left[E_{ipqklm} \frac{\partial^3 \phi_k}{\partial x_m \partial x_l \partial x_p} \right] \\ -\delta\phi_i n_q \left[\frac{\partial E_{ipqklm}}{\partial \Delta\varepsilon_{st}^0} \frac{\partial^2 \phi_s}{\partial x_t \partial x_p} \frac{\partial^2 \phi_k}{\partial x_m \partial x_l} \right] \\ +\frac{\partial \delta\phi_i}{\partial x_q} n_p \left[E_{ipqklm} \frac{\partial^2 \phi_k}{\partial x_m \partial x_l} \right] \end{bmatrix} d\Gamma.$$

(B2-9)

$$\int_{\Omega} \frac{\partial \delta\omega_i}{\partial x_q}\left[G_{iqjl} \frac{\partial \Delta\omega_j}{\partial x_l} \right] d\Omega = \int_{\Gamma} \delta\omega_i n_q \left[G_{iqjl} \frac{\partial \Delta\omega_j}{\partial x_l} \right] d\Gamma$$

(B2-10)

where:

$$\Delta\sigma^0_{iq} = A_{iqkl}\Delta\varepsilon^0_{kl} = A_{iqkl}\frac{\partial \phi_k}{\partial x_l}$$

$$\Delta\sigma^I_{ipq} = E_{ipqklm}\Delta\varepsilon^I_{klm} = E_{ipqklm}\frac{\partial^2 \phi_k}{\partial x_m \partial x_l}$$

$$\frac{\partial \Delta\sigma^I_{ipq}}{\partial x_p} = E_{ipqklm}\frac{\partial \Delta\varepsilon^I_{klm}}{\partial x_p} + \frac{\partial E_{ipqklm}}{\partial \Delta\varepsilon_{st}}\frac{\partial \Delta\varepsilon_{st}}{\partial x_p}\varepsilon^I_{klm} = E_{ipqklm}\frac{\partial^3 \phi_k}{\partial x_m \partial x_l \partial x_p} + \frac{\partial E_{ipqklm}}{\partial \Delta\varepsilon_{st}}\frac{\partial^2 \phi_s}{\partial x_t \partial x_p}\frac{\partial^2 \phi_k}{\partial x_m \partial x_l}$$

$$\Delta\mu^0_{iq} = G_{iqjl}\Delta\gamma^0_{jl} = G_{iqjl}\frac{\partial \Delta\omega_j}{\partial x_l}$$

Then, the weak form equations can be rewritten as:

$$\int_{\Omega} \frac{\partial \delta\phi_i}{\partial x_q} A_{iqkl}\frac{\partial \phi_k}{\partial x_l}\, d\Omega + \int_{\Omega} \frac{\partial^2 \delta\phi_i}{\partial x_q \partial x_p}\left[E_{ipqklm}\frac{\partial^2 \phi_k}{\partial x_m \partial x_l} \right] d\Omega = \int_{\Gamma} \left[\delta\phi_i n_q \left(\Delta\sigma^0_{iq} - \frac{\partial \Delta\sigma^I_{ipq}}{\partial x_p} \right). + n_p \frac{\partial \delta\phi_i}{\partial x_q}\Delta\sigma^I_{ipq} \right] d\Gamma$$

(B2-12)

$$\int_{\Omega} \frac{\partial \delta\omega_i}{\partial x_q}\left[G_{iqjl}\frac{\partial \Delta\omega_j}{\partial x_l} \right] d\Omega = \int_{\Gamma} \delta\omega_i n_q \Delta\mu^0_{iq} d\Gamma$$

(B2-13)